

CHEMICAL AND THERMODYNAMIC PROPERTIES OF ACCEPT2.0 CLUSTERS

By

Dana Lindsey Koeppe

A DISSERTATION

Submitted to
Michigan State University
in partial fulfillment of the requirements
for the degree of

Astrophysics and Astronomy – Doctor of Philosophy

2021

ABSTRACT

CHEMICAL AND THERMODYNAMIC PROPERTIES OF ACCEPT2.0 CLUSTERS

By

Dana Lindsey Koeppé

Clusters of galaxies offer tremendous insight into the formation and evolution of large scale structure in the Universe. While most of the total mass of a cluster is in the form of dark matter, the bulk of observable matter exists as a hot X-ray emitting gas called the intracluster medium (ICM). Studies of X-ray emission from the ICM reveal the thermodynamic and chemical processes that affect cluster formation and evolution. Additionally, measurements of emission lines in the X-ray spectra of clusters revealed that the ICM is polluted with heavy elements that originated in stars, mostly in galaxies. The radial distributions of those heavy elements show evidence of interplay between the ICM and the cluster core.

In chapter 2, we describe the data reduction and spectral analysis of an archival sample of X-ray observations of clusters from the second catalog of the Archive of *Chandra* Cluster Entropy Profile Tables (ACCEPT2.0). These clusters are used throughout this thesis to show how cluster X-ray properties can be used to test and constrain our theories of structure growth in the Universe. We also find that our analysis for the $L_X - T$ relation is consistent with previous works.

We explore an analysis application of the $L_X - T$ relation for ACCEPT2.0 data in chapter 3 by testing a recent claim that the expansion of the Universe is not uniform in all directions. If the expansion of the universe were isotropic, the luminosity and temperature should scale similarly for clusters in all directions. Using global core-excised luminosities and temperatures for 302 ACCEPT2.0 clusters, we found that our sample measurements support the assumption of isotropic expansion.

Chapter 4 investigates how the amount of metals in clusters' ICM changes with redshift. Previous works have shown varying results, which are more scattered when including core emission. We show that the core-excised abundances for 302 ACCEPT2.0 clusters are not statistically different

between cool-core (CC) and non-cool core (NCC) clusters, and that the global metallicity content of the ICM does not change significantly as a function of luminosity or redshift. Furthermore, we explore the degree to which a small systematic bias arising from model uncertainties that affect hot and cool spectra can look like evolution if luminosity bias is not taken into account.

Finally, chapter 5 describes the ongoing work of a data reduction pipeline for the SOAR Adaptive-Module Optical Spectrograph (*SAMOS*). *SAMOS* is a multi-object spectrograph which will be commissioned on the SOuthern Astrophysical Research Telescope (SOAR) in 2021. The current version of the pipeline is able to produce wavelength calibrated spectra from test data using SOAR *Goodman*, and is in active development.

To my sister, mom, and dad—Thank you for always supporting me. I love you forever.

ACKNOWLEDGEMENTS

The completion of this work is owed to the support and friendship of many colleagues over the years. I would like to thank my cat, Gus (the best work-from-home buddy and the best cat, no matter what anybody else says), Massimo Robberto, Rachel Frisbie, Mark Voit, Laura Chomiuk, Kim Crosslan, Sam Swihart, Danny Huijenga, Carl Fields, Jenn Ranta, Austin Edmister, Laura Shishkovsky, Kelsey Funkhouser, Jessica Maldonado, Thomas Connor, Dan Kelson, Michael McDonald. I owe many thanks to my committee members Brian O’Shea, Steve Zepf, Jay Strader, and Kirsten Tollefson. Finally, I am especially grateful for the encouragement and support of my advisor, Megan Donahue, without whom this dissertation would not have been possible.

The financial support for this dissertation was provided by the following grants: NASA NNX13A141G (HST Treasury Program/CLASH), a Chandra program GO5-16132-x, an HST grant HST-GO-15661.002-A. The majority of the support came from an NSF/JHU subaward JHU-2003349346 grant (SOAR Adaptive-optics Multi-Object Spectrograph, or SAMOS). The pipeline I designed in this project is described in Chapter 4. This dissertation work was also supported by the MSU College of Natural Science Continuation (Fall 2019) and Completion (Summer 2020) Fellowships.

TABLE OF CONTENTS

LIST OF TABLES	viii
LIST OF FIGURES	ix
CHAPTER 1 INTRODUCTION	1
1.1 Cluster Observables	2
1.2 Terminology	3
1.2.1 Cosmology vernacular	3
1.2.2 Anatomy of galaxy clusters	5
1.3 X-ray scaling relations	6
1.4 Metals in the ICM	11
1.5 This work	14
CHAPTER 2 ACCEPT2.0	15
2.1 Archive of Chandra Cluster Entropy Profile Tables (ACCEPT)	15
2.2 ACCEPT2.0	16
2.3 K-correction and bolometric correction	18
2.4 Vetting of the Data	19
2.4.1 Initial Cuts	20
2.4.2 Radially weighted temperature and abundance	22
2.4.3 $L_X - T$ relation	23
CHAPTER 3 LUMINOSITY-TEMPERATURE RELATION OF ACCEPT2.0 CLUSTERS	59
3.1 The Sample	61
3.2 Methods	63
3.3 Results	64
3.4 Discussion	67
3.4.1 Core-excised vs. core included L_X	68
3.4.2 Different spectral energy bandpasses	70
3.5 Conclusion	75
CHAPTER 4 GLOBAL METALLICITY EVOLUTION OF ACCEPT2.0 CLUSTERS	88
4.1 The Sample	89
4.2 Methods	90
4.3 Results	91
4.3.1 Dependence on core status	91
4.3.2 Luminosity dependence	93
4.3.3 Redshift Dependence	94
4.3.4 Multiple Linear Regression Analysis	95
4.3.5 Comparison to Maughan et al. (2008)	97
4.4 Discussion	105
4.4.1 Comparison to observations	105

4.4.2	Comparison to simulations	106
4.5	Summary and Conclusions	107
CHAPTER 5 PIPELINE FOR THE REDUCTION OF DATA FROM THE SOAR ADAPTIVE-OPTICS MULTI-OBJECT SPECTROGRAPH (SAMOS)		120
5.1	Pipeline Organization	122
5.2	Step 0: Pipeline Initialization	124
5.3	Step 1: CCD Image Processing	126
5.4	Step 2: Slit tracing and extraction	127
5.4.1	Note on spectral extraction and tracing	128
5.5	Step 3: Wavelength calibration	128
5.6	Remaining steps	131
APPENDICES		134
APPENDIX A	BOLOMETRIC AND K- CORRECTION PROCEDURE	135
APPENDIX B	RADIAL ABUNDANCE PROFILES FOR ACCEPT2.0 CLUSTERS	139
APPENDIX C	RADIAL TEMPERATURE PROFILES FOR ACCEPT2.0 CLUSTERS	158
BIBLIOGRAPHY		177

LIST OF TABLES

Table 2.1: ACCEPT vs. ACCEPT2.0	16
Table 2.2: ACCEPT2.0 Redshift Updates.	21
Table 2.3: Global CE properties for 432 ACCEPT2.0 clusters	26
Table 2.4: Table of full cluster names and coordinates in ACCEPT2.0.	43
Table 3.1: Best fit $L_X - T$ using tied and separate models	68
Table 3.2: Difference in normalization of $L_X - T$	69
Table 3.3: Global CE $L_X - T$ properties for clusters separated by sky region.	76
Table 4.1: Median global CE abundances of ACCEPT2.0 sub samples.	96
Table 4.2: Best fit parameters to the $Z(L_X, z)$ model.	96
Table 4.3: Median CE global abundances comparison for ACCEPT2.0 and M08 overlap.	100
Table 4.4: Global CE luminosities and metallicities M08 and ACCEPT2.0 overlap.	100
Table 4.5: Global CE temperatures M08 and ACCEPT2.0 overlap.	103
Table 4.6: Full global metallicity table for 302 ACCEPT2.0 clusters.	108
Table 5.1: SAMOS reduction pipeline status.	123

LIST OF FIGURES

Figure 1.1: CC vs. NCC surface brightness profiles.	7
Figure 1.2: CC vs. NCC radial temperature profiles.	8
Figure 1.3: CC vs. NCC X-ray emission	11
Figure 1.4: Simulated X-ray spectra.	13
Figure 2.1: $L_X - T$ core-included and core-excised posterior distributions.	24
Figure 2.2: $L_X - T$ core-included vs. core-excised.	25
Figure 3.1: ACCEPT2.0 all-sky map.	63
Figure 3.2: Posterior $L_X - T$ distributions for RF, RB, and NR clusters.	65
Figure 3.3: Posterior distributions for the tied $L_X - T$ model.	66
Figure 3.4: Best fit $L_X - T$ for NR clusters.	70
Figure 3.5: Best fit $L_X - T$ for RB clusters.	71
Figure 3.6: Best fit $L_X - T$ for RF clusters.	72
Figure 3.7: Stacked tied and separate $L_X - T$ for NR, RF, and RB clusters.	73
Figure 3.8: $L_X - T$ for bandpass vs. bolometric luminosities.	73
Figure 4.1: Global Z null model MCMC results.	92
Figure 4.2: Redshift distribution of CC and NCC clusters in ACCEPT2.0.	93
Figure 4.3: Binned weighted mean metallicity profiles for CCs and NCCs.	94
Figure 4.4: Stacked weighted median metallicity profiles for CC and NCC clusters.	95
Figure 4.5: Metallicity differences between simulated clusters.	97
Figure 4.6: Best fit results global CE abundance as a function of L_X and Z .	98
Figure 4.7: Temperatures from M08 vs. ACCEPT2.0.	99

Figure 5.1: Cartoon multi-object spectra.	121
Figure 5.2: First CCD data reduction steps.	127
Figure 5.3: Slit cutout diagram.	129
Figure 5.4: Cartoon diffraction grating.	130
Figure 5.5: Wavelength calibrated spectrum output for <i>SAMOS</i> pipeline.	131
Figure B.1: Radial metallicity profile for clusters A0013 through A0160.	140
Figure B.2: Radial metallicity profile for clusters 011502+002441 through A3094.	141
Figure B.3: Radial metallicity profile for clusters A3128 through AS0463.	142
Figure B.4: Radial metallicity profile for clusters 04371+0043 through A3376.	143
Figure B.5: Radial metallicity profile for clusters A3391 through A0611.	144
Figure B.6: Radial metallicity profile for clusters A0644 through HydraA.	145
Figure B.7: Radial metallicity profile for clusters 0947124+762313 through A1033.	146
Figure B.8: Radial metallicity profile for clusters A1068 through A1423.	147
Figure B.9: Radial metallicity profile for clusters 4-33144 through A1664.	148
Figure B.10: Radial metallicity profile for clusters A1689 through LCDCS0829.	149
Figure B.11: Radial metallicity profile for clusters A1835 through 145715+222009.	150
Figure B.12: Radial metallicity profile for clusters AS0780 through 15328+3021.	151
Figure B.13: Radial metallicity profile for clusters A2107 through A2204.	152
Figure B.14: Radial metallicity profile for clusters A2218 through 43072.	153
Figure B.15: Radial metallicity profile for clusters A2261 through A2384.	154
Figure B.16: Radial metallicity profile for clusters A2390 through A3921.	155
Figure B.17: Radial metallicity profile for clusters A2537 through A4038.	156
Figure B.18: Radial metallicity profile for A2670.	157

Figure C.1: Radial temperature profile for clusters A0013 through A0160.	159
Figure C.2: Radial temperature profile for clusters 011502+002441 through A3094.	160
Figure C.3: Radial temperature profile for clusters A3128 through AS0463.	161
Figure C.4: Radial temperature profile for clusters 04371+0043 through A3376.	162
Figure C.5: Radial temperature profile for clusters A3391 through A0611.	163
Figure C.6: Radial temperature profile for clusters A0644 through HydraA.	164
Figure C.7: Radial temperature profile for clusters 0947124+762313 through A1033.	165
Figure C.8: Radial temperature profile for clusters A1068 through A1423.	166
Figure C.9: Radial temperature profile for clusters 4-33144 through A1664.	167
Figure C.10: Radial temperature profile for clusters A1689 through LCDCS0829.	168
Figure C.11: Radial temperature profile for clusters A1835 through 145715+222009.	169
Figure C.12: Radial temperature profile for clusters AS0780 through 15328+3021.	170
Figure C.13: Radial temperature profile for clusters A2107 through A2204.	171
Figure C.14: Radial temperature profile for clusters A2218 through 43072.	172
Figure C.15: Radial temperature profile for clusters A2261 through A2384.	173
Figure C.16: Radial temperature profile for clusters A2390 through A3921.	174
Figure C.17: Radial temperature profile for clusters A2537 through A4038.	175
Figure C.18: Radial temperature profile for A2670.	176

CHAPTER 1

INTRODUCTION

As their name suggests, galaxy clusters are made from many individual galaxies living together in a large gravitational potential. These structures are typically $10^{14} - 10^{15} M_{\odot}$ ¹ and contain anywhere from a few hundred to tens of thousands of galaxies which are visible to us. Zwicky (1933) made one of the first mass estimates of the Coma cluster from observations of galaxy velocity dispersions, and the application of the virial theorem. Zwicky (1933, 1937) showed that if clusters are long-lived structures, there must be 10-100 times more unobserved matter, or “dark matter,” than can be accounted for by the stars in the galaxies. This dark matter comprises 80-85% of the mass of a cluster, with the remainder in the form of observable baryons.

Before X-ray telescopes, clusters were defined by their optical properties. For instance, one could estimate the size of a cluster by the luminosity of its brightest members, or its “optical richness”. Originally defined by Abell (1958), optical richness is the number of galaxies brighter than some magnitude limit, with the richest clusters containing over 300 such galaxies, and fewer than 100 in poor clusters. In the 1960s and ‘70s, extended X-ray emission from the nearby Virgo, Coma, and Perseus clusters (Bradt et al., 1967; Meekins et al., 1971; Gursky et al., 1971; Forman et al., 1972) revealed that most of a cluster’s baryonic mass is in the form of hot X-ray emitting plasma that permeates the intracluster medium (ICM). The ubiquity of this hot gas naturally has led us to questions about the origin of the ICM, and its relation to cluster formation and evolution.

With larger sample sizes, we have been able to study clusters in a broader context, and better understand their general characteristics. However, many samples in the past have been a combination of previously analyzed data from multiple works. Consequently, combining different catalogs necessitates the use of correction factors to account for systematic differences between samples. The second release of the Archive of Chandra Cluster Entropy Profile Tables (Donahue, Baldi, et al, in prep, hereafter, ACCEPT2.0) will be the largest publicly available catalog of uniformly derived

¹ $M_{\odot} \equiv 1$ solar mass $\sim 2 \times 10^{30}$ kg.

X-ray properties from X-ray observations of clusters of galaxies available from the Chandra Data Archive. Its predecessor ACCEPT (Cavagnolo et al., 2009) produced radial profiles of density, gas temperature, and entropy, which are related to the thermal history of a cluster. ACCEPT2.0 is an expansion of ACCEPT, as it includes measurements for more X-ray observables and contains more than twice as many clusters.

This dissertation will investigate the differences between the average global X-ray properties of clusters of galaxies at different cosmological epochs, and in different directions on the sky, using X-ray data from ACCEPT2.0. Section 1.1 of this introduction will describe the X-ray observables relevant to this dissertation. Section 1.2 defines the terms used throughout this work. Section 1.3 will give an overview of recent literature regarding scaling relations. Section 1.4 covers abundance measurements from X-ray spectra. Finally, Section 1.5 will present an overview of this dissertation.

1.1 Cluster Observables

The obvious cluster observables come from optical properties such as cluster richness (number of galaxies within 2 magnitudes² of the third brightest galaxy member) and compactness (number of galaxies within some characteristic radius of the cluster center) (Abell, 1958), but X-ray observables are most important for this research, as most of the baryons in a cluster are in the form of hot X-ray emitting gas. For reviews of galaxy clusters and how they relate to cosmology, see the review by Voit (2005). Reviews regarding X-ray emission from clusters are provided by Sarazin (1986) and Böhringer & Werner (2009). We study clusters of galaxies to understand the largest structures in the Universe. One aspect of the theory of gravitational assembly of cosmic structure is the prediction of the cluster mass function. The cluster mass function is the number density of clusters above a certain mass M as a function of redshift, and shows how many clusters of mass M exist a redshift. The cluster mass function would give insights into how large scale structures have grown over the history of the Universe. Unfortunately, mass is not a directly observable quantity, which

²The astronomical magnitude system quantifies the measured flux of visible light with a logarithmic brightness scale in which a difference of +5 magnitudes corresponds to a 100 factor decrease in brightness or flux. So an increase of two magnitudes corresponds to a factor of $100^{2/5} = 6.3$ fainter.

is where X-ray observations come in handy. Temperature T and luminosity L_X are easily derived from X-ray spectra. The temperature is tightly correlated with the mass, while the luminosity is more affected by processes such as recent mergers or AGN activity. Due to the dynamics affecting cluster luminosity, the scaling of luminosity with temperature ($L_X - T$) and mass ($L_X - M$) are more scattered than the mass-temperature ($M - T$) scaling. Therefore, we can use temperature and (less directly) luminosity in lieu of direct mass measurements.

Another spectral probe of the ICM comes in the form of emission lines. The ubiquitous presence of heavy elements such as iron in the spectra of clusters is evidence that the ICM is comprised of gas processed in stars and subsequently distributed throughout the cluster. The global metallicity content (amount of elements heavier than hydrogen or helium) of the clusters acts as a tracer for when stellar byproducts became part of the ICM, and spatially-resolved measurements give clues for how this enrichment occurs.

1.2 Terminology

Before proceeding, it is important to define some terminology that will be used throughout this dissertation.

1.2.1 Cosmology vernacular

An object’s redshift z is a dimensionless distance estimate based on the Doppler effect which arises from the finite speed of light and the expanding Universe. Consequently, the rest-frame wavelength of light from an object is lengthened—or “redshifted”—as light travels through the expanding Universe. The wavelength of emitted light increases by a factor of $1 + z$ i.e., $\lambda_{\text{obs}} = \lambda_{\text{rest}}(1 + z)$. Nearly a century ago, Edwin Hubble noticed that the recession velocity of galaxies increased in proportion to their distance, so more distant objects are moving away from us more quickly than nearby objects. We now characterize this expansion of the Universe through the Hubble parameter $H(z)$, where the present day Hubble constant H_0 is related to an object’s recessional

velocity v and its distance d ,³

$$v = H_0 \times d. \quad (1.1)$$

Here, the expansion rate of the present day Universe is H_0 . For this work, we assume single digit precision such that $H_0 = 70 \text{ km s}^{-1} \text{ Mpc}^{-1}$, where $1 \text{ Mpc} (\text{mega-parsec}) = 3.26 \times 10^6 \text{ light-years} = 3.086 \times 10^{24} \text{ cm}$.

We relate the Hubble constant as a function of redshift to the present day value via

$$H(z) = H_0 E(z), \quad (1.2)$$

where $E(z) = \sqrt{\Omega_M(1+z)^3 + \Omega_\Lambda}$, and the cosmological parameters $\Omega_m \simeq 0.3$ and $\Omega_\Lambda \simeq 0.7$ refer to the matter and dark energy content of the local Universe where $\Omega_X = \rho_X/\rho_{c,0}$ (I will define $\rho_{c,0}$ soon.) and redshift z serves as a distance measure. Objects that are moving outward along the line of sight experience a redshift due to the Doppler Effect, so z is able to give a general idea of the distance to a source based on its recession velocity. For local systems, redshift is $z \sim 0$. The redshift of a cluster is important for estimating its properties because it tells us about the environment in which it formed. For a given redshift and Hubble parameter, there is some critical density $\rho_c(z)$ at which the gravitational potential of material within some radius overcomes and slows the expansion of space. The critical density is the maximum average density a Universe without dark energy can have before it would continue to expand forever. For reference, the present day critical density is

$$\rho_{c,0} = \frac{3H_0^2}{8\pi G} \approx 10^{-29} \text{ g cm}^{-3}, \quad (1.3)$$

where $G = 6.67 \times 10^{-8} \text{ cm}^3 \text{ g}^{-1} \text{ s}^{-2}$ is the gravitational constant. We relate the critical density at different cosmological epochs to the present day critical density $\rho_{c,0}$ via

$$\rho_c(z) = E(z)^2 \rho_{c,0}. \quad (1.4)$$

³ $H(z) \simeq H_0$ (constant) when $z \ll 1$. For larger z , the co-moving radial distance is $d(z) = c \int_0^z dz/H(z)$. For flat universes, the luminosity distance, used to relate bolometric flux and bolometric luminosity by the equation $L = 4\pi d_L^2 F$ is $d_L = (1+z)d$.

1.2.2 Anatomy of galaxy clusters

Ideally, clusters are spherical virialized structures in which a sphere of gas is supported against further collapse by outward pressure provided by the kinetic energy of the particles. According to the virial theorem, the average kinetic energy (E_K) of gas in an idealized ICM model is related to its gravitational potential energy (E_G) by

$$E_K = -\frac{1}{2}E_G. \quad (1.5)$$

Based on a virialized sphere of gas with mass M_v , the virial radius R_v is often used as a reference point for the “edge” of a cluster. Assuming the gas has been heated solely by gravitational processes, R_v is the radius inside which the temperature of the gas (i.e. the virial temperature, T_v) provides enough thermal pressure to support the ICM against further collapse. In simulations, R_v turns out to be the radius at which the density of material is ~ 180 - 200 times the critical density of the Universe at the epoch of interest (Voit, 2005). However, R_v is out of the typical X-ray instrument field of view for most nearby systems, and X-ray observations have to be fairly sensitive to detect an X-ray cluster this far from its much brighter center, so we often use scaled radii R_Δ to define our regions of interest for a cluster. R_Δ refers to the radius at which the density is Δ times the critical density of the Universe at the redshift of the cluster. Similarly, we define characteristic mass M_Δ and temperatures T_Δ as the mass and temperature within the scaled radius. Two commonly used values of Δ are 2500 and 500 . Keep in mind that a smaller R_Δ refers to a region of lower density and is therefore at larger radial distances, with virial radius being $\sim R_{200}$. The use of scaled radii is also important for comparing clusters at different epochs because, as shown in Equation 1.4, the critical density changes with redshift as $\rho_c(z) \sim (1+z)^3$. Due to expansion, the Universe is less dense today than in the past. Therefore, the angular size of R_Δ is larger for a cluster at low z than for an identical such cluster at high z . Similarly, the angular size R_Δ can differ between clusters of different masses at the same z . Scaled radii are therefore useful because they factor out the angular size differences of clusters and allow us to directly compare their properties within similarly defined regions.

An interesting distinction between clusters is their status as either cool-core (CC) or non-cool core (NCC). The term “cool-core” arises from the drop in temperature towards the center. Increased density towards the centers of CCs result in sharper peaks in surface brightness aligning with the drop in the temperature profile. NCCs, however, show less dramatic central luminosity peaks and flatter temperature profiles in their cores. Outside the core radius, their temperatures and X-ray surface brightness profiles are nearly indistinguishable when scaled by size. The stacked profiles of CC Abell 2390 and NCC Abell 2219 give good examples of differences in surface brightness (Figure 1.1) and radial temperature profiles (Figure 1.2) between CCs and NCCs. Choice of aperture is therefore crucial when characterizing clusters by global X-ray properties.

With adequate spatial resolution, global X-ray properties can be estimated for clusters within a full aperture, or for a core-excised aperture. We use core-excised global properties because they minimize dependence on a cluster’s core status. The “core” is used to describe the region inside which the density is such that thermodynamics unrelated to gravity can affect the gas in times comparable to the Hubble time, and shorter timescales increase the scatter in observable properties (Vikhlinin et al., 2005; Pratt et al., 2006). For the clusters in this work, we define the core in terms of scale radius: $R_c = 0.3R_{2500}$. Inside this core radius, there is more variability in the X-ray emission between clusters, whereas cluster properties are less scattered in the region $[0.3 - 1]R_{2500}$. The radial profiles in Figures 1.1 and 1.2 show how clusters compare in these two regions, where R_c and R_{2500} are plotted as vertical dashed lines.

1.3 X-ray scaling relations

Early X-ray observations showed a strong correlation between luminosity and temperature, or $L_X - T$ (Mitchell & Culhane, 1977; Mushotzky, 1984). Scaling relations such as this one are used for comparison to expectations from theoretical models. It is easiest to model the ICM as a hydrostatic sphere which has collapsed under gravitational pressure and is supported against further collapse via thermal pressure. The gravitational potential of the system, and therefore the temperature, is set by the size of the initial overdensity from which it originated. Because gravity is scale-invariant, the simplified hydrostatic model of the ICM results in clusters which are identical

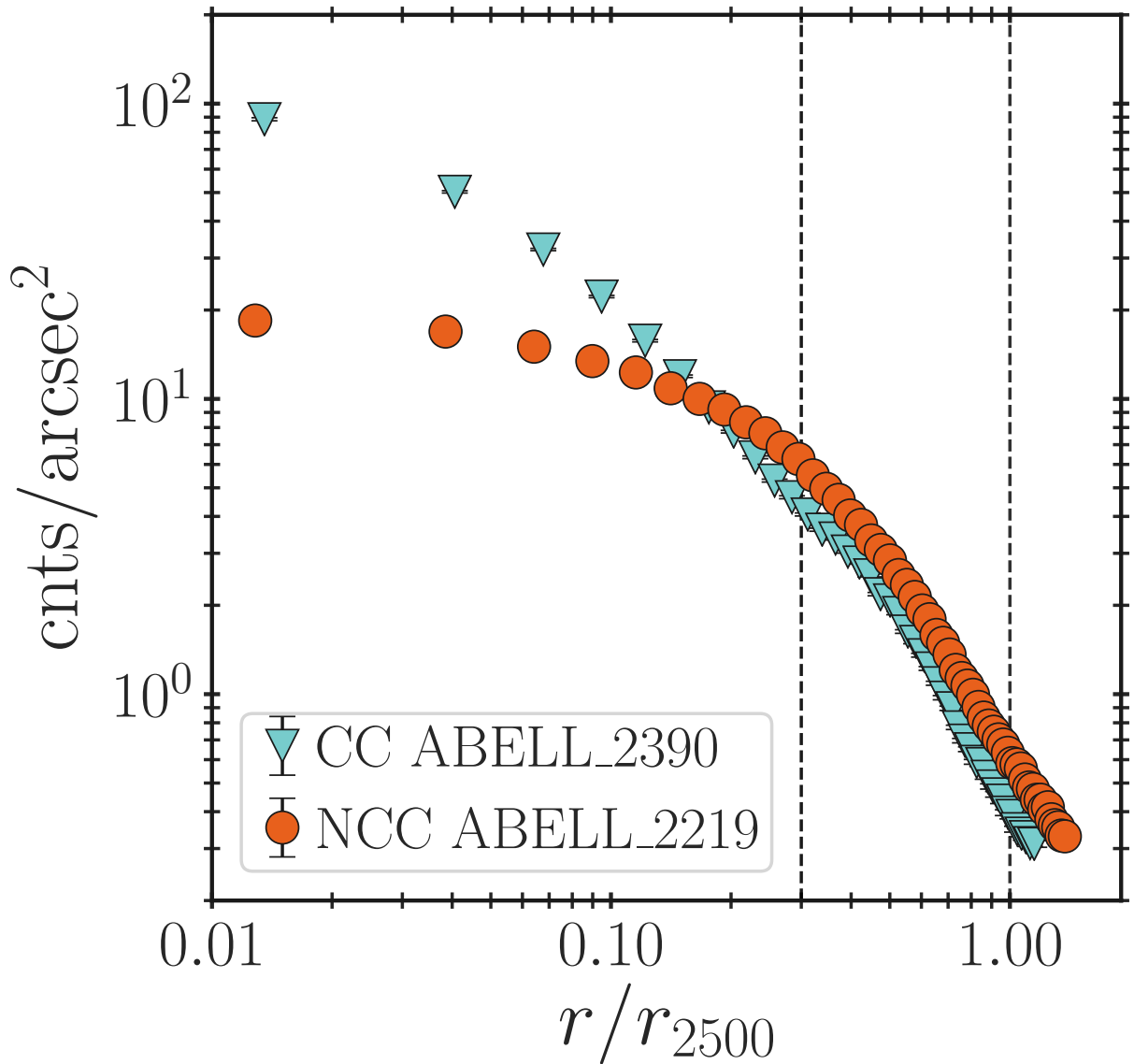


Figure 1.1: **CC vs. NCC surface brightness profiles.** ACCEPT2.0 surface brightness profile and the 1σ errors for cool-core cluster Abell 2390 (*blue triangles*) and non-cool core cluster (of similar mass) Abell 2219 (*red circles*). The dotted lines represent the core-excised region $0.3R_{2500} < r < 1R_{2500}$, where R_{2500} is the distance at which the mean density is 2500 times the background density.

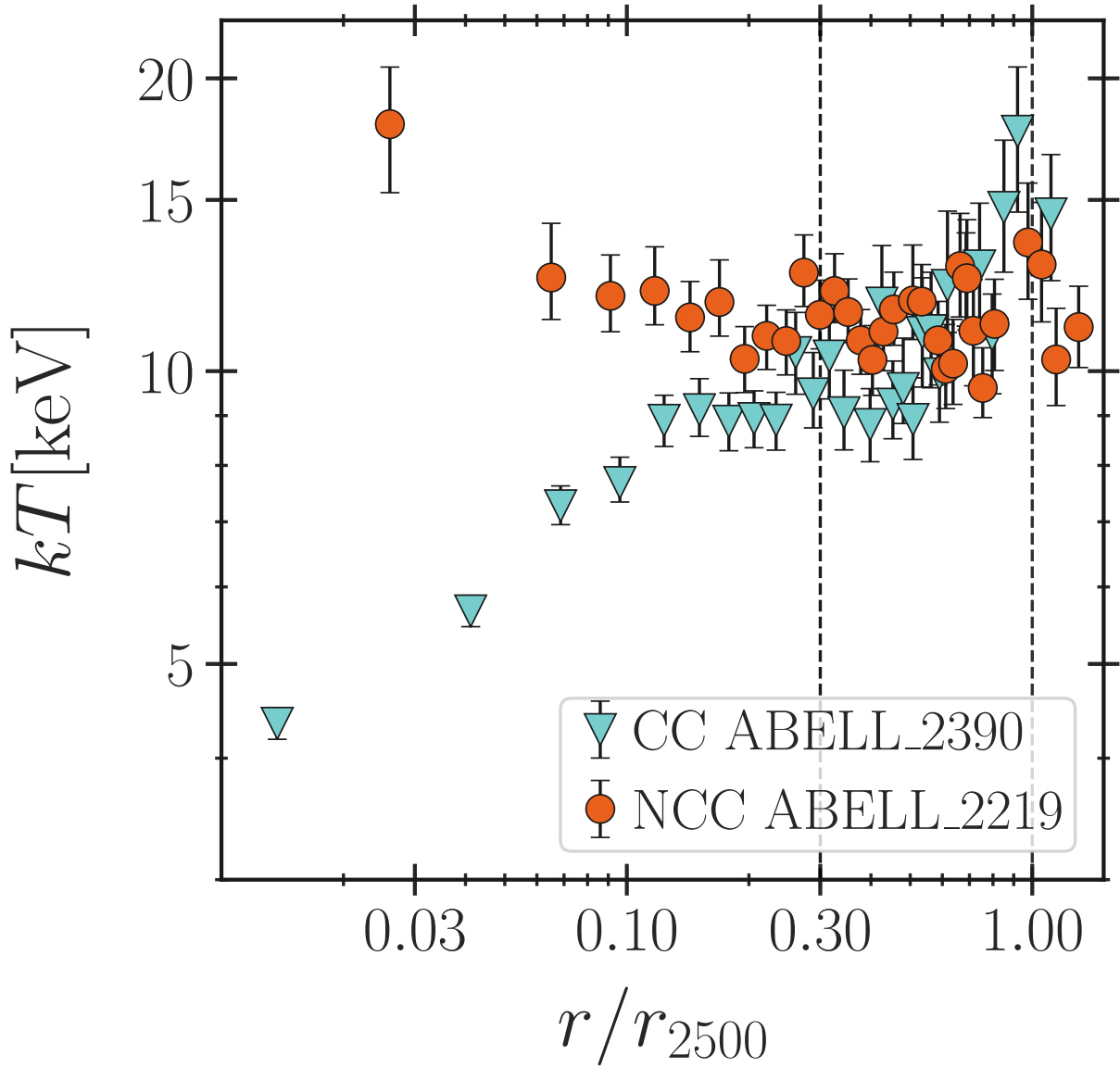


Figure 1.2: **CC vs. NCC radial temperature profiles.** Projected radial temperature profiles and their 1σ errors using the same labels as Figure 1.1.

when scaled by mass. This model leads to predictable, self-similar scaling relations between the observables and the mass (Kaiser, 1986). For this model, the mass enclosed within some scaled radius is,

$$M_\Delta = \Delta \frac{4}{3} \pi R_\Delta^3 \rho_c(z) \propto E(z)^2 R_\Delta^3. \quad (1.6)$$

Remember that the Δ in equation 1.6 is a scalar number reflecting the factor of the overdensity compared to the critical density at the redshift of the cluster (i.e, 200, 500, 2500, etc.).

The virial theorem states that bound particles in a spherical volume in hydrostatic equilibrium will have an average kinetic energy equal to half the total gravitational potential energy. According to the theorem, potential and kinetic energy of the particles are related by,

$$\frac{M_\Delta}{R_\Delta} \propto \sigma_v^2 \propto T. \quad (1.7)$$

Temperature should therefore scale with mass as

$$T \propto [E(z)M]^{2/3}. \quad (1.8)$$

For typical ICM temperatures of 10^7 - 10^8 K, the ICM radiates primarily via thermal bremsstrahlung due to collisions between ions and electrons. Assuming the gas is isothermal, the bolometric luminosity is $L_X \propto r^3 n_e^2 \Lambda(T)$, where the cooling function $\Lambda(T) \propto T^{1/2} e^{-E/kT}$ for thermal bremsstrahlung. Observations of the Perseus cluster by Branduardi-Raymont et al. (1981) showed a strongly peaked surface brightness profile which deviated from the isothermal model inside of ~ 10 kpc. The profile of the Coma cluster, which is recovering from a recent merger (White et al., 1993), was shown to be consistent with the expected model (Branduardi-Raymont et al., 1985; Briel et al., 1992; Jones & Forman, 1999). Other works which considered larger cluster samples showed that clusters could generally be separated into two categories: those with a discernible peak in the surface brightness and those with a flatter profile inside the core (Jones & Forman, 1984). CC clusters have been observed to have a steep decline in temperature and increased luminosity towards the center, as opposed to NCC clusters (Fabian, 1994; Arnaud et al., 2002; Maughan et al.,

2012). Outside of the denser regions, clusters are more well-behaved because the cooling time for the gas there is longer than the Hubble time, and therefore tracks the results of cosmological processes with longer timescales. Scaling relations of luminosity and temperature with cluster mass are therefore often evaluated using both core-excised CE and core-included CI measurements, where excising the core has been found to significantly reduce the scatter in the $L_X - T$ relation (e.g., Markevitch, 1998; Pratt et al., 2009; Maughan et al., 2012). These results suggests that clusters evolve self-similarly outside of the core region.

Still, the outer regions of clusters have been shown to deviate from the self-similar model. In the absence of extra heating and cooling of the gas, numerical simulations based on analytic theory predict,

$$\frac{L_X}{E(z)} \propto [M_\Delta E(z)]^{4/3} \propto T^2. \quad (1.9)$$

However, early CI observations showed slopes closer to ~ 3 instead of 2 (Mushotzky, 1984; Sarazin, 1988, and references therein; Edge & Stewart, 1991). Later generations of telescopes which were able to excise the core showed that the removing core emission only marginally reduces the slope of $L_X - T$ to just below 3 (Arnaud & Evrard, 1999; Ettori et al., 2004; Pratt et al., 2009; Mittal et al., 2011). Additionally, the observed $L_X - T$ relation may steepen even further for lower temperature systems (Maughan et al., 2012; Sun, 2012), although the increased scatter in the lower luminosity systems and the effects of selection bias makes this steepening challenging to verify. The deviation from the predictions of self-similarity models in the $L_X - T$ relation for all clusters and groups may be indicative of some source of non-gravitational processes such as AGN feedback, supernovae feedback, and radiative cooling. These processes may become more important compared to the energy per particle incurred from gravitational accretion for systems with shallower potential wells, such as groups of galaxies or individual galaxies. Heating/cooling of gas does not necessarily raise/lower the temperature of the gas so much as it decreases/increases the density, or, more specifically, increases/lowers the gas entropy. When heat is injected into the ICM, the gas puffs up and decreases the luminosity. Gas entropy, here scaled as $K \propto T n_e^{-2/3}$, is useful

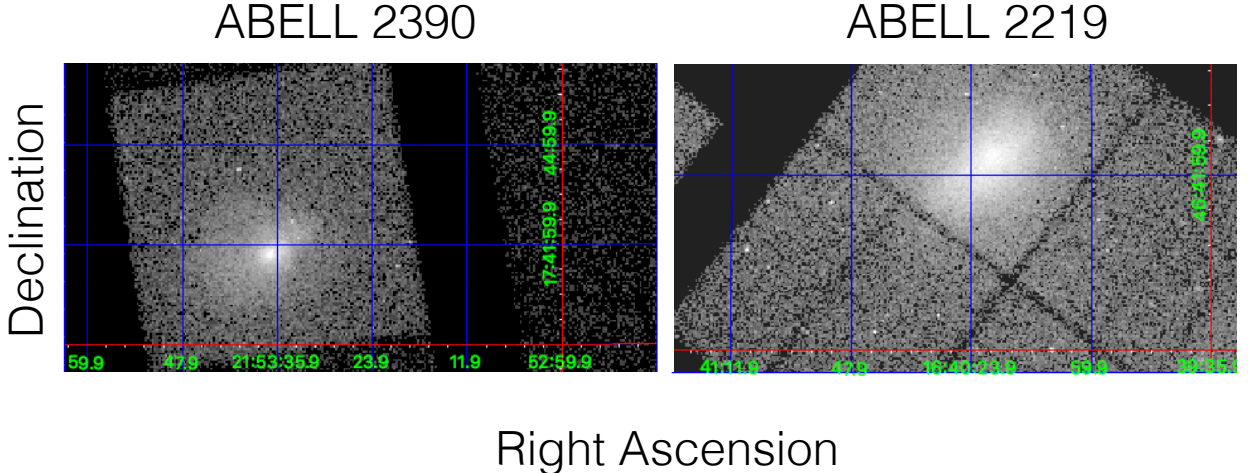


Figure 1.3: **CC vs. NCC X-ray emission.** The core is much brighter and more concentrated in CC Abell 2390 (*left*) than that of NCC cluster Abell 2219 has more diffuse X-ray emission (*right*).

because it is able to track changes in density with temperature when they are normally independent of each other (Ponman et al., 1999; Voit, 2005). Relaxed CC clusters with high central densities (and therefore strongly peaked surface brightness profiles, as discussed previously in Section 1.2.2) have low central entropy. Conversely, NCC clusters may have higher central entropies as a result of recent mergers or AGN outbursts. This difference in central entropy between CC and NCC clusters is well-demonstrated by the entropy profiles in ACCEPT. ACCEPT (Cavagnolo et al. (2009)), further described in Section 2.1, is a catalog of entropy profiles, and the corresponding radial data, for 239 clusters observed with *Chandra*.

1.4 Metals in the ICM

In addition to gas temperature, the X-ray spectrum is influenced by chemical abundance. Heavy, non-primordial⁴ elements can be detected and measured in a spectrum through the analysis of an X-ray spectrum that includes emission lines generated by radiative de-excitation of ions, following collisions between electrons and the various ion species in the ICM. Detection of iron in the X-ray

⁴Primordial gas is hydrogen or helium that has never been in any star. All other elements are considered “heavy.”

spectra of the Perseus, Virgo, Coma, and Centaurus clusters gave the first evidence that gas is not primordial in nature, but was contained heavy elements from stars in galaxies which had been ejected and distributed throughout the ICM (Mitchell et al., 1976; Mitchell & Culhane, 1977; Serlemitsos et al., 1977). The quantity of hot gas in clusters of galaxies far exceeds the mass in stars by at least a factor of 5, which means that most of this gas *does* contain primordial H and He, but it is polluted with heavier elements. This pollution is caused by stars and their end-states (particularly merging white dwarfs, merging neutron stars, and massive star supernovae) which are very good at making and heavy elements and then sharing them with their environments. Energy ranges available to the *ROSAT* and *Einstein* missions were limited to below $\sim 2 - 4$ keV, where the brightest lines are part of a region called the iron-L complex, near 1 keV. With *ASCA* (Tanaka et al., 1994), astronomers were able to sample a much broader energy range to include more line features, including the Fe-K complex at ~ 7 keV. For reviews of observations of ICM metallicity, see Werner et al. (2008) and Mernier et al. (2018). Metals are formed from stars and supernovae (mostly SNIa but also a little SNII, a little contribution from asymptotic giant branch stars, and very heavy elements like gold which are formed in neutron star mergers). Excellent spectral resolution is needed to measure individual elements, but the most important emission feature for a relatively hot ICM is the Fe-K complex. Figure 1.4 shows an example of how the spectrum changes with respect to temperature and metallicity. The abundance is estimated from the strength of the emission line in comparison to the continuum. At higher gas temperatures, the strength of the Fe-K lines are easier to discern than the Fe-L features at lower energies, while at lower temperatures the spectra become more dominated by emission lines as the hydrogen-helium bremsstrahlung continuum cuts off at lower energies ($E \sim kT$, because of the exponential cutoff). The difference in the spectra has to do with the ionization state of the gas at a given temperature and the atomic structure of the iron ions. Gas with hydrogen-like iron⁵ is hot enough to be stripped of its outer L-shell electrons, leaving mostly K-shell transitions. At cooler temperatures, the iron ions with bound electrons in the L-shell dominate.

⁵A “hydrogen-like” atom is one that can be ionized to have a single electron. Similarly, a helium-like atom is one where a nucleus is paired with two electrons.

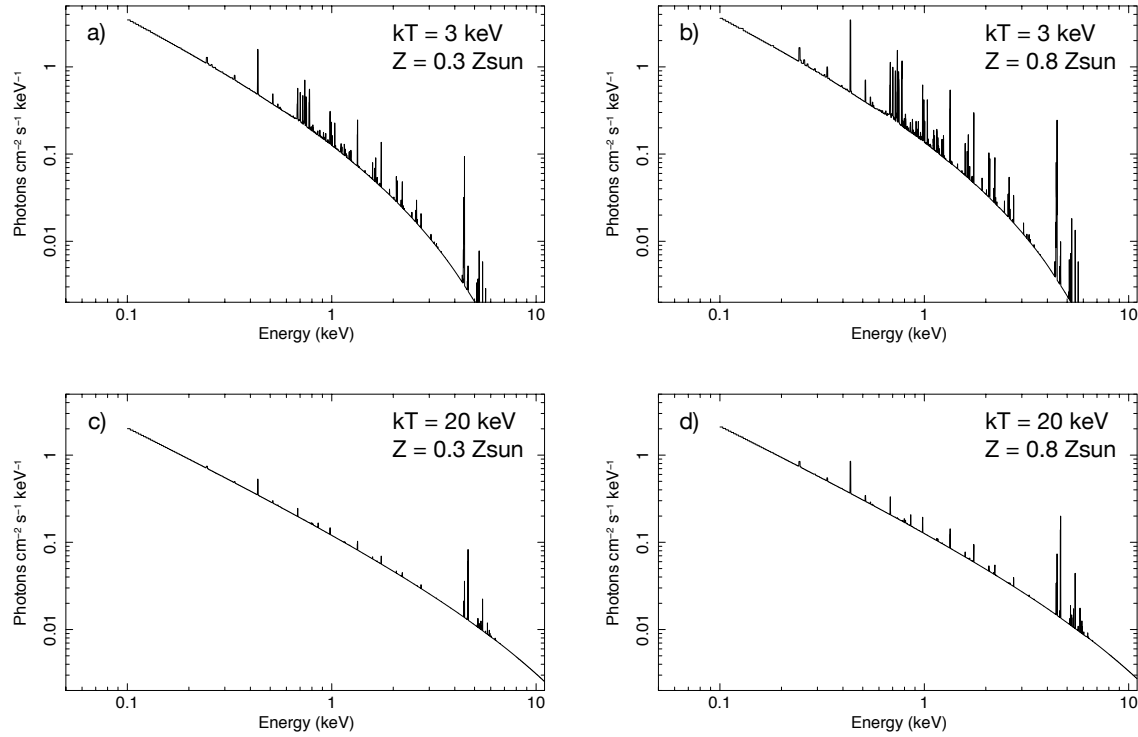


Figure 1.4: Simulated X-ray spectra. Simulated X-ray spectra for gases with varying temperatures and metallicities. a) Relatively cool ($kT=3$ keV) gas with Solar abundance ($Z=0.3$ Z_{\odot}). b) Cool gas with higher metallicity shows stronger emission lines. The spectra were generated using *XSPECv12.11* (Arnaud, 1996).

The presence of heavy elements in the ICM leads to questions of when and how the gas made it out of individual galaxies (where most of the stars are) and into the ICM. Spatially resolved observations showed characteristic differences in the radial distribution of metals which coincided with the differences in surface brightness and temperature profiles between CC and NCC clusters. CCs typically have stronger metallicity gradients which increase towards the core, whereas NCCs have flatter, although still peaked⁶, profiles (De Grandi & Molendi, 2001). Simulations have been able to replicate the metallicity profiles with AGN feedback models. At larger radii and outside of the reach of the AGN, the ICM of massive clusters appear to be independent of core status, which

⁶Because metallicity is emission-weighted, metallicities of very low density environments are more difficult to measure because the amount of photons observed from the source is comparable to the amount of non-source photons. That is, observations of the ICM are subject to low signal-to-noise ratio (SNR).

agrees with the notion that the characteristics of gas in the outer regions evolve on cosmological timescales, and can therefore be used to track the metal distribution history of a cluster. Recently, larger cluster samples with wider redshift ranges seem to support a model for early enrichment ($z \gtrsim 1$), which is supported by the CE global abundances in ACCEPT2.0 (described in Chapter 4).

1.5 This work

This dissertation will use measurements from ACCEPT2.0 to show how X-ray observations of galaxy clusters can be used to constrain our understanding of their thermodynamic and chemical properties, and how they relate to the formation and evolution of large-scale structure in the Universe. Chapter 2 describes the ACCEPT2.0 data used throughout this work. We will show that the global properties are able to reproduce previous observations of the $L_X - T$ relation described in Section 1.3. In Chapter 3, we continue our work with this scaling relation and use global core-excised temperatures and luminosities to test the standard assumption of the isotropic expansion of the Universe. Chapter 4 looks at the relationship between the heavy metal content of the ICM and other properties such as core status, luminosity, and cluster redshift. We also compare our results with those obtained from another sample which used different data reduction methods. Finally, Chapter 5 describes the active development of a data reduction pipeline for the *SOAR* Adaptive-optics Multi-Object Spectrograph (*SAMOS*).

CHAPTER 2

ACCEPT2.0

2.1 Archive of Chandra Cluster Entropy Profile Tables (ACCEPT)

The Archive of Chandra Cluster Entropy Profile Tables (ACCEPT) began as an analysis of entropy profiles for 239 clusters (Cavagnolo et al., 2009). The goal was to understand what X-ray observations of the intracluster medium (ICM) can teach us about how the core interacts with the rest of a cluster. Entropy, $K \propto kTn^{-2/3}$, is associated with changes in gas density and temperature and is a well-known tracer for the thermal history of the ICM (Bower, 1997; Ponman et al., 1999; Pearce et al., 2000). Left alone, the ICM will convect until $dK/dr \geq 0$ (i.e., $K(r) \propto r^\alpha$) everywhere, or all the high density/low temperature (low entropy) gas is below the low density/high temperature (high entropy) gas. A “relaxed” cluster (no recent merger event) would likely have a dominant galaxy at the center, called the brightest cluster galaxy, or BCG. Entropy profiles are, for the most part, compatible with hierarchical formation models outside of the core, but have been shown to flatten inside of $R_c \sim 100$ kpc¹ (Ponman et al., 2003; Donahue et al., 2006). With 239 entropy profiles in ACCEPT, Cavagnolo et al. (2009) showed that clusters generally follow model predictions and decrease in entropy from the outskirts, but flatten to a nearly constant central entropy K_0 in the core. Later assessments of cluster entropy profiles showed that CC systems could also be modeled with the broken power law (equation 2.1), with a steeper outer component ($\propto r^{1.1}$) and a shallower inner slope ($\propto r^{0.67}$), where NCCs have even flatter core entropy profiles (Tozzi & Norman, 2001; Voit, 2005; Cavagnolo et al., 2009). The entropy profile is modeled as,

$$K(r) = K_0 + K_{100} \left(\frac{r}{100 \text{ kpc}} \right)^\alpha, \quad (2.1)$$

at 100 kpc, where K_0 is the entropy excess over a simple power law, K_{100} is the normalization constant, and α is the slope of the entropy profile. The flattened profiles indicate that something

¹1 kpc = 3.26×10^3 ly = 3.086×10^{21} cm

Table 2.1: **ACCEPT vs. ACCEPT2.0.** Main differences between ACCEPT and ACCEPT2.0. Major updates for ACCEPT2.0 include spatially resolved temperature and metallicity profiles, global estimates for temperature, luminosity and metallicity, and morphological classifications.

	ACCEPT	ACCEPT2.0
# of clusters	239	606
# of entropy profiles	239	348
# of kT, Z profiles	...	398
Global T, L_X, Z	...	✓
Morphology	...	✓

prevents gas from cooling and condensing past some limit by displacing large amounts of gas around the core. We now know this phenomenon is caused by a feedback relationship between a cluster’s active galactic nucleus (AGN) and its environment (Bower et al., 2006; McNamara & Nulsen, 2007). When turned on, the AGN puffs up the surrounding gas and raises the entropy. Consequently, the effects of feedback from AGN in addition to other thermodynamic processes such as radiative cooling and feedback from supernovae (SNe) are seen in other X-ray observables.

Until now, ACCEPT was the largest publicly-available collection of uniformly-derived radial profiles of density, temperature, and entropy. ACCEPT2.0 (Donahue, Baldi, et al, in prep) adds more clusters and expands the suite of derived X-ray properties. In addition to more than doubling the number of targets in its predecessor, ACCEPT2.0 includes estimates for morphological properties, global X-ray observables for temperature, luminosity, and metallicity, as well as ~ 400 radial temperature and metallicity profiles. The major differences between ACCEPT and ACCEPT2.0 are highlighted in Table 2.1.

2.2 ACCEPT2.0

In this section, I will describe the essential elements of the ACCEPT2.0 pipeline. The specific work described here is the (yet) unpublished work of Baldi, Donahue (the ACCEPT2.0 pipeline), and Frisbie (the classification of clusters by their core entropy profiles).

The main ACCEPT2.0 data analysis was performed by Alessandro Baldi using CIAO v4.7 (Fruscione et al., 2006) and SHERPA (Freeman et al., 2001) with the *Chandra* calibration database CALDBv4.5. The pipeline initially ran an automated quick spectral analysis of all clusters available

in the *Chandra* archive in order to have a rough estimate of the temperature of each cluster. The temperature estimate was used to set a count threshold to decide whether to include a cluster in the sample. Based on simulations, Alessandro Baldi determined that a minimum number of counts in the 0.5-7 keV band of $n_{min,res} = 1377 \cdot kT - 537$ (where kT is the temperature of the cluster in keV) is necessary to have a 20% error on the measure of the cluster temperature in at least three spatial bins, whereas $n_{min,glb} = (1377 \cdot kT - 537)/3$ is necessary to have the same error on the temperature in a single spatial bin. The pipeline therefore enforces $n_{min,glb}$ and $n_{min,res}$ as the minimum counts necessary to include a cluster in the total sample and in the spatially resolved sample, respectively. Images and exposure maps are created with a binning factor of 2, corresponding to a pixel size in the image of 0.984 arcsec. A likelihood function function based on cstat was minimized to fit the spectrum to models for both the source and the background.

ACCEPT2.0 global properties were estimated for three spatial regions: the cluster with the core included (CI, $r < R_\Delta$), core of the cluster (C, $r < r_{core}$), and the cluster with the core excised (CE, $r_{core} < r < R_\Delta$), where $\Delta=2500$ or 500 . The core radius is usually taken to be some fraction of the scale radius. The quantities of interest to this dissertation are approximated for radius R_{2500} because the aperture extent is consistent across 535 ACCEPT2.0 objects and we define the core radius as $r_{core} = 0.3 R_{2500}$. The fits to R_{2500} , and the relative average temperature, T_{2500} , were performed using the formula derived by Vikhlinin et al. (2006),

$$R_{2500} h E(z) = 0.501 \left(\frac{T_{2500}}{5 \text{ keV}} \right)^{0.55} \text{ Mpc}, \quad (2.2)$$

where $E(z) = \sqrt{\Omega_m(1+z)^3 + \Omega_\Lambda}$ and $h = H_0/(100) \text{ km s}^{-1} \text{ Mpc}^{-1}$. The pipeline used an input value of $T_{2500} = 5 \text{ keV}$ to estimate the first-guess for R_{2500} and extracting the core-excised ($0.3R_{2500} < r < R_{2500}$) region from the spectrum. The pipeline then iterated over values for T_{2500} and R_{2500} until the model achieves convergence to a stable temperature ($\Delta T_{2500} \leq 0.01 \text{ keV}$ between two successive iterations). The three different global regions were used because gas inside the core region evolve on time scales shorter than the age of the Universe, which results in high variation between the X-ray observables for clusters of the same mass. Outside of this region,

clusters appear mostly self-similar (Maughan et al., 2012).

The source spectra and background were fitted simultaneously using spectral models in *Sherpa*. There are several different models useful for observations of the ICM because it involves numerous calculations for various atomic interactions. ACCEPT2.0 source emission was fit to a model for a hot diffuse gas called a *mekal* model (Kaastra et al., 1996; Liedahl et al., 1995) with the following parameters: The ratio between the elements were fixed to the Solar value as in Anders & Grevesse (1989a). The pipeline considered line-of-sight absorption fixed at the Galactic value N_H (Stark et al., 1992), and an additional internal absorption component left free to vary (consistent with zero in the large majority of clusters). The free parameters in the *mekal* model were the temperature kT , the metal abundance Z , and the normalization. The redshift z has been fixed at the literature value for the cluster. The background model used was made by two power-law models, several fixed instrumental gaussian emission lines and an *apec* thermal model at low temperature ($kT = 0.17$ keV, to take into account the soft diffuse X-ray background). The slopes of the power-laws and the quantity, position and strength of the instrumental emission lines depend on the specific ACIS chips and they are adjusted accordingly. The shape of this spectrum is held fixed.

The core entropy profiles and core excess K_0 values in ACCEPT2.0 were calculated by Rachel Frisbie (Frisbie, MSU dissertation, October 2020).

2.3 K-correction and bolometric correction

In this section, I return to describing work that is primarily my own.

Spectra were fit by the pipeline tasks over the observed 0.5-8 keV band. The pipeline did not compute the bolometric and K-corrections² of the observed fluxes and luminosities, so those calculations were done by this author to support further scientific use. We used bolometric corrections to convert the bandpass spectral energy distribution (SED) to a spectrum that covers the full range of energies, and the K-correction to account for cosmology. Because of expansion,

²The “K” here is an arbitrary variable that Hubble adopted in 1936 (Hubble, 1936) for the “K” correction, in magnitudes, to a bandpass-limited flux estimate arising from the Doppler shift of a spectrum.

photons from distant objects become redshifted as they travel towards us. Thus, their observed energies are lower than those of the photons emitted in the rest-frame and require correction.

We perform the bolometric and K-corrections by generating spectral shapes using the best-fit results for the thermal plasma (kT , Z/Z_{\odot}) from the ACCEPT2.0 pipeline and the cluster redshift using *XSPEC v12.11.0* (Arnaud, 1996). Then, we convert the observed fluxes and luminosities to rest-frame energies. This conversion is done by calculating the ratios of integrated luminosity in the rest-frame energy range [0.5-8.0] keV with the integrated luminosity in the observed energy range [0.5-8.0] keV via $E_{\text{rest}} = (1+z)E_{\text{observed}}$. We then extrapolate the best-fit spectrum to a very broad energy range for “bolometric”³ values, and calculate the ratio between the integrated luminosity over this broad energy range and the integrated luminosity of the canonical rest-frame energies. We compute the correction factors by simulating observations of each cluster based on the temperature, metallicity, and redshift.

Each simulated cluster returned values for the observed flux (after correction for Galactic and internal absorption) and luminosity with their corresponding rest-frame and bolometric quantities. The ratios of rest-frame and bolometric values to those of the observer frame were used as the correction factors for the real data. The specific process and the code for the K-correction procedure is provided in Appendix A.

2.4 Vetting of the Data

For nearby clusters and groups with strong temperature gradients, global temperature and (emission-weighted) abundance estimates have been shown as biased towards those of the core region when fit to an isothermal model, and may be better characterized by a multi-temperature model (Buote, 2000) because the line of sight passes through gas of different temperatures, even with a simple radial temperature gradient. However, as mentioned in Section 1.3, previous works have shown that after excising the core region, the ICM spectra extracted from within R_{2500} or

³These are not true bolometric values, as that would imply integration over all energies and *XSPEC* does not formally allow extrapolation to infinitely high energy, but contributions from very high energies gets vanishingly small because of the exponential drop off ($\propto \exp(-E/kT)$). The maximum energy allowed by the tabulated models is typically XX keV rest frame.

R_{500} fit well with a single temperature.

One of the goals of ACCEPT2.0 was to assign uniformly measured global properties to each cluster. These measurements come from spectroscopic fits to a single temperature *mekal* model for spectra obtained by a single large aperture. We obtained global properties in two main types of aperture: core-excised (CE), core-included (CI).

To verify that the CE spectra for clusters in ACCEPT2.0 are adequately characterized by a single-temperature model, we compared ACCEPT2.0 spatially resolved temperature profiles of 154 objects to their global spectral temperatures. In summary, we found that 91% of the spectrum-approximated CE temperatures are within 1 standard deviation of the radially averaged value. The CE global properties here refer to measurements obtained within the region $[0.3\text{-}1]R_{2500}$. We do the same thing with the CI region defined as $[0\text{-}1]R_{2500}$.

2.4.1 Initial Cuts

Originally 536 ACCEPT2.0 objects have global spectra for the $[0.3\text{-}1]R_{2500}$ aperture, 68 of which were removed from further analysis for any of the following reasons (the total numbers of affected clusters are listed in parentheses):

- Clusters with updated redshift measurements, $\Delta z/z > 10\%$. (12)
- Spectral fits did not achieve a reliable temperature convergence. (20)
- Too much of the core-excised aperture was outside the field of view to produce reliable global estimates for the aperture. (35)

There are 15 clusters (Table 2.2) that were found to have updated redshifts, but three of them had percent changes below 10%. For these clusters with small redshift updates, we refit the global temperatures and abundances for the CE R_{2500} spectra and they have been flagged. Formally, the apertures used to compute the luminosities for these clusters should have been updated, and therefore the luminosities based on fluxes from the original apertures from the pipeline are not

Table 2.2: **ACCEPT2.0 Redshift Updates.** There are 15 ACCEPT2.0 clusters that have had updated redshifts since their spectra were analyzed. These clusters were left out of any further analysis, except for clusters marked with a † which had their CE global temperatures and abundances refit (but were left out of the $L_X - T$ analysis). The references are as follows: Ah2012-Ahn et al. (2012), Al2015-Alam et al. (2015), AS2017-Andrade-Santos et al. (2017), B2015-Bleem et al. (2015), C2017-Caminha et al. (2017), D2002-Donahue et al. (2002), M2016-McDonald et al. (2016), P2011-Piffaretti et al. (2011), S2013-Sifón et al. (2013), R2016-Rykoff et al. (2016), Wb2013-Webb et al. (2013), Wn2012-Wen et al. (2012), Wn2015-Wen & Han (2015).

ACCEPT2.0 Name	z_{old}	z_{new}	<i>Chandra</i> Obs. ID	Reference
ABELL_3084	0.098	0.219	9413	P2011
ABELL_3140	0.062	0.173	9416	P2011
ACT-CL_J0235-5121	0.430	0.278	12262	S2013
ACT-CL_J0237-4939	0.400	0.334	12266	S2013
ACT-CL_J0304-4921	0.470	0.392	12265	S2013
†ACT-CL_J0616-5227	0.710	0.684	12261,1312	S2013
ACT-CL_J0707-5522	0.430	0.296	12271	S2013
G115.71+17.52	0.400	0.300	13383	AS2017
†MACS_J0416.1-2403	0.420	0.396	16237,1044	C2017
NSCS_J144726+082824	0.195	0.376	10481	Ah2012, Wb2013
OC06_J1119+2127	0.400	0.061	5790	D2002, P2011
RCS_J2327-0204	0.200	0.700	14361,7355	Wn2015
SPT-CL_J0102-4915	0.750	0.870	14022,1402	S2013, B2015, M2016
†SPT-CL_J2344-4243	0.620	0.596	13401	S2013
ZwCl_1309.1+2216	0.266	0.170	7898,14014	R2016

quite right, even if they are calculated using the correct luminosity distance. To be conservative, the luminosities for these clusters were therefore left out of the $L_X - T$ analysis in this work.

There are therefore 468 objects with spectral analysis in the global CE aperture ($0.3 \lesssim r/R_{2500} \lesssim 1$). Using the procedure described in the next section, we removed 21 non-spatially resolved objects with reduced chi-square $\chi^2/\text{d.o.f} \gtrsim 1.5$. Below this value, we found general agreement between the global measurements and those calculated from the radially averaged profiles, although for clusters with radial profiles, we replaced the X-ray properties measured from single-aperture spectral fits with weighted means.

2.4.2 Radially weighted temperature and abundance

This section’s goal is to define a reasonable reduced χ^2 beyond which to cut global temperature and abundance approximations in the region $[0.3-1]R_{2500}$ for the non-spatially resolved objects in the sample.

Objects lacking radial profiles that host multiphase gas in their ICM can lead to misleading results from the spectral fit. Measurements for high S/N systems with multi-temperature plasma can have misleading goodness-of-fits when applied to an isothermal model, despite having reliable parameter estimates. Here, we use a sub sample of spatially resolved ACCEPT2.0 clusters and compared their spectrum-derived temperature estimates to those computed via their radial profiles to test the reliability of ACCEPT2.0 global properties.

There are ~ 400 clusters in ACCEPT2.0 with spatially resolved data, 154 of which have at least 3 data points in the region of interest, $0.3 < r/R_{2500} < 1$. We used projected radial temperature profiles to calculate each cluster’s weighted mean (\bar{X}_w), mean error (σ_w), and standard deviation (σ_{std}), defined as follows,

$$\bar{X}_w = \frac{\sum w_i X_i}{\sum w_i} \quad (2.3)$$

$$\sigma_w = \sqrt{\frac{1}{\sum w_i}} \quad (2.4)$$

$$\sigma_{\text{std}} = \sqrt{\frac{\sum w_i (X_i - \bar{X}_w)^2}{\sum w_i}}, \quad (2.5)$$

where the weight on each radial data point is $w_i = 1/\sigma_i^2$. If a cluster hosts a relatively flat temperature profile outside the core, then $\sigma_{\text{std}}/\sigma_w$ should be of order unity. We compute radially weighted abundances in the same manner as above, but use the temperatures in the vetting process.

We found that $\sim 91\%$ of the weighted means were well within their stated uncertainties, and global properties with suspicious reduced χ^2 (and therefore underestimated uncertainties) were limited to clusters with unresolved temperature structure in the ICM.

In general, the values obtained from the global spectral fits are good estimates for the global average, despite the occasional underestimation of the error bars due to poor χ^2 . In general, we found good agreement between global properties and the weighted average. When possible we replaced global temperatures, metallicities, and their respective errors with values from the radially weighted profiles. For good fits ($\chi^2/\text{d.o.f} \lesssim 1.2$), we found no difference between using the global and radially averaged values. Beyond that, the data uncertainties were more representative of the quality of spectral fit for $1.2 \lesssim \chi^2/\text{d.o.f} \lesssim 1.5$. Of the clusters without radial profiles, we removed only 21 global measurements for having poor (reduced) χ^2 . The radial metallicity profiles are in Appendix B, and the radial temperature profiles are shown in Appendix C. The global CE properties for the final 447 ACCEPT2.0 clusters and groups is provided in Table 2.3. We followed the same procedure for the CI global properties. This replacement procedure ensured that objects with resolved multi-temperature gas are represented by data points with error bars based on good fits.

2.4.3 $L_X - T$ relation

Here, we use the global CE and CI L_X and T values for 301 clusters (with CE bolometric luminosities $L_X \gtrsim 4 \times 10^{43} \text{ erg s}^{-1}$) to illustrate that the global CE quantities do a good job of removing scatter in the relation caused by core emission. There is a noticeable separation between CC (blue triangles) and NCC (red circles) clusters in the upper panel of Figure 2.2. In the lower panel, this scatter is significantly reduced. As mentioned previously in Section 1.3, CCs typically have higher core densities (lower central excess K_0 ⁴) than NCCs, which makes them brighter. For our sample, CCs are defined as having excess entropies of $K_0 < 30 \text{ keV cm}^2$, and those with higher K_0 are NCCs. Clusters with no core status are plotted as crosses.

We use the package emcee (Foreman-Mackey et al., 2013) to fit⁵ both the CE and the CI values to the $L_X - T$ relation of the form,

⁴Central entropies were calculated by Rachel Frisbie (Frisbie, MSU dissertation, October 2020).

⁵More details of the fitting procedure for the $L_X - T$ relation are in Chapter 3.

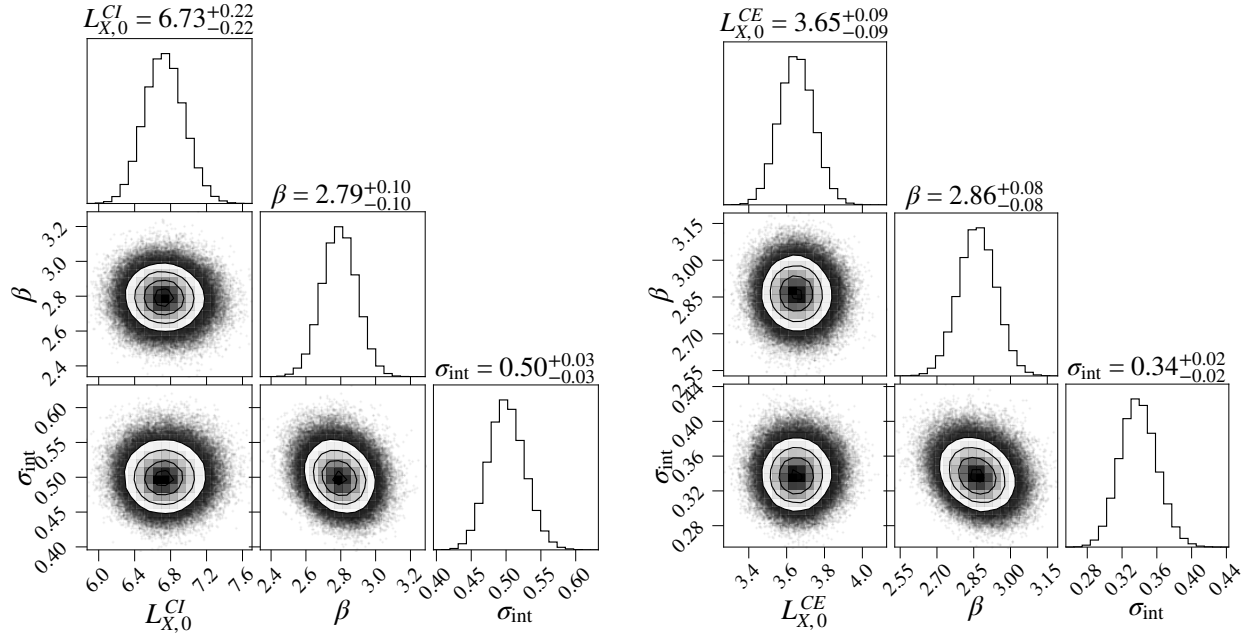


Figure 2.1: **$L_X - T$ core-included and core-excised posterior distributions.** The posterior probability distributions for the variables of the $L_X - T$ relation for CI (left) and CE (right) clusters.

$$\ln \frac{L_X E(z)^{-1}}{10^{44} \text{ erg s}^{-1}} = \ln L_{X,0} + \beta \ln \frac{kT}{6 \text{ keV}}, \quad (2.6)$$

where normalization $L_{X,0}$, slope β , and intrinsic scatter σ_{int} , are assumed to have Gaussian data and errors. The results of the fit are shown in Figure 2.2, where the upper panel contains the best fit model for the CI measurements, and the lower panel shows the CE results. The model for the CI cluster properties have a higher normalization of $L_{X,0}^{\text{CI}} = 6.728^{+0.223}_{-0.216}$ (due to higher luminosity measurements) compared to the CE normalization $L_{X,0}^{\text{CE}} = 3.652^{+0.092}_{-0.090}$, but the slopes are similar for both ($\beta^{\text{CI}} = 2.793 \pm 0.099$ and $\beta^{\text{CE}} = 2.864 \pm 0.076$). The errors on the variables represent the 16th and 84th percentiles from the probability distributions returned by the fit.

As expected from the larger scatter between CCs and NCCs in the top panel of Figure 2.2 (and the lack thereof in the lower panel), the scatter σ_{int} in the relation is reduced when using CE measurements, with $\sigma_{\text{int}}^{\text{CI}} = 0.500^{+0.027}_{-0.025}$ and $\sigma_{\text{int}}^{\text{CE}} = 0.339^{+0.021}_{-0.020}$. These $L_X - T$ results agree with previous works (Pratt et al., 2009; Mittal et al., 2011; Maughan et al., 2012), and reassures us of the quality of the data in ACCEPT2.0.

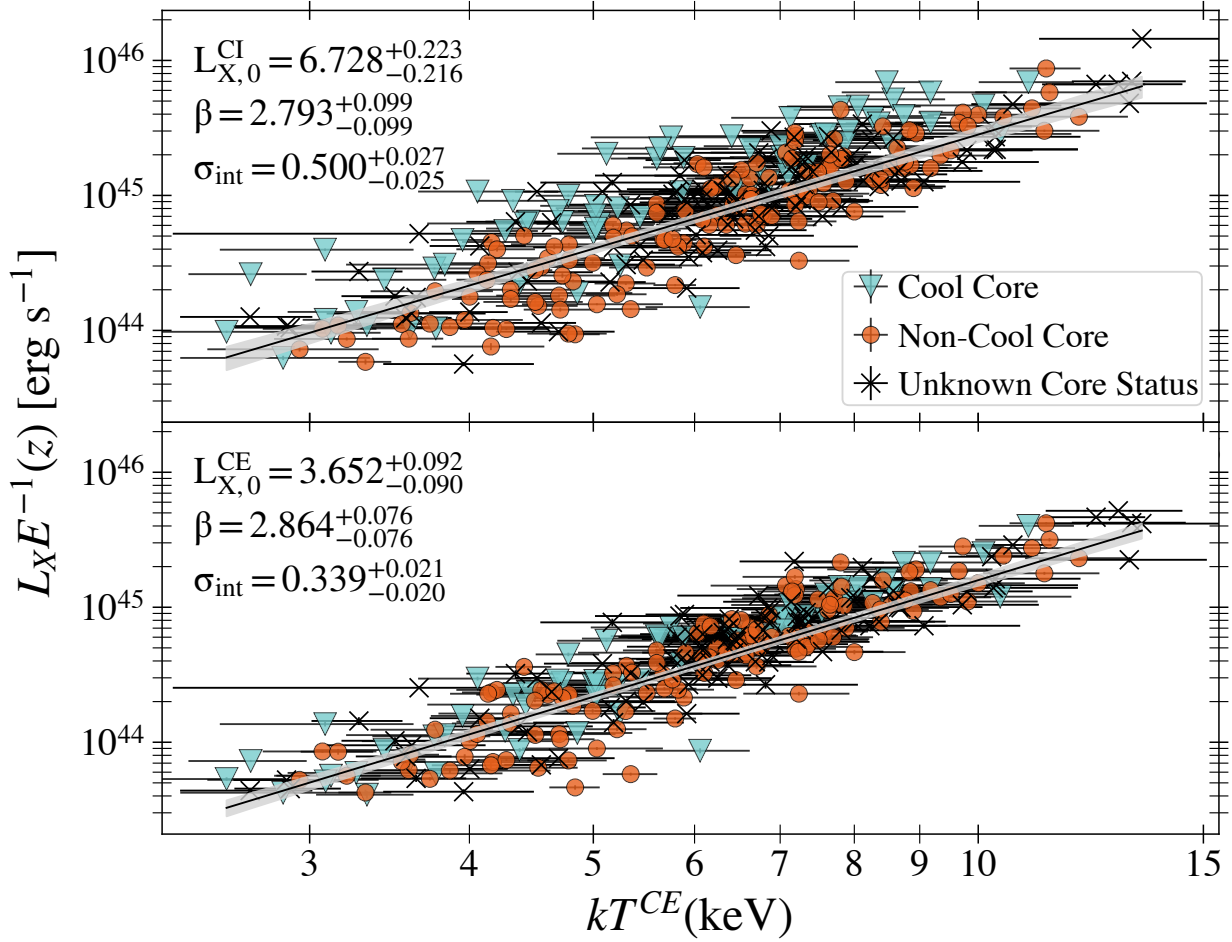


Figure 2.2: **$L_X - T$ core-included vs. core-excised.** Best fit $L_X - T$ relation for 301 clusters with global CI ($[0-1]R_{2500}$) and CE $[0.3-1]R_{2500}$ quantities. The upper panel shows the relation with luminosities measured in the CI aperture, and the lower panel shows the CE luminosities (both use CE temperatures.). The errors on the data points and best fit parameters are 1σ .

Table 2.3: **Global CE properties for 432 ACCEPT2.0 clusters.** Full list of 432 ACCEPT2.0 clusters presented in this dissertation. This table includes the clusters that had their global temperatures and abundances refit. The columns are as follows: col(1) is ACCEPT2.0 name, col(2) is the cluster redshift, col(3) is the R_{2500} radius in kpc, cols(4,5) and cols(6,7) are the [0.5-8 keV] energy bandpass and bolometric luminosities in units of 10^{44} erg s $^{-1}$, cols(8,9) is the temperature and error in keV, cols(10,11) is the metallicity in solar units Z_{\odot} , col(12) is the reduced chi-square value obtained from the X-ray spectral fit, and col(13) is checked if the temperatures and metallicities obtained from the spectral fit were replaced with their radially averaged values.

Name	z	R_{2500}	L_X	e_L_X	L_X	e_L_X	kT	e_kT	Z	e_Z	χ^2	WTD
			[0.5-7 keV]			[bol]						
		kpc	(10^{44} erg s $^{-1}$)		(10^{44} erg s $^{-1}$)		(keV)		(Z_{\odot})			(d.o.f)
000619+105206	0.167	466	1.85	0.072	2.636	0.102	5.184	0.399	0.35	0.092	1.073	
00088+5215	0.104	456	0.751	0.03	1.052	0.043	4.711	0.3	0.164	0.087	1.264	
00117-1523	0.378	451	6.014	0.194	8.839	0.285	5.892	0.399	0.271	0.066	1.132	
A0013	0.094	461	0.641	0.016	0.899	0.023	4.767	0.257	0.24	0.058	1.048	✓
A2744	0.308	640	13.17	0.165	23.686	0.296	10.245	0.77	0.299	0.102	1.234	✓
0014-4952	0.752	388	5.112	0.336	7.853	0.517	6.88	0.966	0.406	0.162	1.096	
Cl0016+16	0.541	557	16.147	0.355	28.163	0.619	9.727	0.745	0.198	0.063	0.964	
00254-1222	0.584	470	8.852	0.347	14.205	0.557	7.817	0.597	0.256	0.06	1.134	
00278+2616	0.367	477	3.049	0.194	4.615	0.294	6.438	0.978	0.039	0.082	1.086	
30484-4142	0.41	559	7.488	0.269	13.102	0.47	9.797	1.232	0.15	0.096	1.17	
00305+2618	0.5	286	1.158	0.254	1.513	0.332	2.853	0.494	0.669	0.358	1.074	
00354-2015	0.364	509	10.772	0.355	16.792	0.554	7.187	0.645	0.338	0.09	1.146	
A0068	0.255	618	5.993	0.281	10.429	0.489	9.717	1.436	0.662	0.21	1.27	
A0085	0.055	543	2.609	0.019	3.925	0.028	6.17	0.588	0.358	0.15	2.29	✓
A2813	0.292	559	7.287	0.223	11.762	0.361	7.95	0.739	0.287	0.086	1.303	
00408+2404	0.083	437	0.823	0.028	1.129	0.038	3.826	0.623	0.291	0.102	1.28	✓
A0098N	0.104	405	0.332	0.026	0.445	0.034	3.782	0.387	0.54	0.166	1.278	
A98ss	0.129	331	0.209	0.028	0.277	0.037	2.639	0.402	0.465	0.272	1.163	
351-021	0.057	228	0.027	0.004	0.037	0.006	1.28	0.054	0.417	0.098	1.169	✓
A0119	0.044	541	1.115	0.013	1.628	0.019	5.916	0.591	0.29	0.131	3.338	✓
0058-6145	0.83	322	3.844	0.629	5.312	0.869	4.416	1.052	0.341	0.229	1.053	
200428	0.274	420	2.509	0.217	3.514	0.304	4.643	0.809	0.115	0.133	1.254	

Table 2.3 (cont'd)

Name	z	R_{2500}	L_X	e_L_X	L_X	e_L_X	kT	e_kT	Z	e_Z	χ^2	WTD
			[0.5-7 keV]		[bol]							
			kpc	$(10^{44} \text{ erg s}^{-1})$	$(10^{44} \text{ erg s}^{-1})$		(keV)		(Z_\odot)		(d.o.f)	
A0141	0.23	525	3.05	0.122	4.635	0.186	6.576	0.772	0.184	0.12	1.383	
0106-5943	0.348	426	3.107	0.249	4.416	0.354	5.114	0.725	0.326	0.158	1.192	
01670077+0105926	0.254	419	2.126	0.07	2.961	0.098	4.565	0.271	0.217	0.074	1.028	✓
01077+5408	0.107	634	3.881	0.057	6.191	0.092	6.642	1.385	0.184	0.136	1.257	✓
A0160	0.045	275	0.084	0.006	0.117	0.009	1.807	0.375	0.094	0.069	2.12	✓
011502+002441	0.045	353	0.197	0.006	0.261	0.008	2.482	0.382	0.306	0.132	3.115	✓
A2895	0.227	594	4.742	0.143	7.809	0.236	8.394	0.858	0.301	0.107	1.471	
UGC00842	0.045	265	0.038	0.003	0.054	0.004	1.669	0.085	0.226	0.049	1.095	✓
0123-4821	0.62	340	2.711	0.3	3.751	0.415	4.551	0.743	0.464	0.195	1.07	
A0193	0.049	407	0.398	0.011	0.536	0.015	3.645	0.138	0.342	0.054	1.191	✓
A0209	0.206	607	6.31	0.161	10.466	0.266	8.547	0.665	0.25	0.082	1.313	
Abell222	0.211	404	1.664	0.067	2.287	0.092	4.137	0.274	0.216	0.07	1.032	
Abell223	0.207	473	1.37	0.062	1.981	0.089	5.47	0.5	0.247	0.1	1.152	
01400-0555	0.454	476	7.056	0.392	10.985	0.61	7.139	0.822	0.256	0.103	1.149	
01420+2131	0.28	526	5.46	0.165	8.543	0.258	7.218	0.649	0.118	0.09	1.265	
01502127-1005305	0.365	378	3.501	0.257	4.825	0.354	4.233	0.485	0.229	0.112	1.19	
0151-5954	1.03	246	2.655	0.702	3.561	0.941	3.561	0.956	0.386	0.316	1.039	
01525-2853	0.341	457	4.091	0.126	6.018	0.186	5.815	0.584	0.058	0.081	1.125	
A0267	0.231	563	4.166	0.105	6.6	0.166	7.57	0.63	0.393	0.106	1.224	
0156-5541	1.22	266	8.173	1.394	11.753	2.004	5.334	1.101	0.017	0.081	1.075	
02209-3829	0.229	414	2.352	0.136	3.225	0.187	4.346	0.368	0.546	0.14	1.23	
A3017	0.22	538	3.931	0.175	6.124	0.272	7.115	0.939	0.111	0.106	1.08	
0228259+003202	0.414	373	0.286	0.174	0.394	0.239	2.425	1.333	0.018	0.373	1.006	
MZ10451	0.061	179	0.01	0.002	0.016	0.004	0.733	0.041	0.158	0.167	1.073	
0232-4421	0.284	541	8.792	0.304	13.995	0.485	7.636	0.811	0.218	0.095	1.259	
0234-5831	0.415	556	4.706	0.41	8.628	0.752	10.958	3.63	0.244	0.314	1.12	
A0368	0.22	497	3.443	0.181	5.101	0.268	6.08	0.768	0.305	0.138	1.276	
4000237-5224	0.136	355	0.303	0.048	0.403	0.065	3.171	0.43	0.385	0.201	1.319	

Table 2.3 (cont'd)

Name	z	R_{2500}	L_X	e_L_X	L_X	e_L_X	kT	e_kT	Z	e_Z	χ^2	WTD
			[0.5-7 keV]		[bol]							
			kpc	(10^{44} erg s $^{-1}$)	(10^{44} erg s $^{-1}$)		(keV)		(Z_\odot)		(d.o.f)	
A0370	0.375	558	6.827	0.11	11.422	0.183	8.753	0.459	0.285	0.074	1.206	
02426-2132	0.314	459	4.837	0.298	7.085	0.436	5.751	0.774	0.151	0.115	1.156	
0243-5930	0.635	410	5.702	0.535	8.615	0.808	6.502	1.066	0.347	0.14	1.042	
AS0295	0.3	529	9.202	0.31	14.464	0.487	7.348	0.706	0.214	0.076	1.2	✓
4000245+0936	0.147	323	0.169	0.041	0.22	0.054	2.629	0.538	0.7	0.541	1.27	
A0376	0.048	468	0.515	0.011	0.713	0.016	4.174	0.67	0.346	0.208	1.875	✓
A0383	0.187	470	2.012	0.064	2.881	0.092	5.438	0.297	0.338	0.11	1.239	✓
0252-4824	0.421	453	2.527	0.249	3.793	0.373	6.352	1.45	0.313	0.191	1.072	
NGC1132	0.023	211	0.012	0.001	0.018	0.002	1.045	0.023	0.245	0.032	1.211	
0256-5617	0.58	410	4.804	0.41	7.044	0.602	5.82	1.006	0.241	0.136	1.096	
A0402	0.322	552	4.452	0.19	7.293	0.311	8.228	1.236	0.045	0.085	1.175	
A0399	0.072	574	2.554	0.021	3.926	0.032	6.857	0.581	0.243	0.136	3.135	✓
A0401	0.074	609	4.434	0.016	7.035	0.025	7.881	0.877	0.282	0.099	1.488	✓
03016+0155	0.17	432	1.687	0.079	2.341	0.11	4.45	0.333	0.233	0.09	1.19	
4000302-0423	0.35	410	3.657	0.341	5.08	0.473	4.755	0.748	0.617	0.241	1.096	
03037-7752	0.274	630	6.901	0.197	11.84	0.338	9.344	0.891	0.318	0.085	1.143	
A3088	0.253	576	5.317	0.193	8.344	0.302	7.316	0.762	0.236	0.099	1.279	
0307-6225	0.579	341	1.857	0.297	2.54	0.406	4.325	1.059	0.616	0.361	1.036	
0307-5042	0.55	400	4.468	0.408	6.486	0.592	5.538	0.936	0.173	0.127	1.1	
03089+2645	0.324	603	10.682	0.298	18.58	0.518	9.656	1.047	0.159	0.085	1.285	
0310-4647	0.709	360	3.699	0.296	5.329	0.427	5.37	0.927	0.206	0.189	1.154	
A3094	0.068	371	0.242	0.013	0.323	0.017	3.029	0.092	0.272	0.103	1.421	✓
4000318-0302	0.37	447	2.455	0.252	3.587	0.368	5.621	1.316	0.027	0.108	1.168	
0324-6236	0.73	361	4.985	0.724	7.213	1.047	5.38	1.158	0.032	0.092	1.003	
4000328-2140	0.59	404	3.038	0.308	4.494	0.456	6.033	0.995	0.262	0.168	1.137	
A3126	0.086	476	1.212	0.037	1.707	0.052	4.994	0.309	0.47	0.083	1.203	
A3128	0.06	373	0.316	0.015	0.423	0.02	2.86	0.484	0.269	0.111	1.502	✓
03311-2100	0.188	495	2.604	0.104	3.827	0.153	5.859	0.528	0.204	0.092	1.38	

Table 2.3 (cont'd)

Name	z	R_{2500}	L_X	e_{-L_X}	L_X	e_{-L_X}	kT	e_{-kT}	Z	e_Z	χ^2	WTD
			[0.5-7 keV]		[bol]							
			kpc	(10^{44} erg s $^{-1}$)	(10^{44} erg s $^{-1}$)		(keV)		(Z_\odot)		(d.o.f)	
0334-4659	0.485	427	3.884	0.379	5.702	0.556	5.822	1.133	0.182	0.147	1.145	
3C089	0.139	439	0.464	0.02	0.647	0.028	4.528	0.333	0.166	0.096	1.164	
03408-4542	0.07	338	0.189	0.02	0.251	0.027	2.419	0.42	0.298	0.184	1.756	✓
IIIIZw054	0.029	335	0.169	0.007	0.229	0.009	2.255	0.217	0.196	0.11	3.292	✓
A3158	0.06	480	2.057	0.018	2.899	0.026	5.435	0.313	0.387	0.082	2.722	✓
0346-5438	0.55	359	3.95	0.44	5.499	0.613	4.573	0.813	0.253	0.158	0.989	
0352-5647	0.67	427	3.616	0.269	5.573	0.415	6.834	1.37	0.006	0.095	1.135	
03529+1941	0.109	364	1.013	0.041	1.362	0.055	3.135	0.165	0.2	0.052	1.111	✓
03588-2955	0.425	548	12.749	0.337	21.346	0.564	8.747	0.487	0.143	0.052	1.13	
4000405-4100	0.686	362	2.769	0.287	4.0	0.415	5.318	1.079	0.012	0.076	1.088	
A0478	0.088	598	5.866	0.038	9.322	0.06	7.609	0.166	0.259	0.022	1.116	✓
04161-2403	0.42	550	9.072	0.326	15.127	0.544	8.664	0.734	0.214	0.071	1.13	
0417-4748	0.62	396	9.277	0.832	13.66	1.225	5.91	0.897	0.205	0.123	1.077	
04175-1154	0.44	624	21.55	0.366	40.079	0.68	11.324	0.499	0.197	0.044	1.108	✓
04258-0833	0.04	379	0.384	0.016	0.514	0.022	3.088	0.125	0.256	0.073	3.255	✓
0426-5455	0.63	358	2.94	0.473	4.245	0.683	5.347	1.715	0.066	0.141	1.051	
AS0463	0.039	353	0.094	0.004	0.125	0.005	2.503	0.532	0.214	0.139	2.257	✓
04296-0253	0.399	491	5.376	0.254	8.315	0.393	7.0	0.9	0.302	0.132	1.159	
04371+0043	0.285	518	4.937	0.134	7.58	0.205	6.101	0.632	0.265	0.041	1.251	✓
04390+0715	0.23	513	5.31	0.166	8.038	0.252	6.528	0.534	0.293	0.083	1.16	
04390+0520	0.208	451	1.883	0.103	2.67	0.145	5.024	0.48	0.251	0.107	1.22	
04431+0210	0.19	406	1.189	0.087	1.628	0.12	4.147	0.474	0.348	0.149	0.998	
A0514	0.071	402	0.317	0.014	0.43	0.018	3.959	0.534	0.257	0.035	1.588	✓
A3292	0.172	416	1.775	0.082	2.441	0.112	4.204	0.297	0.271	0.098	1.41	
04519+0006	0.43	443	5.882	0.364	8.608	0.533	5.844	0.829	0.411	0.206	1.101	
04541-0300	0.55	576	15.974	0.296	28.925	0.536	10.644	0.768	0.206	0.082	1.309	
552-020	0.031	316	0.074	0.004	0.099	0.006	2.455	0.267	0.536	0.173	4.796	✓
04552+0657	0.425	478	6.452	0.414	9.878	0.634	6.845	0.998	0.571	0.226	1.135	

Table 2.3 (cont'd)

Name	z	R_{2500}	L_X	e_L_X	L_X	e_L_X	kT	e_kT	Z	e_Z	χ^2	WTD
			[0.5-7 keV]		[bol]							
		kpc	(10^{44} erg s $^{-1}$)		(10^{44} erg s $^{-1}$)		(keV)		(Z_\odot)			(d.o.f)
0456-5116		0.562 419	3.322	0.29	4.981	0.435	6.352	1.188	0.376	0.176	1.079	
0509-5342		0.463 565	4.295	0.208	7.291	0.353	9.069	1.716	0.145	0.164	1.176	
A3322		0.2 544	3.793	0.142	5.786	0.216	6.649	0.599	0.146	0.092	1.104	
05107-0801		0.22 552	8.412	0.212	13.101	0.33	7.152	0.434	0.28	0.06	1.082	
A0539		0.028 362	0.269	0.007	0.359	0.01	2.909	0.272	0.251	0.095	4.717	✓
AS0520		0.295 573	6.561	0.201	10.757	0.33	8.269	0.732	0.14	0.076	1.167	
05207-1328		0.34 515	5.821	0.181	9.131	0.284	7.335	0.692	0.345	0.111	1.265	
052215-481816		0.296 458	1.036	0.106	1.504	0.154	5.616	1.217	0.319	0.274	1.249	
A3343		0.191 513	3.027	0.089	4.563	0.135	6.429	0.528	0.269	0.099	1.175	
05282-2942		0.158 434	1.634	0.086	2.245	0.119	4.607	0.499	0.564	0.197	1.327	✓
RBS0653		0.284 594	7.669	0.109	13.057	0.185	9.151	0.339	0.234	0.041	1.153	✓
28658-3125		0.21 536	3.759	0.128	5.678	0.194	6.484	0.54	0.301	0.091	1.06	
A0545		0.154 582	3.448	0.047	5.431	0.073	7.372	0.311	0.124	0.052	1.265	
05329-3701		0.275 594	6.799	0.197	11.333	0.329	8.644	0.843	0.136	0.08	1.134	
3060170-		0.036 352	0.18	0.007	0.238	0.01	2.569	0.426	0.304	0.175	2.696	✓
0542-4100		0.64 410	3.762	0.216	5.691	0.327	6.455	0.885	0.108	0.125	1.168	
05470-3904		0.21 457	0.974	0.06	1.398	0.086	5.186	0.699	0.046	0.106	1.352	
A3364		0.148 571	3.151	0.079	4.925	0.124	7.194	0.546	0.126	0.081	1.411	
A0548A		0.04 371	0.261	0.012	0.348	0.016	3.221	0.352	0.335	0.188	1.56	✓
0551-5709		0.423 363	1.975	0.204	2.7	0.279	4.06	0.603	0.296	0.176	1.074	
A0550		0.099 507	2.168	0.062	3.165	0.09	5.669	0.298	0.141	0.067	1.202	
05534-3342		0.407 649	13.416	0.212	24.118	0.382	10.463	0.68	0.192	0.055	1.119	
0559-5249		0.611 357	3.915	0.379	5.512	0.534	4.818	0.622	0.17	0.095	1.073	
A3376		0.046 496	0.541	0.006	0.762	0.008	4.696	0.499	0.386	0.121	3.323	✓
A3378		0.141 453	3.198	0.099	4.474	0.139	4.78	0.273	0.36	0.088	1.16	
06163-2156		0.171 557	2.994	0.067	4.678	0.105	7.236	0.511	0.313	0.086	1.178	
AS0579		0.152 449	1.508	0.056	2.119	0.078	4.789	0.352	0.213	0.092	1.146	
0616-5227		0.71 441	6.591	0.809	10.537	1.293	7.749	1.798	0.318	0.208	1.043	

Table 2.3 (cont'd)

Name	z	R_{2500}	L_X	e_{-L_X}	L_X	e_{-L_X}	kT	e_{-kT}	Z	e_Z	χ^2	WTD
			[0.5-7 keV]		[bol]							
		kpc	(10^{44} erg s $^{-1}$)		(10^{44} erg s $^{-1}$)		(keV)		(Z_\odot)		(d.o.f)	
13959+2418	0.27	539	7.876	0.283	12.273	0.44	7.189	0.635	0.378	0.086	1.169	
A3391	0.051	549	1.028	0.021	1.498	0.031	5.794	0.222	0.232	0.068	3.227	✓
A3399	0.203	542	3.297	0.073	5.045	0.111	6.759	0.453	0.276	0.084	1.084	
16765+1764	0.174	517	4.844	0.111	7.219	0.165	6.176	0.412	0.229	0.08	1.14	
AS0592	0.222	598	7.97	0.188	13.233	0.313	8.581	0.651	0.312	0.08	1.363	
A3402	0.146	311	0.189	0.049	0.251	0.065	2.399	0.42	0.372	0.284	1.087	
A3404	0.167	640	6.357	0.151	10.236	0.244	7.851	0.642	0.049	0.062	1.148	
A0562	0.11	353	0.392	0.019	0.526	0.025	2.943	0.193	0.182	0.056	1.122	✓
Bullet	0.296	708	24.166	0.131	46.462	0.252	12.364	1.145	0.208	0.066	1.326	✓
07123+5931	0.328	409	2.554	0.218	3.563	0.304	4.676	0.539	0.289	0.126	1.176	
0717+3745	0.546	647	25.993	0.368	51.818	0.734	13.243	0.62	0.219	0.042	1.136	✓
4000720+7108	0.231	320	0.245	0.029	0.325	0.038	2.801	0.309	0.408	0.161	1.181	
A0578	0.087	331	0.149	0.012	0.197	0.016	2.641	0.148	0.417	0.067	1.408	✓
A0586	0.171	516	3.337	0.093	4.977	0.139	6.241	0.395	0.374	0.075	1.157	
07357+7421	0.216	516	3.873	0.033	5.843	0.05	6.447	0.632	0.331	0.103	1.236	✓
07449+3927	0.698	442	13.375	0.576	21.465	0.924	7.805	0.634	0.179	0.067	1.114	
PKS0745-19	0.103	628	5.794	0.034	9.484	0.055	8.36	0.483	0.304	0.083	1.593	✓
WBL154	0.022	179	0.024	0.001	0.035	0.001	1.199	0.178	0.15	0.116	1.485	✓
A0598	0.189	457	1.695	0.085	2.417	0.121	5.052	0.538	0.068	0.091	1.291	
A0611	0.288	571	4.697	0.124	7.783	0.205	8.546	0.731	0.377	0.103	1.017	✓
08065+2822	0.3	552	1.869	0.191	2.874	0.293	6.806	1.897	0.071	0.21	1.211	
43062	0.064	446	0.191	0.038	0.252	0.051	3.764	0.538	1.025	1.219	1.418	
A0644	0.07	567	2.89	0.031	4.41	0.047	6.58	0.821	0.317	0.089	2.778	✓
08196+6336	0.119	384	0.758	0.044	1.025	0.06	3.498	0.321	0.17	0.088	1.238	
UGC1120	0.029	276	0.047	0.009	0.063	0.012	1.896	0.116	0.456	0.17	1.499	
08232+0425	0.225	427	1.718	0.107	2.383	0.148	4.66	0.514	0.51	0.168	1.271	
A0665	0.182	614	4.817	0.059	7.91	0.096	8.136	0.857	0.26	0.075	1.314	✓
2MFGC06756	0.241	445	2.694	0.055	3.823	0.078	5.053	0.229	0.277	0.049	1.057	✓

Table 2.3 (cont'd)

Name	z	R_{2500}	L_X	e_L_X	L_X	e_L_X	kT	e_kT	Z	e_Z	χ^2	WTD
			[0.5-7 keV]		[bol]							
		kpc	(10^{44} erg s $^{-1}$)		(10^{44} erg s $^{-1}$)		(keV)		(Z_\odot)			(d.o.f)
4000838+1948	0.123	334	0.166	0.043	0.219	0.056	2.815	0.673	0.534	0.424	1.314	
A3411	0.169	519	2.842	0.053	4.247	0.079	6.249	0.307	0.275	0.054	1.119	✓
084254+292723	0.194	505	1.485	0.048	2.174	0.07	5.89	0.439	0.486	0.136	1.052	✓
A0697	0.282	713	12.109	0.291	23.094	0.555	11.987	1.107	0.333	0.106	1.311	
08488+4455	0.543	248	0.393	0.081	0.524	0.108	2.498	0.491	0.355	0.249	1.104	
08485+3341	0.371	504	2.719	0.21	4.25	0.328	7.258	1.76	0.38	0.288	1.054	
08579+2107	0.23	414	2.167	0.079	2.994	0.11	4.389	0.256	0.31	0.074	0.993	✓
A0744	0.073	316	0.15	0.014	0.203	0.019	2.331	0.226	0.215	0.081	1.418	
+1373+110+018	0.18	475	2.688	0.078	3.869	0.112	5.382	0.311	0.274	0.073	1.14	✓
09112+1746	0.505	460	5.371	0.324	8.253	0.497	6.808	0.894	0.133	0.102	1.124	
HCG037	0.022	203	0.003	0.004	0.004	0.006	0.963	0.238	0.205	0.174	1.12	
20913454+405628	0.442	457	4.631	0.189	6.963	0.284	6.416	0.59	0.406	0.092	1.152	
A0773	0.217	581	5.866	0.132	9.528	0.214	7.63	0.833	0.272	0.081	1.237	✓
HydraA	0.055	431	1.145	0.005	1.566	0.006	3.951	0.219	0.289	0.046	1.219	✓
0918343+295318	0.289	235	0.424	0.349	0.558	0.46	1.703	0.589	0.639	1.389	0.906	
092017+303027	0.258	506	3.036	0.123	4.554	0.184	6.352	0.661	0.352	0.105	1.115	
0922076+034558	0.28	596	1.787	0.209	2.951	0.345	8.434	3.353	0.165	0.354	1.204	
A0795	0.136	466	1.863	0.048	2.645	0.068	5.002	0.3	0.164	0.062	1.275	
4000926+1242	0.489	405	1.533	0.14	2.217	0.202	5.471	1.018	0.239	0.209	1.067	
0938209+520243	0.36	477	5.414	0.181	8.169	0.274	6.417	0.504	0.165	0.073	1.081	
A0853	0.166	430	0.861	0.054	1.194	0.075	4.441	0.481	0.236	0.129	1.146	
A0868	0.153	432	2.61	0.086	3.615	0.119	4.414	0.222	0.252	0.07	1.137	
0947124+762313	0.354	550	7.738	0.176	12.772	0.291	8.464	0.567	0.409	0.076	1.088	✓
09498+1708	0.383	576	9.104	0.381	16.267	0.681	10.311	1.712	0.184	0.151	1.258	
09496+5207	0.214	479	2.228	0.048	3.243	0.069	5.642	0.211	0.256	0.046	1.088	✓
0954+1738	0.828	271	1.806	0.359	2.407	0.478	3.574	0.901	0.587	0.357	1.087	
4000956+4107	0.587	357	2.522	0.289	3.542	0.406	4.894	0.859	0.424	0.196	1.114	
A0907	0.153	504	2.833	0.056	4.152	0.083	5.772	0.537	0.335	0.142	1.381	✓

Table 2.3 (cont'd)

Name	z	R_{2500}	L_X	e_{-L_X}	L_X	e_{-L_X}	kT	e_{-kT}	Z	e_Z	χ^2	WTD
			[0.5-7 keV]		[bol]							
		kpc	(10^{44} erg s $^{-1}$)		(10^{44} erg s $^{-1}$)		(keV)		(Z_\odot)			(d.o.f)
26441+1948	0.24	567	3.615	0.128	5.726	0.203	7.503	0.702	0.09	0.077	1.126	
10005+4409	0.154	367	1.065	0.07	1.437	0.095	3.278	0.268	0.183	0.095	1.243	
10069+3200	0.359	638	4.249	0.342	6.562	0.528	6.89	1.667	0.045	0.114	1.209	
10061+1201	0.221	488	2.803	0.071	4.111	0.105	5.861	0.328	0.313	0.062	1.133	✓
10105-1239	0.301	494	4.06	0.084	6.139	0.127	6.484	0.395	0.222	0.062	1.108	
A0963	0.206	527	4.534	0.076	6.861	0.115	6.364	0.782	0.226	0.113	1.259	✓
A0970	0.059	454	0.817	0.027	1.134	0.038	4.504	0.402	0.276	0.014	1.387	✓
10220+3830	0.049	343	0.047	0.003	0.062	0.004	2.664	0.237	0.361	0.098	1.229	
A0980	0.158	529	3.039	0.09	4.606	0.136	5.902	1.038	0.22	0.086	1.204	✓
10236+04111	0.291	589	8.464	0.127	14.162	0.213	8.052	0.966	0.285	0.096	1.289	✓
1023399+490838	0.144	533	3.321	0.111	5.034	0.168	6.513	0.589	0.156	0.083	1.099	
A3444	0.253	552	7.473	0.123	12.037	0.197	7.915	0.451	0.338	0.06	0.974	
1029+2623	0.584	397	3.401	0.23	5.0	0.338	5.809	0.958	0.074	0.099	1.136	
A1033	0.126	501	1.475	0.025	2.143	0.037	5.886	0.583	0.266	0.038	1.207	✓
08842	0.426	323	0.317	0.082	0.427	0.11	3.294	1.238	0.233	0.284	1.109	
EAD2007188	0.072	351	0.269	0.02	0.359	0.027	2.84	0.221	0.275	0.095	1.157	
A1068	0.138	463	1.884	0.042	2.664	0.06	4.963	0.253	0.25	0.057	1.078	✓
3402	0.015	179	0.006	0.001	0.008	0.001	0.824	0.013	0.385	0.048	1.052	✓
10537+5452	0.07	281	0.196	0.021	0.276	0.029	1.769	0.167	0.137	0.037	1.103	✓
10569-03373	0.823	401	7.212	0.383	11.42	0.607	7.494	1.083	0.096	0.107	1.444	
A1142	0.035	311	0.032	0.002	0.044	0.003	2.147	0.169	0.145	0.051	1.246	
11057-1014	0.466	589	7.646	0.598	12.986	1.015	9.115	2.406	0.383	0.258	1.249	
11089+0906	0.449	472	5.708	0.269	8.786	0.414	6.863	0.744	0.193	0.106	1.128	
NGC3551	0.032	271	0.023	0.002	0.032	0.002	1.623	0.062	0.32	0.051	1.229	
A1190	0.075	397	0.599	0.028	0.808	0.038	3.597	0.19	0.271	0.083	1.247	
A1201	0.169	492	2.527	0.054	3.681	0.079	5.309	0.543	0.359	0.06	1.254	✓
11130-2615	0.725	310	1.505	0.15	2.058	0.205	4.239	0.552	0.498	0.262	1.149	
A1204	0.171	423	1.629	0.066	2.253	0.092	4.327	0.277	0.218	0.084	1.31	

Table 2.3 (cont'd)

Name	z	R_{2500}	L_X	e_L_X	L_X	e_L_X	kT	e_kT	Z	e_Z	χ^2	WTD
			[0.5-7 keV]		[bol]							
			kpc	(10^{44} erg s $^{-1}$)	(10^{44} erg s $^{-1}$)		(keV)		(Z_\odot)		(d.o.f)	
1115+5319		0.466 604	8.139	0.364	14.554	0.651	10.328	1.639	0.141	0.157	1.084	
11158+0129		0.352 589	8.02	0.227	13.674	0.388	9.18	0.73	0.189	0.068	1.253	
11201+4318		0.6 348	5.466	0.67	7.677	0.941	4.71	0.906	0.088	0.128	1.022	
4001120+2326		0.562 355	2.181	0.169	3.024	0.234	4.457	0.577	0.279	0.159	1.152	
HCG051		0.026 235	0.014	0.001	0.02	0.002	1.319	0.031	0.294	0.038	1.156	
A1240		0.159 415	0.492	0.032	0.675	0.044	4.158	0.42	0.279	0.137	1.411	
11300+3637		0.06 269	0.07	0.004	0.1	0.006	1.738	0.083	0.13	0.032	1.188	✓
A1285		0.106 496	2.267	0.042	3.281	0.06	5.361	0.617	0.314	0.026	1.219	✓
A1300		0.307 786	9.614	0.24	17.836	0.446	11.265	1.174	0.262	0.099	1.285	
11375+6625		0.782 334	5.411	0.347	7.728	0.495	5.174	0.629	0.228	0.122	1.088	
1142248+583205		0.311 609	7.812	0.182	13.142	0.306	8.855	0.679	0.127	0.073	1.166	
4-33018		0.051 341	0.089	0.005	0.119	0.007	2.516	0.44	0.328	0.144	1.265	✓
A1413		0.143 578	4.175	0.044	6.581	0.07	7.35	0.558	0.231	0.089	1.459	✓
A1423		0.213 441	0.323	0.01	0.447	0.014	5.932	0.945	0.245	0.115	1.393	✓
17981192+4979669		0.383 569	7.801	0.394	13.915	0.702	10.276	1.691	0.267	0.141	1.111	
4-33144		0.081 269	0.077	0.005	0.106	0.007	1.766	0.077	0.247	0.051	1.001	✓
29251+2198		0.3 606	5.929	0.172	9.902	0.287	8.702	0.784	0.233	0.076	1.104	
A1446		0.104 390	0.707	0.019	0.95	0.025	3.526	0.117	0.354	0.048	1.123	✓
4001202+5751		0.677 275	1.944	0.352	2.532	0.458	3.184	0.758	0.949	0.609	1.112	
12062-0847		0.44 606	16.98	0.49	31.633	0.913	11.369	1.423	0.225	0.109	1.235	
4104		0.028 279	0.02	0.001	0.029	0.002	1.696	0.236	0.118	0.055	1.249	✓
12154-3900		0.119 494	1.605	0.038	2.315	0.055	5.505	0.361	0.429	0.11	1.167	
121733+033929		0.077 576	2.565	0.05	3.947	0.077	6.694	0.647	0.292	0.17	2.787	✓
121831+401236		0.32 475	4.257	0.182	6.32	0.271	6.09	0.651	0.21	0.116	1.216	
4001221+4918		0.7 428	4.586	0.318	7.143	0.495	7.16	1.083	0.299	0.138	1.08	
4325		0.025 202	0.018	0.001	0.027	0.002	0.976	0.018	0.263	0.026	1.141	✓
122648+215157		0.37 407	1.608	0.082	2.259	0.115	4.785	0.474	0.191	0.095	1.082	
12269+3332		0.89 539	11.315	0.521	22.466	1.035	13.126	1.968	0.193	0.189	1.117	

Table 2.3 (cont'd)

Name	z	R_{2500}	L_X	e_L_X	L_X	e_L_X	kT	e_kT	Z	e_Z	χ^2	WTD
			[0.5-7 keV]		[bol]							
		kpc	(10^{44} erg s $^{-1}$)		(10^{44} erg s $^{-1}$)		(keV)		(Z_\odot)			(d.o.f)
12303+1339	0.975	325	4.4	0.455	6.5	0.671	6.0	1.033	0.244	0.154	1.126	
A1553	0.165	568	3.879	0.113	6.048	0.176	7.238	0.587	0.518	0.105	1.136	
12342+0947	0.229	421	1.747	0.111	2.439	0.154	4.552	0.485	0.134	0.112	1.255	
A1569	0.074	315	0.261	0.02	0.348	0.027	2.223	0.326	0.239	0.089	1.575	✓
A1576	0.279	566	2.87	0.107	4.654	0.174	8.001	0.772	0.057	0.063	1.187	
12525-3116	0.054	352	0.229	0.013	0.301	0.017	2.869	0.165	0.515	0.102	1.344	
A1644	0.047	481	0.818	0.007	1.171	0.009	4.858	0.506	0.344	0.141	3.047	✓
A1650	0.084	514	2.247	0.018	3.278	0.026	5.726	0.524	0.286	0.106	1.737	✓
1259334+600409	0.33	501	3.904	0.145	6.024	0.223	6.894	0.515	0.112	0.068	1.062	
125947+312215	0.058	190	0.026	0.008	0.04	0.012	0.91	0.104	0.142	0.075	1.349	
A1664	0.128	468	1.93	0.041	2.747	0.059	5.018	0.211	0.093	0.04	1.178	✓
A1668	0.063	383	0.304	0.019	0.409	0.026	3.326	0.291	0.245	0.094	1.442	
1305589+263048	0.305	537	4.356	0.192	6.829	0.3	7.269	0.948	0.151	0.097	1.082	
A1682	0.234	550	3.71	0.105	5.803	0.164	7.205	0.618	0.116	0.092	1.131	
13110-0311	0.494	428	4.349	0.189	6.435	0.28	6.031	0.482	0.228	0.071	1.128	
A1689	0.183	676	8.559	0.103	15.062	0.181	10.0	0.874	0.279	0.11	1.41	✓
4001312+3900	0.404	390	1.239	0.146	1.725	0.204	4.481	1.148	0.138	0.235	1.106	
1315052+514902	0.291	583	6.692	0.136	11.224	0.229	8.765	0.771	0.025	0.048	1.149	
NGC5044	0.009	187	0.001	0.0	0.001	0.0	1.32	0.026	0.404	0.049	0.996	
A1722	0.328	631	3.531	0.237	5.955	0.399	8.969	2.186	0.553	0.267	1.251	
5098	0.037	213	0.024	0.001	0.037	0.002	1.134	0.06	0.188	0.066	1.257	✓
A1736	0.046	387	0.638	0.013	0.854	0.017	3.07	0.313	0.322	0.158	3.124	✓
SSGC081	0.05	398	0.418	0.015	0.565	0.02	3.207	0.393	0.282	0.087	2.178	✓
a1750ss	0.091	330	0.138	0.016	0.185	0.021	2.405	0.202	0.238	0.096	1.175	
A1750C	0.068	450	0.445	0.017	0.617	0.024	3.861	0.768	0.263	0.095	1.31	✓
A1750N	0.084	397	0.458	0.022	0.621	0.029	3.586	0.23	0.165	0.07	1.35	
213312961+1107566	0.079	155	0.008	0.004	0.012	0.006	0.64	0.042	0.206	0.173	1.022	
SC1329-313	0.048	406	0.269	0.014	0.362	0.019	3.182	0.222	0.184	0.092	2.819	✓

Table 2.3 (cont'd)

Name	z	R_{2500}	L_X	e_{-L_X}	L_X	e_{-L_X}	kT	e_{-kT}	Z	e_Z	χ^2	WTD
			[0.5-7 keV]		[bol]							
			kpc	(10^{44} erg s $^{-1}$)	(10^{44} erg s $^{-1}$)		(keV)		(Z_\odot)		(d.o.f)	
A3562	0.049	470	0.826	0.018	1.149	0.026	4.701	0.503	0.34	0.125	3.211	✓
A1763	0.223	555	6.919	0.18	11.013	0.286	7.669	0.593	0.388	0.084	1.252	
A1767	0.07	495	1.188	0.037	1.703	0.053	5.301	0.29	0.293	0.081	1.412	
4001340+4017	0.171	244	0.074	0.015	0.101	0.021	1.583	0.167	0.36	0.155	1.021	
A1775	0.072	408	0.923	0.011	1.238	0.015	3.76	0.413	0.503	0.11	1.616	✓
LCDCS0829	0.451	718	20.538	0.248	41.656	0.503	13.75	0.532	0.225	0.034	1.16	✓
1348502+491801	0.162	421	0.451	0.034	0.624	0.048	4.274	0.675	0.163	0.17	1.392	
4001354-0221	0.546	351	1.525	0.239	2.111	0.331	4.417	1.07	0.275	0.231	1.025	
13546+7715	0.397	467	4.673	0.251	7.024	0.378	6.384	0.815	0.314	0.119	1.103	
1357168+623249	0.563	382	2.449	0.255	3.513	0.366	5.225	1.059	0.127	0.155	1.052	
13592-1929	0.447	456	2.59	0.194	3.938	0.296	6.565	1.197	0.103	0.124	1.198	
A1831	0.062	399	0.538	0.017	0.72	0.023	3.541	0.159	0.447	0.077	1.347	
1359495+623047	0.322	509	4.018	0.121	6.184	0.186	6.859	0.59	0.199	0.084	1.468	
A1835	0.253	646	12.004	0.17	21.457	0.303	9.175	1.354	0.348	0.157	1.213	✓
3C295	0.464	246	3.038	0.462	4.172	0.634	2.115	0.261	0.16	0.096	1.144	
11382+4435	0.226	495	2.62	0.128	3.891	0.189	6.017	0.68	0.004	0.053	1.037	
A1882a	0.14	385	0.316	0.017	0.424	0.022	3.556	0.226	0.403	0.102	1.129	✓
1416238+444528	0.386	345	1.653	0.149	2.195	0.197	3.649	0.283	0.75	0.269	1.1	
LCDCS0954	0.67	213	1.323	0.599	1.794	0.812	2.017	0.679	0.295	0.377	0.932	
21594948+2407846	0.543	462	6.151	0.118	9.624	0.185	7.262	0.364	0.302	0.067	1.0	✓
A1914	0.171	633	9.446	0.147	15.799	0.246	8.422	1.044	0.213	0.053	1.398	✓
1427161+440730	0.498	601	6.679	0.271	11.975	0.486	10.403	1.424	0.236	0.142	1.328	
14276-2521	0.318	410	2.061	0.095	2.865	0.132	4.689	0.34	0.443	0.114	1.186	
A1930	0.131	440	0.951	0.038	1.311	0.053	4.366	0.629	0.587	0.028	1.235	✓
A1942	0.224	465	1.401	0.046	2.016	0.066	5.305	0.486	0.373	0.031	1.219	✓
WBL518	0.027	368	0.14	0.005	0.186	0.006	2.895	0.37	0.269	0.134	3.427	✓
A1991	0.059	346	0.329	0.01	0.438	0.013	2.766	0.059	0.316	0.038	1.106	✓
145715+222009	0.258	452	3.947	0.081	5.65	0.115	5.266	0.216	0.299	0.044	1.135	✓

Table 2.3 (cont'd)

Name	z	R_{2500}	L_X	e_{-L_X}	L_X	e_{-L_X}	kT	e_{-kT}	Z	e_Z	χ^2	WTD
			[0.5-7 keV]		[bol]							
		kpc	(10^{44} erg s $^{-1}$)		(10^{44} erg s $^{-1}$)		(keV)		(Z_\odot)		(d.o.f)	
AS0780	0.236	551	5.352	0.074	8.395	0.117	7.326	0.292	0.314	0.057	1.065	✓
A2009	0.153	543	3.537	0.097	5.386	0.148	6.695	0.309	0.443	0.071	1.392	✓
150117+422152	0.292	483	2.468	0.193	3.686	0.289	6.182	1.276	0.111	0.149	1.26	
1504075-024816	0.215	620	9.519	0.13	16.069	0.219	8.482	0.751	0.238	0.07	1.463	✓
A2034	0.113	595	2.975	0.031	4.685	0.049	7.555	0.875	0.303	0.108	1.568	✓
15149-1523	0.223	616	5.561	0.09	9.372	0.151	8.899	0.481	0.141	0.048	1.105	
A2061	0.078	457	1.171	0.022	1.631	0.031	4.619	0.136	0.284	0.042	1.083	✓
MKW03s	0.045	394	0.65	0.006	0.875	0.008	3.434	0.404	0.261	0.113	2.072	✓
A2069	0.116	525	1.793	0.032	2.675	0.048	5.936	0.646	0.301	0.128	1.712	✓
15242-3154	0.103	444	1.365	0.019	1.9	0.026	4.426	0.719	0.362	0.129	1.326	✓
15246+0957	0.516	338	2.21	0.156	2.988	0.21	4.02	0.378	0.61	0.2	1.079	
15328+3021	0.345	522	6.57	0.112	10.388	0.177	7.486	0.413	0.203	0.048	1.141	✓
A2107	0.041	434	0.433	0.009	0.588	0.012	3.766	0.48	0.265	0.114	3.251	✓
A2111	0.229	567	3.754	0.081	5.996	0.129	7.7	0.575	0.186	0.085	1.146	
A2104	0.153	565	3.731	0.049	5.815	0.077	7.2	1.018	0.245	0.153	1.354	✓
A2125	0.246	343	0.632	0.031	0.85	0.042	3.158	0.206	0.197	0.089	1.133	
A2124	0.066	485	0.326	0.012	0.463	0.017	5.092	0.4	0.35	0.113	1.104	✓
A2142	0.091	626	4.832	0.043	7.887	0.069	7.675	0.57	0.276	0.08	3.074	✓
15583-1410	0.097	483	2.001	0.021	2.85	0.029	5.018	0.356	0.371	0.106	1.33	✓
A2147	0.035	449	0.537	0.007	0.737	0.01	4.275	0.343	0.321	0.101	4.436	✓
A2151	0.037	358	0.183	0.023	0.243	0.031	2.794	0.342	0.268	0.174	3.062	✓
161314+564930	0.871	392	6.243	0.566	9.876	0.895	7.485	1.895	0.161	0.205	1.09	
A2163	0.203	795	20.636	0.14	42.292	0.288	13.183	1.347	0.24	0.045	1.603	✓
16213+3810	0.465	482	4.964	0.186	7.763	0.291	7.226	0.58	0.199	0.066	1.167	
16235+2634	0.426	449	3.854	0.228	5.798	0.342	6.365	0.908	0.201	0.124	1.005	
A2187	0.184	554	2.384	0.1	3.644	0.152	6.709	0.765	0.183	0.122	1.389	
A2204	0.152	654	6.25	0.044	10.792	0.077	8.269	1.172	0.319	0.143	1.623	✓
A2218	0.176	520	4.315	0.084	6.482	0.127	6.318	0.55	0.201	0.076	1.287	✓

Table 2.3 (cont'd)

Name	z	R_{2500}	L_X	e_L_X	L_X	e_L_X	kT	e_kT	Z	e_Z	χ^2	WTD
			[0.5-7 keV]		[bol]							
			kpc	$(10^{44} \text{ erg s}^{-1})$		$(10^{44} \text{ erg s}^{-1})$		(keV)		(Z_\odot)		(d.o.f)
A2219	0.226	699	14.778	0.091	27.42	0.169	11.017	0.888	0.28	0.093	1.223	✓
4001641+4001	0.464	346	1.098	0.149	1.488	0.203	3.941	0.826	0.423	0.285	1.103	
HerculesA	0.155	419	1.836	0.034	2.531	0.047	3.653	1.309	0.181	0.097	1.224	✓
NGC6269	0.035	308	0.078	0.004	0.108	0.006	1.813	0.314	0.107	0.111	3.295	✓
021701+6412	0.453	453	2.479	0.125	3.72	0.188	6.371	0.771	0.379	0.154	1.122	
A2244	0.097	515	2.68	0.024	3.927	0.036	5.812	0.105	0.268	0.028	1.106	✓
A2256	0.058	586	3.438	0.033	5.363	0.052	6.782	0.465	0.381	0.135	1.886	✓
A2249	0.082	486	1.267	0.035	1.811	0.051	5.153	0.342	0.168	0.086	1.204	
A2255	0.081	530	2.107	0.026	3.133	0.038	6.086	0.559	0.325	0.113	1.828	✓
NGC6338	0.027	336	0.106	0.003	0.144	0.004	2.233	0.328	0.186	0.091	4.791	✓
A2259	0.164	508	3.248	0.119	4.806	0.176	6.089	0.502	0.427	0.128	1.254	
43072	0.164	560	4.348	0.075	6.753	0.116	7.066	0.427	0.413	0.059	1.371	✓
17202+3536	0.391	530	6.766	0.206	10.872	0.331	7.87	0.653	0.367	0.08	1.279	
A2261	0.224	593	7.182	0.156	11.669	0.253	7.714	1.178	0.349	0.077	1.276	✓
A2294	0.169	570	4.578	0.17	7.178	0.266	7.303	0.736	0.26	0.106	1.415	
17316+2251	0.366	551	6.784	0.211	11.278	0.351	8.608	0.849	0.299	0.123	1.32	
Abell2276	0.141	338	0.501	0.046	0.672	0.061	2.831	0.277	0.202	0.104	1.249	
17421+3306	0.076	437	1.099	0.017	1.507	0.024	4.076	0.352	0.374	0.179	1.653	✓
174715+451155	0.156	447	1.518	0.066	2.128	0.093	4.729	0.378	0.182	0.084	1.142	
17502+3504	0.171	442	1.689	0.078	2.364	0.109	4.639	0.356	0.126	0.083	1.187	
18044+1002	0.152	545	5.159	0.144	8.034	0.225	7.097	0.592	0.092	0.075	1.225	
A2302	0.179	447	1.324	0.055	1.862	0.077	4.821	0.382	0.203	0.096	1.157	
18243+4309	0.487	476	1.922	0.182	2.995	0.283	7.102	2.235	0.06	0.211	1.099	
18290+6913	0.203	402	0.843	0.044	1.151	0.06	4.057	0.305	0.335	0.109	1.234	
18521+5711	0.109	418	0.465	0.019	0.635	0.026	4.003	0.283	0.259	0.096	1.345	
18539+6822	0.093	423	1.031	0.025	1.419	0.034	4.129	0.221	0.19	0.074	1.199	
33709-2597	0.264	563	6.544	0.138	10.438	0.221	7.658	0.539	0.118	0.07	1.181	
A2319	0.056	670	5.846	0.046	10.028	0.078	8.664	1.413	0.319	0.131	3.532	✓

Table 2.3 (cont'd)

Name	z	R_{2500}	L_X	e_{-L_X}	L_X	e_{-L_X}	kT	e_{-kT}	Z	e_Z	χ^2	WTD
			[0.5-7 keV]		[bol]							
			kpc	(10^{44} erg s $^{-1}$)	(10^{44} erg s $^{-1}$)		(keV)		(Z_\odot)		(d.o.f)	
19318-2635	0.352	540	8.805	0.104	14.152	0.168	7.793	0.786	0.374	0.147	1.326	✓
AS0821	0.237	511	5.443	0.174	8.184	0.261	6.386	0.506	0.302	0.072	1.108	
19383+5409	0.26	539	8.739	0.35	13.629	0.546	7.202	0.728	0.356	0.091	1.124	
19473-7623	0.217	574	5.483	0.179	8.604	0.28	7.337	0.632	0.338	0.086	1.214	
A3653	0.109	450	0.524	0.015	0.733	0.021	4.781	0.341	0.345	0.071	1.222	
19582-3011	0.117	399	0.088	0.012	0.119	0.016	3.283	0.982	0.182	0.452	1.212	
20035-2323	0.317	599	7.858	0.19	13.401	0.324	9.178	0.804	0.131	0.072	1.222	
20113-5725	0.279	363	2.134	0.151	2.886	0.205	3.629	0.373	0.231	0.11	1.156	
20148-2430	0.161	560	4.182	0.099	6.499	0.154	7.148	0.389	0.467	0.088	1.19	✓
2023-5535	0.232	609	5.848	0.172	9.627	0.283	8.387	0.761	0.291	0.085	1.121	
20318-4037	0.342	494	7.965	0.43	12.201	0.659	6.735	0.918	0.128	0.117	1.116	
2034-5936	0.92	298	6.077	0.871	8.49	1.216	4.721	0.886	0.298	0.17	1.101	
A3695	0.089	550	1.909	0.042	2.887	0.064	6.465	0.427	0.161	0.084	1.352	
2043-5035	0.723	356	6.36	0.474	9.192	0.685	5.436	0.683	0.19	0.099	1.073	
20460-3430	0.423	428	4.194	0.216	6.1	0.314	5.606	0.447	0.212	0.086	1.136	
20499-3216	0.325	528	5.29	0.221	8.338	0.348	7.423	0.952	0.262	0.109	1.259	
A3739	0.165	516	2.874	0.12	4.251	0.177	6.084	0.527	0.413	0.111	1.096	
2106-5844	1.132	329	22.47	1.818	34.961	2.829	7.158	0.782	0.193	0.096	1.044	
IC1365	0.049	429	0.574	0.025	0.781	0.034	3.966	0.438	0.509	0.083	2.48	✓
2129-0741	0.589	479	12.133	0.669	19.708	1.086	8.117	0.943	0.454	0.126	1.13	
2135-0102	0.325	557	4.768	0.219	7.826	0.36	8.365	1.066	0.58	0.154	1.246	
A2355	0.124	586	1.465	0.045	2.29	0.071	7.24	0.69	0.289	0.118	1.276	
2135-5726	0.427	477	3.586	0.199	5.541	0.307	6.922	1.301	0.108	0.157	1.099	
WBL671	0.051	208	0.012	0.004	0.019	0.006	1.004	0.119	0.111	0.061	1.187	
21402-2339	0.313	468	3.985	0.11	5.86	0.162	5.922	0.343	0.314	0.059	1.07	✓
2145-5644	0.48	462	4.965	0.361	7.663	0.557	6.866	1.278	0.006	0.078	1.053	
2146-4633	0.933	339	3.815	0.471	5.731	0.707	6.267	1.339	0.01	0.092	1.102	
A3809	0.062	354	0.426	0.014	0.565	0.019	3.117	0.292	0.413	0.138	1.303	✓

Table 2.3 (cont'd)

Name	z	R_{2500}	L_X	e_L_X	L_X	e_L_X	kT	e_kT	Z	e_Z	χ^2	WTD
			[0.5-7 keV]		[bol]							
		kpc	(10^{44} erg s $^{-1}$)		(10^{44} erg s $^{-1}$)		(keV)		(Z_\odot)		(d.o.f)	
2148-6116	0.571	436	3.484	0.229	5.327	0.351	6.735	1.175	0.272	0.195	1.039	
A2384	0.094	516	1.119	0.018	1.628	0.026	5.246	0.839	0.39	0.162	2.33	✓
A2390	0.228	668	13.625	0.092	25.178	0.169	11.164	0.313	0.28	0.032	1.068	✓
21538+3746	0.292	608	11.047	0.148	19.077	0.256	9.495	0.365	0.258	0.036	1.148	✓
A2409	0.148	510	4.281	0.134	6.289	0.197	5.955	0.382	0.462	0.093	1.292	
A3827	0.098	585	3.243	0.032	5.08	0.05	7.338	0.789	0.339	0.144	1.302	✓
A2415	0.058	344	0.401	0.012	0.534	0.016	2.583	0.284	0.347	0.094	1.236	✓
22117-0349	0.27	655	6.301	0.219	11.029	0.383	9.815	1.315	0.221	0.121	1.394	
3C444	0.153	473	0.613	0.021	0.876	0.03	4.379	0.393	0.332	0.098	1.334	✓
A2426	0.098	522	1.671	0.053	2.451	0.077	5.825	0.389	0.251	0.1	1.305	
2214-1359	0.483	530	10.888	0.419	18.292	0.705	8.833	0.989	0.194	0.093	1.12	
A3854	0.149	472	2.281	0.081	3.256	0.116	5.181	0.394	0.258	0.092	1.197	
22186-3853	0.138	499	3.292	0.092	4.789	0.134	5.604	0.33	0.2	0.075	1.24	
2218-4519	0.65	398	3.405	0.277	4.965	0.405	5.831	1.117	0.619	0.292	1.132	
A2445	0.166	414	1.718	0.057	2.34	0.077	4.162	0.215	0.545	0.086	1.19	
A3880	0.058	356	0.341	0.018	0.453	0.023	2.897	0.277	0.305	0.143	2.28	✓
22286+2036	0.412	550	10.081	0.348	16.485	0.569	8.249	0.824	0.352	0.116	1.176	
22298-2756	0.324	464	4.07	0.19	5.967	0.279	5.882	0.562	0.397	0.108	1.233	
514-050	0.017	241	0.003	0.0	0.005	0.0	1.231	0.043	0.225	0.029	1.337	
2232-5959	0.594	394	4.175	0.545	5.792	0.756	4.53	1.074	0.33	0.218	1.104	
2233-5339	0.48	466	4.392	0.264	6.75	0.406	6.791	1.168	0.075	0.121	1.089	
A2457	0.059	414	0.55	0.015	0.744	0.021	3.595	0.099	0.326	0.059	1.352	✓
A2465	0.245	294	0.343	0.03	0.457	0.04	2.378	0.209	0.354	0.143	1.165	
22428+5301	0.192	595	4.117	0.053	6.747	0.088	8.271	0.345	0.206	0.03	1.048	✓
2243198-093530	0.432	488	14.006	0.52	21.842	0.811	7.179	0.672	0.267	0.085	1.214	
2245-6206	0.58	416	4.606	0.55	6.897	0.823	6.221	1.324	0.077	0.121	1.051	
22450+2637	0.304	499	4.48	0.241	6.835	0.368	6.71	0.933	0.33	0.146	1.224	
A3911	0.096	544	2.198	0.061	3.262	0.09	6.106	0.393	0.285	0.081	1.183	

Table 2.3 (cont'd)

Name	z	R_{2500}	L_X	e_{-L_X}	L_X	e_{-L_X}	kT	e_{-kT}	Z	e_Z	χ^2	WTD
			[0.5-7 keV]		[bol]							
		kpc	(10^{44} erg s $^{-1}$)		(10^{44} erg s $^{-1}$)		(keV)		(Z_\odot)		(d.o.f)	
A2485	0.247	511	2.703	0.119	4.043	0.178	6.25	0.714	0.231	0.129	1.247	
AS1063	0.348	663	22.56	0.412	41.905	0.765	11.302	0.722	0.359	0.07	1.219	
A3921	0.093	522	1.981	0.037	2.916	0.054	5.766	0.762	0.36	0.085	1.879	✓
A2507	0.196	414	1.003	0.065	1.377	0.089	4.309	0.433	0.426	0.154	1.069	
2259-6057	0.75	411	4.949	0.246	7.715	0.384	7.265	1.064	0.694	0.215	1.2	
23028+0843	0.722	407	1.736	0.111	2.667	0.17	6.818	1.234	0.169	0.18	1.139	
A2537	0.295	506	4.65	0.104	7.083	0.158	6.649	0.368	0.243	0.054	1.157	✓
23115+0338	0.3	598	7.26	0.281	12.544	0.486	9.518	1.005	0.334	0.103	1.333	
A2550	0.123	276	0.216	0.015	0.297	0.02	1.929	0.124	0.231	0.049	1.077	✓
A2556	0.087	413	0.814	0.018	1.105	0.024	3.86	0.155	0.281	0.041	1.157	✓
AS1101	0.058	345	0.541	0.01	0.726	0.013	2.698	0.286	0.199	0.089	2.076	✓
23185+0034	0.78	382	2.373	0.178	3.611	0.271	6.597	1.195	0.152	0.138	1.091	
A2597	0.085	442	0.878	0.01	1.214	0.015	4.266	0.259	0.279	0.08	1.31	✓
2331-5051	0.571	419	3.893	0.38	5.899	0.575	6.486	1.747	0.096	0.143	1.078	
A2626	0.055	382	0.443	0.012	0.593	0.016	3.264	0.111	0.349	0.044	1.119	✓
A2627	0.126	601	0.319	0.036	0.581	0.065	10.85	4.147	0.736	0.77	1.287	
2337-5942	0.781	435	15.389	1.279	25.287	2.101	8.326	1.621	0.186	0.161	1.065	
A2631	0.273	580	7.191	0.246	11.658	0.398	8.024	0.961	0.169	0.1	1.254	
A4023	0.193	507	1.996	0.082	2.984	0.123	6.256	0.635	0.268	0.117	1.216	
2341-5119	0.998	384	7.073	0.735	11.579	1.203	8.27	1.573	0.336	0.195	1.085	
A2645	0.251	512	3.698	0.171	5.582	0.258	6.47	0.782	0.297	0.119	1.118	
23442-0422	0.079	450	1.473	0.038	2.031	0.052	4.501	0.143	0.406	0.261	1.422	✓
2344-4243	0.62	529	21.473	1.351	37.864	2.383	9.981	1.819	0.114	0.134	1.096	
A2657	0.04	403	0.583	0.016	0.785	0.021	3.567	0.307	0.302	0.165	3.162	✓
2345-6405	0.94	379	5.516	0.406	8.901	0.656	7.9	1.51	0.072	0.128	1.095	
HCG097	0.022	197	0.007	0.001	0.012	0.002	0.812	0.035	0.135	0.03	1.166	
A4038	0.028	369	0.394	0.007	0.525	0.009	2.878	0.263	0.286	0.118	3.54	✓
AS1150	0.261	453	0.851	0.103	1.217	0.148	5.221	1.32	0.23	0.291	1.079	

Table 2.3 (cont'd)

Name	z	R_{2500}	L_X	e_L_X	L_X	e_L_X	kT	e_kT	Z	e_Z	χ^2	WTD
			[0.5-7 keV]		[bol]							
		kpc	(10^{44} erg s $^{-1}$)	(10^{44} erg s $^{-1}$)			(keV)		(Z_\odot)			(d.o.f)
A2665	0.056	458	0.489	0.018	0.68	0.025	4.553	0.294	0.31	0.095	1.412	
A2667	0.23	556	7.819	0.208	12.434	0.331	7.604	0.677	0.163	0.084	1.046	
A2670	0.076	435	0.743	0.021	1.019	0.028	4.001	0.706	0.31	0.114	2.206	✓
2355-5056	0.35	395	2.27	0.258	3.154	0.358	4.536	0.913	0.273	0.202	1.119	
2359-5009	0.76	294	1.729	0.295	2.35	0.401	4.011	0.806	0.423	0.215	1.006	

Table 2.4: **Table of full cluster names and coordinates in ACCEPT2.0.** This table contains the coordinates of ACCEPT2.0 clusters and defines the naming convention used throughout this dissertation. Col(1) is the truncated cluster name, col(2) is the full name in ACCEPT2.0, cols(3,4) are the RA and DEC (J2000) in degrees, and cols(5,6) are the entropy excess K_0 and error, if available.

Name	Full ACCEPT2.0 Name	RA	DEC (deg)	K_0	e_{K_0} (keV cm 2)
000619+105206	NSCS_J000619+105206	1.5845	10.8643	58.428	11.089
00088+5215	ZwCl_0008.8+5215	2.8647	52.5265	170.494	40.772
00117-1523	MACS_J0011.7-1523	2.9286	-15.3892		
A0013	ABELL_0013	3.4098	-19.5005	130.014	31.3
A2744	ABELL_2744	3.5807	-30.3909		
0014-4952	SPT-CLJ0014-4952	3.7037	-49.8838		
Cl0016+16	Cl_0016+16	4.6402	16.4359	165.464	19.834
00254-1222	MACS_J0025.4-1222	6.3737	-12.3761	149.815	20.362
00278+2616	MCXC_J0027.8+2616	6.9383	26.2756		
30484-4142	PLCKESZ_G304.84-41.42	7.026	-75.6358		
00305+2618	WARP_J0030.5+2618	7.6427	26.3027		
00354-2015	MCXC_J0035.4-2015	8.8586	-20.2623	136.376	16.255
A0068	ABELL_0068	9.2775	9.1578		
A0085	ABELL_0085	10.4599	-9.3029		
A2813	ABELL_2813	10.8535	-20.6234		
00408+2404	ZwCl_0040.8+2404	10.9678	24.4059	9.048	1.165
A0098N	ABELL_0098N	11.6029	20.6218	10.598	5.928
A98ss	A98ss	11.6516	20.2567		
351-021	ESO_351-_G_021	13.7497	-35.3214	3.731	0.865
A0119	ABELL_0119	14.0755	-1.2422		
0058-6145	SPT-CLJ0058-6145	14.588	-61.7679		
200428	_SBV2004_RS_28	16.2302	0.0596		
A0141	ABELL_0141	16.3979	-24.6301	158.783	28.161
0106-5943	SPT-CLJ0106-5943	16.6175	-59.7204		
01670077+0105926	MaxBCG_J016.70077+01.05926	16.7062	1.0563	11.751	0.707
01077+5408	CIZA_J0107.7+5408	16.9381	54.1327	305.475	45.983

Table 2.4 (cont'd)

Name	Full ACCEPT2.0 Name	RA	DEC (deg)	K_0	e_K0 (keV cm ²)
A0160	ABELL_0160	18.2737	15.5298		
011502+002441	NSCS_J011502+002441	18.7658	0.4041		
A2895	ABELL_2895	19.5469	-26.9653	168.687	33.931
UGC00842	UGC_00842	19.7235	-1.0021		
0123-4821	SPT-CLJ0123-4821	20.7992	-48.3566		
A0193	ABELL_0193	21.2802	8.7003	134.938	9.008
A0209	ABELL_0209	22.9701	-13.6114	86.644	24.724
Abell222	Abell_222	24.3946	-12.9931	148.849	21.545
Abell223	Abell_223	24.4835	-12.8198		
01400-0555	MACS0140.0-0555	25.0065	-5.9191		
01420+2131	MCXC_J0142.0+2131	25.5134	21.5212		
01502127-1005305	SDSS_J015021.27-100530.5_GROUP	27.5885	-10.0915	2.481	6.357
0151-5954	SPT-CLJ0151-5954	27.8452	-59.9075		
01525-2853	MCXC_J0152.5-2853	28.1437	-28.8937		
A0267	ABELL_0267	28.1774	1.0123	148.399	16.487
0156-5541	SPT-CLJ0156-5541	29.0423	-55.6987		
02209-3829	MCXC_J0220.9-3829	35.2357	-38.4804		
A3017	ABELL_3017	36.4715	-41.9152	36.916	7.731
0228259+003202	WHL_J022825.9+003202	37.1072	0.5328		
MZ10451	MZ_10451	37.4397	-29.6287	11.591	10.746
0232-4421	SPT-CL_J0232-4421	38.0777	-44.3462		
0234-5831	SPT-CL_J0234-5831	38.6747	-58.5236		
A0368	ABELL_0368	39.3652	-26.508		
4000237-5224	400d_J0237-5224	39.5034	-52.4198		
A0370	ABELL_0370	39.9707	-1.5793	256.699	27.693
02426-2132	MACS_J0242.6-2132	40.6495	-21.5406	9.402	1.573
0243-5930	SPT-CLJ0243-5930	40.863	-59.5172		
AS0295	ABELL_S0295	41.3616	-53.03	165.939	21.589
4000245+0936	400d_J0245+0936	41.4538	9.6106		

Table 2.4 (cont'd)

Name	Full ACCEPT2.0 Name	RA	DEC (deg)	K_0	e_K0
				(keV	cm ²)
A0376	ABELL_0376	41.5164	36.9055	61.935	16.644
A0383	ABELL_0383	42.0141	-3.5293	10.28	1.047
0252-4824	SPT-CLJ0252-4824	43.2076	-48.4163		
NGC1132	NGC_1132	43.2158	-1.2748		
0256-5617	SPT-CLJ0256-5617	44.1056	-56.2982		
A0402	ABELL_0402	44.4217	-22.1549		
A0399	ABELL_0399	44.4726	13.0253		
A0401	ABELL_0401	44.7438	13.5788	154.597	14.171
03016+0155	MCXC_J0301.6+0155	45.4092	1.9208	12.181	1.87
4000302-0423	400d_J0302-0423	45.588	-4.39		
03037-7752	MCXC_J0303.7-7752	45.9413	-77.8792	187.074	34.239
A3088	ABELL_3088	46.7581	-28.6658		
0307-6225	SPT-CLJ0307-6225	46.8203	-62.4458		
0307-5042	SPT-CLJ0307-5042	46.9607	-50.7019		
03089+2645	MACS_J0308.9+2645	47.2331	26.7611	144.011	31.449
0310-4647	SPT-CLJ0310-4647	47.6349	-46.7862		
A3094	ABELL_3094	47.8989	-26.8985	31.063	66.818
4000318-0302	400d_J0318-0302	49.6437	-3.0509		
0324-6236	SPT-CLJ0324-6236	51.0518	-62.5988		
4000328-2140	400d_J0328-2140	52.1494	-21.6736		
A3126	ABELL_3126	52.1494	-55.718	158.222	13.322
A3128	ABELL_3128	52.4609	-52.5804	12.128	60.726
03311-2100	MCXC_J0331.1-2100	52.775	-21.0089	11.718	1.574
0334-4659	SPT-CLJ0334-4659	53.546	-46.996		
3C089	3C_089	53.5625	-1.1882	30.855	5.532
03408-4542	MCXC_J0340.8-4542	55.2241	-45.6768	189.419	55.692
III Zw054	III_Zw_054	55.3153	15.4097		
A3158	ABELL_3158	55.7139	-53.6297		
0346-5438	ACT-CL_J0346-5438	56.7326	-54.6485		

Table 2.4 (cont'd)

Name	Full ACCEPT2.0 Name	RA	DEC (deg)	K_0	e_K0 (keV cm ²)
0352-5647	SPT-CLJ0352-5647	58.2416	-56.7955		
03529+1941	MCXC_J0352.9+1941	58.2457	19.683	7.106	0.38
03588-2955	MACS_J0358.8-2955	59.7263	-29.9259	26.151	14.956
4000405-4100	400d_J0405-4100	61.3517	-41.0054		
A0478	ABELL_0478	63.355	10.4653	11.58	0.91
04161-2403	MACS_J0416.1-2403	64.0393	-24.0655	76.272	106.522
0417-4748	SPT-CL_J0417-4748	64.3465	-47.8134		
04175-1154	MACS_J0417.5-1154	64.3926	-11.9096	23.919	8.332
04258-0833	MCXC_J0425.8-0833	66.4634	-8.5604	6.656	1.32
0426-5455	SPT-CLJ0426-5455	66.5191	-54.9116		
AS0463	ABELL_S0463	67.1569	-53.8402	117.469	23.573
04296-0253	MACS_J0429.6-0253	67.4	-2.8854	12.169	3.11
04371+0043	MCXC_J0437.1+0043	69.2898	0.7322	39.939	4.172
04390+0715	MCXC_J0439.0+0715	69.7523	7.2684	57.207	11.956
04390+0520	MCXC_J0439.0+0520	69.759	5.3454	6.155	1.597
04431+0210	MCXC_J0443.1+0210	70.7914	2.172		
A0514	ABELL_0514	72.007	-20.4478		
A3292	ABELL_3292	72.483	-44.6731	108.116	10.191
04519+0006	MACS_J0451.9+0006	72.9766	0.1055		
04541-0300	MCXC_J0454.1-0300	73.5471	-3.0159		
552-020	ESO_552-_G_020	73.7181	-18.1154		
04552+0657	MACS_J0455.2+0657	73.822	6.9634		
0456-5116	SPT-CLJ0456-5116	74.1149	-51.2789		
0509-5342	SPT-CL_J0509-5342	77.3385	-53.7035		
A3322	ABELL_3322	77.5713	-45.3215	104.613	17.637
05107-0801	MCXC_J0510.7-0801	77.6985	-8.0275	122.172	51.636
A0539	ABELL_0539	79.1556	6.4406		
AS0520	ABELL_S0520	79.1571	-54.5131	320.133	39.838
05207-1328	MCXC_J0520.7-1328	80.1751	-13.4803		

Table 2.4 (cont'd)

Name	Full ACCEPT2.0 Name	RA	DEC (deg)	K_0	e_K0 (keV cm ²)
052215-481816	CXOU_J052215-481816	80.5635	-48.3045		
A3343	ABELL_3343	81.4534	-47.2528	163.757	19.794
05282-2942	MCXC_J0528.2-2942	82.0607	-29.7219	88.463	18.81
RBS0653	RBS_0653	82.2209	-39.4705	27.862	4.749
28658-3125	PLCKESZ_G286.58-31.25	82.8695	-75.1768	149.127	62.571
A0545	ABELL_0545	83.1057	-11.5422	146.987	21.961
05329-3701	MCXC_J0532.9-3701	83.2314	-37.0264	98.106	24.012
3060170-	ESO3060170-A	85.0278	-40.8366		
0542-4100	RDCS_J0542-4100	85.7091	-40.9996		
05470-3904	MCXC_J0547.0-3904	86.7563	-39.074		
A3364	ABELL_3364	86.9065	-31.8712	205.019	17.037
A0548A	ABELL_0548A	87.1596	-25.4779	23.658	10.142
0551-5709	SPT-CL_J0551-5709	87.8876	-57.1491		
A0550	ABELL_0550	88.2159	-21.0536	120.247	24.385
05534-3342	MACS_J0553.4-3342	88.3574	-33.7085	106.577	46.574
0559-5249	SPT-CL_J0559-5249	89.9283	-52.8309		
A3376	ABELL_3376	90.548	-39.9498		
A3378	ABELL_3378	91.4749	-35.3022	8.528	3.136
06163-2156	CIZA_J0616.3-2156	94.1033	-21.9383	234.527	60.544
AS0579	ABELL_S0579	94.1339	-39.7968	129.966	24.011
0616-5227	ACT-CL_J0616-5227	94.1427	-52.4521		
13959+2418	G139.59+24.18	95.4541	74.7014	32.801	8.952
A3391	ABELL_3391	96.5785	-53.6926	203.151	29.569
A3399	ABELL_3399	99.3088	-48.4719	59.435	16.441
16765+1764	PLCKESZ_G167.65+17.64	99.5162	47.7986	209.979	18.217
AS0592	ABELL_S0592	99.702	-53.9742		
A3402	ABELL_3402	100.4229	-49.7947		
A3404	ABELL_3404	101.37	-54.2284	95.055	18.879
A0562	ABELL_0562	103.3394	69.331	122.537	34.177

Table 2.4 (cont'd)

Name	Full ACCEPT2.0 Name	RA	DEC	K_0	e_K0
			(deg)	(keV cm ²)	
Bullet	Bullet_Cluster	104.6276	-55.9388		
07123+5931	MACS_J0712.3+5931	108.0864	59.5389		
0717+3745	MACS_J0717+3745	109.3756	37.76		
4000720+7108	400d_J0720+7108	110.2248	71.1497		
A0578	ABELL_0578	111.223	66.9854	16.576	48.228
A0586	ABELL_0586	113.0847	31.6325	116.11	10.286
07357+7421	ZwCl_0735.7+7421	115.4346	74.244	16.14	0.906
07449+3927	MACS_J0744.9+3927	116.2201	39.4573	53.443	7.508
PKS0745-19	PKS_0745-19	116.8795	-19.2947	8.581	0.315
WBL154	WBL_154	117.8364	50.2339		
A0598	ABELL_0598	117.855	17.5139	8.32	2.293
A0611	ABELL_0611	120.237	36.0566		
08065+2822	ZwCl_0806.5+2822	122.4251	28.2023		
43062	SDSS-C4_3062	122.5973	42.2739	46.651	12.194
A0644	ABELL_0644	124.3585	-7.5088	70.24	6.441
08196+6336	MCXC_J0819.6+6336	124.858	63.6238		
UGC1120	UGCl_120	125.8402	4.3726		
08232+0425	ZwCl_0823.2+0425	126.4913	4.2467	72.063	16.331
A0665	ABELL_0665	127.7468	65.8395		
2MFGC06756	2MFGC_06756	128.7284	55.5722		
4000838+1948	400d_J0838+1948	129.6288	19.8055		
A3411	ABELL_3411	130.4664	-17.4627	194.021	24.317
084254+292723	NSC_J084254+292723	130.7329	29.4576	22.863	2.043
A0697	ABELL_0697	130.7399	36.3664	229.645	22.639
08488+4455	RX_J0848.8+4455	132.199	44.9378		
08485+3341	ZwCl_0848.5+3341	132.9121	33.5188		
08579+2107	ZwCl_0857.9+2107	135.1535	20.8944		
A0744	ABELL_0744	136.8355	16.6517		
+1373+110+018	SDSS_+137.3+11.0+0.18	137.3031	10.9748	88.2	16.425

Table 2.4 (cont'd)

Name	Full ACCEPT2.0 Name	RA	DEC (deg)	K_0	e_K0 (keV cm ²)
09112+1746	MACS_J0911.2+1746	137.7988	17.7757		
HCG037	HCG_037	138.4146	29.9928	2.267	1.28
20913454+405628	2MASSi_J0913454+405628	138.4395	40.9413	23.534	2.754
A0773	ABELL_0773	139.4711	51.728	179.097	21.364
HydraA	Hydra_A	139.5246	-12.0957	15.711	0.627
0918343+295318	WHL_J091834.3+295318	139.6502	29.8919		
092017+303027	NSC_J092017+303027	140.1118	30.4927	128.487	76.673
0922076+034558	WHL_J092207.6+034558	140.5428	3.7775		
A0795	ABELL_0795	141.0241	14.1739	27.927	3.477
4000926+1242	400d_J0926+1242	141.6531	12.7178		
0938209+520243	WHL_J093820.9+520243	144.5847	52.0484	92.459	18.089
A0853	ABELL_0853	145.5609	15.3818		
A0868	ABELL_0868	146.3589	-8.6568	192.942	14.459
0947124+762313	GALEX_J094712.4+762313	146.8027	76.3871	25.087	1.568
09498+1708	MACS_J0949.8+1708	147.4651	17.1187		
09496+5207	ZwCl_0949.6+5207	148.2055	51.8842		
0954+1738	XMMU_J0954+1738	148.5707	17.6349		
4000956+4107	400d_J0956+4107	149.0114	41.1226		
A0907	ABELL_0907	149.5917	-11.064		
26441+1948	PLCKESZ_G264.41+19.48	150.0067	-30.2772	94.347	40.037
10005+4409	MCXC_J1000.5+4409	150.1307	44.1458		
10069+3200	MACS_J1006.9+3200	151.728	32.0286		
10061+1201	ZwCl_1006.1+1201	152.1981	11.7908		
10105-1239	MCXC_J1010.5-1239	152.6355	-12.6633		
A0963	ABELL_0963	154.2652	39.0471		
A0970	ABELL_0970	154.3481	-10.6851	102.112	18.122
10220+3830	MCXC_J1022.0+3830	155.5416	38.523		
A0980	ABELL_0980	155.6182	50.1061	150.124	21.661
10236+04111	BLOX_J1023.6+0411.1	155.9154	4.1863	8.947	0.96

Table 2.4 (cont'd)

Name	Full ACCEPT2.0 Name	RA	DEC (deg)	K_0	e_K0
				(keV	cm ²)
1023399+490838	WHL_J102339.9+490838	155.9162	49.1445	128.079	20.582
A3444	ABELL_3444	155.9592	-27.2564	20.762	1.805
1029+2623	SDSS_J1029+2623	157.3007	26.3931		
A1033	ABELL_1033	157.9363	35.0407	122.945	16.451
08842	SDSSCGB_08842	159.6786	48.8224		
EAD2007188	_EAD2007__188	159.9115	5.1757		
A1068	ABELL_1068	160.1854	39.9534	6.283	0.705
3402	NGC_3402_GROUP	162.6086	-12.845	1.666	0.119
10537+5452	MCXC_J1053.7+5452	163.3842	54.8754	63.3	12.56
10569-03373	BLOX_J1056.9-0337.3	164.2327	-3.6272	126.798	36.945
A1142	ABELL_1142	165.1936	10.5478		
11057-1014	MACS_J1105.7-1014	166.4435	-10.2438		
11089+0906	MACS_J1108.9+0906	167.2304	9.0989	80.249	38.94
NGC3551	NGC_3551	167.4352	21.7591		
A1190	ABELL_1190	167.9159	40.8402	213.612	19.437
A1201	ABELL_1201	168.2278	13.4339	63.6	8.173
11130-2615	WARP_J1113.0-2615	168.2717	-26.261		
A1204	ABELL_1204	168.3351	17.5944	14.727	1.691
1115+5319	SDSS_J1115+5319_CLUSTER	168.8116	53.3333		
11158+0129	MACS_J1115.8+0129	168.9661	1.499	22.147	2.422
11201+4318	WARP_J1120.1+4318	170.0296	43.3022		
4001120+2326	400d_J1120+2326	170.2379	23.4419		
HCG051	HCG_051	170.6098	24.2986		
A1240	ABELL_1240	170.9073	43.0975	196.271	92.437
11300+3637	MCXC_J1130.0+3637	172.5131	36.637		
A1285	ABELL_1285	172.5932	-14.5807	186.247	29.134
A1300	ABELL_1300	172.9775	-19.9291	65.709	26.357
11375+6625	CIG_1137.5+6625	175.0935	66.1376		
1142248+583205	WHL_J114224.8+583205	175.598	58.5203	459.851	44.958

Table 2.4 (cont'd)

Name	Full ACCEPT2.0 Name	RA	DEC (deg)	K_0	e_K0
					(keV cm ²)
4-33018	SDSS-C4-DR3_3018	176.8046	55.7291	130.902	37.892
A1413	ABELL_1413	178.8247	23.4057	57.42	5.077
A1423	ABELL_1423	179.3218	33.611		
17981192+4979669	GMBCG_J179.81192+49.79669	179.8078	49.7943		
4-33144	SDSS-C4-DR3_3144	179.9675	55.5348	3.097	0.714
29251+2198	PLCKESZ_G292.51+21.98	180.2724	-39.8745		
A1446	ABELL_1446	180.5176	58.0332		
4001202+5751	400d_J1202+5751	180.5777	57.8659		
12062-0847	MACS_J1206.2-0847	181.5504	-8.8005	54.2	11.443
4104	NGC_4104_GROUP	181.6621	28.1742	0.021	0.396
12154-3900	MCXC_J1215.4-3900	183.853	-39.0355	275.446	63.7
121733+033929	NSC_J121733+033929	184.4215	3.6555		
121831+401236	NSCS_J121831+401236	184.6202	40.2075		
4001221+4918	400d_J1221+4918	185.3669	49.3067		
4325	NGC_4325_GROUP	185.7776	10.6213	3.284	0.201
122648+215157	NSCS_J122648+215157	186.7123	21.8323	57.719	16.388
12269+3332	WARP_J1226.9+3332	186.7423	33.5463		
12303+1339	XMMU_J1230.3+1339	187.5711	13.6519		
A1553	ABELL_1553	187.697	10.554	180.396	25.875
12342+0947	MCXC_J1234.2+0947	188.6008	9.7876	194.608	65.368
A1569	ABELL_1569	189.1027	16.5398	136.449	21.463
A1576	ABELL_1576	189.2436	63.1868	103.88	22.109
12525-3116	MCXC_J1252.5-3116	193.1446	-31.2666		
A1644	ABELL_1644	194.3015	-17.4092	21.222	1.461
A1650	ABELL_1650	194.6728	-1.762		
1259334+600409	WHL_J125933.4+600409	194.8877	60.0706	327.114	56.118
125947+312215	NSC_J125947+312215	194.9665	31.352		
A1664	ABELL_1664	195.9271	-24.2452	14.131	0.879
A1668	ABELL_1668	195.9442	19.2703	6.156	1.317

Table 2.4 (cont'd)

Name	Full ACCEPT2.0 Name	RA	DEC (deg)	K_0	e_K0 (keV cm ²)
1305589+263048	WHL_J130558.9+263048	196.4983	26.5157		
A1682	ABELL_1682	196.708	46.5592		
13110-0311	MACS_J1311.0-0311	197.7569	-3.1773	32.423	3.781
A1689	ABELL_1689	197.873	-1.3412	61.841	4.922
4001312+3900	400d_J1312+3900	198.083	39.0153		
1315052+514902	WHL_J131505.2+514902	198.7682	51.8201	159.895	30.277
NGC5044	NGC_5044	198.8497	-16.3854	1.305	0.143
A1722	ABELL_1722	200.0351	70.0771		
5098	NGC_5098_GROUP	200.061	33.1431	4.798	0.944
A1736	ABELL_1736	201.7204	-27.171	139.631	39.368
SSGC081	SSGC_081	202.449	-31.6069	44.512	20.29
a1750ss	a1750ss	202.5397	-2.0986	34.901	69.701
A1750C	ABELL_1750C	202.7107	-1.8618	159.868	10.761
A1750N	ABELL_1750N	202.7956	-1.7282	93.06	22.131
213312961+1107566	2MASX_J13312961+1107566	202.8734	11.1325	4.504	1.406
SC1329-313	SC_1329-313	202.8808	-31.8245	167.33	16.567
A3562	ABELL_3562	203.4055	-31.6716	70.592	12.786
A1763	ABELL_1763	203.8333	41.0005	186.619	22.108
A1767	ABELL_1767	204.0343	59.2055	136.566	62.655
4001340+4017	400d_J1340+4017	205.1365	40.2942		
A1775	ABELL_1775	205.4517	26.3709	56.894	3.877
LCDCS0829	LCDCS_0829	206.8776	-11.7524		
1348502+491801	WHL_J134850.2+491801	207.2526	49.3115		
4001354-0221	400d_J1354-0221	208.572	-2.3674		
13546+7715	MACS_J1354.6+7715	208.6858	77.2551		
1357168+623249	WHL_J135716.8+623249	209.3195	62.5472		
13592-1929	MACS_J1359.2-1929	209.7926	-19.4903	19.013	3.628
A1831	ABELL_1831	209.8156	27.9753	77.354	12.848
1359495+623047	WHL_J135949.5+623047	209.9609	62.518	21.238	6.093

Table 2.4 (cont'd)

Name	Full ACCEPT2.0 Name	RA	DEC (deg)	K_0	e_K0
				(keV	cm ²)
A1835	ABELL_1835	210.2581	2.8789	11.299	1.211
3C295	3C_295	212.835	52.2029		
11382+4435	G113.82+44.35	213.4699	71.3009		
A1882a	A1882a	213.7785	-0.492	61.304	63.352
1416238+444528	WHL_J141623.8+444528	214.1161	44.7792	18.734	17.583
LCDCS0954	LCDCS_0954	215.118	-11.5705		
21594948+2407846	GMBCG_J215.94948+24.07846	215.9495	24.0785		
A1914	ABELL_1914	216.5132	37.8238	84.494	15.9
1427161+440730	WHL_J142716.1+440730	216.8172	44.1252	12.595	3.479
14276-2521	MACS_J1427.6-2521	216.9143	-25.3508	9.474	4.811
A1930	ABELL_1930	218.1582	31.6471		
A1942	ABELL_1942_AND_CLUMP	219.5915	3.6702		
WBL518	WBL_518	220.1649	3.471		
A1991	ABELL_1991	223.6314	18.6445		
145715+222009	NSCS_J145715+222009	224.3129	22.3425	12.779	1.247
AS0780	ABELL_S0780	224.8706	-18.1793	20.933	1.311
A2009	ABELL_2009	225.0816	21.3699	18.811	2.582
150117+422152	NSCS_J150117+422152	225.3442	42.3462		
1504075-024816	WHL_J150407.5-024816	226.0311	-2.8045	9.077	0.494
A2034	ABELL_2034	227.556	33.5124		
15149-1523	MCXC_J1514.9-1523	228.7621	-15.3895	356.147	108.545
A2061	ABELL_2061	230.2929	30.6115	224.737	24.178
MKW03s	MKW_03s	230.466	7.7081	18.044	1.755
A2069	ABELL_2069	231.0356	29.8818		
15242-3154	MCXC_J1524.2-3154	231.0535	-31.9064	5.444	0.428
15246+0957	WARP_J1524.6+0957	231.1614	9.9604		
15328+3021	MACS_J1532.8+3021	233.2242	30.3497	13.365	0.901
A2107	ABELL_2107	234.9126	21.7827	10.155	3.138
A2111	ABELL_2111	234.9244	34.4162	189.915	27.115

Table 2.4 (cont'd)

Name	Full ACCEPT2.0 Name	RA	DEC (deg)	K_0	e_K0
					(keV cm ²)
A2104	ABELL_2104	235.034	-3.3038	159.142	31.845
A2125	ABELL_2125	235.3106	66.2659	171.248	17.883
A2124	ABELL_2124	236.2458	36.1091	91.073	24.555
A2142	ABELL_2142	239.5847	27.231		
15583-1410	MCXC_J1558.3-1410	239.5913	-14.1658	28.469	1.712
A2147	ABELL_2147	240.5694	15.9768	163.008	18.556
A2151	ABELL_2151	241.1494	17.7215	6.426	3.102
161314+564930	SpARCS_J161314+564930	243.3121	56.8253		
A2163	ABELL_2163	243.9412	-6.1491		
16213+3810	MACS_J1621.3+3810	245.3537	38.1689		
16235+2634	MCXC_J1623.5+2634	245.8973	26.5707		
A2187	ABELL_2187	246.0585	41.24	91.556	19.021
A2204	ABELL_2204	248.1956	5.5755	7.763	0.351
A2218	ABELL_2218	248.9614	66.2101		
A2219	ABELL_2219	250.0829	46.7119	258.49	19.763
4001641+4001	400d_J1641+4001	250.4731	40.0292		
HerculesA	Hercules_A	252.7842	4.9925		
NGC6269	NGC_6269	254.4921	27.8543	1.305	1.932
021701+6412	OC02_J1701+6412	255.3482	64.2365		
A2244	ABELL_2244	255.6778	34.0608		
A2256	ABELL_2256	255.8096	78.649	111.092	33.408
A2249	ABELL_2249	257.4381	34.4552		
A2255	ABELL_2255	258.1724	64.0728		
NGC6338	NGC_6338	258.8454	57.4112		
A2259	ABELL_2259	260.0317	27.6705		
43072	SDSS-C4_3072	260.0416	26.6251	19.703	1.477
17202+3536	MACS_J1720.2+3536	260.0701	35.6073	12.312	2.523
A2261	ABELL_2261	260.6133	32.1328	41.818	9.759
A2294	ABELL_2294	261.0495	85.8863		

Table 2.4 (cont'd)

Name	Full ACCEPT2.0 Name	RA	DEC	K_0	e_K0
			(deg)	(keV cm ²)	
17316+2251	MCXC_J1731.6+2251	262.9159	22.8606		
Abell2276	Abell_2276	263.7693	64.1017	24.173	11.035
17421+3306	ZwCl_1742.1+3306	266.0598	32.9911		
174715+451155	NSC_J174715+451155	266.8113	45.1968	290.692	35.204
17502+3504	MCXC_J1750.2+3504	267.5704	35.0828		
18044+1002	CIZA_J1804.4+1002	271.131	10.0571	26.268	48.513
A2302	ABELL_2302	274.9917	57.1561	190.544	77.382
18243+4309	MACS_J1824.3+4309	276.0792	43.1635		
18290+6913	MACS_J1829.0+6913	277.2735	69.2353	36.357	4.091
18521+5711	MCXC_J1852.1+5711	283.0358	57.1949		
18539+6822	MCXC_J1853.9+6822	283.5094	68.3827	76.431	14.615
33709-2597	PLCKESZ_G337.09-25.97	288.6564	-59.4722	78.316	8.85
A2319	ABELL_2319	290.2945	43.9516		
19318-2635	MACS_J1931.8-2635	292.9569	-26.5759	20.746	1.385
AS0821	ABELL_S0821	293.7197	-50.8761		
19383+5409	CIZA_J1938.3+5409	294.5768	54.1597	82.492	12.545
19473-7623	MCXC_J1947.3-7623	296.8121	-76.3958	17.503	8.752
A3653	ABELL_3653	298.2641	-52.0369	174.821	44.382
19582-3011	MCXC_J1958.2-3011	299.5623	-30.1866		
20035-2323	MCXC_J2003.5-2323	300.8713	-23.3734	217.888	91.725
20113-5725	MCXC_J2011.3-5725	302.8622	-57.4199	39.441	8.622
20148-2430	MCXC_J2014.8-2430	303.7153	-24.5062	5.104	0.8
2023-5535	SPT-CL_J2023-5535	305.8388	-55.5967	186.127	83.939
20318-4037	MCXC_J2031.8-4037	307.9602	-40.6252		
2034-5936	SPT-CLJ2034-5936	308.5382	-59.6052		
A3695	ABELL_3695	308.6888	-35.812	307.183	36.618
2043-5035	SPT-CLJ2043-5035	310.8231	-50.5923	15.848	3.138
20460-3430	MACS_J2046.0-3430	311.5021	-34.5048	6.476	2.108
20499-3216	MCXC_J2049.9-3216	312.484	-32.2803		

Table 2.4 (cont'd)

Name	Full ACCEPT2.0 Name	RA	DEC (deg)	K_0	e_K0
					(keV cm ²)
A3739	ABELL_3739	316.0787	-41.3446	81.936	38.149
2106-5844	SPT-CLJ2106-5844	316.5214	-58.7419		
IC1365	IC_1365	318.4822	2.5652	160.833	19.732
2129-0741	MACS_J2129-0741	322.3606	-7.6908		
2135-0102	MACS_J2135-0102	323.7959	-1.0484		
A2355	ABELL_2355	323.8204	1.4185	393.293	86.869
2135-5726	SPT-CLJ2135-5726	323.9094	-57.441		
WBL671	WBL_671	324.2849	0.4464		
21402-2339	MACS_J2140.2-2339	325.0633	-23.6611	12.928	1.101
2145-5644	SPT-CLJ2145-5644	326.4669	-56.7477		
2146-4633	SPT-CLJ2146-4633	326.6447	-46.5492		
A3809	ABELL_3809	326.7462	-43.8987	10.277	3.844
2148-6116	SPT-CLJ2148-6116	327.1843	-61.2784		
A2384	ABELL_2384	328.0888	-19.5474	25.359	2.675
A2390	ABELL_2390	328.4032	17.6954	14.26	1.929
21538+3746	CIG_2153.8+3746	328.9675	38.0068	55.189	6.284
A2409	ABELL_2409	330.2184	20.9687		
A3827	ABELL_3827	330.4713	-59.9456	133.726	15.264
A2415	ABELL_2415	331.4105	-5.5925	2.83	0.781
22117-0349	MCXC_J2211.7-0349	332.9415	-3.83	96.79	15.187
3C444	3C_444	333.6066	-17.0267	0.958	1.15
A2426	ABELL_2426	333.6347	-10.3705	54.818	12.515
2214-1359	MACS_J2214-1359	333.739	-14.0038	150.198	23.601
A3854	ABELL_3854	334.441	-35.7244	103.513	18.154
22186-3853	MCXC_J2218.6-3853	334.6644	-38.9009	132.838	15.498
2218-4519	SPT-CLJ2218-4519	334.7479	-45.3158		
A2445	ABELL_2445	336.7336	25.8351	69.915	11.294
A3880	ABELL_3880	336.9766	-30.577		
22286+2036	MCXC_J2228.6+2036	337.1424	20.6206		

Table 2.4 (cont'd)

Name	Full ACCEPT2.0 Name	RA	DEC (deg)	K_0	e_K0
					(keV cm ²)
22298-2756	MACS_J2229.8-2756	337.4384	-27.9267	7.679	1.376
514-050	CGCG_514-050	337.8359	39.3581	0.932	2.217
2232-5959	SPT-CLJ2232-5959	338.1405	-59.998		
2233-5339	SPT-CLJ2233-5339	338.3131	-53.6552		
A2457	ABELL_2457	338.9221	1.4867	24.049	17.816
A2465	ABELL_2465	339.9125	-5.7242		
22428+5301	CIZA_J2242.8+5301	340.6647	52.9958		
2243198-093530	WHL_J224319.8-093530	340.8379	-9.5935		
2245-6206	SPT-CLJ2245-6206	341.2621	-62.1167		
22450+2637	MACS_J2245.0+2637	341.2692	26.6348	38.968	6.768
A3911	ABELL_3911	341.6117	-52.7398	338.381	36.851
A2485	ABELL_2485	342.1291	-16.1079	74.814	26.486
AS1063	ABELL_S1063	342.1835	-44.5304	78.785	19.913
A3921	ABELL_3921	342.4861	-64.4302	75.119	14.847
A2507	ABELL_2507	344.2194	5.5046	198.227	27.121
2259-6057	SPT-CLJ2259-6057	344.7541	-60.9603		
23028+0843	WARP_J2302.8+0843	345.7006	8.7307		
A2537	ABELL_2537	347.0929	-2.1916	78.806	12.795
23115+0338	MCXC_J2311.5+0338	347.8885	3.6353	85.303	14.556
A2550	ABELL_2550	347.8993	-21.7462		
A2556	ABELL_2556	348.2556	-21.6344	12.041	1.363
AS1101	ABELL_S1101	348.4946	-42.7253	11.526	0.499
23185+0034	RCS_J2318.5+0034	349.6296	0.5674		
A2597	ABELL_2597	351.3326	-12.1242	9.501	0.288
2331-5051	SPT-CL_J2331-5051	352.9632	-50.8649		
A2626	ABELL_2626	354.1267	21.1468	13.528	2.257
A2627	ABELL_2627	354.1754	23.9248		
2337-5942	SPT-CL_J2337-5942	354.3532	-59.7064		
A2631	ABELL_2631	354.4082	0.2672		

Table 2.4 (cont'd)

Name	Full ACCEPT2.0 Name	RA	DEC	K_0	e_K0
		(deg)		(keV cm ²)	
A4023	ABELL_4023	355.0288	-85.1974		
2341-5119	SPT-CL_J2341-5119	355.302	-51.3287		
A2645	ABELL_2645	355.3232	-9.0165		
23442-0422	MCXC_J2344.2-0422	356.0769	-4.3816	108.571	13.251
2344-4243	SPT-CL_J2344-4243	356.1833	-42.7201		
A2657	ABELL_2657	356.2389	9.1921		
2345-6405	SPT-CLJ2345-6405	356.2485	-64.0963		
HCG097	HCG_097	356.8459	-2.3005		
A4038	ABELL_4038	356.9374	-28.1406		
AS1150	ABELL_S1150	356.9555	-35.5867		
A2665	ABELL_2665	357.7108	6.1503		
A2667	ABELL_2667	357.9141	-26.0837	19.098	2.169
A2670	ABELL_2670	358.5571	-10.4192	30.012	4.629
2355-5056	SPT-CL_J2355-5056	358.9477	-50.9281		
2359-5009	SPT-CL_J2359-5009	359.9283	-50.1688		

CHAPTER 3

LUMINOSITY-TEMPERATURE RELATION OF ACCEPT2.0 CLUSTERS

We characterize galaxy clusters through observations of the X-ray spectra of the intracluster medium (ICM). Observed correlations between X-ray observables like temperature T and luminosity L_X (Mitchell et al., 1976; Cavaliere et al., 1997; Pratt et al., 2009; Maughan et al., 2012; Migkas et al., 2020) are known as scaling relations for clusters of galaxies. Such relations are effective tools for understanding large scale structure and its evolution. Simple models of the ICM lead to predictions for how cluster mass M relates to T and L_X and therefore, how T and L_X should relate to each other. Observations connecting the cluster observable properties (such as L_X and T) to properties of clusters well-constrained by theory (such as cluster mass M) allow us to constrain our cosmological models and improve our understanding of how overdensities in the early Universe have grown and evolved over time (full review by Voit, 2005).

We make predictions for cluster temperatures and luminosities by assuming the ICM is a self-gravitating sphere. The virial theorem states that the kinetic energy (E_K) is related to gravitational potential energy (E_G) by $E_K = |E_G/2|$. The virial radius, R_v , for a cluster at some redshift z is the radius inside which the virial theorem for bound galaxies or particles is satisfied. In a simulation, R_v can be estimated based on this condition because the simulator can know the exact positions and velocities of all the galaxies in their simulation. In the real Universe, R_v is based on calibration by simulations. These simulations indicate that R_v is the radius at which the average interior density is ~ 200 times the critical density ($\rho_c(z)$) at the redshift in question. Recall from Section 1.2.1 that $\rho_c(z)$ is the maximum average density and is defined as,

$$\rho_c(z) = E(z)^2 \rho_{c,0}, \quad (3.1)$$

where $\rho_{c,0} = \rho_c(z=0) = 3H_0^2/8\pi G$ is the present day critical density, $H(z) = H_0 E(z)$, with $H_0 = 70 \text{ km s}^{-1} \text{ Mpc}^{-1}$ and $E(z) = \sqrt{\Omega_M(1+z)^3 + \Omega_\Lambda}$ where $\Omega_M = 0.3$ and $\Omega_\Lambda = 0.7$ account for the matter and dark energy content of the Universe.

The virial radius is large and outside of the typical X-ray telescope’s instrumental field of view for most nearby systems, so we often characterize cluster properties for some radius R_Δ within which the density is Δ times the critical density $\rho_c(z)$. For a cluster with mass M_Δ at scaled radius R_Δ ,

$$M_\Delta \propto E(z)^2 R_\Delta^3. \quad (3.2)$$

The virial theorem assumes that the ICM temperature is due to heating from the gas as it falls into the gravitational potential, leading to the expected relation,

$$T \propto [E(z) M_\Delta^{2/3}], \quad (3.3)$$

where T is isothermal throughout the cluster.

The scaling of temperature and mass of a cluster through its luminosity is less straightforward, as it requires an assumption of the density structure and knowledge of radiative processes of the gas including bremsstrahlung (or free-free) emission, and collisionally-excited emission lines from iron K- and L- shell transitions, and transitions from other elements. At typical cluster temperatures, radiation emitted by the gas is dominated by bremsstrahlung emission wherein electrons are deflected by the Coulomb field of an ion. We are able to express the radiation from all processes in terms of a cooling function $\Lambda(T, Z)$. The cooling function is integrated over all emission processes and then weighted by the energy of emitted photons (Peterson & Fabian, 2006). Recalling from section 1.3 that $L_X \propto n_e^2 r^3 \Lambda(T)$ for an isothermal gas, and for thermal bremsstrahlung emission, $\Lambda(T) \propto T^{1/2}$. When these relations are combined with Equations 3.2 and 3.3, it leads to the expectation that $L_X \propto T^2$. However, observations have shown steeper slopes and increased scatter among the lower temperature clusters and groups (Cavaliere et al., 1997; Arnaud & Evrard, 1999; Pratt et al., 2009; Maughan et al., 2012).

The existence of a reliable $L_X - T$ relation for clusters of galaxies could, in principle, allow for their use as standard candles. However, they are not generally considered as “good” standard candles because the extended emission is by nature difficult to measure in an exact manner. Additionally,

their luminosities—particularly in the core—are affected by local astrophysics, adding scatter to the $L_X - T$ relation. Although clusters are not great standard candles in practice, large sample sizes might lead to interesting tests of cosmology. For example, cosmology generally assumes homogeneous isotropic expansion. A test of this assumption was conducted recently by Migkas et al. (2020) (hereafter, M20), who used a sample of 313 clusters to investigate the $L_X - T$ relation towards different directions on the sky. Intriguingly, they found a significant difference in normalization factor when observing the $L_X - T$ relation from different regions of the sky. They found that clusters within a 60° radius of galactic coordinates $(l, b) \sim (281^\circ, -16^\circ)$ are systematically fainter than those towards $(l, b) \sim (34^\circ, +4^\circ)$ by up to a factor of 36%. They suggest that their results may be due to inconsistencies in the Hubble constant H_0 , and thus caused by anisotropic expansion.

We performed a followup analysis for 302 clusters from the second catalog of the Archive of Chandra Cluster Entropy Profile Tables (Donahue, Baldi, et al, in prep, hereafter, ACCEPT2.0) and do not find the same difference in normalizations. We surmise that the discrepancies between ours and the results of M20 can be attributed to differences in the X-ray cluster luminosity measurements (ACCEPT2.0 luminosities are based on a broader X-ray energy bandpass and exclude the cluster cores) and possibly underestimates of the systematics related to Galactic absorption, since the direction of the discrepancies are relatively close to the Galactic plane.

The outline of this chapter is as follows: Section 3.1 describes the cluster sample from ACCEPT2.0. Section 3.2 gives the $L_X - T$ model and fitting procedure, followed by the results in Section 3.3. We compare our results to M20 in Section 3.4 and discuss reasons for the discrepancy between results, and summarize our analysis in Section 3.5. We assume a Λ CDM cosmology throughout the paper with $H_0=70 \text{ km s}^{-1}\text{Mpc}^{-1}$, $\Omega_m=0.3$, and $\Omega_\Lambda=0.7$.

3.1 The Sample

The $L_X - T$ relation becomes more scattered with decreasing temperature (or equivalently, mass) (Maughan et al., 2012). For a sample with selection based on luminosity, an $L_X - T$ relation with higher scatter will be more affected by luminosity selection bias than a sample with low scatter in $L_X - T$. We aim to limit the effects of this selection bias by restricting the luminosities to a

range similar to M20. We selected a subsample of 302 clusters with global bolometric luminosity $L_X > 4 \times 10^{43}$ erg s $^{-1}$ (although for analysis, we used luminosities measured in the bandpass [0.5-8] keV. M20 used *ROSAT* luminosities in the energy range [0.1-2.5] keV).

Scatter in the relation also arises from the differences between cool core (CC) and non-cool core (NCC) clusters. CCs have profiles with steep drops in temperature towards the center, whereas NCCs have comparatively flat temperature profiles and a less centrally concentrated density structure. The CC clusters can be classified most straight forwardly by using the central entropy $K_0 = kTn^{-2/3}$ keV cm 2 . Here, we follow the classification of Cavagnolo et al. (2009) and ACCEPT2.0¹, which defines $K_0 \simeq 30$ keV cm 2 as the threshold below which a cluster is considered a CC. There are 67 CCs (~22%) and 135 (~44%) NCCs in our sample, where the remaining 106 (~34%) clusters are undetermined.

The difference in temperature and density profiles for CC and NCC clusters can increase the scatter in the $L_X - T$ relation, the angular resolution of *Chandra* allows us to obtain global temperature and luminosity estimates for a core-excised aperture of [0.3-1] R_{2500} . M20 however, used luminosities for the full aperture inside of R_{500} , because the angular resolution of *ROSAT* does not allow core-excised measurements.

There are 46 and 41 ACCEPT2.0 clusters in the 60° radius surrounding the regions $(l, b) \sim (281^\circ, -16^\circ)$ and $(l, b) \sim (34^\circ, +4^\circ)$, respectively. Migkas et al. (2020) found that clusters towards $(281^\circ, -16^\circ)$ were fainter, while those of the comparison region tended to be brighter. Therefore, the samples in these two regions will be designated as RF and RB, and the sample of clusters lying outside either sky region will be called NR. The full sample covers a redshift range of $z \sim [0.02 - 0.9]$. The RF clusters cover a redshift range of $z \sim [0.05 - 0.75]$, and RB clusters cover the range $z \sim [0.04 - 0.47]$. M20 uses a sample of local clusters with redshifts $z \lesssim 0.4$ ².

¹ K_0 estimates are from ACCEPT2.0 (Frisbie, MSU dissertation, October 2020)

²We find no difference in our results when restricting our redshift range to be $z \lesssim 0.4$, so for this work, we report the results of an analysis for the largest, unrestricted redshift sample.

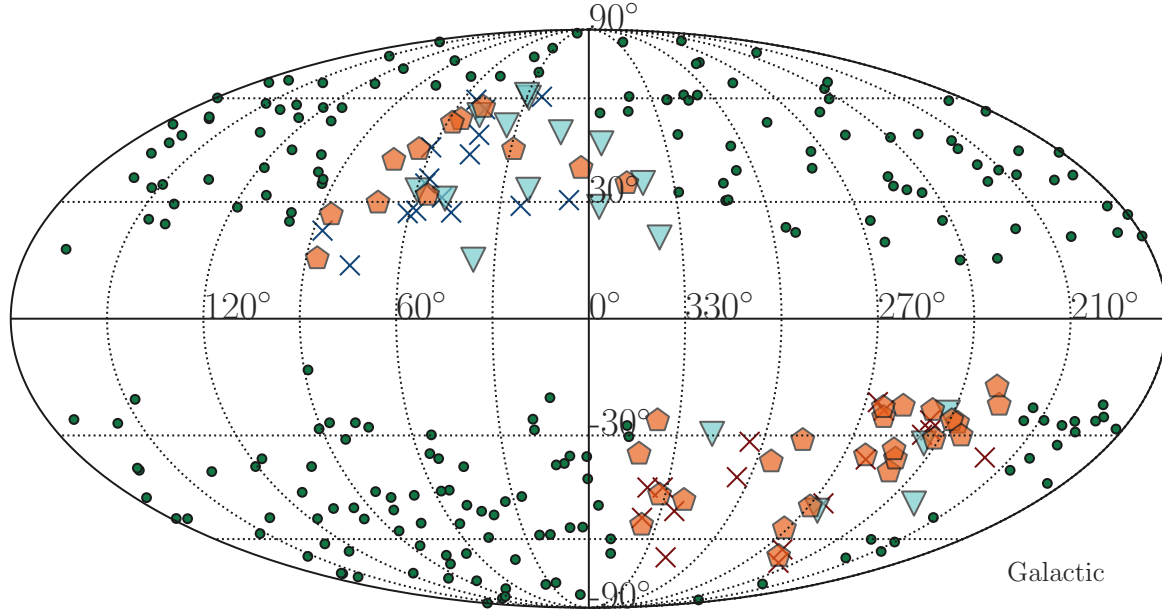


Figure 3.1: ACCEPT2.0 all-sky map. Distribution of ACCEPT2.0 clusters colored according to region or core status. Red pentagons are NCC clusters and blue triangles are CC clusters, while clusters with no core status are red or blue crosses. Clusters that do not belong to a region subset are plotted in green. Red crosses are part of the region centered on galactic coordinates $(l, b) \sim (281^\circ, -16^\circ)$ (RF), blue crosses are inside the region centered on $(l, b) \sim (34^\circ, +4^\circ)$ (RB). Clusters within 10° of the galactic latitude $b = 0^\circ$ were excluded from all subsamples.

3.2 Methods

Starting with a standard power-law,

$$\frac{L_X E(z)^{-1}}{10^{44} \text{ erg s}^{-1}} = L_{X,0} \left(\frac{kT}{6 \text{ keV}} \right)^\beta, \quad (3.4)$$

we scale the power-law relation to the following linear model—including intrinsic scatter σ_{int} —to be used an estimate for the underlying $L_X - T$ relation,

$$l = l_0 + \beta t, \quad (3.5)$$

where $l \equiv \ln \frac{L_X E(z)^{-1}}{10^{44} \text{ erg s}^{-1}}$, $E(z) = \sqrt{\Omega_m(1+z)^3 + \Omega_\Lambda}$ accounts for the redshift evolution of the relation, $l_0 \equiv \ln L_{X,0}$ is the normalization constant, and $t \equiv \ln \frac{kT}{6 \text{ keV}}$. We implemented an MCMC

algorithm to obtain independent normalization, slope, and intrinsic scatter estimates for each sample using a likelihood function that assumes the data and errors are Gaussian.

$$\ln \mathcal{L} = -\frac{1}{2} \sum_i \left[\frac{(l_i - \bar{l})^2}{\sigma_{\text{int}}^2 + \sigma_{l,i}^2} + \ln(2\pi(\sigma_{\text{int}}^2 + \sigma_{l,i}^2)) \right] \quad (3.6)$$

We use flat priors, where each parameter was allowed to vary over a generous range of values. M20 found that the normalization is the biggest contributor to the difference of the $L_X - T$ relation towards different regions of the sky. They used a model similar to Equation 3.2 and fixed the slope to the value obtained from the full sample. We therefore performed a second fit of our data assuming that the slope (β) and intrinsic scatter (σ_{int}) for all three samples are the same. However, instead of fixing these parameters in the analyses, we performed the regression over the three subsamples simultaneously and allowed only the normalization to vary between them. We chose a log-likelihood (Equation 3.6) which tied the three subsamples because, while M20 was able to show that fixing the slope did not significantly affect their results, that method does not take into account the uncertainty of the slope for the full sample.

We fit the five parameters, ${}^{\text{NR}}l_0$, ${}^{\text{RB}}l_0$, ${}^{\text{RF}}l_0$, β , and σ_{int} using the following log-likelihood:

$$\begin{aligned} \ln \mathcal{L} = & -\frac{1}{2} \left[\sum_i \left(\ln({}^{\text{NR}}\sigma_i^2 + \sigma_{\text{int}}^2) + \frac{({}^{\text{NR}}l_i - ({}^{\text{NR}}l_0 + {}^{\text{NR}}t_i\beta))^2}{{}^{\text{NR}}\sigma_i^2 + \sigma_{\text{int}}^2} \right) \right. \\ & + \sum_j \left(\ln({}^{\text{RF}}\sigma_j^2 + \sigma_{\text{int}}^2) + \frac{({}^{\text{RF}}l_j - ({}^{\text{RF}}l_0 + {}^{\text{RB}}t_j\beta))^2}{{}^{\text{RF}}\sigma_j^2 + \sigma_{\text{int}}^2} \right) \\ & \left. + \sum_k \left(\ln({}^{\text{RB}}\sigma_k^2 + \sigma_{\text{int}}^2) + \frac{({}^{\text{RB}}l_k - ({}^{\text{RB}}l_0 + {}^{\text{RB}}t_k\beta))^2}{{}^{\text{RB}}\sigma_k^2 + \sigma_{\text{int}}^2} \right) \right] \quad (3.7) \end{aligned}$$

3.3 Results

The posterior distributions for the parameters are shown in Figure 3.2 for individually fit regions, and Figure 3.3 for the tied model.

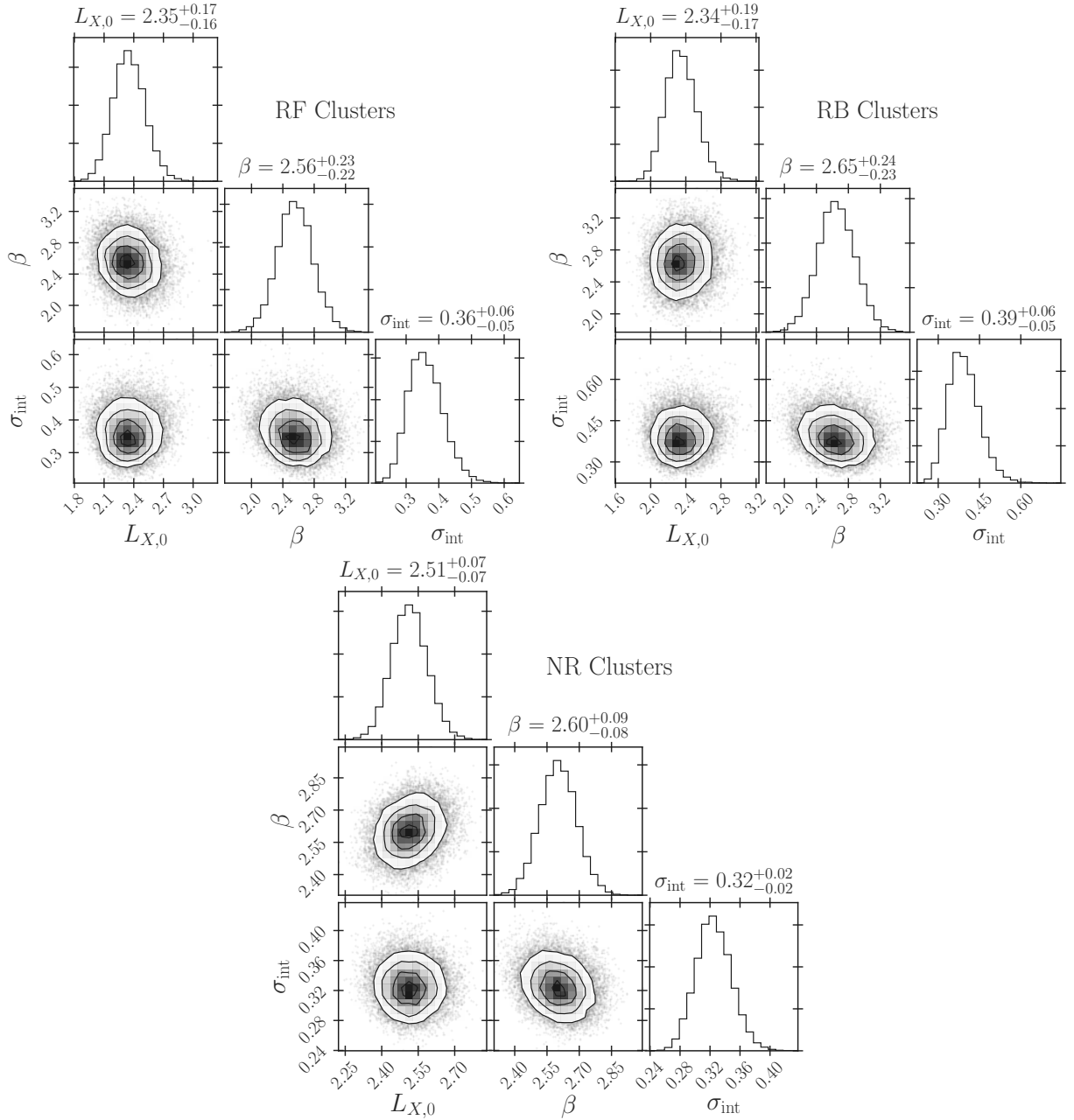


Figure 3.2: Posterior $L_X - T$ distributions for RF, RB, and NR clusters. The posterior probability distributions for the variables of the $L_X - T$ relation for RF (top left), RB (top right), and NR (bottom) clusters. The 1-, 2-, and 3 σ contour levels correspond to 39th, 86th, and 99th percentiles.

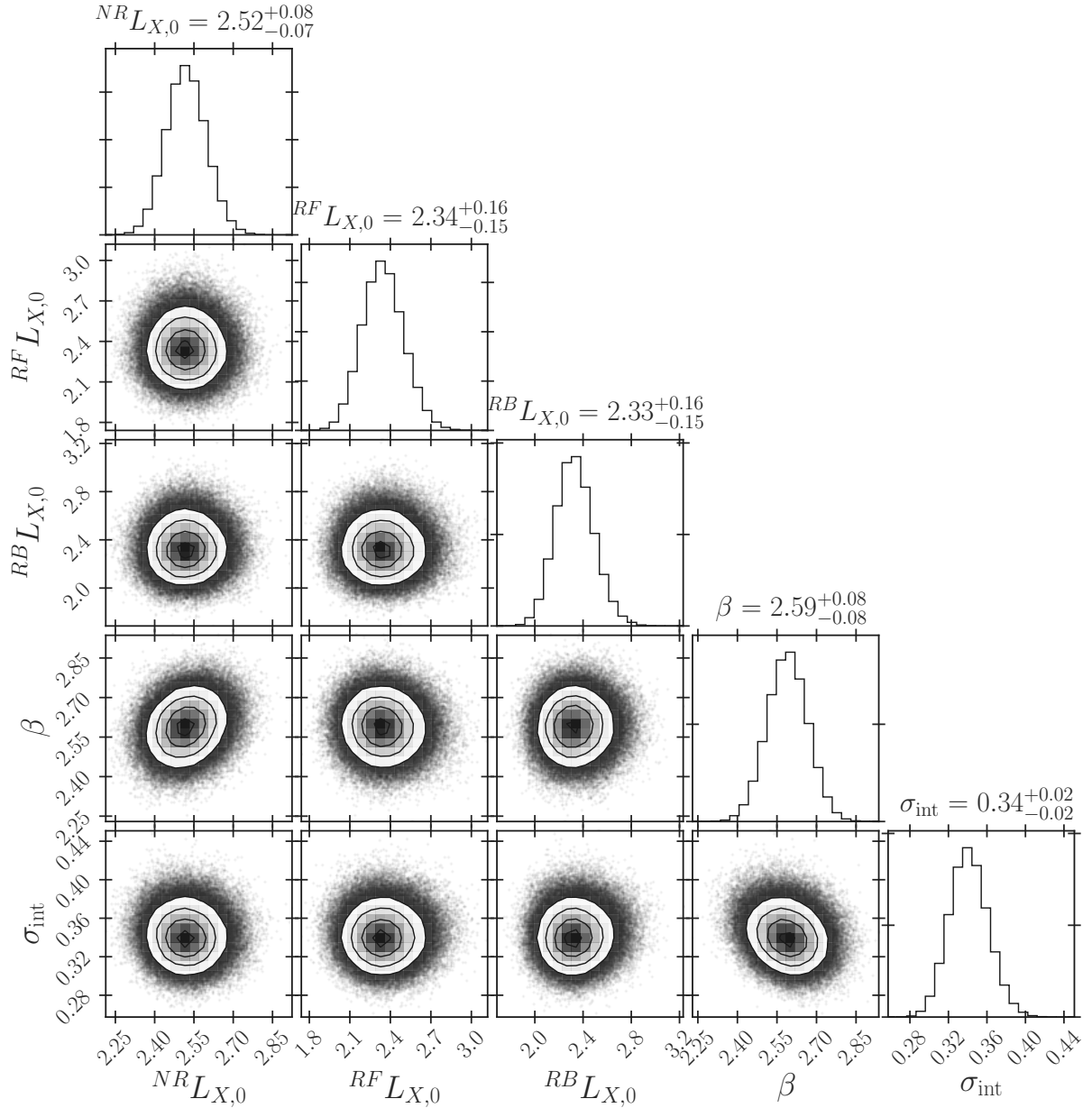


Figure 3.3: Posterior distributions for the tied $L_X - T$ model. The posterior probability distributions for the variables of the multi-parameter $L_X - T$ fit. The contour levels are the same as in 3.2.

Results for the model parameters according to region are shown in table 3.1, with the errors reported as the 16th and 84th percentiles (i.e., 68% confidence intervals) of the output parameter chains. The upper panel shows parameter output using tied log-likelihood (Equation 3.7) for simultaneous fitting and the lower panel shows the results for the separate fits (Equation 3.6. The left panel of Figure 3.7 contains the over-plotted simultaneous fits, and the right panel shows the individual model fits, with the shaded regions representing the 1σ uncertainty for the model. The differences between normalizations $L_{X,0}$ are $\frac{R^1}{R^2} \Delta L_{X,0} \equiv^{R^1} L_{X,0} -^{R^2} L_{X,0}$, where the error on this value comes from adding in quadrature the uncertainties on $L_{X,0}$.

Our best fit parameters show no significant difference between using the tied or separate fitting models for any one subsample. Tied model values for slope ($\beta = 2.514 \pm 0.076$) and intrinsic scatter ($\sigma_{\text{int}} = 0.322^{+0.020}_{-0.019}$) were consistent with those of the individual fits, with the faint region RF having the smallest individually fit slope of ${}^{RF} \beta = 2.332^{+0.226}_{-0.223}$. Upon comparison of results from the tied and untied models, we find no statistical difference in β or σ_{int} between subsamples, which is consistent with Migkas et al. (2020).

There was no statistical difference in $L_{X,0}$ between RB and RF, with $\frac{RB}{RF} \Delta L_{X,0} = -0.018 \pm 0.218$ for the tied model, and $\frac{RB}{RF} \Delta L_{X,0} = -0.019 \pm 0.238$ for the separate model. For both the tied and separate fitting mechanisms, $\Delta L_{X,0}$ was smaller between RB and RF than between NR and either RB or RF. For the simultaneous fits, $\frac{NR}{RB} \Delta L_{X,0} = 0.269 \pm 0.173$ and $\frac{NR}{RF} \Delta L_{X,0} = 0.251 \pm 0.170$. For the individual fits, $\frac{NR}{RB} \Delta L_{X,0} = 0.267 \pm 0.190$, and $\frac{NR}{RF} \Delta L_{X,0} = 0.248 \pm 0.176$.

3.4 Discussion

None of the differences in $L_{X,0}$ between the regions are statistically significant, which is contrary to the result of M20. In fact, ACCEPT2.0 clusters towards the extreme bright region RB described by M20 appear marginally *fainter* ($\frac{RB}{RF} \Delta L_{X,0} = -0.017 \pm 0.220$ for the tied model and $\frac{RB}{RF} \Delta L_{X,0} = -0.009 \pm 0.238$ for the separate model) than those towards the extreme faint region RF. The low significance in $\Delta L_{X,0}$ across all three samples can be attributed to systematic differences in the data between *ROSAT* and *Chandra*. Possible reasons for the discrepancy between ours and M20's results are described below.

Table 3.1: **Best fit $L_X - T$ using tied and separate models.** Output parameters for the fit to Equation 3.2. The upper half refers to parameters fit using the tied log-likelihood model (Equation 3.7). Parameters in the bottom half were computed for each subsample using separate log-likelihoods (3.6).

Model	Subsample	$L_{X,0}$	β	σ_{int}
Tied model	NR	$2.446^{+0.077}_{-0.074}$		
	RB	$2.177^{+0.162}_{-0.150}$	$2.514^{+0.076}_{-0.076}$	$0.322^{+0.020}_{-0.019}$
	RF	$2.195^{+0.157}_{-0.148}$		
Separate models	NR	$2.446^{+0.077}_{-0.074}$	$2.517^{+0.085}_{-0.084}$	$0.302^{+0.024}_{-0.023}$
	RB	$2.174^{+0.185}_{-0.166}$	$2.421^{+0.239}_{-0.227}$	$0.338^{+0.061}_{-0.052}$
	RF	$2.194^{+0.165}_{-0.156}$	$2.332^{+0.226}_{-0.223}$	$0.309^{+0.056}_{-0.048}$

3.4.1 Core-excised vs. core included L_X

Both samples for this analysis use core-excised (CE) measurements within the region [0.3-1] R_{2500} . However, M20 uses luminosities from *ROSAT* because its large field of view allows for global parameters for apertures within R_{500} . Unfortunately, *ROSAT*'s low spatial resolution means their luminosity measurements are not (and cannot be) core-excised. Core excision is important because cores of “cool-core” (CC) clusters have higher gas densities than the cores of non-cool core clusters (NCC), and therefore radiate more efficiently which results in higher SNR data. Unfortunately, measurements including core emission are subject to a bias in the luminosity because of the brighter central regions of CCs compared to those of NCCs. Core contribution to $L_X - T$, regardless of core status, is illustrated in section 2.4.3, where we fit the model using luminosity measurements from both the CE aperture and the CI (core-included) aperture. Similarly, we demonstrate how cores of

Table 3.2: **Difference in normalization of $L_X - T$.** Differences in normalization $L_{X,0}$ between clusters towards different parts of the sky. Top half shows differences between normalization subsamples evaluated independently and the lower half shows the differences from the tied model with an extra column containing the results reported by Migkas et al. (2020) (M20) for comparison. M20 fit for each sample separately using the same fixed slope ($\beta = 2.102 \pm 0.064$) obtained from the full sample and allowing only the normalization to vary.

Model	Subsample	$\Delta L_{X,0}$	Migkas et al. (2020) $\Delta L_{X,0}$
		[$10^{44} \text{ ergs}^{-1}$]	[$10^{44} \text{ ergs}^{-1}$]
Tied	(RB-RF)	-0.018 ± 0.218	
	(NR-RB)	0.269 ± 0.173	
	(NR-RF)	0.251 ± 0.170	
Separate	(RB-RF)	-0.019 ± 0.238	0.406 ± 0.086
	(NR-RB)	0.267 ± 0.190	0.198 ± 0.070
	(NR-RF)	0.248 ± 0.176	0.208 ± 0.084

CCs affect the $L_X - T$ relation by fitting the model as described in Section 3.2 to 135 NCC and 67 CC clusters using both CE and CI luminosities. We found that with CE luminosities, there is a slight difference in the relation between CC and NCC clusters, with normalizations of $L_{X,0}^{CC} = 2.777^{+0.154}_{-0.145}$ for the CC sample and $L_{X,0}^{NCC} = 2.251^{+0.093}_{-0.089}$ for the NCC sample. These parameters correspond to a difference of $\frac{CC}{NCC} \Delta L_{X,0} = 0.526 \pm 0.175$. When using the CI luminosities, the normalization parameters are $L_{X,0}^{CC} = 7.587^{+0.592}_{-0.541}$ for the CC sample and $L_{X,0}^{NCC} = 3.642^{+0.159}_{-0.151}$ for the NCC sample, with a nearly 7σ difference of $\frac{CC}{NCC} \Delta L_{X,0} = 3.945 \pm 0.587$.

Presumably, excess luminosity in CCs would not affect the results as much if both regions had equal distributions of CC and NCC clusters. This perfect mixing of CCs and NCCs is not the case for our samples, which can be seen in Figure 3.1. Out of 46 RF clusters, 29 have K_0 estimates—5 CCs and 24 NCCs. For the 41 clusters in RB, 25 have K_0 measurements and are more evenly split

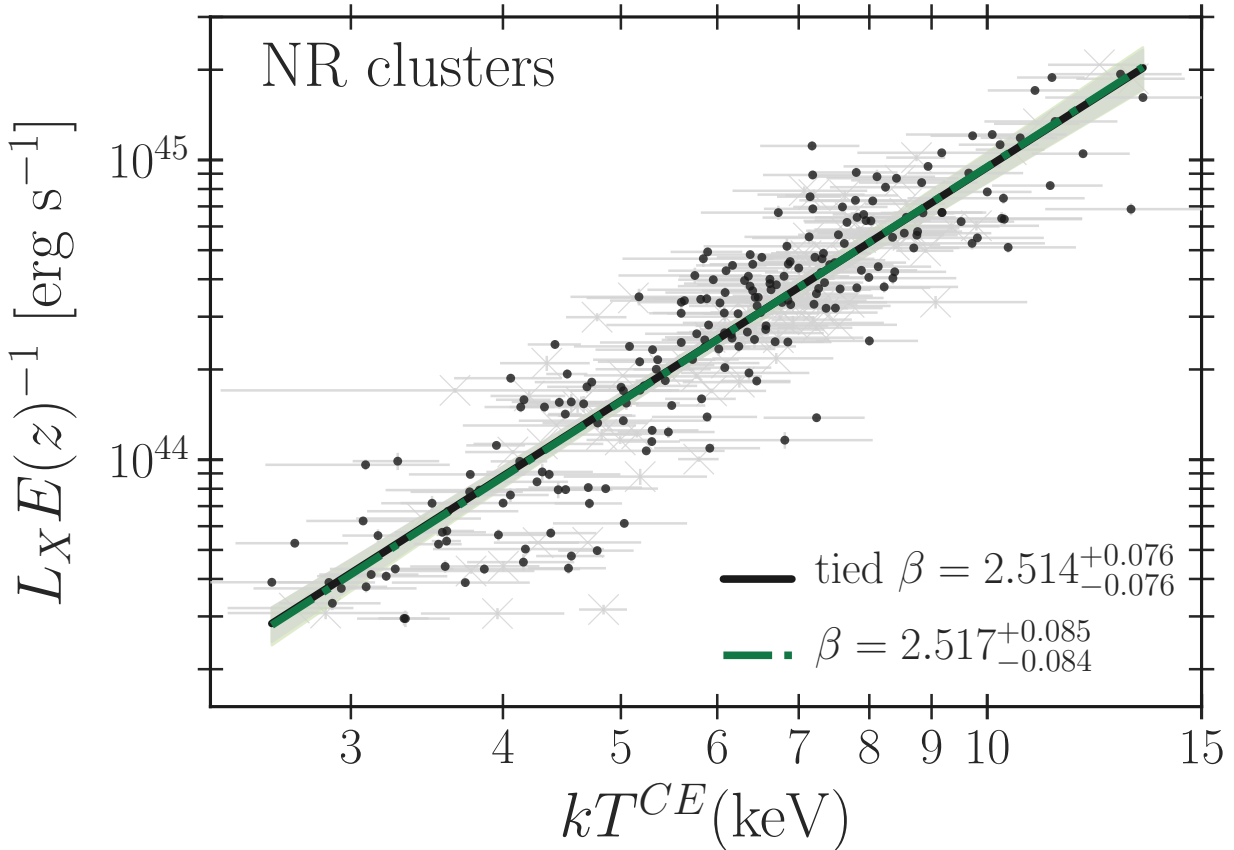


Figure 3.4: **Best fit $L_X - T$ for NR clusters.** Best fit models for the luminosity-temperature for 215 NR clusters. The best fit parameters of normalization and intrinsic scatter are $L_{X,0} = 2.446^{+0.077}_{-0.074}$ and $\sigma_{\text{int}} = 0.322^{+0.020}_{-0.019}$ for the tied model, and $L_{X,0} = 2.442^{+0.074}_{-0.072}$ and $\sigma_{\text{int}} = 0.302^{+0.024}_{-0.023}$ for the separate model. Filled circles represent clusters used for the fit. Gray crosses are the clusters which were left out of the fit to NR because they belong to either RB or RF.

with 13 CCs and 12 NCCs. RF has a lower fraction of clusters with bright cores, which could bias the normalization parameter of the $L_X - T$ relation low for that region. Because the luminosities used in M20 are for the full $r \lesssim R_{500}$ aperture, a random excess or paucity of CCs in one region of the sky could affect $L_{X,0}$, particularly for core included luminosity estimates.

3.4.2 Different spectral energy bandpasses

Contributions from different radiation processes affect X-ray emissivity over different bandpasses. Therefore, the spectral energy range over which luminosity is measured can affect the observed $L_X - T$ relation. For instance, *ROSAT* is sensitive to soft X-rays in the bandpass [0.1-2.5] keV. Within

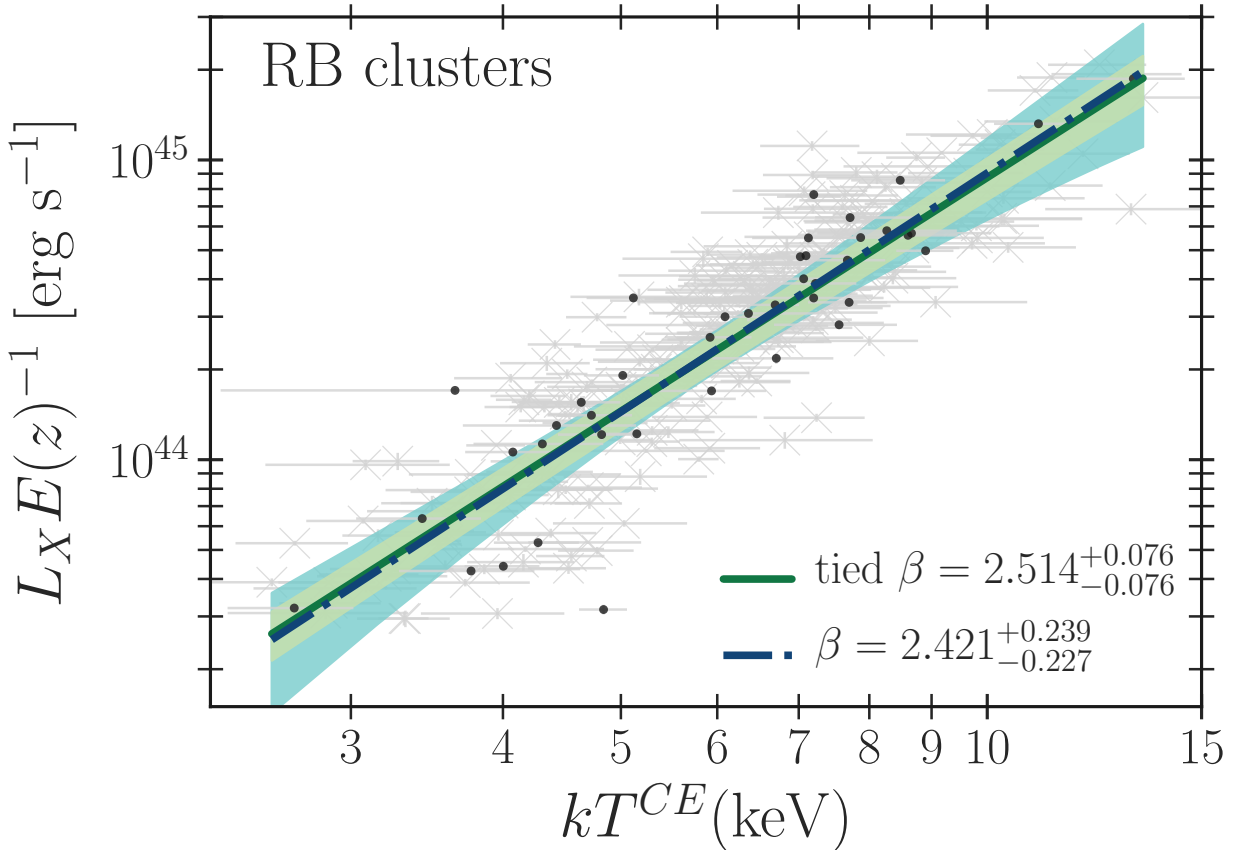


Figure 3.5: **Best fit $L_X - T$ for RB clusters.** Same plot as Figure 3.4 but for 41 RB clusters in the region surrounding $RB = (l, b) \sim (34^\circ, +4^\circ)$. The best fit parameters of normalization and intrinsic scatter are $L_{X,0} = 2.177^{+0.162}_{-0.150}$ and $\sigma_{\text{int}} = 0.322^{+0.020}_{-0.019}$ for the tied model, and $L_{X,0} = 2.174^{+0.185}_{-0.166}$ and $\sigma_{\text{int}} = 0.338^{+0.061}_{-0.052}$ for the separate model.

this bandpass, the spectrum is less sensitive to the exponential cutoff at $E \sim kT$, characteristic of radiation from thermal bremsstrahlung, and the soft X-ray luminosity is less dependent on temperature. The $L_X - T$ relation will therefore be shallower for a bandpass-limited L_X , particularly when confined to the lower energy range [0.1-2] keV. This effect can be seen in Figure 3.8 which shows the best fit tied model for ACCEPT2.0 NR clusters using bolometric luminosities versus their values measured in the energy range [0.5-8] keV. The slope of the $L_X - T$ relation using bandpass luminosities is $\beta = 2.514^{+0.076}_{-0.076}$ and $\beta = 2.740^{+0.076}_{-0.077}$ for bolometric luminosities. For comparison, the slope of the relation for the full sample in M20 is $\beta = 2.102 \pm 0.064$ using bandpass luminosities in the energy range [0.1-2.5] keV.

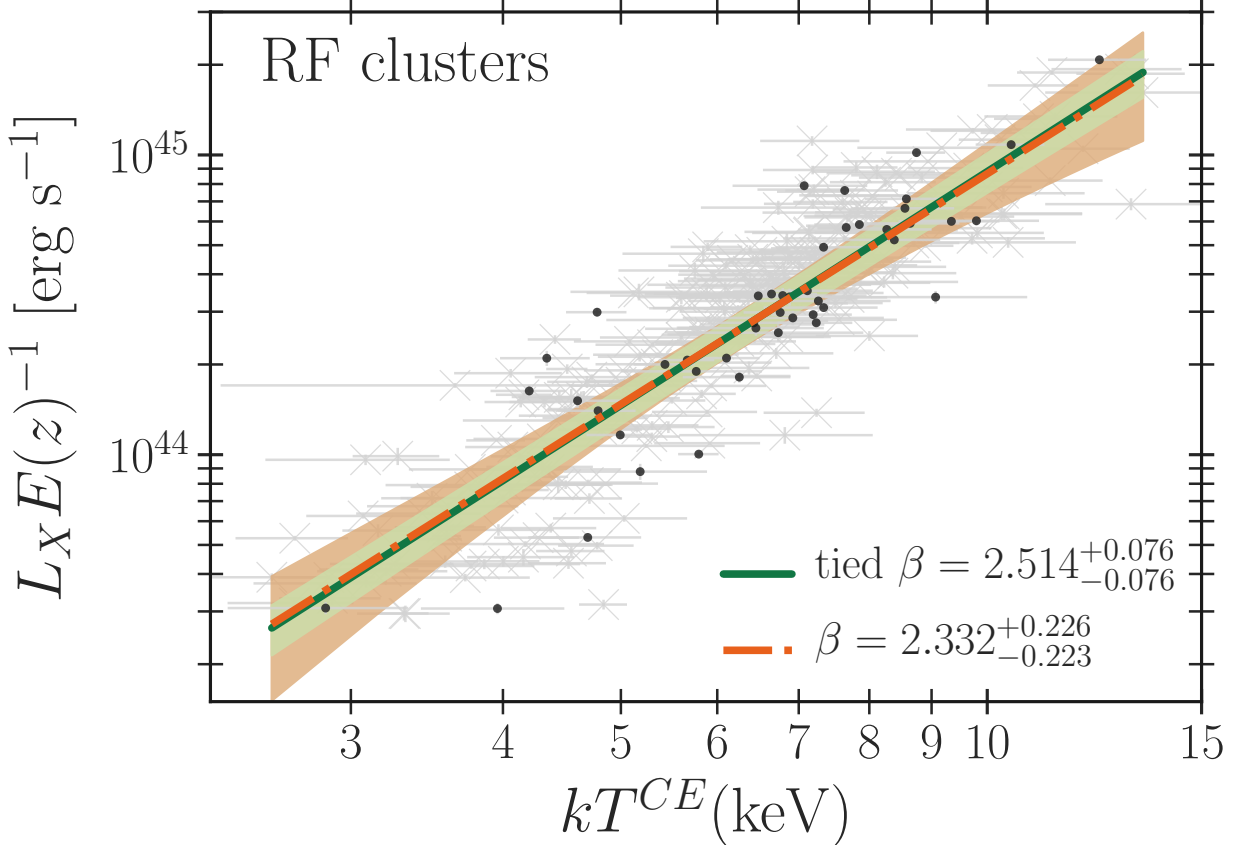


Figure 3.6: **Best fit $L_X - T$ for RF clusters.** Same plot as Figures 3.4 and 3.5 but for 46 RF clusters in the region surrounding $\text{RF} = (l, b) \sim (281^\circ, -16^\circ)$. The best fit parameters of normalization and intrinsic scatter are $L_{X,0} = 2.195^{+0.157}_{-0.148}$ and $\sigma_{\text{int}} = 0.322^{+0.020}_{-0.019}$ for the tied model, and $L_{X,0} = 2.194^{+0.165}_{-0.156}$ and $\sigma_{\text{int}} = 0.309^{+0.056}_{-0.048}$ for the separate model.

More importantly, below energies of $kT \sim 2$ keV, X-ray observables are more subject to systematics from Galactic absorption N_H . To correct for the total absorption due to neutral hydrogen and related metals, each cluster in ACCEPT2.0 was assigned a single line-of-sight absorption value for neutral hydrogen N_{HI} given by Stark et al. (1992), whereas M20 reversed the N_{HI} correction from the parent catalogs and applied a new correction to their L_X values based on total N_H (which includes atomic and molecular hydrogen) provided by Willingale et al. (2013). That correction is not the likely source of the differences, but the correction for Galactic absorption is important for estimating intrinsic X-ray luminosity, and higher gas column densities require larger corrections. However, X-ray column densities arise from absorption due to metals along the line of sight. Such

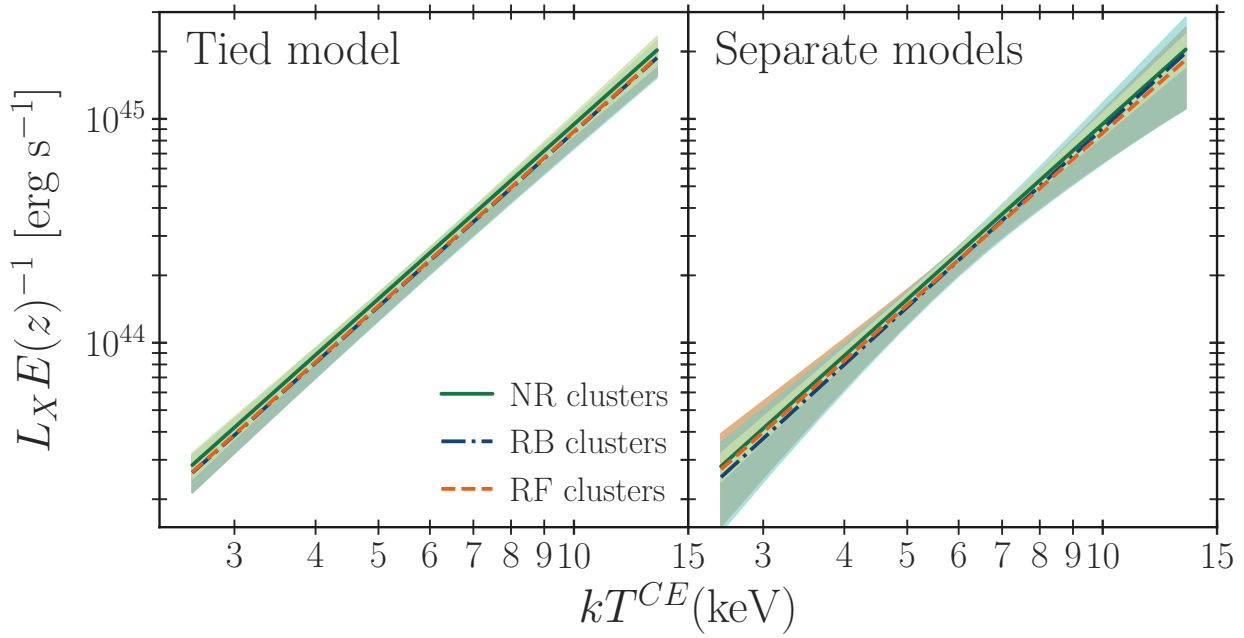


Figure 3.7: **Stacked tied and separate L_X – T for NR, RF, and RB clusters.** Best fit models for the luminosity-temperature for the tied parameter model (*left*) and independent models (*right*).

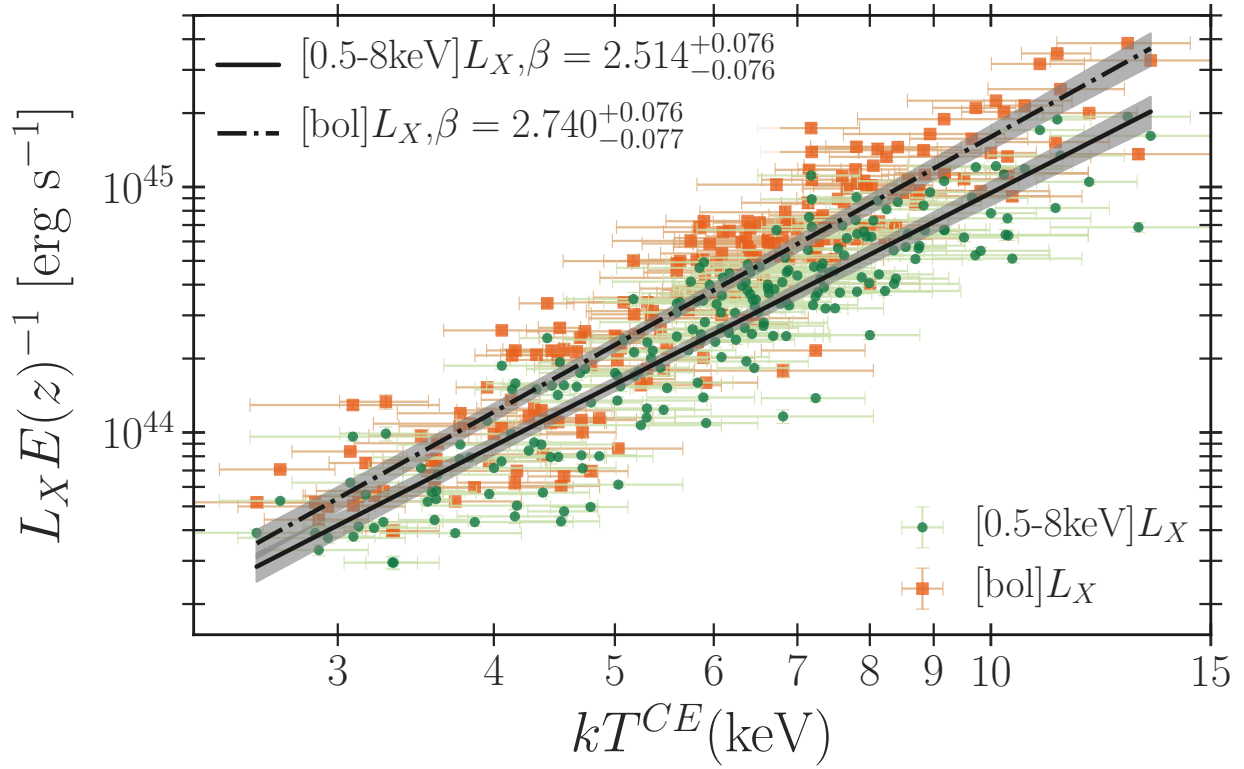


Figure 3.8: **L_X – T for bandpass vs. bolometric luminosities.** Best fit models for NR clusters using bolometric and bandpass luminosities. Luminosity is less dependent on temperature for low energy ranges, which results in a weaker relation when using [0.5–8] keV luminosities.

metals are related to hydrogen, rather than being hydrogen itself. Therefore, the absorption correction based on a neutral hydrogen column might not account for all the material along the line of sight with a scaling between neutral and X-ray absorbing materials, especially for objects near the Galactic plane. If the difference reported by M20 is real, the result should not change with a different bandpass or N_H treatment.

The result in M20 was surprising because a statistical difference in the normalization of the $L_X - T$ relation would suggest that, when correcting for redshift, different regions of the sky are subject to different cosmologies. If clusters in RF are truly fainter, it would suggest that their redshift-corrected, or comoving distance D_C is larger towards that region, which would be a consequence of greater H_0 . Luminosity L_X of an object with flux S_X at redshift z is,

$$L_X = S_X [(1+z)D_C]^2. \quad (3.8)$$

D_C is the comoving distance and relates to the Hubble constant H_0 via,

$$D_C = \frac{c}{H_0} \int \frac{dz}{E(z)}, \quad (3.9)$$

where $E(z) = \sqrt{(1+z)^3\Omega_M + \Omega_\Lambda}$. A true difference in luminosity would suggest that H_0 differs depending on where one looks on the sky and that the Universe is not expanding uniformly in all directions.

M20's conclusion is also surprising because the $L_X - T$ relation is (as far as we know) the only standard candle to show anisotropic expansion. For instance, distance estimates can be extrapolated from observations of objects with known absolute magnitude. For instance, if the value of H_0 were truly anisotropic, we would expect to see differences in type Ia supernovae (SNe Ia), which have well-defined peak magnitudes and predictable light curves (Colgate, 1979). At the highest redshifts, the Cosmic Microwave Background (CMB) should show large-scale temperature anisotropy that correlates with observed small fluctuations, but various tests have not yielded statistically significant results (Bennett et al., 2011). Instead, it is more likely that the result in M20 can be attributed to differences in systematics rather than differences in cosmology.

3.5 Conclusion

We used global core-excised temperatures and luminosities for 302 ACCEPT2.0 clusters to investigate differences in the $L_X - T$ relation towards different regions of the sky based on the results reported by Migkas et al. (2020) (M20). They found that 78 clusters within a 60 degree cone towards galactic coordinates $(34^\circ, +4^\circ)$, or bright region (RB), were up to 36% brighter than 84 clusters belonging to a faint region (RF) towards $(281^\circ, -16^\circ)$. M20 fit their data to a linear model similar to that of Equation 3.2 and found that the difference in normalization parameter ($L_{X,0}$) between clusters in the bright and faint regions is $\frac{RB}{RF} \Delta L_0 = 0.406 \pm 0.086$, a significance of nearly 5σ . This difference is contrary to our findings which resulted from models where clusters in each region were fit simultaneously ($\frac{RB}{RF} \Delta L_{X,0} = -0.018 \pm 0.218$) and separately ($\frac{RB}{RF} \Delta L_{X,0} = -0.019 \pm 0.238$).

The implication of an $L_X - T$ relation that changes depending on sky location is that expansion of the Universe is not the same in all directions, and it would require us to learn a new cosmological model and give different treatments of cluster samples depending on their distance and where they are on the sky. We performed a similar analysis for 302 ACCEPT2.0 clusters divided into 46 clusters towards the RF direction, 41 towards the RB direction, and 215 remaining clusters covering the rest of the sky (NR). We performed the fit for two different model assumptions: a separate model for which all the parameters are independent of sky location, and a tied model where each subset is fit simultaneously and only the normalizations are allowed to vary between the subsamples. We found no statistical difference in the $L_X - T$ relation in different directions on the sky for either model, suggesting that the more likely explanation for results found by M20 are due to systematic effects.

Table 3.3: **Global CE $L_X - T$ properties for clusters separated by sky region.** Full list of 302 ACCEPT2.0 global core-excised X-ray properties (in order of increasing RA) and their region ID on the sky, where RB refers to the region $(l, b) \sim (34^\circ, +4^\circ)$, RF refers to the region $(l, b) \sim (281^\circ, -16^\circ)$, and NR clusters belong to neither region. The columns are as follows: col(1) is ACCEPT2.0 name, col(2) is the cluster region ID, col(3) is redshift, cols(4,5) and cols(6,7) are the [0.5-8 keV] energy bandpass and bolometric luminosities in units of $10^{44} \text{ erg s}^{-1}$, cols(8,9) is the temperature and error in keV, cols(10,11) is the metallicity in solar units Z_\odot , col(12) is the reduced chi-square value obtained from the X-ray spectral fit. The full version of this table can be found at the end of chapter 2.

Name	ID	z	LX [0.5-8 keV]	e_LX $10^{44} \text{ erg s}^{-1}$	LX [bol]	e_LX $10^{44} \text{ erg s}^{-1}$	kT	e_kT	Z	e_Z	χ^2
000619+105206	NR	0.167	1.850	0.072	2.636	0.102	5.184	0.399	0.350	0.092	1.073
00088+5215	NR	0.104	0.751	0.030	1.052	0.043	4.711	0.300	0.164	0.087	1.264
00117-1523	NR	0.378	6.014	0.194	8.839	0.285	5.892	0.399	0.271	0.066	1.132
A0013	NR	0.094	0.641	0.016	0.899	0.023	5.032	0.635	0.209	0.124	1.048
A2744	NR	0.308	13.170	0.165	23.686	0.296	10.245	0.770	0.299	0.102	1.234
0014-4952	RF	0.752	5.112	0.336	7.853	0.517	6.880	0.966	0.406	0.162	1.096
Cl0016+16	NR	0.541	16.147	0.355	28.163	0.619	9.727	0.745	0.198	0.063	0.964
00254-1222	NR	0.584	8.852	0.347	14.205	0.557	7.817	0.597	0.256	0.060	1.134
00278+2616	NR	0.367	3.049	0.194	4.615	0.294	6.438	0.978	0.039	0.082	1.086
30484-4142	RF	0.410	7.488	0.269	13.102	0.470	9.797	1.232	0.150	0.096	1.170
00354-2015	NR	0.364	10.772	0.355	16.792	0.554	7.187	0.645	0.338	0.090	1.146
A0068	NR	0.255	5.993	0.281	10.429	0.489	9.717	1.436	0.662	0.210	1.270
A0085	NR	0.055	2.609	0.019	3.925	0.028	6.170	0.588	0.358	0.150	2.290
A2813	NR	0.292	7.287	0.223	11.762	0.361	7.950	0.739	0.287	0.086	1.303
00408+2404	NR	0.083	0.823	0.028	1.129	0.038	3.826	0.623	0.291	0.102	1.280
A0119	NR	0.044	1.115	0.013	1.628	0.019	5.916	0.591	0.290	0.131	3.338
A0141	NR	0.230	3.050	0.122	4.635	0.186	6.576	0.772	0.184	0.120	1.383
01077+5408	NR	0.107	3.881	0.057	6.191	0.092	6.642	1.385	0.184	0.136	1.257
A2895	NR	0.227	4.742	0.143	7.809	0.236	8.394	0.858	0.301	0.107	1.471
A0193	NR	0.049	0.398	0.011	0.536	0.015	3.725	0.483	0.307	0.115	1.191
A0209	NR	0.206	6.310	0.161	10.466	0.266	8.547	0.665	0.250	0.082	1.313

Table 3.3 (cont'd)

Name	ID	z	LX	e_LX	LX	e_LX	kT	e_kT	Z	e_Z	χ^2	
			[0.5-8 keV]		[bol]							
			10^{44} erg s $^{-1}$		10^{44} erg s $^{-1}$		keV		Z_\odot	d.o.f		
Abell222		NR	0.211	1.664	0.067	2.287	0.092	4.137	0.274	0.216	0.070	1.032
Abell223		NR	0.207	1.370	0.062	1.981	0.089	5.470	0.500	0.247	0.100	1.152
01400-0555		NR	0.454	7.056	0.392	10.985	0.610	7.139	0.822	0.256	0.103	1.149
01420+2131		NR	0.280	5.460	0.165	8.543	0.258	7.218	0.649	0.118	0.090	1.265
01525-2853		NR	0.341	4.091	0.126	6.018	0.186	5.815	0.584	0.058	0.081	1.125
A0267		NR	0.231	4.166	0.105	6.600	0.166	7.570	0.630	0.393	0.106	1.224
02209-3829		RF	0.229	2.352	0.136	3.225	0.187	4.346	0.368	0.546	0.140	1.230
A3017		RF	0.220	3.931	0.175	6.124	0.272	7.115	0.939	0.111	0.106	1.080
0232-4421		RF	0.284	8.792	0.304	13.995	0.485	7.636	0.811	0.218	0.095	1.259
A0368		NR	0.220	3.443	0.181	5.101	0.268	6.080	0.768	0.305	0.138	1.276
A0370		NR	0.375	6.827	0.110	11.422	0.183	8.753	0.459	0.285	0.074	1.206
02426-2132		NR	0.314	4.837	0.298	7.085	0.436	5.751	0.774	0.151	0.115	1.156
AS0295		RF	0.300	9.202	0.310	14.464	0.487	7.072	0.896	0.257	0.059	1.200
A0376		NR	0.048	0.515	0.011	0.713	0.016	4.174	0.670	0.346	0.208	1.875
A0383		NR	0.187	2.012	0.064	2.881	0.092	5.438	0.297	0.338	0.110	1.239
A0402		NR	0.322	4.452	0.190	7.293	0.311	8.228	1.236	0.045	0.085	1.175
A0399		NR	0.072	2.554	0.021	3.926	0.032	6.857	0.581	0.243	0.136	3.135
A0401		NR	0.074	4.434	0.016	7.035	0.025	7.881	0.877	0.282	0.099	1.488
03016+0155		NR	0.170	1.687	0.079	2.341	0.110	4.450	0.333	0.233	0.090	1.190
03037-7752		RF	0.274	6.901	0.197	11.840	0.338	9.344	0.891	0.318	0.085	1.143
A3088		NR	0.253	5.317	0.193	8.344	0.302	7.316	0.762	0.236	0.099	1.279
03089+2645		NR	0.324	10.682	0.298	18.580	0.518	9.656	1.047	0.159	0.085	1.285
A3126		RF	0.086	1.212	0.037	1.707	0.052	4.994	0.309	0.470	0.083	1.203
A3128		RF	0.060	0.316	0.015	0.423	0.020	2.860	0.484	0.269	0.111	1.502
03311-2100		NR	0.188	2.604	0.104	3.827	0.153	5.859	0.528	0.204	0.092	1.380
3C089		NR	0.139	0.464	0.020	0.647	0.028	4.528	0.333	0.166	0.096	1.164
A3158		RF	0.060	2.057	0.018	2.899	0.026	5.435	0.313	0.387	0.082	2.722
03529+1941		NR	0.109	1.013	0.041	1.362	0.055	3.085	0.533	0.263	0.124	1.111

Table 3.3 (cont'd)

Name	ID	z	LX	e_LX	LX	e_LX	kT	e_kT	Z	e_Z	χ^2		
			[0.5-8 keV]		[bol]								
			10^{44} erg s $^{-1}$		10^{44} erg s $^{-1}$		keV		Z_\odot	d.o.f			
03588-2955			RF	0.425	12.749	0.337	21.346	0.564	8.747	0.487	0.143	0.052	1.130
A0478			NR	0.088	5.866	0.038	9.322	0.060	7.546	0.554	0.270	0.121	1.116
04175-1154			NR	0.440	21.550	0.366	40.079	0.680	10.945	0.936	0.211	0.093	1.108
04258-0833			NR	0.040	0.384	0.016	0.514	0.022	3.088	0.125	0.256	0.073	3.255
04296-0253			NR	0.399	5.376	0.254	8.315	0.393	7.000	0.900	0.302	0.132	1.159
04371+0043			NR	0.285	4.937	0.134	7.580	0.205	6.101	0.632	0.265	0.041	1.251
04390+0715			NR	0.230	5.310	0.166	8.038	0.252	6.528	0.534	0.293	0.083	1.160
04390+0520			NR	0.208	1.883	0.103	2.670	0.145	5.024	0.480	0.251	0.107	1.220
A0514			RF	0.071	0.317	0.014	0.430	0.018	3.959	0.534	0.257	0.035	1.588
A3292			RF	0.172	1.775	0.082	2.441	0.112	4.204	0.297	0.271	0.098	1.410
04519+0006			NR	0.430	5.882	0.364	8.608	0.533	5.844	0.829	0.411	0.206	1.101
04541-0300			NR	0.550	15.974	0.296	28.925	0.536	10.644	0.768	0.206	0.082	1.309
04552+0657			NR	0.425	6.452	0.414	9.878	0.634	6.845	0.998	0.571	0.226	1.135
0509-5342			RF	0.463	4.295	0.208	7.291	0.353	9.069	1.716	0.145	0.164	1.176
A3322			RF	0.200	3.793	0.142	5.786	0.216	6.649	0.599	0.146	0.092	1.104
05107-0801			NR	0.220	8.412	0.212	13.101	0.330	7.152	0.434	0.280	0.060	1.082
AS0520			RF	0.295	6.561	0.201	10.757	0.330	8.269	0.732	0.140	0.076	1.167
05207-1328			NR	0.340	5.821	0.181	9.131	0.284	7.335	0.692	0.345	0.111	1.265
A3343			RF	0.191	3.027	0.089	4.563	0.135	6.429	0.528	0.269	0.099	1.175
05282-2942			RF	0.158	1.634	0.086	2.245	0.119	4.607	0.499	0.564	0.197	1.327
RBS0653			RF	0.284	7.669	0.109	13.057	0.185	8.558	0.836	0.258	0.066	1.153
28658-3125			RF	0.210	3.759	0.128	5.678	0.194	6.484	0.540	0.301	0.091	1.060
A0545			NR	0.154	3.448	0.047	5.431	0.073	7.372	0.311	0.124	0.052	1.265
05329-3701			RF	0.275	6.799	0.197	11.333	0.329	8.644	0.843	0.136	0.080	1.134
0542-4100			RF	0.640	3.762	0.216	5.691	0.327	6.455	0.885	0.108	0.125	1.168
05470-3904			RF	0.210	0.974	0.060	1.398	0.086	5.186	0.699	0.046	0.106	1.352
A3364			RF	0.148	3.151	0.079	4.925	0.124	7.194	0.546	0.126	0.081	1.411
A0550			RF	0.099	2.168	0.062	3.165	0.090	5.669	0.298	0.141	0.067	1.202

Table 3.3 (cont'd)

Name	ID	z	LX	e_LX	LX	e_LX	kT	e_kT	Z	e_Z	χ^2
			[0.5-8 keV]		[bol]						
			10^{44} erg s $^{-1}$		10^{44} erg s $^{-1}$			keV		Z_\odot	d.o.f
05534-3342	RF	0.407	13.416	0.212	24.118	0.382	10.463	0.680	0.192	0.055	1.119
A3376	RF	0.046	0.541	0.006	0.762	0.008	4.696	0.499	0.386	0.121	3.323
A3378	RF	0.141	3.198	0.099	4.474	0.139	4.780	0.273	0.360	0.088	1.160
06163-2156	RF	0.171	2.994	0.067	4.678	0.105	7.236	0.511	0.313	0.086	1.178
AS0579	RF	0.152	1.508	0.056	2.119	0.078	4.789	0.352	0.213	0.092	1.146
13959+2418	NR	0.270	7.876	0.283	12.273	0.440	7.189	0.635	0.378	0.086	1.169
A3391	RF	0.051	1.028	0.021	1.498	0.031	5.794	0.222	0.232	0.068	3.227
A3399	RF	0.203	3.297	0.073	5.045	0.111	6.759	0.453	0.276	0.084	1.084
16765+1764	NR	0.174	4.844	0.111	7.219	0.165	6.176	0.412	0.229	0.080	1.140
AS0592	RF	0.222	7.970	0.188	13.233	0.313	8.581	0.651	0.312	0.080	1.363
A3404	RF	0.167	6.357	0.151	10.236	0.244	7.851	0.642	0.049	0.062	1.148
A0562	NR	0.110	0.392	0.019	0.526	0.025	2.946	0.451	0.237	0.083	1.122
Bullet	RF	0.296	24.166	0.131	46.462	0.252	12.364	1.145	0.208	0.066	1.326
0717+3745	NR	0.546	25.993	0.368	51.818	0.734	12.868	1.576	0.181	0.048	1.136
A0586	NR	0.171	3.337	0.093	4.977	0.139	6.241	0.395	0.374	0.075	1.157
07357+7421	NR	0.216	3.873	0.033	5.843	0.050	6.447	0.632	0.331	0.103	1.236
07449+3927	NR	0.698	13.375	0.576	21.465	0.924	7.805	0.634	0.179	0.067	1.114
PKS0745-19	NR	0.103	5.794	0.034	9.484	0.055	8.360	0.483	0.304	0.083	1.593
A0598	NR	0.189	1.695	0.085	2.417	0.121	5.052	0.538	0.068	0.091	1.291
A0611	NR	0.288	4.697	0.124	7.783	0.205	7.993	0.430	0.408	0.118	1.017
A0644	NR	0.070	2.890	0.031	4.410	0.047	6.580	0.821	0.317	0.089	2.778
08196+6336	NR	0.119	0.758	0.044	1.025	0.060	3.498	0.321	0.170	0.088	1.238
08232+0425	NR	0.225	1.718	0.107	2.383	0.148	4.660	0.514	0.510	0.168	1.271
A0665	NR	0.182	4.817	0.059	7.910	0.096	8.136	0.857	0.260	0.075	1.314
2MFGC06756	NR	0.241	2.694	0.055	3.823	0.078	5.082	0.508	0.287	0.098	1.057
A3411	NR	0.169	2.842	0.053	4.247	0.079	6.161	0.454	0.348	0.095	1.119
084254+292723	NR	0.194	1.485	0.048	2.174	0.070	5.023	0.901	0.519	0.181	1.052
A0697	NR	0.282	12.109	0.291	23.094	0.555	11.987	1.107	0.333	0.106	1.311

Table 3.3 (cont'd)

Name	ID	z	LX	e_LX	LX	e_LX	kT	e_kT	Z	e_Z	χ^2		
			[0.5-8 keV]		[bol]								
			10^{44} erg s $^{-1}$		10^{44} erg s $^{-1}$		keV		Z_\odot	d.o.f			
08579+2107			NR	0.230	2.167	0.079	2.994	0.110	4.517	0.176	0.356	0.160	0.993
+1373+110+018			NR	0.180	2.688	0.078	3.869	0.112	5.605	0.799	0.248	0.072	1.140
09112+1746			NR	0.505	5.371	0.324	8.253	0.497	6.808	0.894	0.133	0.102	1.124
20913454+405628			NR	0.442	4.631	0.189	6.963	0.284	6.416	0.590	0.406	0.092	1.152
A0773			NR	0.217	5.866	0.132	9.528	0.214	7.630	0.833	0.272	0.081	1.237
HydraA			NR	0.055	1.145	0.005	1.566	0.006	3.951	0.219	0.289	0.046	1.219
092017+303027			NR	0.258	3.036	0.123	4.554	0.184	6.352	0.661	0.352	0.105	1.115
A0795			NR	0.136	1.863	0.048	2.645	0.068	5.002	0.300	0.164	0.062	1.275
0938209+520243			NR	0.360	5.414	0.181	8.169	0.274	6.417	0.504	0.165	0.073	1.081
A0853			NR	0.166	0.861	0.054	1.194	0.075	4.441	0.481	0.236	0.129	1.146
A0868			NR	0.153	2.610	0.086	3.615	0.119	4.414	0.222	0.252	0.070	1.137
0947124+762313			NR	0.354	7.738	0.176	12.772	0.291	8.581	0.841	0.286	0.196	1.088
09498+1708			NR	0.383	9.104	0.381	16.267	0.681	10.311	1.712	0.184	0.151	1.258
09496+5207			NR	0.214	2.228	0.048	3.243	0.069	5.346	0.581	0.291	0.096	1.088
A0907			NR	0.153	2.833	0.056	4.152	0.083	5.772	0.537	0.335	0.142	1.381
26441+1948			NR	0.240	3.615	0.128	5.726	0.203	7.503	0.702	0.090	0.077	1.126
10005+4409			NR	0.154	1.065	0.070	1.437	0.095	3.278	0.268	0.183	0.095	1.243
10061+1201			NR	0.221	2.803	0.071	4.111	0.105	5.860	0.459	0.305	0.027	1.133
10105-1239			NR	0.301	4.060	0.084	6.139	0.127	6.484	0.395	0.222	0.062	1.108
A0963			NR	0.206	4.534	0.076	6.861	0.115	6.364	0.782	0.226	0.113	1.259
A0970			NR	0.059	0.817	0.027	1.134	0.038	4.504	0.402	0.276	0.014	1.387
A0980			NR	0.158	3.039	0.090	4.606	0.136	5.902	1.038	0.220	0.086	1.204
10236+04111			NR	0.291	8.464	0.127	14.162	0.213	8.052	0.966	0.285	0.096	1.289
1023399+490838			NR	0.144	3.321	0.111	5.034	0.168	6.513	0.589	0.156	0.083	1.099
A3444			NR	0.253	7.473	0.123	12.037	0.197	7.915	0.451	0.338	0.060	0.974
A1033			NR	0.126	1.475	0.025	2.143	0.037	5.886	0.583	0.266	0.038	1.207
A1068			NR	0.138	1.884	0.042	2.664	0.060	5.225	0.552	0.370	0.092	1.078
10569-03373			NR	0.823	7.212	0.383	11.420	0.607	7.494	1.083	0.096	0.107	1.444

Table 3.3 (cont'd)

Name	ID	z	LX	e_LX	LX	e_LX	kT	e_kT	Z	e_Z	χ^2	
			[0.5-8 keV]		[bol]							
			10^{44} erg s $^{-1}$		10^{44} erg s $^{-1}$			keV		Z_\odot	d.o.f	
11089+0906			NR 0.449	5.708	0.269	8.786	0.414	6.863	0.744	0.193	0.106	1.128
A1190			NR 0.075	0.599	0.028	0.808	0.038	3.597	0.190	0.271	0.083	1.247
A1201			NR 0.169	2.527	0.054	3.681	0.079	5.309	0.543	0.359	0.060	1.254
A1204			NR 0.171	1.629	0.066	2.253	0.092	4.327	0.277	0.218	0.084	1.310
1115+5319			NR 0.466	8.139	0.364	14.554	0.651	10.328	1.639	0.141	0.157	1.084
11158+0129			NR 0.352	8.020	0.227	13.674	0.388	9.180	0.730	0.189	0.068	1.253
A1240			NR 0.159	0.492	0.032	0.675	0.044	4.158	0.420	0.279	0.137	1.411
A1285			NR 0.106	2.267	0.042	3.281	0.060	5.361	0.617	0.314	0.026	1.219
A1300			NR 0.307	9.614	0.240	17.836	0.446	11.265	1.174	0.262	0.099	1.285
11375+6625			NR 0.782	5.411	0.347	7.728	0.495	5.174	0.629	0.228	0.122	1.088
1142248+583205			NR 0.311	7.812	0.182	13.142	0.306	8.855	0.679	0.127	0.073	1.166
A1413			NR 0.143	4.175	0.044	6.581	0.070	7.350	0.558	0.231	0.089	1.459
17981192+4979669			NR 0.383	7.801	0.394	13.915	0.702	10.276	1.691	0.267	0.141	1.111
29251+2198			NR 0.300	5.929	0.172	9.902	0.287	8.702	0.784	0.233	0.076	1.104
A1446			NR 0.103	0.707	0.019	0.950	0.025	3.606	0.513	0.332	0.163	1.123
12062-0847			NR 0.440	16.980	0.490	31.633	0.913	11.369	1.423	0.225	0.109	1.235
12154-3900			NR 0.119	1.605	0.038	2.315	0.055	5.505	0.361	0.429	0.110	1.167
121733+033929			NR 0.077	2.565	0.050	3.947	0.077	6.694	0.647	0.292	0.170	2.787
121831+401236			NR 0.320	4.257	0.182	6.320	0.271	6.090	0.651	0.210	0.116	1.216
122648+215157			NR 0.370	1.608	0.082	2.259	0.115	4.785	0.474	0.191	0.095	1.082
12269+3332			NR 0.890	11.315	0.521	22.466	1.035	13.126	1.968	0.193	0.189	1.117
A1553			NR 0.165	3.879	0.113	6.048	0.176	7.238	0.587	0.518	0.105	1.136
12342+0947			NR 0.229	1.747	0.111	2.439	0.154	4.552	0.485	0.134	0.112	1.255
A1576			NR 0.279	2.870	0.107	4.654	0.174	8.001	0.772	0.057	0.063	1.187
A1644			NR 0.047	0.818	0.007	1.171	0.009	4.858	0.506	0.344	0.141	3.047
A1650			NR 0.084	2.247	0.018	3.278	0.026	5.726	0.524	0.286	0.106	1.737
1259334+600409			NR 0.330	3.904	0.145	6.024	0.223	6.894	0.515	0.112	0.068	1.062
A1664			NR 0.128	1.930	0.041	2.747	0.059	4.732	0.484	0.239	0.047	1.178

Table 3.3 (cont'd)

Name	ID	z	LX [0.5-8 keV]	e_LX $10^{44} \text{ erg s}^{-1}$	LX [bol]	e_LX $10^{44} \text{ erg s}^{-1}$	kT	e_kT	Z	e_Z	χ^2
A1668	NR	0.063	0.304	0.019	0.409	0.026	3.326	0.291	0.245	0.094	1.442
1305589+263048	NR	0.305	4.356	0.192	6.829	0.300	7.269	0.948	0.151	0.097	1.082
A1682	NR	0.234	3.710	0.105	5.803	0.164	7.205	0.618	0.116	0.092	1.131
13110-0311	NR	0.494	4.349	0.189	6.435	0.280	6.031	0.482	0.228	0.071	1.128
A1689	NR	0.183	8.559	0.103	15.062	0.181	10.000	0.874	0.279	0.110	1.410
1315052+514902	NR	0.291	6.692	0.136	11.224	0.229	8.765	0.771	0.025	0.048	1.149
A1736	NR	0.046	0.638	0.013	0.854	0.017	3.070	0.313	0.322	0.158	3.124
SSGC081	NR	0.050	0.418	0.015	0.565	0.020	3.207	0.393	0.282	0.087	2.178
A1750C	NR	0.068	0.445	0.017	0.617	0.024	3.861	0.768	0.263	0.095	1.310
A1750N	NR	0.084	0.458	0.022	0.621	0.029	3.586	0.230	0.165	0.070	1.350
A3562	NR	0.049	0.826	0.018	1.149	0.026	4.701	0.503	0.340	0.125	3.211
A1763	NR	0.223	6.919	0.180	11.013	0.286	7.669	0.593	0.388	0.084	1.252
A1767	NR	0.070	1.188	0.037	1.703	0.053	5.301	0.290	0.293	0.081	1.412
A1775	NR	0.072	0.923	0.011	1.238	0.015	3.760	0.413	0.503	0.110	1.616
LCDCS0829	NR	0.451	20.538	0.248	41.656	0.503	13.426	2.267	0.213	0.073	1.160
13546+7715	NR	0.397	4.673	0.251	7.024	0.378	6.384	0.815	0.314	0.119	1.103
A1831	NR	0.061	0.538	0.017	0.720	0.023	3.541	0.159	0.447	0.077	1.347
1359495+623047	NR	0.322	4.018	0.121	6.184	0.186	6.859	0.590	0.199	0.084	1.468
A1835	NR	0.253	12.004	0.170	21.457	0.303	9.175	1.354	0.348	0.157	1.213
11382+4435	NR	0.226	2.620	0.128	3.891	0.189	6.017	0.680	0.004	0.053	1.037
A1882a	NR	0.141	0.316	0.017	0.424	0.022	3.317	0.158	0.302	0.080	1.129
21594948+2407846	NR	0.543	6.151	0.118	9.624	0.185	6.887	0.360	0.327	0.029	1.000
A1914	NR	0.171	9.446	0.147	15.799	0.246	8.422	1.044	0.213	0.053	1.398
1427161+440730	NR	0.498	6.679	0.271	11.975	0.486	10.403	1.424	0.236	0.142	1.328
14276-2521	NR	0.318	2.061	0.095	2.865	0.132	4.689	0.340	0.443	0.114	1.186
A1930	NR	0.131	0.951	0.038	1.311	0.053	4.366	0.629	0.587	0.028	1.235
A1942	NR	0.224	1.401	0.046	2.016	0.066	5.305	0.486	0.373	0.031	1.219
A1991	RB	0.059	0.329	0.010	0.438	0.013	2.695	0.319	0.299	0.114	1.106

Table 3.3 (cont'd)

Name	ID	z	LX [0.5-8 keV]	e_LX [bol]	LX 10^{44} erg s $^{-1}$	e_LX 10^{44} erg s $^{-1}$	kT	e_kT	Z	e_Z	χ^2
145715+222009	RB	0.258	3.947	0.081	5.650	0.115	5.120	0.434	0.296	0.101	1.135
AS0780	RB	0.236	5.352	0.074	8.395	0.117	7.021	0.628	0.310	0.122	1.065
A2009	RB	0.153	3.537	0.097	5.386	0.148	6.695	0.309	0.443	0.071	1.392
1504075-024816	RB	0.215	9.519	0.130	16.069	0.219	8.482	0.751	0.238	0.070	1.463
A2034	RB	0.113	2.975	0.031	4.685	0.049	7.555	0.875	0.303	0.108	1.568
15149-1523	RB	0.223	5.561	0.090	9.372	0.151	8.899	0.481	0.141	0.048	1.105
A2061	RB	0.078	1.171	0.022	1.631	0.031	4.310	0.527	0.278	0.118	1.083
MKW03s	RB	0.045	0.650	0.006	0.875	0.008	3.434	0.404	0.261	0.113	2.072
01670077	NR	0.254	2.126	0.070	2.961	0.098	4.059	0.412	0.267	0.111	1.028
A2069	RB	0.116	1.793	0.032	2.675	0.048	5.936	0.646	0.301	0.128	1.712
15242-3154	RB	0.103	1.365	0.019	1.900	0.026	4.426	0.719	0.362	0.129	1.326
15328+3021	RB	0.345	6.570	0.112	10.388	0.177	7.129	0.720	0.239	0.065	1.141
A2107	RB	0.041	0.433	0.009	0.588	0.012	3.766	0.480	0.265	0.114	3.251
A2111	RB	0.229	3.754	0.081	5.996	0.129	7.700	0.575	0.186	0.085	1.146
A2104	RB	0.153	3.731	0.049	5.815	0.077	7.200	1.018	0.245	0.153	1.354
A2125	NR	0.246	0.632	0.031	0.850	0.042	3.158	0.206	0.197	0.089	1.133
A2124	RB	0.066	0.326	0.012	0.463	0.017	4.839	0.219	0.354	0.091	1.104
A2142	RB	0.091	4.832	0.043	7.887	0.069	7.675	0.570	0.276	0.080	3.074
15583-1410	RB	0.097	2.001	0.021	2.850	0.029	5.018	0.356	0.371	0.106	1.330
A2147	RB	0.035	0.537	0.007	0.737	0.010	4.275	0.343	0.321	0.101	4.436
A2163	RB	0.203	20.636	0.140	42.292	0.288	13.183	1.347	0.240	0.045	1.603
16213+3810	RB	0.465	4.964	0.186	7.763	0.291	7.226	0.580	0.199	0.066	1.167
16235+2634	RB	0.426	3.854	0.228	5.798	0.342	6.365	0.908	0.201	0.124	1.005
A2187	RB	0.184	2.384	0.100	3.644	0.152	6.709	0.765	0.183	0.122	1.389
A2204	RB	0.152	6.250	0.044	10.792	0.077	8.269	1.172	0.319	0.143	1.623
A2218	NR	0.176	4.315	0.084	6.482	0.127	6.318	0.550	0.201	0.076	1.287
A2219	RB	0.226	14.778	0.091	27.420	0.169	11.017	0.888	0.280	0.093	1.223
HerculesA	RB	0.155	1.836	0.034	2.531	0.047	3.653	1.309	0.181	0.097	1.224

Table 3.3 (cont'd)

Name	ID	z	LX	e_LX	LX	e_LX	kT	e_kT	Z	e_Z	χ^2		
			[0.5-8 keV]			[bol]							
			10^{44} erg s $^{-1}$		10^{44} erg s $^{-1}$			keV		Z_\odot	d.o.f		
021701+6412			NR	0.453	2.479	0.125	3.720	0.188	6.371	0.771	0.379	0.154	1.122
A2244			RB	0.097	2.680	0.024	3.927	0.036	5.919	0.484	0.327	0.096	1.106
A2256			NR	0.058	3.438	0.033	5.363	0.052	6.782	0.465	0.381	0.135	1.886
A2249			RB	0.082	1.267	0.035	1.811	0.051	5.153	0.342	0.168	0.086	1.204
A2255			NR	0.081	2.107	0.026	3.133	0.038	6.086	0.559	0.325	0.113	1.828
A2259			RB	0.164	3.248	0.119	4.806	0.176	6.089	0.502	0.427	0.128	1.254
43072			RB	0.164	4.348	0.075	6.753	0.116	7.066	0.427	0.413	0.059	1.371
17202+3536			RB	0.391	6.766	0.206	10.872	0.331	7.870	0.653	0.367	0.080	1.279
A2261			RB	0.224	7.182	0.156	11.669	0.253	7.714	1.178	0.349	0.077	1.276
A2294			NR	0.169	4.578	0.170	7.178	0.266	7.303	0.736	0.260	0.106	1.415
17316+2251			RB	0.366	6.784	0.211	11.278	0.351	8.608	0.849	0.299	0.123	1.320
17421+3306			RB	0.076	1.099	0.017	1.507	0.024	4.076	0.352	0.374	0.179	1.653
174715+451155			RB	0.157	1.518	0.066	2.128	0.093	4.729	0.378	0.182	0.084	1.142
17502+3504			RB	0.171	1.689	0.078	2.364	0.109	4.639	0.356	0.126	0.083	1.187
18044+1002			RB	0.152	5.159	0.144	8.034	0.225	7.097	0.592	0.092	0.075	1.225
A2302			RB	0.179	1.324	0.055	1.862	0.077	4.821	0.382	0.203	0.096	1.157
18290+6913			NR	0.203	0.843	0.044	1.151	0.060	4.057	0.305	0.335	0.109	1.234
18521+5711			RB	0.109	0.465	0.019	0.635	0.026	4.003	0.283	0.259	0.096	1.345
18539+6822			NR	0.093	1.031	0.025	1.419	0.034	4.129	0.221	0.190	0.074	1.199
33709-2597			RF	0.264	6.544	0.138	10.438	0.221	7.658	0.539	0.118	0.070	1.181
A2319			RB	0.056	5.846	0.046	10.028	0.078	8.664	1.413	0.319	0.131	3.532
19318-2635			NR	0.352	8.805	0.104	14.152	0.168	7.793	0.786	0.374	0.147	1.326
AS0821			NR	0.237	5.443	0.174	8.184	0.261	6.386	0.506	0.302	0.072	1.108
19383+5409			RB	0.260	8.739	0.350	13.629	0.546	7.202	0.728	0.356	0.091	1.124
19473-7623			RF	0.217	5.483	0.179	8.604	0.280	7.337	0.632	0.338	0.086	1.214
A3653			NR	0.109	0.524	0.015	0.733	0.021	4.781	0.341	0.345	0.071	1.222
20035-2323			NR	0.317	7.858	0.190	13.401	0.324	9.178	0.804	0.131	0.072	1.222
20148-2430			NR	0.161	4.182	0.099	6.499	0.154	6.629	0.996	0.447	0.125	1.190

Table 3.3 (cont'd)

Name	ID	z	LX	e_LX	LX	e_LX	kT	e_kT	Z	e_Z	χ^2	
			[0.5-8 keV]		[bol]							
			10^{44} erg s $^{-1}$		10^{44} erg s $^{-1}$		keV		Z_\odot	d.o.f		
2023-5535		RF	0.232	5.848	0.172	9.627	0.283	8.387	0.761	0.291	0.085	1.121
20318-4037		NR	0.342	7.965	0.430	12.201	0.659	6.735	0.918	0.128	0.117	1.116
A3695		NR	0.089	1.909	0.042	2.887	0.064	6.465	0.427	0.161	0.084	1.352
20460-3430		NR	0.423	4.194	0.216	6.100	0.314	5.606	0.447	0.212	0.086	1.136
20499-3216		NR	0.325	5.290	0.221	8.338	0.348	7.423	0.952	0.262	0.109	1.259
A3739		NR	0.165	2.874	0.120	4.251	0.177	6.084	0.527	0.413	0.111	1.096
IC1365		NR	0.049	0.574	0.025	0.781	0.034	3.966	0.438	0.509	0.083	2.480
2129-0741		NR	0.589	12.133	0.669	19.708	1.086	8.117	0.943	0.454	0.126	1.130
2135-0102		NR	0.325	4.768	0.219	7.826	0.360	8.365	1.066	0.580	0.154	1.246
A2355		NR	0.124	1.465	0.045	2.290	0.071	7.240	0.690	0.289	0.118	1.276
2135-5726		RF	0.427	3.586	0.199	5.541	0.307	6.922	1.301	0.108	0.157	1.099
21402-2339		NR	0.313	3.985	0.110	5.860	0.162	5.638	0.740	0.306	0.144	1.070
A3809		NR	0.062	0.426	0.014	0.565	0.019	3.117	0.292	0.413	0.138	1.303
2148-6116		RF	0.571	3.484	0.229	5.327	0.351	6.735	1.175	0.272	0.195	1.039
A2384		NR	0.094	1.119	0.018	1.628	0.026	5.246	0.839	0.390	0.162	2.330
A2390		NR	0.228	13.625	0.092	25.178	0.169	10.095	1.521	0.290	0.096	1.068
21538+3746		NR	0.292	11.047	0.148	19.077	0.256	8.940	1.321	0.240	0.103	1.148
A2409		NR	0.148	4.281	0.134	6.289	0.197	5.955	0.382	0.462	0.093	1.292
A3827		RF	0.098	3.243	0.032	5.080	0.050	7.338	0.789	0.339	0.144	1.302
A2415		NR	0.058	0.401	0.012	0.534	0.016	2.583	0.284	0.347	0.094	1.236
22117-0349		NR	0.270	6.301	0.219	11.029	0.383	9.815	1.315	0.221	0.121	1.394
3C444		NR	0.153	0.613	0.021	0.876	0.030	4.379	0.393	0.332	0.098	1.334
A2426		NR	0.098	1.671	0.053	2.451	0.077	5.825	0.389	0.251	0.100	1.305
2214-1359		NR	0.483	10.888	0.419	18.292	0.705	8.833	0.989	0.194	0.093	1.120
A3854		NR	0.149	2.281	0.081	3.256	0.116	5.181	0.394	0.258	0.092	1.197
22186-3853		NR	0.138	3.292	0.092	4.789	0.134	5.604	0.330	0.200	0.075	1.240
A2445		NR	0.166	1.718	0.057	2.340	0.077	4.162	0.215	0.545	0.086	1.190
A3880		NR	0.058	0.341	0.018	0.453	0.023	2.897	0.277	0.305	0.143	2.280

Table 3.3 (cont'd)

Name	ID	z	LX [0.5-8 keV]	e_LX [bol]	LX 10^{44} erg s $^{-1}$	e_LX 10^{44} erg s $^{-1}$	kT	e_kT	Z	e_Z	χ^2	
22286+2036		NR	0.412	10.081	0.348	16.485	0.569	8.249	0.824	0.352	0.116	1.176
22298-2756		NR	0.324	4.070	0.190	5.967	0.279	5.882	0.562	0.397	0.108	1.233
2233-5339		RF	0.480	4.392	0.264	6.750	0.406	6.791	1.168	0.075	0.121	1.089
A2457		NR	0.059	0.550	0.015	0.744	0.021	3.595	0.099	0.326	0.059	1.352
22428+5301		NR	0.192	4.117	0.053	6.747	0.088	7.813	1.165	0.183	0.120	1.048
2243198-093530		NR	0.432	14.006	0.520	21.842	0.811	7.179	0.672	0.267	0.085	1.214
22450+2637		NR	0.304	4.480	0.241	6.835	0.368	6.710	0.933	0.330	0.146	1.224
A3911		RF	0.097	2.198	0.061	3.262	0.090	6.106	0.393	0.285	0.081	1.183
A2485		NR	0.247	2.703	0.119	4.043	0.178	6.250	0.714	0.231	0.129	1.247
AS1063		NR	0.347	22.560	0.412	41.905	0.765	11.302	0.722	0.359	0.070	1.219
A3921		RF	0.093	1.981	0.037	2.916	0.054	5.766	0.762	0.360	0.085	1.879
A2507		NR	0.196	1.003	0.065	1.377	0.089	4.309	0.433	0.426	0.154	1.069
2259-6057		RF	0.750	4.949	0.246	7.715	0.384	7.265	1.064	0.694	0.215	1.200
23028+0843		NR	0.722	1.736	0.111	2.667	0.170	6.818	1.234	0.169	0.180	1.139
A2537		NR	0.295	4.650	0.104	7.083	0.158	6.629	0.625	0.224	0.038	1.157
23115+0338		NR	0.300	7.260	0.281	12.544	0.486	9.518	1.005	0.334	0.103	1.333
A2556		NR	0.087	0.814	0.018	1.105	0.024	3.756	0.398	0.356	0.086	1.157
AS1101		NR	0.058	0.541	0.010	0.726	0.013	2.698	0.286	0.199	0.089	2.076
A2597		NR	0.085	0.878	0.010	1.214	0.015	4.266	0.259	0.279	0.080	1.310
A2626		NR	0.055	0.443	0.012	0.593	0.016	3.263	0.379	0.378	0.131	1.119
A2631		NR	0.273	7.191	0.246	11.658	0.398	8.024	0.961	0.169	0.100	1.254
A4023		RF	0.193	1.996	0.082	2.984	0.123	6.256	0.635	0.268	0.117	1.216
A2645		NR	0.251	3.698	0.171	5.582	0.258	6.470	0.782	0.297	0.119	1.118
23442-0422		NR	0.079	1.473	0.038	2.031	0.052	4.501	0.143	0.406	0.261	1.422
A2657		NR	0.040	0.583	0.016	0.785	0.021	3.567	0.307	0.302	0.165	3.162
A4038		NR	0.028	0.394	0.007	0.525	0.009	2.878	0.263	0.286	0.118	3.540
A2665		NR	0.056	0.489	0.018	0.680	0.025	4.553	0.294	0.310	0.095	1.412
A2667		NR	0.230	7.819	0.208	12.434	0.331	7.604	0.677	0.163	0.084	1.046

Table 3.3 (cont'd)

Name	ID	z	LX	e_LX	LX	e_LX	kT	e_kT	Z	e_Z	χ^2
			[0.5-8 keV]			[bol]					
			10^{44} erg s $^{-1}$		10^{44} erg s $^{-1}$			keV		Z_\odot	d.o.f
A2670	NR	0.076	0.743	0.021	1.019	0.028	4.001	0.706	0.310	0.114	2.206

CHAPTER 4

GLOBAL METALLICITY EVOLUTION OF ACCEPT2.0 CLUSTERS

The first detection of iron in the X-ray spectra of galaxy clusters was evidence that the intracluster medium (ICM) is enriched with heavy elements that have been made by stars in galaxies (Mitchell et al., 1976; Mushotzky et al., 1996; Renzini, 1997). Therefore, we can study the metallicity of the ICM over a wide range of redshifts to understand when enrichment occurs, and if enrichment processes are the same for most clusters. For clusters with high signal-to-noise data, we can map out the Fe/H distribution and figure out where heavy metals have ended up. Consequently, simulations of galaxy clusters began to implement feedback from stellar and AGN sources, together with the enrichment associated with stars, to reproduce the observed chemical properties of the ICM.

Early spatially-resolved observations of the ICM by *ASCA* and *BeppoSAX* showed that certain clusters, now referred to as cool core (CC), exhibit a significant excess in metallicity towards their centers, and a comparatively uniform radial distribution in non-cool core (NCC) clusters (Fabian et al., 1994; Fukazawa et al., 1994; De Grandi & Molendi, 2001). CCs are characterized by a dramatic decrease in gas temperature towards the center in comparison to flatter temperature profiles of NCC clusters. Outside of their core radii, the ICM is similar for both CC and NCC clusters, suggesting that differences in the global abundance is localized to the region surrounding a brightest cluster galaxy (BCG) (De Grandi & Molendi, 2001; De Grandi et al., 2004; Baldi et al., 2012; Ettori et al., 2015; McDonald et al., 2016). Therefore, X-ray cluster astronomers often use measurements excluding the core regions of clusters when studying their global metallicity. Previous works, such as those by Baldi et al. (2012); Ettori et al. (2015), and McDonald et al. (2016), have not shown statistically significant evolution for metallicities measured within a single core-excised (CE) aperture. McDonald et al. (2016) analyzed X-ray data from 153 clusters and found no evidence for metallicity evolution outside the core. Mantz et al. (2017) had the largest data set to date with 245 cluster observations compiled from four separate catalogues.

The analysis reported in this chapter uses a sample of global CE metallicities for 302 clusters

from ACCEPT2.0 (Chapter 2) to assess the abundance evolution of the ICM. In Section 4.1, we give an overview of the clusters used in this analysis. Section 4.2 goes over the methods. Section 4.3 details the dependence of our sample of global CE abundance on a cluster’s CC status (Section 4.3.1), luminosity (Section 4.3.2, and redshift (Section 4.3.3). Section 4.3.4 fits the data to a linear model with dependence on luminosity and redshift. Then we apply the methods to more targeted samples in section 4.3.5.

4.1 The Sample

For this analysis, we selected 302 clusters from ACCEPT2.0 (introduced in Chapter 2) with $\text{SNR} > 15$ and bolometric $L_X \gtrsim 4 \times 10^{43} \text{ erg s}^{-1}$. We did not include low luminosity systems because their X-ray observables differ from those of clusters due to their shallower gravitational potential wells and because, for the coolest systems, the metallicity and the electron density (the parameter that affects the normalization of the X-ray spectrum) become increasingly difficult to disentangle.

Because the difference in observations of the global metallicity content of the ICM can be biased depending on the choice of aperture (Mushotzky & Loewenstein, 1997; Balestra et al., 2006; Maughan et al., 2008; Leccardi & Molendi, 2008; Anderson et al., 2009), we use the CE global X-ray properties (within the aperture [0.3-1] R_{2500}) from ACCEPT2.0 so we may treat CCs and NCCs in the same manner. Additionally, CE flux can be underestimated for nearby objects that are larger than the *Chandra* field of view. We found that systems above this threshold were massive and distant enough where most of their CE apertures fit within the ACIS CCDs.

There are 16 clusters with global CE abundance measurements consistent with zero metallicity within the 1σ ¹ uncertainties, although we find no significant difference in our results when these clusters are excluded. These 16 clusters are plotted according to their 3σ (99.7%) upper limits. The X-ray properties for 302 ACCEPT2.0 clusters used in this chapter are provided in table 4.6. As described in Chapter 2, the source models used for spectral analysis is a *mekal* model (Kaastra et al., 1996; Liedahl et al., 1995) where ratio of elements is fixed to the Solar value as in Anders &

¹The measured data point is smaller than the error.

Grevesse (1989b).

4.2 Methods

The methods described here were used to test the global abundance dependencies on core status, luminosity, and redshift. To summarize, we separated the data according to central entropy, K_0 , CE luminosity, L_X , or cluster redshift, z . We then compared the medians of these sub samples, all of which are provided in Table 4.1. We chose to use the median global abundance so as to minimize contribution from outliers. The errors on the medians are $\sigma = \sigma_{\text{std}}/\sqrt{N}$, with σ_{std} as the weighted standard deviation defined as,

$$\sigma_{\text{std}} = \sqrt{\frac{\sum w_i (X_i - \bar{X}_w)^2}{\sum w_i}}, \quad (4.1)$$

where the weight on each radial data point is $w_i = 1/\sigma_i^2$. We found that, when the sample is divided according to luminosity and redshift, difference in the median global CE metallicities, $\Delta\tilde{Z}$, warrant further investigation at $\sim 3\sigma$.

We test the significance of $\Delta\tilde{Z}$ by simulating clusters based on a null-hypothesis model which assumes a constant metallicity with intrinsic scatter. The simulated points have the same uncertainties as the observed data, but each simulated value was drawn from two Gaussian distributions. The first draw was centered on the sample mean (\bar{Z}) with an intrinsic dispersion (σ_{int}). This first draw is used as a mean for the second Gaussian which has width determined by the uncertainty of the simulated observation.

Each simulated sample was divided at the median redshift or luminosity and compared statistically in the same manner as the real data. We compared the halves of every new simulated sample to the preceding samples to generate a probability distribution of observed differences between them. The simulated clusters are modeled under the null assumption that the global CE metallicities have no dependence on luminosity or redshift. The only source of variation in the measured global abundance is therefore assumed to be due to statistical measurement errors and intrinsic scatter σ_{int} . We therefore approximate the values of \bar{Z} and σ_{int} via likelihood maximization. The

log-likelihood function for data with intrinsic scatter is,

$$\ln \mathcal{L} = -\frac{1}{2} \sum_i \left[\frac{(Z_i - \bar{Z})^2}{\sigma_{\text{int}}^2 + \sigma_{Z,i}^2} + \ln(2\pi(\sigma_{\text{int}}^2 + \sigma_{Z,i}^2)) \right], \quad (4.2)$$

where Z_i is the global CE metallicity for a cluster and $\sigma_{Z,i}$ is the corresponding measurement error.

We perform the fit using the package emcee (Foreman-Mackey et al., 2013), which is based on algorithms described by Goodman & Weare (2010). The bounds for the parameters were $0 \leq \bar{Z} \leq 2$ for abundance, and $-5 \leq \ln \sigma_{\text{int}} \leq 1$ for intrinsic scatter. We run the sampler over 10^5 steps, with the first 10^4 steps being burn-ins. The output chain results in the best-fit parameters $\bar{Z} = 0.260^{+0.007}_{-0.006} Z_\odot$ and $\sigma_{\text{int}} = 0.068^{+0.006}_{-0.006}$, where the values and uncertainties are based on the 50th, 16th and 84th percentiles of the output chain. The results of the fit can be seen in figure 4.1. These parameters are used to define a consistent null hypothesis model where no trend in either luminosity or redshift exists. That model then is used to simulate data with the underlying constant metallicity \bar{Z} and variation from adding randomly selected points from normal distributions with mean zero and widths corresponding to σ_{int} and the original data error. The result is a simulated sample with constant metallicity and variation solely due to underlying intrinsic scatter and errors on our data.

4.3 Results

4.3.1 Dependence on core status

We aim to determine whether the global abundances of clusters have changed significantly since redshift $z \sim 1$. As alluded to in Section 1.4, answering this question requires a general view of each cluster without bias from the inner regions of cool cores. We therefore use the temperature and abundance measurements excluding the region $r < 0.3 R_{2500}$. The difference between CC clusters versus NCC clusters is evidenced by their radial abundance profiles in Figures 4.3 and 4.4. These figures show the median spatial distribution of metals for CC and NCC clusters, where each radial bin contains 100 data points, with the exception of the outermost bins, which contain 56 and 65 points for CC and NCC clusters, respectively. It should be noted, however, that the extent of the data inside $0.3 R_{2500}$ differs between CCs and NCCs because Z is an emission-weighted measurement.

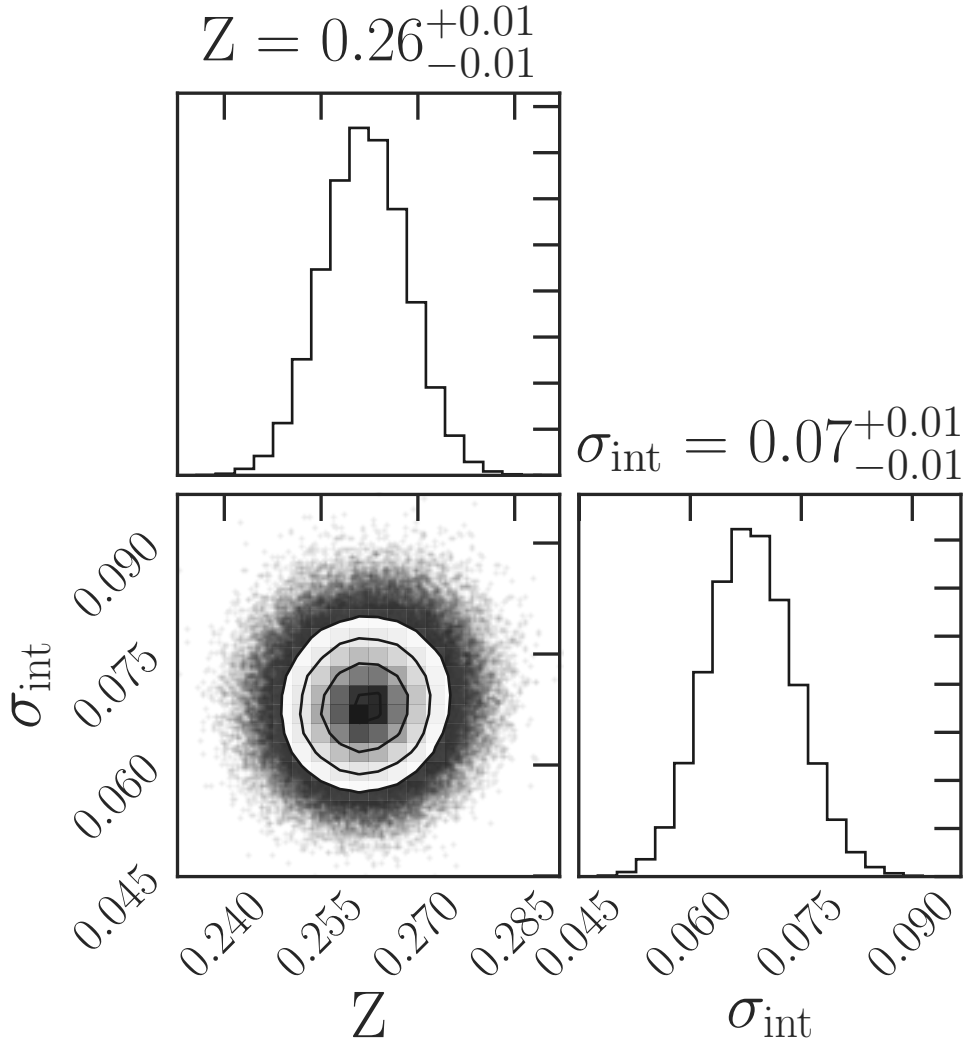


Figure 4.1: **Global Z null model MCMC results.** Resulting constant metallicity, \bar{Z} , and intrinsic scatter, σ_{int} , from the MCMC .

The less dense environment in the cores of NCC clusters does not allow for as many radial bins to meet the count threshold required for spectral extraction. The error bars are centered on the median metallicity, \tilde{Z} , with sizes corresponding to the mean error, $\sigma = (\sum w_i)^{-1/2}$. The shaded region of Figure 4.3 represents the standard deviations, σ_{int} , of each bin. The sizes of these shaded regions in comparison to the error bars is an indication that $\sigma_{\text{int}} \gg \sigma_w$. This profile shows that while radial abundances can vary from cluster to cluster, the profiles as a whole follow a general trend, depending on their central entropy. The binned radial profiles are stacked in Figure 4.4 to better show the contrast in spatial distribution of metals between CC and NCCs.

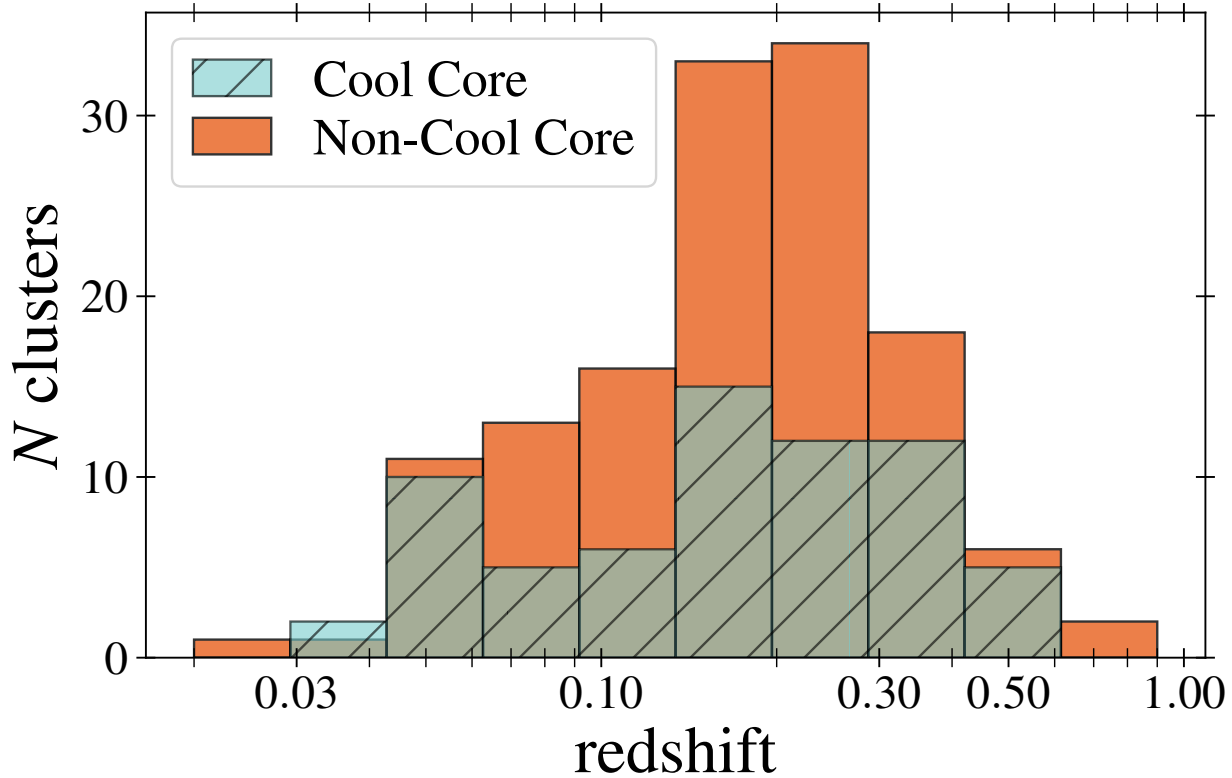


Figure 4.2: **Redshift distribution of CC and NCC clusters in ACCEPT2.0.** Redshift distribution for 66 CC clusters (*hatch blue*) and 132 NCC clusters (*red*).

The median global CE metallicity for 66 CCs is $\tilde{Z}=0.290\pm0.012Z_{\odot}$, and $\tilde{Z}=0.265\pm0.009Z_{\odot}$ for the 132 NCCs. The low significance of their difference, $\Delta\tilde{Z} = 0.025 \pm 0.015$, is consistent with recent works, which found that the state of the ICM at outer radii is virtually independent of core status (Neumann, 2005; Leccardi & Molendi, 2008; Eckert et al., 2011) and provides reassurance that the $0.3 < r < 1 R_{2500}$ aperture adequately excised the core. These results are summarized in Table 4.1.

4.3.2 Luminosity dependence

ACCEPT2.0 contains clusters for which there were enough data to obtain a temperature estimate and radial profiles of the X-ray properties, which means that our sample lacks data from low-luminosity clusters at higher redshifts. If there is some correlation between luminosity and global abundance it would be present in the relation between redshift and abundance. We therefore need to check

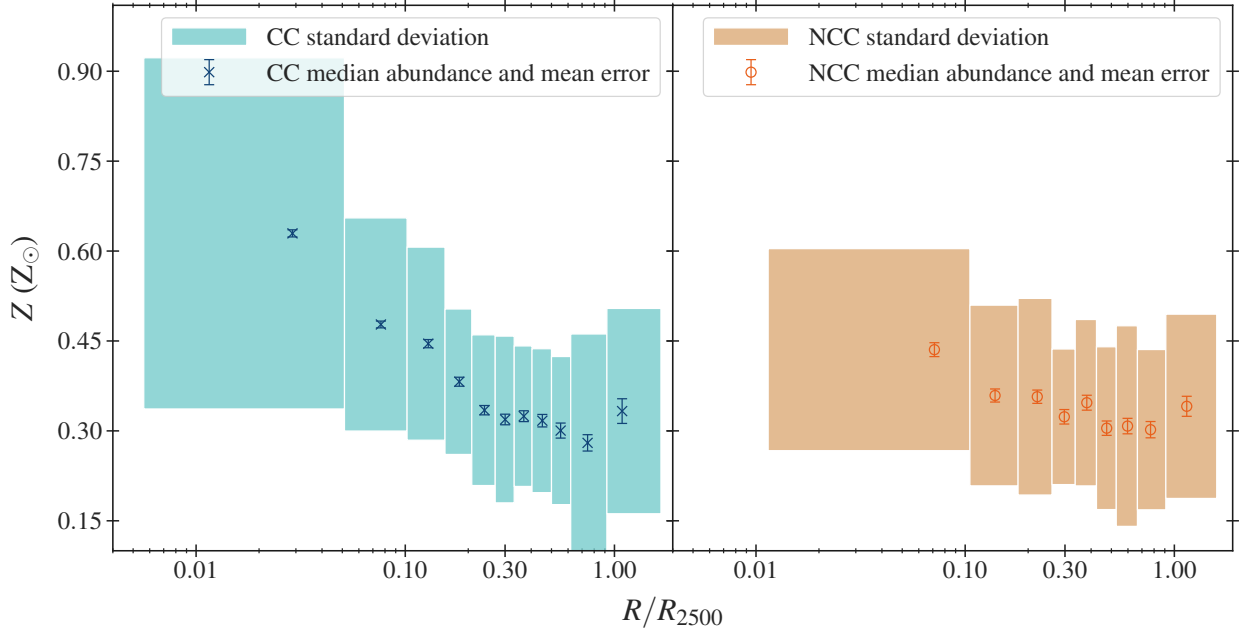


Figure 4.3: **Binned weighted mean metallicity profiles for CCs and NCCs.** Binned weighted means for projected metallicity profiles for CC (*left*) and NCC (*right*) clusters. The innermost radial bin for the NCC clusters is larger because NCCs tend to have lower X-ray central surface brightness, and therefore fewer independent, spatially-resolved X-ray spectra for their cores.

that metallicity is independent of luminosity.

After dividing the full sample at the median bolometric luminosity $L_X \simeq 5.4 \times 10^{44}$ erg s $^{-1}$, the difference in median abundance between low- and high-luminosity clusters is $\Delta\tilde{Z} = 0.033 \pm 0.011$ Z_\odot . This difference is significant at slightly less than 3σ (Figure 4.5, left) using only the standard deviation as an estimator of 1σ . After simulating the null model, we found 68% of the simulations had differences within the range (-0.017,+0.018), and a 3σ upper limit of 0.052, which exceeds the observed difference. With a significance less than 3σ , we conclude that any dependence of global abundance on luminosity here is weak at best.

4.3.3 Redshift Dependence

The difference in the median global CE metallicity for the low- z vs. high- z sub samples is $\Delta\tilde{Z} = 0.035 \pm 0.012$ Z_\odot (Table 4.1). After comparing 10,000 \tilde{Z} pairs based on 100 simulated sets of data, we found that 68% of the simulated null models were in the range (-0.018,+0.019) (Figure

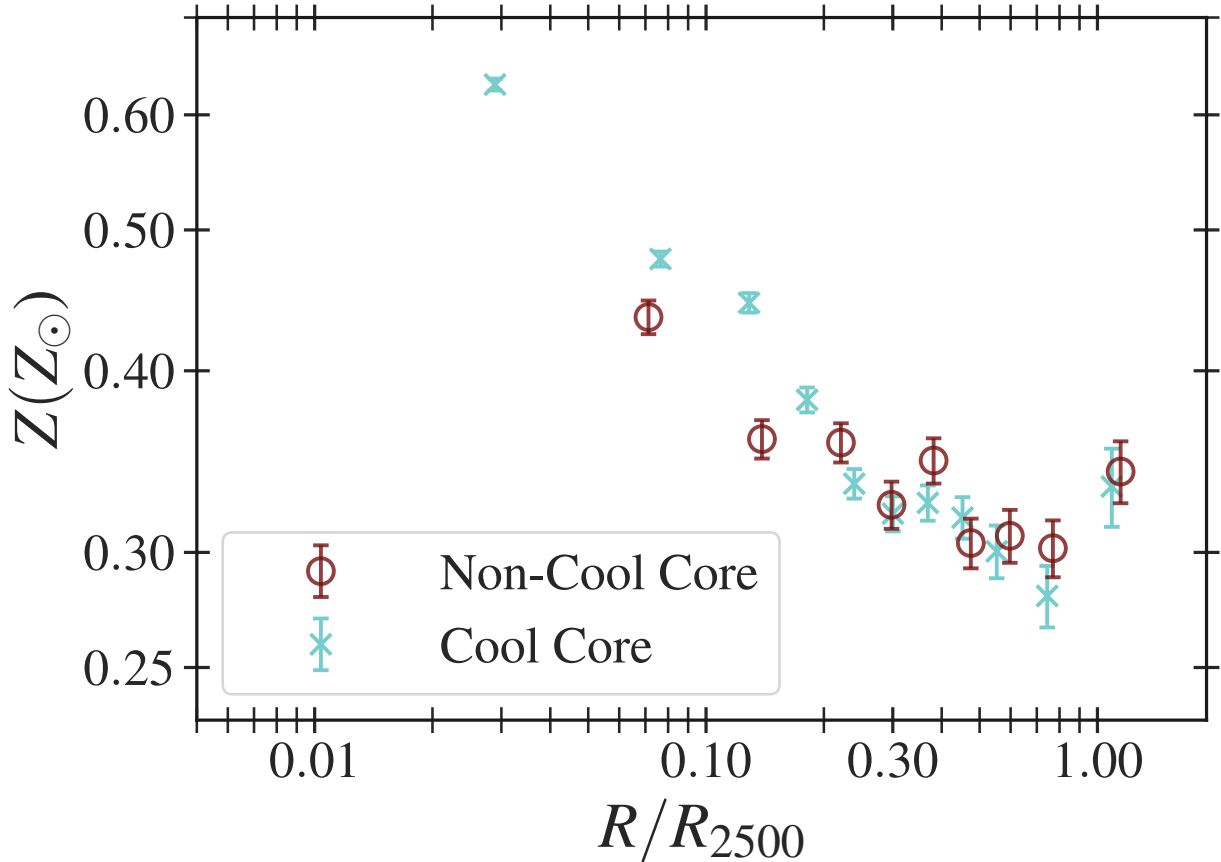


Figure 4.4: **Stacked weighted median metallicity profiles for CC and NCC clusters.** Binned weighted median for projected metallicity profiles for CC (*closed circles*) and NCC (*open diamonds*) clusters.

4.5), with a 3σ upper limit of 0.047. Because the observed difference is below 3σ , we conclude that any dependence on redshift is weak, although it does not appear to be as weak as the dependence on luminosity.

4.3.4 Multiple Linear Regression Analysis

We investigated this further by fitting the data to the functional form,

$$\ln Z(L_X, z) = \ln Z_0 + \alpha \ln \frac{L_X}{L_{\text{piv}}} + \beta \ln z. \quad (4.3)$$

By allowing the function to vary with luminosity and redshift simultaneously, we are able to gauge which dependence is stronger. For the full sample, the model dependence on L_X is $\alpha =$

Table 4.1: **Median global CE abundances of ACCEPT2.0 sub samples.** Median core-excised (CE) global abundances for sub populations of ACCEPT2.0 clusters. Col(1) is the name of the sub sample, col(2) is the value of the parameter used to separate the data, col (3) is the size of the sub sample, cols(4,5) is the median and mean error of the sub sample, and cols(6,7) is the difference between the median abundances and error. Cols(8,9) show the 1σ lower and upper bounds for the simulated differences.

Sub sample	Split Value	N	$\tilde{Z}[Z_\odot]$	$\sigma_{\text{std}}/\sqrt{N}$	$\Delta\tilde{Z}[Z_\odot]$	$\sigma_{\Delta\tilde{Z}}$	68% $\Delta\tilde{Z}^{\text{sim}}$	99.7% $\Delta\tilde{Z}^{\text{sim}}$
Cool Core	30 keV cm ²	66	0.290	0.011		0.024	0.013	...
Non-Cool Core		132	0.266	0.008				
Lo L_X	5.4×10^{44}	151	0.289	0.105		0.033	0.011 (-0.017,+0.018)	0.052
Hi L_X		151	0.256	0.096				
Lo z	0.21	152	0.286	0.104		0.035	0.012 (-0.018,+0.019)	0.047
Hi z		150	0.251	0.098				

Table 4.2: **Best fit parameters to the $Z(L_X, z)$ model.** Output parameters for the linear fit of the full sample to Equation 4.3. When metallicity is fit to both luminosity and redshift simultaneously, there is a greater dependence on L_X than z , but neither are statistically significant.

Z_0 [Z_\odot]	α	β	σ_{int}
$0.290^{+0.025}_{-0.023}$	$-0.047^{+0.030}_{-0.030}$	$-0.015^{+0.047}_{-0.047}$	$0.164^{+0.021}_{-0.019}$

-0.047 ± 0.029 , and on redshift is $\beta = -0.014 \pm 0.046$. Although the best fit model shows a slightly stronger reliance on the luminosity component, neither α nor β are significant. The results are summarized in Table 4.2.

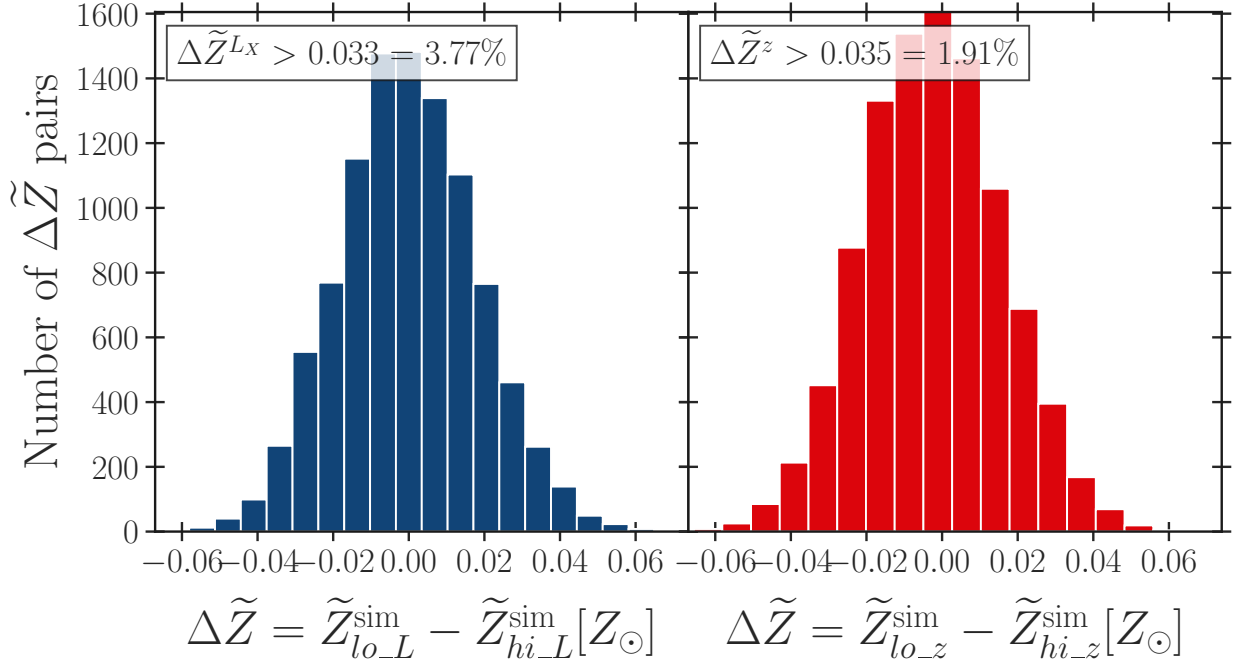


Figure 4.5: **Metallicity differences between simulated clusters.** Distribution of differences between pairs of simulated data based on the null model. Sub sample pairs were separated by either luminosity (*left*) or redshift (*right*).

4.3.5 Comparison to Maughan et al. (2008)

We compared the results of our above analysis to those by M08, which used 115 clusters observed with *Chandra* and uniformly reduced for two apertures ([0-1] R_{500} and [0.15-1] R_{500}). Their model for constant metallicity was rejected at 99.9% for the core-included (CI) aperture, but this significance was not present when the CE values were used, in agreement with the results of Section 4.3.1. We found 64 clusters in our sample that we share with M08, so we were able to redo the M08 analysis using their metallicities and compare them to what we get using our own. We found that temperatures from M08 are on average lower than ours in ACCEPT2.0, with increasing disparity at higher ACCEPT2.0 temperatures. The higher temperatures in ACCEPT2.0 result in slightly lower abundances than M08 (Figure 4.7). Private communication from Maughan revealed that he finds his temperatures from Maughan et al. (2012) and presumably M08 may be overestimated by a factor of about 15% owing to difference in the statistical treatments and the energy binning scheme used. This 15% correction appears as the dashed line in Figure 4.7.

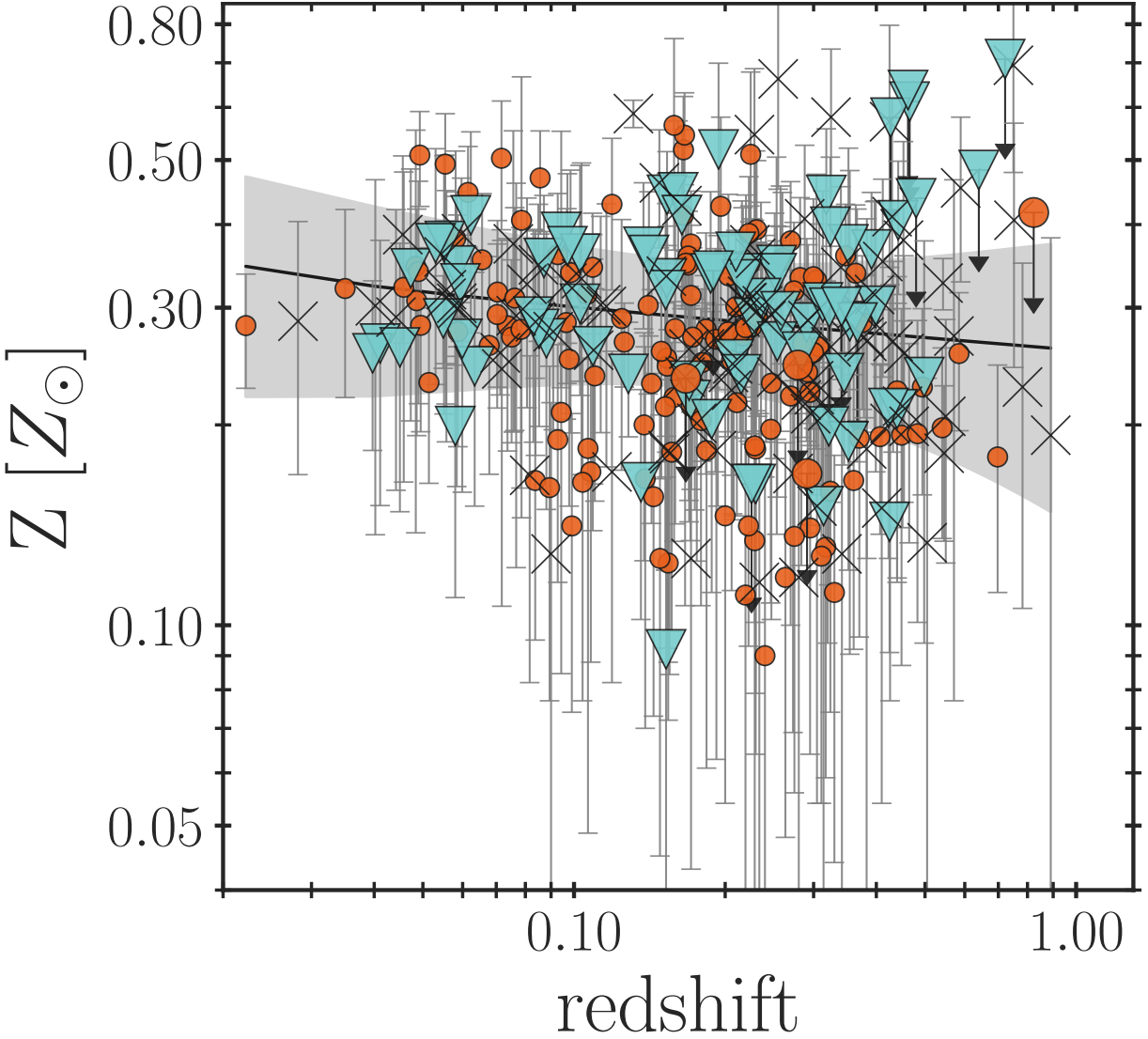


Figure 4.6: **Best fit results global CE abundance as a function of L_X and Z .** Results of the fit to the model. When ICM metallicity is allowed to vary as a function of luminosity and redshift, dependence on luminosity is stronger than the dependence on metallicity, but neither dependence is statistically significant.

Table 4.5 shows the ACCEPT2.0 cluster temperatures in comparison to M08, and Table 4.4 shows the comparison between our luminosities and metallicities. We divided the overlapping M08 and ACCEPT2.0 clusters by luminosity and redshift, and found the difference in median metallicities for both subsets to be higher for the M08 clusters. When split by luminosity, the ACCEPT2.0 clusters have $\Delta \tilde{Z} = 0.015 \pm 0.021 Z_{\odot}$, and the M08 clusters show $\Delta \tilde{Z} = 0.075 \pm 0.026 Z_{\odot}$. When split by redshift, ACCEPT2.0 clusters have $\Delta \tilde{Z} = 0.045 \pm 0.020 Z_{\odot}$ and M08 clusters have

$\Delta \tilde{Z} = 0.065 \pm 0.027 Z_{\odot}$. When we simulate the clusters with no dependence on luminosity or redshift, the samples do still show the same lack of discernible dependence on luminosity and redshift.

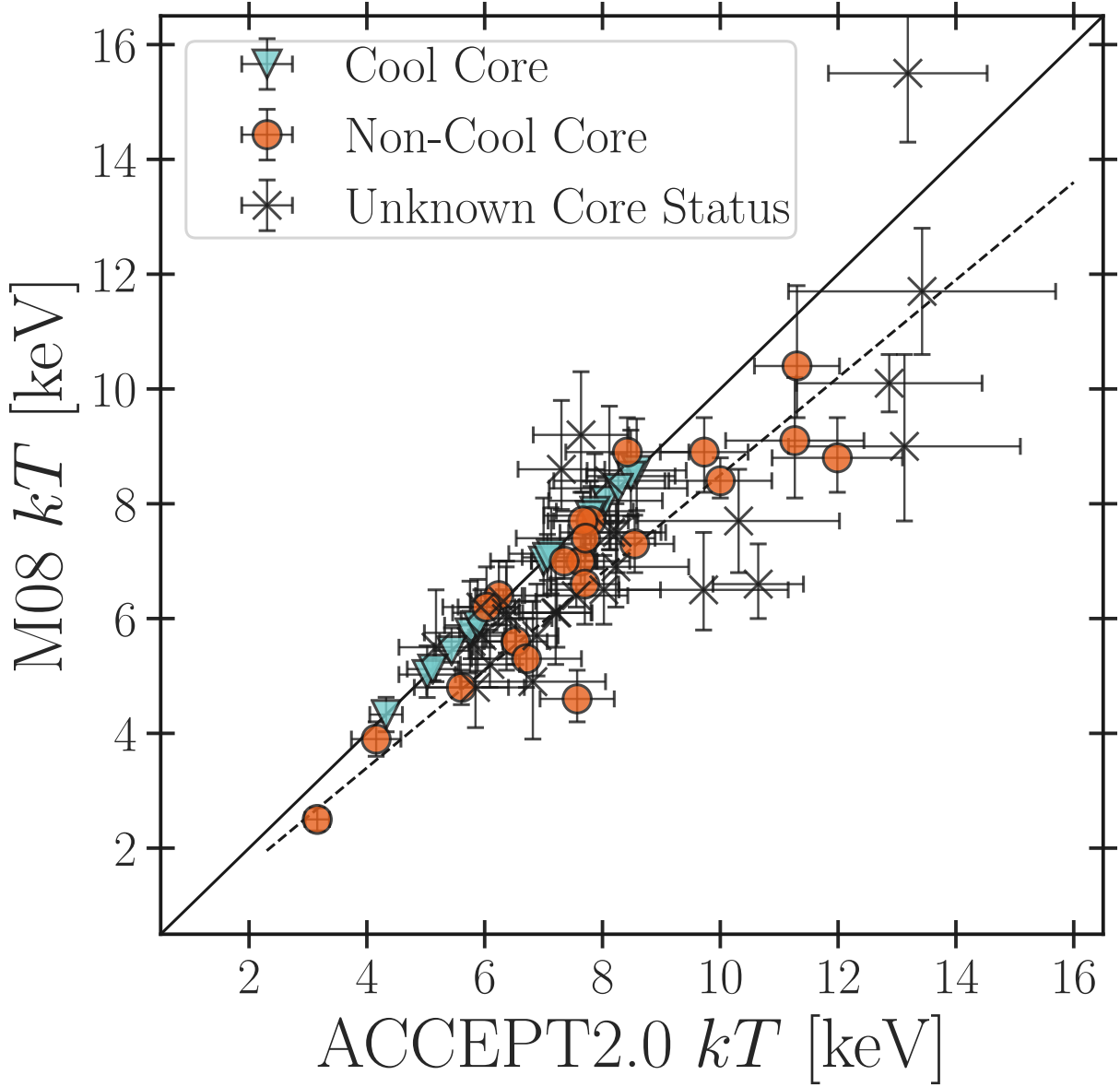


Figure 4.7: **Temperatures from M08 vs. ACCEP2.0.** Comparison of ACCEP2.0 global CE temperatures to those of M08. The solid line represents the 1:1 ratio and the dashed line shows the approximate relation between ACCEP2.0 clusters and M08 clusters that have been reduced by 15%.

Table 4.3: **Median CE global abundances comparison for ACCEPT2.0 and M08 overlap.** Median CE global abundance for the subsets of ACCEPT2.0 (*top half*) and M08 (*bottom half*) clusters that overlap with M08. Columns are the same as in Table 4.1.

Sample	Split Value	$N_{clusters}$	$\bar{Z}[Z_\odot]$	$\sigma_{\text{std}}/\sqrt{N}$	$\Delta\bar{Z}[Z_\odot]$	$\sigma_{\Delta\bar{Z}}$	68% $\Delta\bar{Z}^{\text{sim}}$	$N^{\text{sim}} \geq \Delta\bar{Z}$
ACCEPT2.0 Clusters								
Lo L_X	$8.176 \times 10^{44} \text{ erg s}^{-1}$	32	0.260	0.097	0.015	0.021	(-0.032,0.031)	6325
Hi L_X		32	0.275	0.071				
M08 Clusters								
Lo L_X	$9.250 \times 10^{44} \text{ erg s}^{-1}$	32	0.325	0.104	0.075	0.026	(-0.038,0.036)	333
Hi L_X		32	0.400	0.102				
Lo z	0.265	32	0.279	0.081	0.045	0.020	(-0.030,0.031)	1522
Hi z		32	0.234	0.082				

Table 4.4: **Global CE luminosities and metallicities M08 and ACCEPT2.0 overlap.** Luminosities and metallicities for clusters in ACCEPT2.0 clusters that overlap with M08. ACCEPT2.0 observables are from the [0.3-1] R_{2500} aperture. Column(1) is the ACCEPT2.0 name, column(2) is the ACCEPT2.0 redshift, columns(3,4) are bolometric luminosities and error, columns(5,6) are abundances in solar units. Column(7) is the redshift used by M08. Columns(8,9) are M08 bolometric luminosities, and columns(10-12) are the metallicities measured by M08, where the last two columns are the positive and negative uncertainties on the abundance.

ACCEPT2.0 Name	redshift	L_X	e_{L_X}	Z	e_Z	M08 redshift	L_X	e_{L_X}	Z	E_Z	e_Z
		$10^{44} \text{ erg s}^{-1}$		Z_\odot			$10^{44} \text{ erg s}^{-1}$		Z_\odot		
A0068	0.255	10.429	0.489	0.662	0.210	0.255	9.300	0.500	0.460	0.220	0.210
A0209	0.206	10.466	0.266	0.250	0.082	0.206	12.200	0.300	0.290	0.100	0.090
A0267	0.231	6.600	0.166	0.393	0.106	0.230	7.000	0.500	0.640	0.270	0.240
A0383	0.187	2.881	0.092	0.338	0.110	0.187	3.600	0.100	0.350	0.120	0.110
A0402	0.322	7.293	0.311	0.045	0.085	0.322	8.100	0.300	0.170	0.170	0.170
A0586	0.171	4.977	0.139	0.374	0.075	0.171	6.500	0.300	0.840	0.230	0.210
A0665	0.182	7.910	0.096	0.260	0.075	0.182	15.200	0.200	0.340	0.060	0.050

Table 4.4 (cont'd)

ACCEPT2.0 Name	redshift	L_X 10^{44} erg s $^{-1}$	e_ L_X	Z	e_Z	M08 redshift	L_X 10^{44} erg s $^{-1}$	e_ L_X	Z	E_Z	e_Z
										Z_\odot	Z_\odot
A0697	0.282	23.094	0.555	0.333	0.106	0.282	24.400	0.500	0.470	0.100	0.100
A0773	0.217	9.528	0.214	0.272	0.081	0.217	10.900	0.300	0.570	0.090	0.080
A0907	0.153	4.152	0.083	0.335	0.142	0.153	4.800	0.100	0.360	0.050	0.050
A1204	0.171	2.253	0.092	0.218	0.084	0.171	2.700	0.100	0.130	0.100	0.100
A1240	0.159	0.675	0.044	0.279	0.137	0.159	1.600	0.100	0.180	0.110	0.100
A1300	0.307	17.836	0.446	0.262	0.099	0.307	20.900	0.600	0.410	0.150	0.150
A1413	0.143	6.581	0.070	0.231	0.089	0.143	7.400	0.100	0.340	0.050	0.050
A1682	0.234	5.803	0.164	0.116	0.092	0.234	7.500	0.500	0.330	0.340	0.300
A1689	0.183	15.062	0.181	0.279	0.110	0.183	14.300	0.200	0.400	0.070	0.070
A1763	0.223	11.013	0.286	0.388	0.084	0.223	13.700	0.300	0.260	0.090	0.090
A1914	0.171	15.799	0.246	0.213	0.053	0.171	12.400	0.200	0.280	0.090	0.090
A2034	0.113	4.685	0.049	0.303	0.108	0.113	6.200	0.100	0.360	0.050	0.050
A2069	0.116	2.675	0.048	0.301	0.128	0.116	5.100	0.100	0.260	0.060	0.050
A2111	0.229	5.996	0.129	0.186	0.085	0.229	7.700	0.300	0.200	0.190	0.180
A2125	0.246	0.850	0.042	0.197	0.089	0.246	1.500	0.100	0.200	0.080	0.070
A2163	0.203	42.292	0.288	0.240	0.045	0.203	54.100	1.200	0.480	0.130	0.130
A2204	0.152	10.792	0.077	0.319	0.143	0.152	12.300	0.300	0.320	0.120	0.110
A2218	0.176	6.482	0.127	0.201	0.076	0.176	8.300	0.100	0.350	0.060	0.060
A2259	0.164	4.806	0.176	0.427	0.128	0.164	5.200	0.200	0.410	0.170	0.160
A2261	0.224	11.669	0.253	0.349	0.077	0.224	13.500	0.200	0.330	0.080	0.080
A2294	0.169	7.178	0.266	0.260	0.106	0.178	8.700	0.300	0.230	0.190	0.180
A2409	0.148	6.289	0.197	0.462	0.093	0.148	6.300	0.200	0.320	0.120	0.110
A2631	0.273	11.658	0.398	0.169	0.100	0.273	13.500	0.500	0.430	0.160	0.150
AS1063	0.347	41.905	0.765	0.359	0.070	0.252	16.400	0.400	0.130	0.130	0.130
10236+04111	0.291	14.162	0.213	0.285	0.096	0.291	15.600	0.300	0.220	0.080	0.080
11375+6625	0.782	7.728	0.495	0.228	0.122	0.782	7.100	0.400	0.200	0.220	0.200
Cl0016+16	0.541	28.163	0.619	0.198	0.063	0.541	34.500	0.600	0.240	0.070	0.070
0947124+762313	0.354	12.772	0.291	0.286	0.196	0.354	11.700	0.600	0.540	0.230	0.210
21594948+2407846	0.543	9.624	0.185	0.327	0.029	0.543	11.300	0.700	0.430	0.230	0.210

Table 4.4 (cont'd)

ACCEPT2.0 Name	redshift	L_X 10^{44} erg s $^{-1}$	e_ L_X Z	e_Z	M08 redshift	L_X 10^{44} erg s $^{-1}$	e_ L_X Z	E_Z	e_Z		
Z_\odot	Z_\odot										
LCDCS0829	0.451	41.656	0.503	0.213	0.073	0.451	38.300	0.800	0.480	0.100	0.100
02426-2132	0.314	7.085	0.436	0.151	0.115	0.314	7.900	0.400	0.080	0.180	0.080
04296-0253	0.399	8.315	0.393	0.302	0.132	0.399	9.200	0.400	0.390	0.180	0.180
04519+0006	0.430	8.608	0.533	0.411	0.206	0.430	10.900	0.800	0.440	0.320	0.280
0717+3745	0.546	51.818	0.734	0.181	0.048	0.546	57.100	0.800	0.320	0.060	0.060
07449+3927	0.698	21.465	0.924	0.179	0.067	0.697	26.300	1.000	0.310	0.090	0.090
09498+1708	0.383	16.267	0.681	0.184	0.151	0.384	17.200	0.600	0.270	0.150	0.150
13110-0311	0.494	6.435	0.280	0.228	0.071	0.494	6.700	0.200	0.270	0.140	0.140
15328+3021	0.345	10.388	0.177	0.239	0.065	0.345	12.300	0.600	0.420	0.190	0.180
16213+3810	0.465	7.763	0.291	0.199	0.066	0.463	8.700	0.500	0.260	0.120	0.120
17202+3536	0.391	10.872	0.331	0.367	0.080	0.387	11.200	0.500	0.440	0.200	0.180
19318-2635	0.352	14.152	0.168	0.374	0.147	0.352	15.300	0.500	0.110	0.100	0.100
2129-0741	0.589	19.708	1.086	0.454	0.126	0.594	21.000	1.000	0.400	0.220	0.210
22298-2756	0.324	5.967	0.279	0.397	0.108	0.324	6.900	0.300	0.250	0.180	0.170
22450+2637	0.304	6.835	0.368	0.330	0.146	0.301	6.900	0.400	0.620	0.230	0.210
04390+0520	0.208	2.670	0.145	0.251	0.107	0.208	3.000	0.300	0.350	0.260	0.220
04390+0715	0.230	8.038	0.252	0.293	0.083	0.230	8.700	0.200	0.280	0.110	0.100
04541-0300	0.550	28.925	0.536	0.206	0.082	0.550	28.800	1.200	0.330	0.160	0.150
16235+2634	0.426	5.798	0.342	0.201	0.124	0.426	7.800	0.400	0.540	0.200	0.190
22286+2036	0.412	16.485	0.569	0.352	0.116	0.412	20.800	0.600	0.410	0.130	0.130
145715+222009	0.258	5.650	0.115	0.296	0.101	0.258	6.300	0.100	0.400	0.060	0.060
021701+6412	0.453	3.720	0.188	0.379	0.154	0.453	5.300	0.300	0.540	0.260	0.230
43072	0.164	6.753	0.116	0.413	0.059	0.164	7.800	0.200	0.450	0.070	0.070
+1373+110+018	0.180	3.869	0.112	0.248	0.072	0.180	4.700	0.100	0.220	0.090	0.090
0232-4421	0.284	13.995	0.485	0.218	0.095	0.284	17.600	0.500	0.410	0.160	0.160
12269+3332	0.890	22.466	1.035	0.193	0.189	0.890	21.700	1.100	0.520	0.220	0.220
23028+0843	0.722	2.667	0.170	0.169	0.180	0.722	3.300	0.300	0.040	0.230	0.040
1504075-024816	0.215	16.069	0.219	0.238	0.070	0.215	14.300	0.400	0.350	0.140	0.130

Table 4.5: Global CE temperatures M08 and ACCEPT2.0 overlap. Temperatures for clusters in ACCEPT2.0 clusters that overlap with M08. ACCEPT2.0 observables are from the [0.3-1] R_{2500} aperture. Column(1) is the ACCEPT2.0 name, columns(2,3) are the core-excised temperatures. Column(4) is the truncated cluster name from M08, and columns(5-7) are the temperatures from M08, where column(6) is the positive uncertainty and column(7) is the negative uncertainty.

A2 Name	kT	e_kT	M08 Name	kT	E_	kT
				keV	kT	keV
A0068	9.717	1.436	A68	6.500	1.000	0.700
A0209	8.547	0.665	A209	7.300	0.500	0.500
A0267	7.570	0.630	A267	4.600	0.500	0.400
A0383	5.438	0.297	A383	4.200	0.400	0.200
A0402	8.228	1.236	MACS J0257.6-2209	6.900	1.100	0.700
A0586	6.241	0.395	A586	6.400	0.600	0.500
A0665	8.136	0.857	A665	7.500	0.300	0.300
A0697	11.987	1.107	A697	8.800	0.700	0.600
A0773	7.630	0.833	A773	7.000	0.400	0.400
A0907	5.772	0.537	A907	5.600	0.300	0.300
A1204	4.327	0.277	A1204	3.800	0.300	0.300
A1240	4.158	0.420	A1240	3.900	0.300	0.300
A1300	11.265	1.174	MACS J1131.8-1955	9.100	1.100	1.000
A1413	7.350	0.558	A1413	7.000	0.300	0.300
A1682	7.205	0.618	A1682	6.100	1.100	0.900
A1689	10.000	0.874	A1689	8.400	0.400	0.300
A1763	7.669	0.593	A1763	7.700	0.500	0.500
A1914	8.422	1.044	A1914	8.900	0.600	0.600
A2034	7.555	0.875	A2034	6.400	0.200	0.200
A2069	5.936	0.646	A2069	6.200	0.300	0.300
A2111	7.700	0.575	A2111	6.600	0.900	0.700
A2125	3.158	0.206	A2125	2.500	0.200	0.200
A2163	13.183	1.347	A2163	15.500	1.200	1.200
A2204	8.269	1.172	A2204	7.400	0.600	0.600
A2218	6.318	0.550	A2218	6.300	0.200	0.200
A2259	6.089	0.502	A2259	5.200	0.600	0.400

Table 4.5 (cont'd)

A2 Name	<i>kT</i>	e_< <i>kT</i> >	M08 Name	<i>kT</i>	E_< <i>kT</i> >	
					keV	keV
A2261	7.714	1.178	A2261	7.400	0.400	0.400
A2294	7.303	0.736	A2294	8.600	1.200	0.700
A2409	5.955	0.382	A2409	5.700	0.400	0.400
A2631	8.024	0.961	A2631	6.500	0.600	0.600
AS1063	11.302	0.722	AS 1063	10.400	1.400	0.900
10236+04111	8.052	0.966	Zw 3146	8.200	0.400	0.400
11375+6625	5.174	0.629	MS 1137.5+6625	5.500	1.000	0.600
Cl0016+16	9.727	0.745	MS 0015.9+1609	8.900	0.600	0.700
0947124+762313	8.581	0.841	RBS797	6.300	0.900	0.700
21594948+2407846	6.887	0.360	MACS J1423.8+2404	5.700	0.900	0.700
LCDCS0829	13.426	2.267	RX J1347.5-1145	11.700	1.100	1.100
02426-2132	5.751	0.774	MACS J0242.5-2132	5.900	0.900	0.700
04296-0253	7.000	0.900	MACS J0429.6-0253	6.800	1.100	0.600
04519+0006	5.844	0.829	MACS J0451.9+0006	4.800	1.000	0.700
0717+3745	12.868	1.576	MACS J0717.5+3745	10.100	0.500	0.500
07449+3927	7.805	0.634	MACS J0744.9+3927	7.700	0.600	0.600
09498+1708	10.311	1.712	MACS J0949.8+1708	7.700	0.900	0.900
13110-0311	6.031	0.482	MACS J1311.0-0310	6.200	0.700	0.700
15328+3021	7.129	0.720	RX J1532.9+3021	6.100	0.800	0.700
16213+3810	7.226	0.580	MACS J1621.3+3810	6.100	0.600	0.600
17202+3536	7.870	0.653	MACS J1720.2+3536	7.800	1.000	1.000
19318-2635	7.793	0.786	MACS J1931.8-2634	5.800	0.600	0.500
2129-0741	8.117	0.943	MACS J2129.4-0741	8.400	1.300	1.200
22298-2756	5.882	0.562	MACS J2229.7-2755	5.900	0.800	0.800
22450+2637	6.710	0.933	MACS J2245.0+2637	5.300	0.700	0.500
04390+0520	5.024	0.480	RX J0439+0520	3.800	0.500	0.400
04390+0715	6.528	0.534	RX J0439.0+0715	5.600	0.400	0.400
04541-0300	10.644	0.768	MS 0451.6-0305	6.600	0.700	0.600
16235+2634	6.365	0.908	MS 1621.5+2640	6.100	0.800	0.700

Table 4.5 (cont'd)

A2 Name	kT	e_{kT}	M08 Name	kT	E_{kT}	
					keV	keV
22286+2036	8.249	0.824	MACS J2228.5+2036	7.500	0.800	0.700
145715+222009	5.120	0.434	MS 1455.0+2232	4.700	0.200	0.200
021701+6412	6.371	0.771	RX J1701+6414	6.000	1.000	0.900
43072	7.066	0.427	RX J1720.1+2638	7.200	0.400	0.400
+1373+110+018	5.605	0.799	MS 0906.5+1110	4.800	0.300	0.300
0232-4421	7.636	0.811	RX J0232.2-4420	9.200	1.100	1.000
12269+3332	13.126	1.968	CL J1226.9+3332	9.000	1.600	1.300
23028+0843	6.818	1.234	CL J2302.8+0844	4.900	1.400	1.000
1504075-024816	8.482	0.751	RX J1504-0248	8.300	0.800	0.700

4.4 Discussion

Our results show no statistical dependence of CE metallicity with either redshift or luminosity. At first glance, there appears to be a marginal difference in median metallicity of $\Delta \tilde{Z} = 0.033 \pm 0.011 Z_\odot$ and $\Delta \tilde{Z} = 0.035 \pm 0.012 Z_\odot$ between cluster samples when they are divided by redshift and luminosity, respectively. However, 10,000 simulated pairs of clusters gave 3σ upper limits of $\sim 0.052 Z_\odot$ for luminosity, and $\sim 0.047 Z_\odot$ for redshift. When we fit the full set of data to a linear model with dependence on L_X and z (Equation 4.3), we found no significant dependence of abundance on either variable (although the relationship between Z and L_X was marginally larger).

4.4.1 Comparison to observations

The difference in radial abundance profiles between CC and NCC clusters in Section 4.3.1 has been observed previously, and we found that using CE abundance and luminosity measurements removes most of the core bias from the global abundance approximations, which is consistent with prior results (Buote, 2000; De Grandi et al., 2004; Maughan et al., 2008; Leccardi et al., 2010;

McDonald et al., 2016; Mernier et al., 2017). We also find a lack of statistical dependence of global abundance on both luminosity and redshift. We tested this with a subset of clusters that overlap with those of M08 and found that, while neither sample shows statistical differences in median metallicity according to L_X or z , the differences observed with M08 data were greater than for ACCEPT2.0 clusters. Although both sets used the same clusters, the difference in results can be attributed to systematic differences regarding data reduction, which is evidenced by Figure 4.7 where ACCEPT2.0 shows slightly higher temperature estimates than M08, with the discrepancy becoming larger for higher temperatures.

The difference in temperatures can stem from a number of reasons including how background emission is accounted for and the model used to fit the X-ray spectrum. M08 extracted spectra from source-free regions of each observation, and from the same regions in the corresponding blank-sky background. This method uses the assumption that some of the field of view does not include cluster emission, which can lead to overestimation of the soft background emission. Additionally, M08 source emission was modeled as an absorbed APEC model in the 0.6-9 keV band, while ACCEPT2.0 emission was modeled as an absorbed MEKAL model and includes a robust fit to the background emission. Another difference is that M08 used chi-square and minimum counts per bin to estimate the temperatures, which can result in poor estimates in the low-SNR regime. Rather than subtraction, ACCEPT2.0 statistical analysis used cstat background modeling, which does not require minimum count spectral binning (though in practice workers usually require a minimum of 1 count per energy bin). The way different spectral codes treat sources of X-ray emission introduces an extra level of systematic uncertainty, which can make global abundance approximations a little noisier, especially when combining cluster observables from different catalogs.

4.4.2 Comparison to simulations

Incorporating heavy elements in simulations is a difficult task because it involves using stellar evolution models to create the metals and then various methods to distribute those metals throughout the ICM. In the past few decades, simulations have been able to reproduce the metallicity content

and distribution of the ICM by including contributions from stellar ejecta and AGN (Valdarnini, 2003; Ettori, 2005; Rasia et al., 2015; Biffi et al., 2017a).

The radial distributions of CC and NCC clusters shown in Section 4.3.1 are in agreement with simulations which include AGN feedback (Borgani et al., 2008; Rasia et al., 2015; Biffi et al., 2017a). Our observations of both CC and NCC clusters show higher metallicity inside $r \sim 0.3 R_{2500}$, with a steeper gradient in CC than in NCC clusters and both slopes flattening outside the core to little difference in enrichment outside the cores. Similar abundance profiles are produced by simulations which include a central AGN as the dominant source of metal distribution for massive clusters. However, AGN activity for present day clusters is not enough to enrich the outermost reaches of their gravitational potential wells. Instead, the nearly one-third Solar abundance in the outer ICM can be explained by AGN activity at earlier epochs, when the cluster halo volume was smaller (Biffi et al., 2017b; Biffi et al., 2018). The lack of present day AGN influence on the outer ICM is supported by observations of clusters from the *IllustrisTNG* simulations, which show that abundances of the outer ICM have been relatively constant since redshift $z \sim 2$ (Vogelsberger et al., 2018). Given that we see no statistical evidence for evolution since redshift $z \sim 0.89$, the metallicity data we have analyzed in this chapter is consistent with the notion that the ICM was enriched at times earlier than at least $z \sim 1$. One way to test enrichment scenarios from simulations would be to obtain more iron abundance measurements for the ICM of clusters with $z \gtrsim 1.5 - 2.5$.

4.5 Summary and Conclusions

Improvements in the spatial resolution of X-ray telescopes have allowed for more robust investigations of global abundance trends in the ICM. Previous observations such as those of Balestra et al. (2007), which did not excise core emission, were able to detect some evolution in metallicity, but we later learned that peaks in central metallicity of CC clusters in comparison to NCCs could affect the results. However, at larger radii, the ICM appears to be oblivious to the mechanics of the core, and are thought to evolve on cosmological time scales, which makes the outer ICM a useful place for tracking the stellar evolution history of clusters with respect to redshift. We have used a sample of 302 global core-excised (CE) metallicity estimates from ACCEPT2.0 to test their depen-

dence on luminosity and redshift. First, we confirmed that the presence of CC and NCC clusters in our sample did not affect the global CE metallicity, which supports the idea that AGN activity is confined to the regions surrounding cluster cores. Outside the core, characteristics of the ICM are governed by processes that shape clusters over cosmological time scales. Recent attempts to quantify this evolution have found little evidence for change in recent times. Because ACCEPT2.0 is an archival sample, it is subject to selection biases which can introduce a spurious result for metallicity evolution if it is dependent on the luminosity or temperature of the ICM. We verify that there is a possible weak dependence of metallicity on luminosity or temperature, but if that (small) effect is accounted for, we see no statistically significant indication of redshift evolution in the CE metal abundances of the ICM of clusters of galaxies (with bolometric $L_X \gtrsim 4 \times 10^{43} \text{ erg s}^{-1}$). Additionally, we compared the results of an overlapping sub sample with an additional study and found differing results consistent with differences between analysis techniques, based on private communication with the original study authors. The statistical and systematic limitations of this sample and analysis indicate that outside of the cores, the global cluster abundance has changed by less than $\sim 15\%$ between $0.02 \lesssim z \lesssim 0.9$.

Table 4.6: Full global metallicity table for 302 ACCEPT2.0 clusters. Full sample of 302 clusters. Column(1) is the cluster name, column(2) is the redshift, column(3) is the cluster scaled radius R_{2500} , columns(4,5) and (6,7) are bandpass limited and bolometric luminosities and their errors, columns(8,9) are global temperature and error, columns(10,11) are global abundance and error, and column(12) is the goodness of fit for the global properties. (See Chapter 2 for details.)

ACCEPT2.0 Name	redshift	R_{2500}	L_X	e_{LX}	L_X	e_{LX}	Z	e_Z	kT	e_{kT}	χ^2
			[0.5-8 keV]			[bol]					
		(kpc)	$(10^{44} \text{ erg s}^{-1})$	$(10^{44} \text{ erg s}^{-1})$			(Z_\odot)		(keV)		d.o.f
000619+105206	0.167	466.0	1.850	0.072	2.636	0.102	5.184	0.399	0.350	0.092	1.073
00088+5215	0.104	456.0	0.751	0.030	1.052	0.043	4.711	0.300	0.164	0.087	1.264
00117-1523	0.378	451.0	6.014	0.194	8.839	0.285	5.892	0.399	0.271	0.066	1.132
A0013	0.094	461.0	0.641	0.016	0.899	0.023	5.032	0.635	0.209	0.124	1.048
A2744	0.308	640.0	13.170	0.165	23.686	0.296	10.245	0.770	0.299	0.102	1.234
0014-4952	0.752	388.0	5.112	0.336	7.853	0.517	6.880	0.966	0.406	0.162	1.096

Table 4.6 (cont'd)

ACCEPT2.0 Name	redshift	R2500	LX	e_LX	LX	e_LX	Z	e_Z	kT	e_kT	χ^2
			[0.5-8 keV]			[bol]					
			(kpc)	(10^{44} erg s $^{-1}$)	(10^{44} erg s $^{-1}$)		(Z $_{\odot}$)		(keV)	d.o.f	
Cl0016+16	0.541	557.0	16.147	0.355	28.163	0.619	9.727	0.745	0.198	0.063	0.964
00254-1222	0.584	470.0	8.852	0.347	14.205	0.557	7.817	0.597	0.256	0.060	1.134
00278+2616	0.367	477.0	3.049	0.194	4.615	0.294	6.438	0.978	0.039	0.082	1.086
30484-4142	0.410	559.0	7.488	0.269	13.102	0.470	9.797	1.232	0.150	0.096	1.170
00354-2015	0.364	509.0	10.772	0.355	16.792	0.554	7.187	0.645	0.338	0.090	1.146
A0068	0.255	618.0	5.993	0.281	10.429	0.489	9.717	1.436	0.662	0.210	1.270
A0085	0.055	543.0	2.609	0.019	3.925	0.028	6.170	0.588	0.358	0.150	2.290
A2813	0.292	559.0	7.287	0.223	11.762	0.361	7.950	0.739	0.287	0.086	1.303
00408+2404	0.083	437.0	0.823	0.028	1.129	0.038	3.826	0.623	0.291	0.102	1.280
A0119	0.044	541.0	1.115	0.013	1.628	0.019	5.916	0.591	0.290	0.131	3.338
A0141	0.230	525.0	3.050	0.122	4.635	0.186	6.576	0.772	0.184	0.120	1.383
01670077+0105926	0.254	419.0	2.126	0.070	2.961	0.098	4.059	0.412	0.267	0.111	1.028
01077+5408	0.107	634.0	3.881	0.057	6.191	0.092	6.642	1.385	0.184	0.136	1.257
A2895	0.227	594.0	4.742	0.143	7.809	0.236	8.394	0.858	0.301	0.107	1.471
A0193	0.049	407.0	0.398	0.011	0.536	0.015	3.725	0.483	0.307	0.115	1.191
A0209	0.206	607.0	6.310	0.161	10.466	0.266	8.547	0.665	0.250	0.082	1.313
Abell222	0.211	404.0	1.664	0.067	2.287	0.092	4.137	0.274	0.216	0.070	1.032
Abell223	0.207	473.0	1.370	0.062	1.981	0.089	5.470	0.500	0.247	0.100	1.152
01400-0555	0.454	476.0	7.056	0.392	10.985	0.610	7.139	0.822	0.256	0.103	1.149
01420+2131	0.280	526.0	5.460	0.165	8.543	0.258	7.218	0.649	0.118	0.090	1.265
01525-2853	0.341	457.0	4.091	0.126	6.018	0.186	5.815	0.584	0.058	0.081	1.125
A0267	0.231	563.0	4.166	0.105	6.600	0.166	7.570	0.630	0.393	0.106	1.224
02209-3829	0.229	414.0	2.352	0.136	3.225	0.187	4.346	0.368	0.546	0.140	1.230
A3017	0.220	538.0	3.931	0.175	6.124	0.272	7.115	0.939	0.111	0.106	1.080
0232-4421	0.284	541.0	8.792	0.304	13.995	0.485	7.636	0.811	0.218	0.095	1.259
A0368	0.220	497.0	3.443	0.181	5.101	0.268	6.080	0.768	0.305	0.138	1.276
A0370	0.375	558.0	6.827	0.110	11.422	0.183	8.753	0.459	0.285	0.074	1.206
02426-2132	0.314	459.0	4.837	0.298	7.085	0.436	5.751	0.774	0.151	0.115	1.156

Table 4.6 (cont'd)

ACCEPT2.0 Name	redshift	R2500	LX	e_LX	LX	e_LX	Z	e_Z	kT	e_kT	χ^2
			[0.5-8 keV]		[bol]		(Z $_{\odot}$)	(keV)	d.o.f		
			(kpc)	(10 44 erg s $^{-1}$)	(10 44 erg s $^{-1}$)						
AS0295	0.300	529.0	9.202	0.310	14.464	0.487	7.072	0.896	0.257	0.059	1.200
A0376	0.048	468.0	0.515	0.011	0.713	0.016	4.174	0.670	0.346	0.208	1.875
A0383	0.187	470.0	2.012	0.064	2.881	0.092	5.438	0.297	0.338	0.110	1.239
A0402	0.322	552.0	4.452	0.190	7.293	0.311	8.228	1.236	0.045	0.085	1.175
A0399	0.072	574.0	2.554	0.021	3.926	0.032	6.857	0.581	0.243	0.136	3.135
A0401	0.074	609.0	4.434	0.016	7.035	0.025	7.881	0.877	0.282	0.099	1.488
03016+0155	0.170	432.0	1.687	0.079	2.341	0.110	4.450	0.333	0.233	0.090	1.190
03037-7752	0.274	630.0	6.901	0.197	11.840	0.338	9.344	0.891	0.318	0.085	1.143
A3088	0.253	576.0	5.317	0.193	8.344	0.302	7.316	0.762	0.236	0.099	1.279
03089+2645	0.324	603.0	10.682	0.298	18.580	0.518	9.656	1.047	0.159	0.085	1.285
A3126	0.086	476.0	1.212	0.037	1.707	0.052	4.994	0.309	0.470	0.083	1.203
A3128	0.060	373.0	0.316	0.015	0.423	0.020	2.860	0.484	0.269	0.111	1.502
03311-2100	0.188	495.0	2.604	0.104	3.827	0.153	5.859	0.528	0.204	0.092	1.380
3C089	0.139	439.0	0.464	0.020	0.647	0.028	4.528	0.333	0.166	0.096	1.164
A3158	0.060	480.0	2.057	0.018	2.899	0.026	5.435	0.313	0.387	0.082	2.722
03529+1941	0.109	364.0	1.013	0.041	1.362	0.055	3.085	0.533	0.263	0.124	1.111
03588-2955	0.425	548.0	12.749	0.337	21.346	0.564	8.747	0.487	0.143	0.052	1.130
A0478	0.088	598.0	5.866	0.038	9.322	0.060	7.546	0.554	0.270	0.121	1.116
04175-1154	0.440	624.0	21.550	0.366	40.079	0.680	10.945	0.936	0.211	0.093	1.108
04258-0833	0.040	379.0	0.384	0.016	0.514	0.022	3.088	0.125	0.256	0.073	3.255
04296-0253	0.399	491.0	5.376	0.254	8.315	0.393	7.000	0.900	0.302	0.132	1.159
04371+0043	0.285	518.0	4.937	0.134	7.580	0.205	6.101	0.632	0.265	0.041	1.251
04390+0715	0.230	513.0	5.310	0.166	8.038	0.252	6.528	0.534	0.293	0.083	1.160
04390+0520	0.208	451.0	1.883	0.103	2.670	0.145	5.024	0.480	0.251	0.107	1.220
A0514	0.071	402.0	0.317	0.014	0.430	0.018	3.959	0.534	0.257	0.035	1.588
A3292	0.172	416.0	1.775	0.082	2.441	0.112	4.204	0.297	0.271	0.098	1.410
04519+0006	0.430	443.0	5.882	0.364	8.608	0.533	5.844	0.829	0.411	0.206	1.101
04541-0300	0.550	576.0	15.974	0.296	28.925	0.536	10.644	0.768	0.206	0.082	1.309

Table 4.6 (cont'd)

ACCEPT2.0 Name	redshift	R2500	LX	e_LX	LX	e_LX	Z	e_Z	kT	e_kT	χ^2
			[0.5-8 keV]			[bol]					
		(kpc)	(10^{44} erg s $^{-1}$)		(10^{44} erg s $^{-1}$)		(Z $_{\odot}$)		(keV)		d.o.f
04552+0657	0.425	478.0	6.452	0.414	9.878	0.634	6.845	0.998	0.571	0.226	1.135
0509-5342	0.463	565.0	4.295	0.208	7.291	0.353	9.069	1.716	0.145	0.164	1.176
A3322	0.200	544.0	3.793	0.142	5.786	0.216	6.649	0.599	0.146	0.092	1.104
05107-0801	0.220	552.0	8.412	0.212	13.101	0.330	7.152	0.434	0.280	0.060	1.082
AS0520	0.295	573.0	6.561	0.201	10.757	0.330	8.269	0.732	0.140	0.076	1.167
05207-1328	0.340	515.0	5.821	0.181	9.131	0.284	7.335	0.692	0.345	0.111	1.265
A3343	0.191	513.0	3.027	0.089	4.563	0.135	6.429	0.528	0.269	0.099	1.175
05282-2942	0.158	434.0	1.634	0.086	2.245	0.119	4.607	0.499	0.564	0.197	1.327
RBS0653	0.284	594.0	7.669	0.109	13.057	0.185	8.558	0.836	0.258	0.066	1.153
28658-3125	0.210	536.0	3.759	0.128	5.678	0.194	6.484	0.540	0.301	0.091	1.060
A0545	0.154	582.0	3.448	0.047	5.431	0.073	7.372	0.311	0.124	0.052	1.265
05329-3701	0.275	594.0	6.799	0.197	11.333	0.329	8.644	0.843	0.136	0.080	1.134
0542-4100	0.640	410.0	3.762	0.216	5.691	0.327	6.455	0.885	0.108	0.125	1.168
05470-3904	0.210	457.0	0.974	0.060	1.398	0.086	5.186	0.699	0.046	0.106	1.352
A3364	0.148	571.0	3.151	0.079	4.925	0.124	7.194	0.546	0.126	0.081	1.411
A0550	0.099	507.0	2.168	0.062	3.165	0.090	5.669	0.298	0.141	0.067	1.202
05534-3342	0.407	649.0	13.416	0.212	24.118	0.382	10.463	0.680	0.192	0.055	1.119
A3376	0.046	496.0	0.541	0.006	0.762	0.008	4.696	0.499	0.386	0.121	3.323
A3378	0.141	453.0	3.198	0.099	4.474	0.139	4.780	0.273	0.360	0.088	1.160
06163-2156	0.171	557.0	2.994	0.067	4.678	0.105	7.236	0.511	0.313	0.086	1.178
AS0579	0.152	449.0	1.508	0.056	2.119	0.078	4.789	0.352	0.213	0.092	1.146
13959+2418	0.270	539.0	7.876	0.283	12.273	0.440	7.189	0.635	0.378	0.086	1.169
A3391	0.051	549.0	1.028	0.021	1.498	0.031	5.794	0.222	0.232	0.068	3.227
A3399	0.203	542.0	3.297	0.073	5.045	0.111	6.759	0.453	0.276	0.084	1.084
16765+1764	0.174	517.0	4.844	0.111	7.219	0.165	6.176	0.412	0.229	0.080	1.140
AS0592	0.222	598.0	7.970	0.188	13.233	0.313	8.581	0.651	0.312	0.080	1.363
A3404	0.167	640.0	6.357	0.151	10.236	0.244	7.851	0.642	0.049	0.062	1.148
A0562	0.110	353.0	0.392	0.019	0.526	0.025	2.946	0.451	0.237	0.083	1.122

Table 4.6 (cont'd)

ACCEPT2.0 Name	redshift	R2500	LX	e_LX	LX	e_LX	Z	e_Z	kT	e_kT	χ^2	
			[0.5-8 keV]			[bol]						
		(kpc)	(10^{44} erg s $^{-1}$)		(10^{44} erg s $^{-1}$)		(Z $_{\odot}$)		(keV)		d.o.f	
		0.296	708.0	24.166	0.131	46.462	0.252	12.364	1.145	0.208	0.066	1.326
0717+3745		0.546	647.0	25.993	0.368	51.818	0.734	12.868	1.576	0.181	0.048	1.136
A0586		0.171	516.0	3.337	0.093	4.977	0.139	6.241	0.395	0.374	0.075	1.157
07357+7421		0.216	516.0	3.873	0.033	5.843	0.050	6.447	0.632	0.331	0.103	1.236
07449+3927		0.698	442.0	13.375	0.576	21.465	0.924	7.805	0.634	0.179	0.067	1.114
PKS0745-19		0.103	628.0	5.794	0.034	9.484	0.055	8.360	0.483	0.304	0.083	1.593
A0598		0.189	457.0	1.695	0.085	2.417	0.121	5.052	0.538	0.068	0.091	1.291
A0611		0.288	571.0	4.697	0.124	7.783	0.205	7.993	0.430	0.408	0.118	1.017
A0644		0.070	567.0	2.890	0.031	4.410	0.047	6.580	0.821	0.317	0.089	2.778
08196+6336		0.119	384.0	0.758	0.044	1.025	0.060	3.498	0.321	0.170	0.088	1.238
08232+0425		0.225	427.0	1.718	0.107	2.383	0.148	4.660	0.514	0.510	0.168	1.271
A0665		0.182	614.0	4.817	0.059	7.910	0.096	8.136	0.857	0.260	0.075	1.314
2MFGC06756		0.241	445.0	2.694	0.055	3.823	0.078	5.082	0.508	0.287	0.098	1.057
A3411		0.169	519.0	2.842	0.053	4.247	0.079	6.161	0.454	0.348	0.095	1.119
084254+292723		0.194	505.0	1.485	0.048	2.174	0.070	5.023	0.901	0.519	0.181	1.052
A0697		0.282	713.0	12.109	0.291	23.094	0.555	11.987	1.107	0.333	0.106	1.311
08579+2107		0.230	414.0	2.167	0.079	2.994	0.110	4.517	0.176	0.356	0.160	0.993
+1373+110+018		0.180	475.0	2.688	0.078	3.869	0.112	5.605	0.799	0.248	0.072	1.140
09112+1746		0.505	460.0	5.371	0.324	8.253	0.497	6.808	0.894	0.133	0.102	1.124
20913454+405628		0.442	457.0	4.631	0.189	6.963	0.284	6.416	0.590	0.406	0.092	1.152
A0773		0.217	581.0	5.866	0.132	9.528	0.214	7.630	0.833	0.272	0.081	1.237
HydraA		0.055	431.0	1.145	0.005	1.566	0.006	3.951	0.219	0.289	0.046	1.219
092017+303027		0.258	506.0	3.036	0.123	4.554	0.184	6.352	0.661	0.352	0.105	1.115
A0795		0.136	466.0	1.863	0.048	2.645	0.068	5.002	0.300	0.164	0.062	1.275
0938209+520243		0.360	477.0	5.414	0.181	8.169	0.274	6.417	0.504	0.165	0.073	1.081
A0853		0.166	430.0	0.861	0.054	1.194	0.075	4.441	0.481	0.236	0.129	1.146
A0868		0.153	432.0	2.610	0.086	3.615	0.119	4.414	0.222	0.252	0.070	1.137
0947124+762313		0.354	550.0	7.738	0.176	12.772	0.291	8.581	0.841	0.286	0.196	1.088

Table 4.6 (cont'd)

ACCEPT2.0 Name	redshift	R2500	LX	e_LX	LX	e_LX	Z	e_Z	kT	e_kT	χ^2
			[0.5-8 keV]		[bol]						
		(kpc)	(10^{44} erg s $^{-1}$)	(10^{44} erg s $^{-1}$)		(Z_{\odot})		(keV)		d.o.f	
09498+1708	0.383	576.0	9.104	0.381	16.267	0.681	10.311	1.712	0.184	0.151	1.258
09496+5207	0.214	479.0	2.228	0.048	3.243	0.069	5.346	0.581	0.291	0.096	1.088
A0907	0.153	504.0	2.833	0.056	4.152	0.083	5.772	0.537	0.335	0.142	1.381
26441+1948	0.240	567.0	3.615	0.128	5.726	0.203	7.503	0.702	0.090	0.077	1.126
10005+4409	0.154	367.0	1.065	0.070	1.437	0.095	3.278	0.268	0.183	0.095	1.243
10061+1201	0.221	488.0	2.803	0.071	4.111	0.105	5.860	0.459	0.305	0.027	1.133
10105-1239	0.301	494.0	4.060	0.084	6.139	0.127	6.484	0.395	0.222	0.062	1.108
A0963	0.206	527.0	4.534	0.076	6.861	0.115	6.364	0.782	0.226	0.113	1.259
A0970	0.059	454.0	0.817	0.027	1.134	0.038	4.504	0.402	0.276	0.014	1.387
A0980	0.158	529.0	3.039	0.090	4.606	0.136	5.902	1.038	0.220	0.086	1.204
10236+04111	0.291	589.0	8.464	0.127	14.162	0.213	8.052	0.966	0.285	0.096	1.289
1023399+490838	0.144	533.0	3.321	0.111	5.034	0.168	6.513	0.589	0.156	0.083	1.099
A3444	0.253	552.0	7.473	0.123	12.037	0.197	7.915	0.451	0.338	0.060	0.974
A1033	0.126	501.0	1.475	0.025	2.143	0.037	5.886	0.583	0.266	0.038	1.207
A1068	0.138	463.0	1.884	0.042	2.664	0.060	5.225	0.552	0.370	0.092	1.078
10569-03373	0.823	401.0	7.212	0.383	11.420	0.607	7.494	1.083	0.096	0.107	1.444
11089+0906	0.449	472.0	5.708	0.269	8.786	0.414	6.863	0.744	0.193	0.106	1.128
A1190	0.075	397.0	0.599	0.028	0.808	0.038	3.597	0.190	0.271	0.083	1.247
A1201	0.169	492.0	2.527	0.054	3.681	0.079	5.309	0.543	0.359	0.060	1.254
A1204	0.171	423.0	1.629	0.066	2.253	0.092	4.327	0.277	0.218	0.084	1.310
1115+5319	0.466	604.0	8.139	0.364	14.554	0.651	10.328	1.639	0.141	0.157	1.084
11158+0129	0.352	589.0	8.020	0.227	13.674	0.388	9.180	0.730	0.189	0.068	1.253
A1240	0.159	415.0	0.492	0.032	0.675	0.044	4.158	0.420	0.279	0.137	1.411
A1285	0.106	496.0	2.267	0.042	3.281	0.060	5.361	0.617	0.314	0.026	1.219
A1300	0.307	786.0	9.614	0.240	17.836	0.446	11.265	1.174	0.262	0.099	1.285
11375+6625	0.782	334.0	5.411	0.347	7.728	0.495	5.174	0.629	0.228	0.122	1.088
1142248+583205	0.311	609.0	7.812	0.182	13.142	0.306	8.855	0.679	0.127	0.073	1.166
A1413	0.143	578.0	4.175	0.044	6.581	0.070	7.350	0.558	0.231	0.089	1.459

Table 4.6 (cont'd)

ACCEPT2.0 Name	redshift	R2500	LX	e_LX	LX	e_LX	Z	e_Z	kT	e_kT	χ^2
			[0.5-8 keV]			[bol]					
		(kpc)	(10^{44} erg s $^{-1}$)	(10^{44} erg s $^{-1}$)			(Z $_{\odot}$)		(keV)	d.o.f	
17981192+4979669	0.383	569.0	7.801	0.394	13.915	0.702	10.276	1.691	0.267	0.141	1.111
29251+2198	0.300	606.0	5.929	0.172	9.902	0.287	8.702	0.784	0.233	0.076	1.104
A1446	0.103	390.0	0.707	0.019	0.950	0.025	3.606	0.513	0.332	0.163	1.123
12062-0847	0.440	606.0	16.980	0.490	31.633	0.913	11.369	1.423	0.225	0.109	1.235
12154-3900	0.119	494.0	1.605	0.038	2.315	0.055	5.505	0.361	0.429	0.110	1.167
121733+033929	0.077	576.0	2.565	0.050	3.947	0.077	6.694	0.647	0.292	0.170	2.787
121831+401236	0.320	475.0	4.257	0.182	6.320	0.271	6.090	0.651	0.210	0.116	1.216
122648+215157	0.370	407.0	1.608	0.082	2.259	0.115	4.785	0.474	0.191	0.095	1.082
12269+3332	0.890	539.0	11.315	0.521	22.466	1.035	13.126	1.968	0.193	0.189	1.117
A1553	0.165	568.0	3.879	0.113	6.048	0.176	7.238	0.587	0.518	0.105	1.136
12342+0947	0.229	421.0	1.747	0.111	2.439	0.154	4.552	0.485	0.134	0.112	1.255
A1576	0.279	566.0	2.870	0.107	4.654	0.174	8.001	0.772	0.057	0.063	1.187
A1644	0.047	481.0	0.818	0.007	1.171	0.009	4.858	0.506	0.344	0.141	3.047
A1650	0.084	514.0	2.247	0.018	3.278	0.026	5.726	0.524	0.286	0.106	1.737
1259334+600409	0.330	501.0	3.904	0.145	6.024	0.223	6.894	0.515	0.112	0.068	1.062
A1664	0.128	468.0	1.930	0.041	2.747	0.059	4.732	0.484	0.239	0.047	1.178
A1668	0.063	383.0	0.304	0.019	0.409	0.026	3.326	0.291	0.245	0.094	1.442
1305589+263048	0.305	537.0	4.356	0.192	6.829	0.300	7.269	0.948	0.151	0.097	1.082
A1682	0.234	550.0	3.710	0.105	5.803	0.164	7.205	0.618	0.116	0.092	1.131
13110-0311	0.494	428.0	4.349	0.189	6.435	0.280	6.031	0.482	0.228	0.071	1.128
A1689	0.183	676.0	8.559	0.103	15.062	0.181	10.000	0.874	0.279	0.110	1.410
1315052+514902	0.291	583.0	6.692	0.136	11.224	0.229	8.765	0.771	0.025	0.048	1.149
A1736	0.046	387.0	0.638	0.013	0.854	0.017	3.070	0.313	0.322	0.158	3.124
SSGC081	0.050	398.0	0.418	0.015	0.565	0.020	3.207	0.393	0.282	0.087	2.178
A1750C	0.068	450.0	0.445	0.017	0.617	0.024	3.861	0.768	0.263	0.095	1.310
A1750N	0.084	397.0	0.458	0.022	0.621	0.029	3.586	0.230	0.165	0.070	1.350
A3562	0.049	470.0	0.826	0.018	1.149	0.026	4.701	0.503	0.340	0.125	3.211
A1763	0.223	555.0	6.919	0.180	11.013	0.286	7.669	0.593	0.388	0.084	1.252

Table 4.6 (cont'd)

ACCEPT2.0 Name	redshift	R2500	LX	e_LX	LX	e_LX	Z	e_Z	kT	e_kT	χ^2
			[0.5-8 keV]			[bol]					
			(kpc)	(10^{44} erg s $^{-1}$)	(10^{44} erg s $^{-1}$)		(Z_{\odot})		(keV)	d.o.f	
A1767	0.070	495.0	1.188	0.037	1.703	0.053	5.301	0.290	0.293	0.081	1.412
A1775	0.072	408.0	0.923	0.011	1.238	0.015	3.760	0.413	0.503	0.110	1.616
LCDCS0829	0.451	718.0	20.538	0.248	41.656	0.503	13.426	2.267	0.213	0.073	1.160
13546+7715	0.397	467.0	4.673	0.251	7.024	0.378	6.384	0.815	0.314	0.119	1.103
A1831	0.061	399.0	0.538	0.017	0.720	0.023	3.541	0.159	0.447	0.077	1.347
1359495+623047	0.322	509.0	4.018	0.121	6.184	0.186	6.859	0.590	0.199	0.084	1.468
A1835	0.253	646.0	12.004	0.170	21.457	0.303	9.175	1.354	0.348	0.157	1.213
11382+4435	0.226	495.0	2.620	0.128	3.891	0.189	6.017	0.680	0.004	0.053	1.037
A1882a	0.141	385.0	0.316	0.017	0.424	0.022	3.317	0.158	0.302	0.080	1.129
21594948+2407846	0.543	462.0	6.151	0.118	9.624	0.185	6.887	0.360	0.327	0.029	1.000
A1914	0.171	633.0	9.446	0.147	15.799	0.246	8.422	1.044	0.213	0.053	1.398
1427161+440730	0.498	601.0	6.679	0.271	11.975	0.486	10.403	1.424	0.236	0.142	1.328
14276-2521	0.318	410.0	2.061	0.095	2.865	0.132	4.689	0.340	0.443	0.114	1.186
A1930	0.131	440.0	0.951	0.038	1.311	0.053	4.366	0.629	0.587	0.028	1.235
1942	0.224	465.0	1.401	0.046	2.016	0.066	5.305	0.486	0.373	0.031	1.219
A1991	0.059	346.0	0.329	0.010	0.438	0.013	2.695	0.319	0.299	0.114	1.106
145715+222009	0.258	452.0	3.947	0.081	5.650	0.115	5.120	0.434	0.296	0.101	1.135
AS0780	0.236	551.0	5.352	0.074	8.395	0.117	7.021	0.628	0.310	0.122	1.065
A2009	0.153	543.0	3.537	0.097	5.386	0.148	6.695	0.309	0.443	0.071	1.392
1504075-024816	0.215	620.0	9.519	0.130	16.069	0.219	8.482	0.751	0.238	0.070	1.463
A2034	0.113	595.0	2.975	0.031	4.685	0.049	7.555	0.875	0.303	0.108	1.568
15149-1523	0.223	616.0	5.561	0.090	9.372	0.151	8.899	0.481	0.141	0.048	1.105
A2061	0.078	457.0	1.171	0.022	1.631	0.031	4.310	0.527	0.278	0.118	1.083
MKW03s	0.045	394.0	0.650	0.006	0.875	0.008	3.434	0.404	0.261	0.113	2.072
A2069	0.116	525.0	1.793	0.032	2.675	0.048	5.936	0.646	0.301	0.128	1.712
15242-3154	0.103	444.0	1.365	0.019	1.900	0.026	4.426	0.719	0.362	0.129	1.326
15328+3021	0.345	522.0	6.570	0.112	10.388	0.177	7.129	0.720	0.239	0.065	1.141
A2107	0.041	434.0	0.433	0.009	0.588	0.012	3.766	0.480	0.265	0.114	3.251

Table 4.6 (cont'd)

ACCEPT2.0 Name	redshift	R2500	LX	e_LX	LX	e_LX	Z	e_Z	kT	e_kT	χ^2
			[0.5-8 keV]			[bol]					
			(kpc)	(10^{44} erg s $^{-1}$)	(10^{44} erg s $^{-1}$)		(Z $_{\odot}$)		(keV)	d.o.f	
A2111	0.229	567.0	3.754	0.081	5.996	0.129	7.700	0.575	0.186	0.085	1.146
A2104	0.153	565.0	3.731	0.049	5.815	0.077	7.200	1.018	0.245	0.153	1.354
A2125	0.246	343.0	0.632	0.031	0.850	0.042	3.158	0.206	0.197	0.089	1.133
A2124	0.066	485.0	0.326	0.012	0.463	0.017	4.839	0.219	0.354	0.091	1.104
A2142	0.091	626.0	4.832	0.043	7.887	0.069	7.675	0.570	0.276	0.080	3.074
15583-1410	0.097	483.0	2.001	0.021	2.850	0.029	5.018	0.356	0.371	0.106	1.330
A2147	0.035	449.0	0.537	0.007	0.737	0.010	4.275	0.343	0.321	0.101	4.436
A2163	0.203	795.0	20.636	0.140	42.292	0.288	13.183	1.347	0.240	0.045	1.603
16213+3810	0.465	482.0	4.964	0.186	7.763	0.291	7.226	0.580	0.199	0.066	1.167
16235+2634	0.426	449.0	3.854	0.228	5.798	0.342	6.365	0.908	0.201	0.124	1.005
A2187	0.184	554.0	2.384	0.100	3.644	0.152	6.709	0.765	0.183	0.122	1.389
A2204	0.152	654.0	6.250	0.044	10.792	0.077	8.269	1.172	0.319	0.143	1.623
A2218	0.176	520.0	4.315	0.084	6.482	0.127	6.318	0.550	0.201	0.076	1.287
A2219	0.226	699.0	14.778	0.091	27.420	0.169	11.017	0.888	0.280	0.093	1.223
HerculesA	0.155	419.0	1.836	0.034	2.531	0.047	3.653	1.309	0.181	0.097	1.224
021701+6412	0.453	453.0	2.479	0.125	3.720	0.188	6.371	0.771	0.379	0.154	1.122
A2244	0.097	515.0	2.680	0.024	3.927	0.036	5.919	0.484	0.327	0.096	1.106
A2256	0.058	586.0	3.438	0.033	5.363	0.052	6.782	0.465	0.381	0.135	1.886
A2249	0.082	486.0	1.267	0.035	1.811	0.051	5.153	0.342	0.168	0.086	1.204
A2255	0.081	530.0	2.107	0.026	3.133	0.038	6.086	0.559	0.325	0.113	1.828
A2259	0.164	508.0	3.248	0.119	4.806	0.176	6.089	0.502	0.427	0.128	1.254
43072	0.164	560.0	4.348	0.075	6.753	0.116	7.066	0.427	0.413	0.059	1.371
17202+3536	0.391	530.0	6.766	0.206	10.872	0.331	7.870	0.653	0.367	0.080	1.279
A2261	0.224	593.0	7.182	0.156	11.669	0.253	7.714	1.178	0.349	0.077	1.276
A2294	0.169	570.0	4.578	0.170	7.178	0.266	7.303	0.736	0.260	0.106	1.415
17316+2251	0.366	551.0	6.784	0.211	11.278	0.351	8.608	0.849	0.299	0.123	1.320
17421+3306	0.076	437.0	1.099	0.017	1.507	0.024	4.076	0.352	0.374	0.179	1.653
174715+451155	0.157	447.0	1.518	0.066	2.128	0.093	4.729	0.378	0.182	0.084	1.142

Table 4.6 (cont'd)

ACCEPT2.0 Name	redshift	R2500	LX	e_LX	LX	e_LX	Z	e_Z	kT	e_kT	χ^2
			[0.5-8 keV]			[bol]					
		(kpc)	(10^{44} erg s $^{-1}$)		(10^{44} erg s $^{-1}$)		(Z $_{\odot}$)		(keV)		d.o.f
17502+3504	0.171	442.0	1.689	0.078	2.364	0.109	4.639	0.356	0.126	0.083	1.187
18044+1002	0.152	545.0	5.159	0.144	8.034	0.225	7.097	0.592	0.092	0.075	1.225
A2302	0.179	447.0	1.324	0.055	1.862	0.077	4.821	0.382	0.203	0.096	1.157
18290+6913	0.203	402.0	0.843	0.044	1.151	0.060	4.057	0.305	0.335	0.109	1.234
18521+5711	0.109	418.0	0.465	0.019	0.635	0.026	4.003	0.283	0.259	0.096	1.345
18539+6822	0.093	423.0	1.031	0.025	1.419	0.034	4.129	0.221	0.190	0.074	1.199
33709-2597	0.264	563.0	6.544	0.138	10.438	0.221	7.658	0.539	0.118	0.070	1.181
A2319	0.056	670.0	5.846	0.046	10.028	0.078	8.664	1.413	0.319	0.131	3.532
19318-2635	0.352	540.0	8.805	0.104	14.152	0.168	7.793	0.786	0.374	0.147	1.326
AS0821	0.237	511.0	5.443	0.174	8.184	0.261	6.386	0.506	0.302	0.072	1.108
19383+5409	0.260	539.0	8.739	0.350	13.629	0.546	7.202	0.728	0.356	0.091	1.124
19473-7623	0.217	574.0	5.483	0.179	8.604	0.280	7.337	0.632	0.338	0.086	1.214
A3653	0.109	450.0	0.524	0.015	0.733	0.021	4.781	0.341	0.345	0.071	1.222
20035-2323	0.317	599.0	7.858	0.190	13.401	0.324	9.178	0.804	0.131	0.072	1.222
20148-2430	0.161	560.0	4.182	0.099	6.499	0.154	6.629	0.996	0.447	0.125	1.190
2023-5535	0.232	609.0	5.848	0.172	9.627	0.283	8.387	0.761	0.291	0.085	1.121
20318-4037	0.342	494.0	7.965	0.430	12.201	0.659	6.735	0.918	0.128	0.117	1.116
A3695	0.089	550.0	1.909	0.042	2.887	0.064	6.465	0.427	0.161	0.084	1.352
20460-3430	0.423	428.0	4.194	0.216	6.100	0.314	5.606	0.447	0.212	0.086	1.136
20499-3216	0.325	528.0	5.290	0.221	8.338	0.348	7.423	0.952	0.262	0.109	1.259
A3739	0.165	516.0	2.874	0.120	4.251	0.177	6.084	0.527	0.413	0.111	1.096
IC1365	0.049	429.0	0.574	0.025	0.781	0.034	3.966	0.438	0.509	0.083	2.480
2129-0741	0.589	479.0	12.133	0.669	19.708	1.086	8.117	0.943	0.454	0.126	1.130
2135-0102	0.325	557.0	4.768	0.219	7.826	0.360	8.365	1.066	0.580	0.154	1.246
A2355	0.124	586.0	1.465	0.045	2.290	0.071	7.240	0.690	0.289	0.118	1.276
2135-5726	0.427	477.0	3.586	0.199	5.541	0.307	6.922	1.301	0.108	0.157	1.099
21402-2339	0.313	468.0	3.985	0.110	5.860	0.162	5.638	0.740	0.306	0.144	1.070
A3809	0.062	354.0	0.426	0.014	0.565	0.019	3.117	0.292	0.413	0.138	1.303

Table 4.6 (cont'd)

ACCEPT2.0 Name	redshift	R2500	LX	e_LX	LX	e_LX	Z	e_Z	kT	e_kT	χ^2
			[0.5-8 keV]			[bol]					
		(kpc)	(10^{44} erg s $^{-1}$)		(10^{44} erg s $^{-1}$)		(Z $_{\odot}$)		(keV)		d.o.f
2148-6116	0.571	436.0	3.484	0.229	5.327	0.351	6.735	1.175	0.272	0.195	1.039
A2384	0.094	516.0	1.119	0.018	1.628	0.026	5.246	0.839	0.390	0.162	2.330
A2390	0.228	668.0	13.625	0.092	25.178	0.169	10.095	1.521	0.290	0.096	1.068
21538+3746	0.292	608.0	11.047	0.148	19.077	0.256	8.940	1.321	0.240	0.103	1.148
A2409	0.148	510.0	4.281	0.134	6.289	0.197	5.955	0.382	0.462	0.093	1.292
A3827	0.098	585.0	3.243	0.032	5.080	0.050	7.338	0.789	0.339	0.144	1.302
A2415	0.058	344.0	0.401	0.012	0.534	0.016	2.583	0.284	0.347	0.094	1.236
22117-0349	0.270	655.0	6.301	0.219	11.029	0.383	9.815	1.315	0.221	0.121	1.394
3C444	0.153	473.0	0.613	0.021	0.876	0.030	4.379	0.393	0.332	0.098	1.334
A2426	0.098	522.0	1.671	0.053	2.451	0.077	5.825	0.389	0.251	0.100	1.305
2214-1359	0.483	530.0	10.888	0.419	18.292	0.705	8.833	0.989	0.194	0.093	1.120
A3854	0.149	472.0	2.281	0.081	3.256	0.116	5.181	0.394	0.258	0.092	1.197
22186-3853	0.138	499.0	3.292	0.092	4.789	0.134	5.604	0.330	0.200	0.075	1.240
A2445	0.166	414.0	1.718	0.057	2.340	0.077	4.162	0.215	0.545	0.086	1.190
A3880	0.058	356.0	0.341	0.018	0.453	0.023	2.897	0.277	0.305	0.143	2.280
22286+2036	0.412	550.0	10.081	0.348	16.485	0.569	8.249	0.824	0.352	0.116	1.176
22298-2756	0.324	464.0	4.070	0.190	5.967	0.279	5.882	0.562	0.397	0.108	1.233
2233-5339	0.480	466.0	4.392	0.264	6.750	0.406	6.791	1.168	0.075	0.121	1.089
A2457	0.059	414.0	0.550	0.015	0.744	0.021	3.595	0.099	0.326	0.059	1.352
22428+5301	0.192	595.0	4.117	0.053	6.747	0.088	7.813	1.165	0.183	0.120	1.048
2243198-093530	0.432	488.0	14.006	0.520	21.842	0.811	7.179	0.672	0.267	0.085	1.214
22450+2637	0.304	499.0	4.480	0.241	6.835	0.368	6.710	0.933	0.330	0.146	1.224
A3911	0.097	544.0	2.198	0.061	3.262	0.090	6.106	0.393	0.285	0.081	1.183
A2485	0.247	511.0	2.703	0.119	4.043	0.178	6.250	0.714	0.231	0.129	1.247
AS1063	0.347	663.0	22.560	0.412	41.905	0.765	11.302	0.722	0.359	0.070	1.219
A3921	0.093	522.0	1.981	0.037	2.916	0.054	5.766	0.762	0.360	0.085	1.879
A2507	0.196	414.0	1.003	0.065	1.377	0.089	4.309	0.433	0.426	0.154	1.069
2259-6057	0.750	411.0	4.949	0.246	7.715	0.384	7.265	1.064	0.694	0.215	1.200

Table 4.6 (cont'd)

ACCEPT2.0 Name	redshift	R2500	LX	e_LX	LX	e_LX	Z	e_Z	kT	e_kT	χ^2
			[0.5-8 keV]			[bol]					
			(kpc)	(10^{44} erg s $^{-1}$)	(10^{44} erg s $^{-1}$)		(Z_{\odot})		(keV)	d.o.f	
23028+0843	0.722	407.0	1.736	0.111	2.667	0.170	6.818	1.234	0.169	0.180	1.139
A2537	0.295	506.0	4.650	0.104	7.083	0.158	6.629	0.625	0.224	0.038	1.157
23115+0338	0.300	598.0	7.260	0.281	12.544	0.486	9.518	1.005	0.334	0.103	1.333
A2556	0.087	413.0	0.814	0.018	1.105	0.024	3.756	0.398	0.356	0.086	1.157
AS1101	0.058	345.0	0.541	0.010	0.726	0.013	2.698	0.286	0.199	0.089	2.076
A2597	0.085	442.0	0.878	0.010	1.214	0.015	4.266	0.259	0.279	0.080	1.310
A2626	0.055	382.0	0.443	0.012	0.593	0.016	3.263	0.379	0.378	0.131	1.119
A2631	0.273	580.0	7.191	0.246	11.658	0.398	8.024	0.961	0.169	0.100	1.254
A4023	0.193	507.0	1.996	0.082	2.984	0.123	6.256	0.635	0.268	0.117	1.216
A2645	0.251	512.0	3.698	0.171	5.582	0.258	6.470	0.782	0.297	0.119	1.118
23442-0422	0.079	450.0	1.473	0.038	2.031	0.052	4.501	0.143	0.406	0.261	1.422
A2657	0.040	403.0	0.583	0.016	0.785	0.021	3.567	0.307	0.302	0.165	3.162
A4038	0.028	369.0	0.394	0.007	0.525	0.009	2.878	0.263	0.286	0.118	3.540
A2665	0.056	458.0	0.489	0.018	0.680	0.025	4.553	0.294	0.310	0.095	1.412
A2667	0.230	556.0	7.819	0.208	12.434	0.331	7.604	0.677	0.163	0.084	1.046
A2670	0.076	435.0	0.743	0.021	1.019	0.028	4.001	0.706	0.310	0.114	2.206

CHAPTER 5

PIPELINE FOR THE REDUCTION OF DATA FROM THE SOAR ADAPTIVE-OPTICS MULTI-OBJECT SPECTROGRAPH (SAMOS)

The *SAMOS* instrument is a multi-object spectrograph which uses a Digital Micromirror Device (DMD) (Smee et al., 2018) to focus light towards either an imaging or spectroscopy channel. The DMD allows for multiple slit configurations in a single observing run. Multi-object capabilities of the *Goodman High Throughput Spectrograph* require slit masks to be made in advance, and are installed in the afternoon leading up to the observation. *SAMOS* has the unique feature of being able to create on-the-fly slit patterns, which will be saved in the *FITS* headers. The instrument is not set to be commissioned until at least 2021, so the current version of the *SAMOS* data reduction pipeline (SRP) uses multi-object data from the SOAR Goodman Spectrograph. This SRP will provide the foundation for *SAMOS* data reduction upon its commissioning. The test data used for the SRP was taken by *SOAR Goodman* on March 19, 2014. Eventually, the pipeline will be used to reduce multi-object spectroscopy data taken with the SOAR Adaptive-Module Optical Spectrograph (*SAMOS*).

There are two main parts to the SRP: basic image reduction and spectroscopic reduction. For optical spectroscopy, we use detectors called charge-coupled devices (CCDs) to detect and convert light to a digital signal. When sensors on the CCD are hit by incoming photons, they save the information and it gets read out to a two-dimensional pixel array after the exposure. The exposure is saved as a *FITS* (Flexible Image Transport System) file, which is able to store both the image data and calibration information in a header.

There are a couple important systematics at play during exposure and readout, an obvious one being that CCDs are not perfect photon detectors. This imperfection means that pixels can vary in sensitivity across the array. We correct for this variation by normalizing, or flattening, the data. Additionally, CCDs are not completely cleared of their information after readout, which means that each exposure starts with a certain amount of signal. This “pre-charge” is called the readout bias.

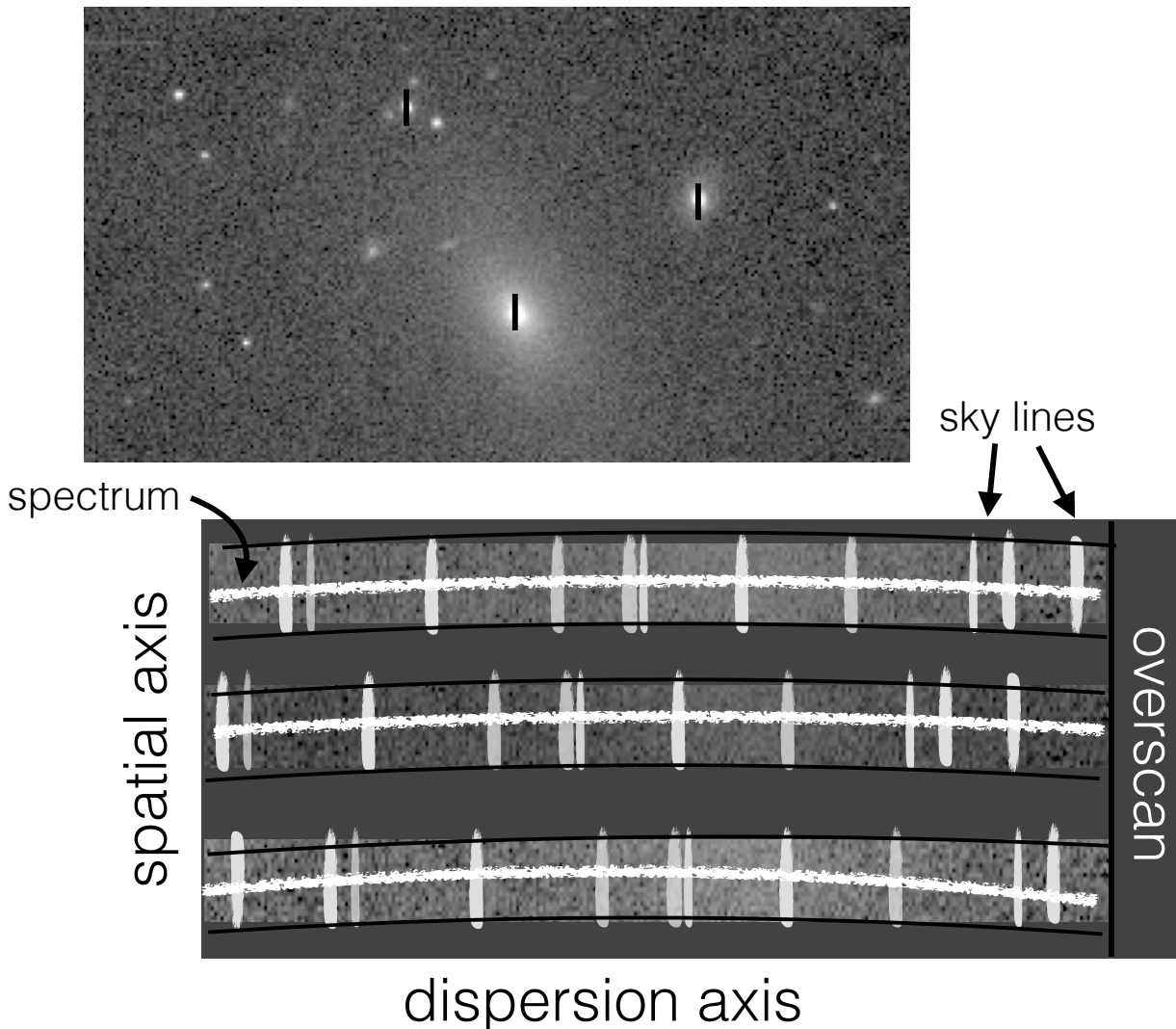


Figure 5.1: **Cartoon multi-object spectra.** Simplified depiction of multi-object spectra. Sky light is also dispersed and appears as emission lines on either side of the spectrum. The lines are the same in each spectrum, but shift depending on slit position.

Sometimes a region of the CCD called the “overscan” is used to correct for this readout noise. A cartoon layout of a CCD is shown in Figure 5.1.

When dispersed photons¹ hit the detector, they are mapped to the 2-D array, the mapping of light intensity—i.e., location along the spectroscopic slit (1 dimension), and wavelength (orthogonal dimension to slit location)—is not perfectly aligned with the pixels. We usually correct for this distortion by fitting the continuum (track of illuminated pixels) of a standard star as a function of

¹Like a rainbow.

pixel location (Marsh, 1989; Horne, 1986). This spectrum trace, shapes measured at different slit positions, can be used to rectify the corresponding science images. Once the correction is applied to the 2-D spectrum, we collapse it to one dimension for wavelength calibration. Wavelength calibration involves converting pixel coordinates of the 1-D spectrum to wavelength coordinates based on characteristics of the spectrum grating.

Because each instrument comes with its own systematics, image reduction is rarely a cookie-cutting exercise, and spectral tracing and wavelength calibration are particularly difficult and tedious. Thus far, the Image Reduction and Analysis Facility (IRAF) (Tody, 1986, 1993) has been the only reduction package with enough robustness and versatility to make it the go-to spectroscopic data reduction source for nearly 30 years. However, the command language (CL) in which IRAF is written has been unable to keep up with more versatile languages such as Python. IRAF’s imminent demise is a source of worry, and there have only been a few efforts made to start the transition to a new generic reduction package (Lucas et al., 2018; Price-Whelan et al., 2018). The goal of the SRP is to have a complete spectral reduction package for *SAMOS* data which is completely independent of IRAF.

5.1 Pipeline Organization

The *SAMOS* reduction pipeline is meant to be run within a *Jupyter* notebook, as it allows for the user to track the reduction progress. Begin each new session with the execution of the `SAMOSNight` class. This class stores the data and information for a particular night (defined by some observation ID), which is updated with each step of the data reduction. The current capabilities of the *SAMOS* pipeline are summarized in table 5.1, and each step is further described in the sections below. Each section is prefaced by the code used to execute the step. The code represented in this chapter is from the tutorial `jupyter_NBtutorial/SAMOS_tutorial`.

Major updates for this pipeline will occur when we obtain test data from the *SAMOS* instrument. It should therefore be noted that some parts of the pipeline in its current state employ more generic data reduction methods, with the plan that more sophisticated methods can be chosen and applied once the actual parameters of the operational system are better known. Until then, we have adapted

Table 5.1: ***SAMOS*** reduction pipeline status. Current status of the *SAMOS* reduction pipeline. Each row describes a step in the data reduction process, its current completion status, and the planned updates for accomodating *SAMOS* data. Each step's current status is in reference to its processing of the Goodman test data.

Reduction Step	Step Description	Current Status	Planned Updates
<code>SAMOSNight(...)</code>	initialize pipeline and organize raw data	complete	This will eventually include the ability to make SQL queries for <i>SAMOS</i> data stored on a separate server
<code>ImageProcessor(...)</code>	image trim, overscan, flat correction	complete	add bias level correction using bias frames
<code>SlitBuckets(...)</code>	trace and crop individual slits	complete	slit tracing method will need to read <i>SAMOS</i> slit mask patterns from the <i>FITS</i> headers
<code>WaveCalBuckets(...)</code>	fits wavelength solution using comparison lamp data	complete	linelists for first-guess solutions will refer to those obtained from calibration lamps observed with SAMOS
Spectral Extraction	extract source spectrum from slit	in progress	method will outline and crop out main spectral source
Sky Subtraction/Flux Calibration	subtract sky contribution from spectrum	in progress	

some working assumptions about the performance of the spectrograph which may differ from its actual performance. For instance, the pipeline assumes that the spectrum will not perfectly co-align with the rows and columns of the detector, the data have an overscan region which can be used for bias calibrations, and that other calibrations such as arc lamp exposures can be taken in the afternoon or during the night. The methods used for *SAMOS* data analysis are heavily influenced by the Goodman Spectroscopic Pipeline (Torres-Robledo & Briceño, 2019) and the Astropy image reduction package `ccdproc` (Craig et al., 2017).

The working directory for SRP contains the following required files and directories:

- `UNCOMP_GDMN_DATA/`: directory containing Goodman observations.
- `SAMOS_DRP/`: directory containing main pipeline modules.
- `comp_refs/`: directory containing linelists and wavelength solutions for comparison lamps in every spectroscopic configuration.
- `slit_refs`: text file containing manually selected slit edges used as a first-guess when cropping slit data.
- `SAMOSenv.yml`: independent environment file which contains the packages necessary to run the pipeline.

5.2 Step 0: Pipeline Initialization

```
from SAMOS_DRP.SAMOS_NIGHT import SAMOSNight

SAMOS_setup = SAMOSNight(obsid='',
                         raw_data_dir='',
                         proc_dir='',
                         LOG_FILENAME='',
                         ignore_flats=False,
                         ignore_bias=True)
```

The *SAMOS* pipeline is initialized when the user executes the code shown above, where `obsid` is the observation ID corresponding to the night on which the data were observed, `raw_data_dir` is the directory containing the raw observation data, `proc_dir` is the directory for storage of pipeline results, `LOG_FILENAME` is the name of the `.log` file (if a file of the same name exists it is overwritten), `ignore_flats` gives the option to apply a flat field correction, and `ignore_bias` tells the pipeline whether to include bias correction from a series of zero exposures in the absence of the overscan region.

First, the pipeline makes a directory for the data products and checks the files in `raw_data_dir`. Data are stored as *FITS* (Flexible Image Transport System) (Wells et al., 1981) files, which store digital information in the form of multi-dimensional arrays. *FITS* is the “standard” archival data

format for astronomers because it is able to store (and transfer) astronomical data that is completely self-contained. A typical *FITS* file has a primary header and data unit (*HDU*) extension, which is split into two arrays. The first array contains the top-level meta data for the exposure and is called the primary header. The primary header stores the information about an image in the form of keywords (observation date, target coordinates, exposure time, etc.) The second array usually contains the main data, but may be empty in a new *FITS* file. They may also contain multiple other extensions, where each extension shares the same primary header information, but the local header contains information specific to that extension’s data (more information on *FITS* files can be found in Pence et al. (2010)).

The pipeline sorts the observations depending on exposure type (e.g. `BIAS`, `FLAT`, `OBJ`) by reading the *FITS* headers. Once the data is organized, the user can view the main information by executing `SAMOS_setup.data_buckets`, and check that the data has been sorted properly. Each subsequent reduction step inherits the attributes of the previous step. Whenever something is done to the data, a new *FITS* file is created. To keep track of what procedures were already performed, the intermediate products have the same base file names as their raw data, but with a new letter based on the intermediate step (e.g. `trimmed+bias-corrected ~ to_fname.FITS`).

The code reads the *FITS* headers and creates arrays which separate the data into flats, comparison lamps, and science data. Information for a night of observations is organized into a `pandas.DataFrame` called a ‘night_bucket’. This bucket object is further divided into the following main data reduction buckets:

- Bias frames: not currently implemented because bias in the Goodman test images is accounted for via the overscan region, but these frames also can be used to verify the gain setting and can verify that the 2-d bias is “quiet”.
- Flats: quartz flats to characterize nonuniformity in CCD pixel sensitivity.
- Comparison lamps: Arc lamp exposures for wavelength calibration.
- Science/Comparison pairs: Object exposures and the corresponding comparison lamps.

5.3 Step 1: CCD Image Processing

```
from SAMOS_DRP.ImageProcessor import ImageProcessor

SAMOS_ccd_proc = ImageProcessor(SAMOS_setup)
SAMOS_ccd_proc()
```

The first step in reducing CCD data is to account for systematic effects during data acquisition and readout. CCDs are made of pixels which are sensitive to specific photon energies. Electrons in the pixel become excited by incoming light, and that charge is read out by the CCD. Every observation contains a bias level due to a combination of the camera noise from the readout process and electric “pre-charge” on a CCD chip by the electronics. Bias-subtraction and flat correction is executed with the command shown at the beginning of this section.

The pipeline parses the FITS data array into regions of bias and target data by reading the FITS headers BIASSEC and DATASEC respectively. The latter section trims the field mask to the correct size.

The BIASSEC header gives the region of overscan, which is a series of detector pixels that are shielded from incoming light. An array of this overscan region is made by grabbing the rows and columns from the data array. The function then takes the median (or mean) of the overscan regions along the rows (axis=1), and subtracts these values from each data value in their respective data rows.

$$\begin{pmatrix} \text{cropped} & \text{and} \\ \text{bias} & \text{subtracted} \\ \text{data} & \text{matrix} \end{pmatrix} = \begin{pmatrix} d_{11} & d_{12} & d_{13} & \dots & d_{1m} \\ d_{21} & d_{22} & \dots & \dots & d_{2m} \\ \dots & \dots & \dots & \dots & \dots \\ d_{n1} & \dots & \dots & \dots & d_{nm} \end{pmatrix} - \left([b_1] \ [b_2] \ [b_3] \ [\dots] \ [b_n] \right) \otimes \begin{pmatrix} 1 \\ 1 \\ \dots \\ \dots \\ 1 \end{pmatrix} \quad (5.1)$$

Flat field images are used to characterize the variation in pixel sensitivity across the detector. During this step, each flat is scaled by its median so that the average pixel correction is ~ 1 . This

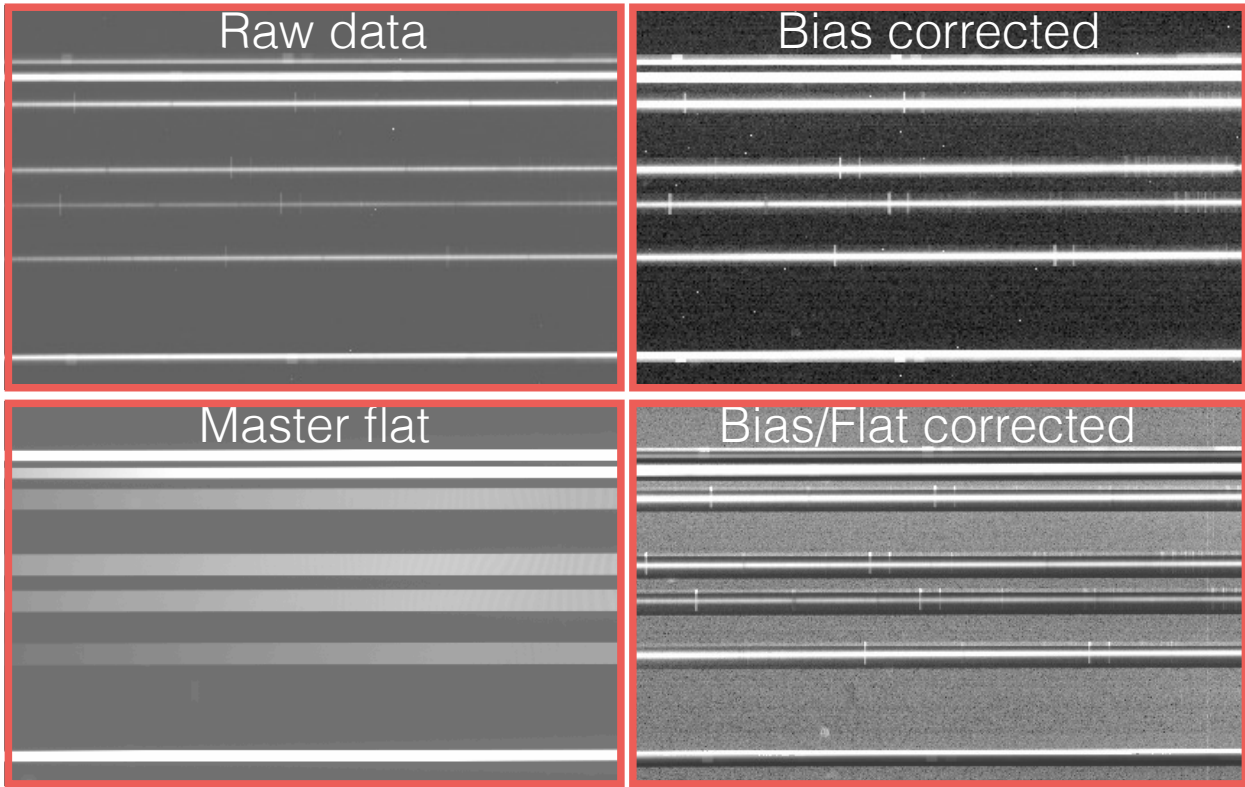


Figure 5.2: **First CCD data reduction steps.** Data output after initial pipeline steps for CCD reduction. The raw data is in the upper left. (make better image and caption)

normalization allows the statistics of the image to be maintained without having to pass along the details of the flat. The data are then median-combined to create the master flat. Finally, the pipeline divides the master flat from the science images. Examples of output of the pipeline through the first few steps are shown in Figure 5.2.

5.4 Step 2: Slit tracing and extraction

```
from SAMOS_DRP.SlitBuckets import SlitBuckets

SAMOS_slits = SlitBuckets(SAMOS_ccd_proc)
SAMOS_slits()
```

SAMOS is designed with a large Digital Micromirror Device (DMD). The mirrors can be selected to direct light to a spectrograph arm or an imaging arm, with the slit configurations stored in the FITS headers for each exposure and accessible to the pipeline upon instantiation. The current version of this pipeline uses data acquired from *Goodman* using multi-slit masks made in advance

of the observation. The most exciting feature of *SAMOS* will be its ability to create slit patterns in real time and save them to the FITS header for easy retrieval by the pipeline. Therefore, the slit location procedure is somewhat brute force as it will be replaced for analysis of *SAMOS* data.

The method for identifying and excising individual slits from the images uses a manually made text file of pixel locations. The mask reference file `slit_refs` contains the y-pixel values for the top middle edge of each slit, obtained by inspection from the master flat file². These reference pixels provide a first guess for the pipeline to map out the slit edges by calculating peaks in the difference of pixel intensity. The mask template is used to crop and pair the individual slits for the science and calibration lamp exposures. The cropped images are stored in a new directory corresponding to each slit number. The output of this procedure is shown in Figure 5.3.

5.4.1 Note on spectral extraction and tracing

As mentioned above, the development version of the pipeline does not deal with spectral extraction as robustly as it will in the future. Once each slit is cut out and saved as its own *FITS* file, instead of fitting the spectrum to a function based on the (minor) tilt with respect to the spatial axis, the pipeline takes sections of the slit and aligns them for a quick look at the pipeline progress. The crop-and-move alignment is adequate for testing purposes, as the spectra from *Goodman* are relatively well-behaved with respect to more extreme spatial distortions. A one-dimensional spectrum is “extracted” by taking the middle few rows of a spectrum and using their median to collapse them to a single row. This spectral extraction is a very crude method and only for the purposes of testing. In the future, the SRP will fit a function to characterize the layout of the spectrum over pixel coordinates. More information about the spatial distortion of spectra can be found in Marsh (1989) and Horne (1986).

5.5 Step 3: Wavelength calibration

²The master flat provides the greatest contrast between the illuminated and non-illuminated sections of the detector. The *SAMOS* instrument team is developing a calibration from DMD to detector that will be verified during engineering testing at SOAR. We hope it goes well and turns out to be robust. Otherwise, the code described here can implement it as a first-guess.

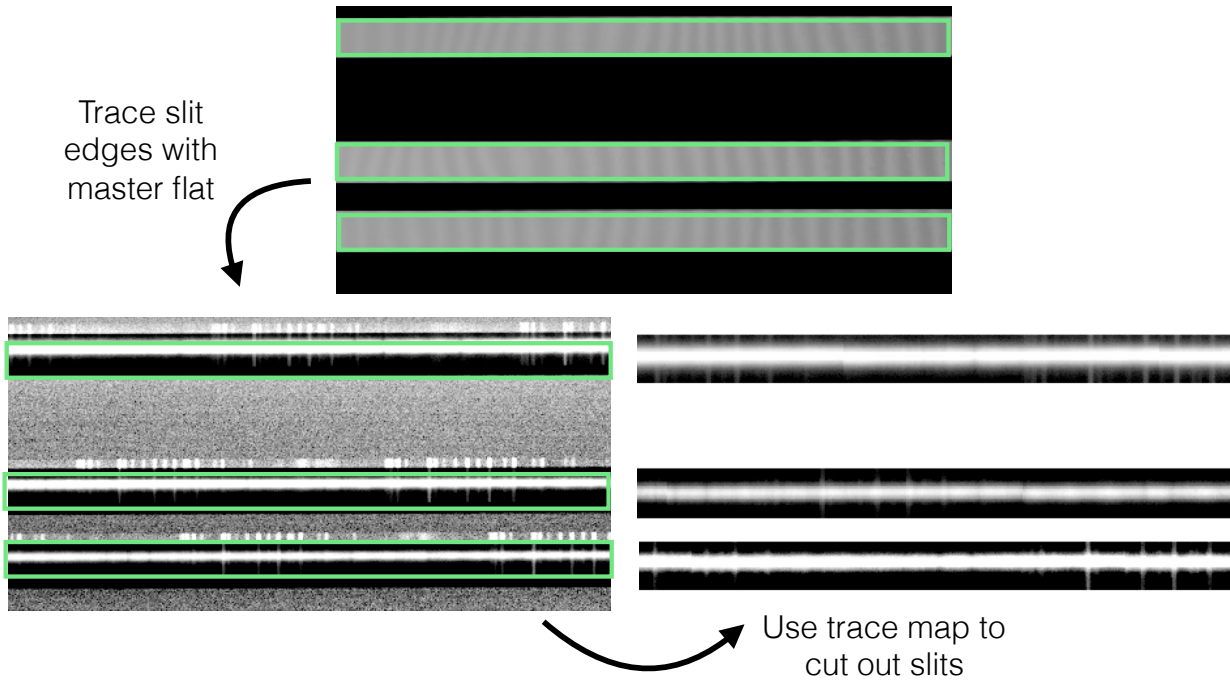


Figure 5.3: **Slit cutout diagram.** Simplified version of slit tracing and extraction. The master flat (*top*) is used to find the slit edges, then a map of the pixel coordinates is applied to the science exposures (*lower left*) exposures. Each slit is saved as a new *FITS* image which is ready to be wavelength calibrated (*lower right*).

```
from SAMOS_DRP.DoWavecal import WaveCalBuckets
```

```
SAMOS_wavecal = WaveCalBuckets(SAMOS_slits)
SAMOS_wavecal()
```

Each science exposure is paired with a calibration lamp. Calibration lamps, or arc lamps, are comprised of gas with emission lines which have been measured in a laboratory setting. Calibration lamp exposures are taken during the observing night so that each science spectrum is calibrated to the correct grating/filter setting. Each slit in the mask is paired with its own set of arc lamp exposures. Therefore, we must choose an arc lamp that features emission lines that are also present in the science spectrum.

The angular dispersion of a grating is the change in angle of diffraction per change in wavelength ($\text{\AA}/\text{arcsec}$). The simple diagram in Figure 5.4 shows how a spectrum is produced. The main source of light passes through a slit and is dispersed by a diffraction grating, after which the spectrum is

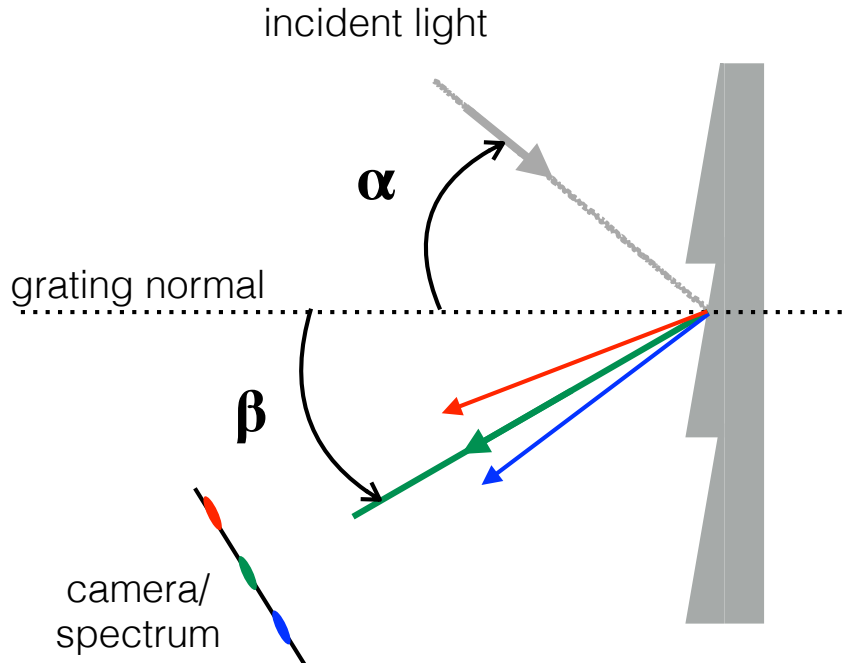


Figure 5.4: **Cartoon diffraction grating.** Simplified depiction of how source light is dispersed by a diffraction grating and becomes a spectrum.

projected onto the CCD. The angular dispersion is related to linear dispersion by the plate scale (arcsec/pixel). Therefore, the solution requires us to compare the linear pixel distance between emission lines in the uncorrected arc lamp exposure to change in wavelength $\Delta\lambda$. It should be noted that the wavelength calibration for the *SAMOS* pipeline is not original code and it performs the fit using procedures from the GSP (Torres-Robledo & Briceño, 2019). The *SAMOS* pipeline will be updated to work with real *SAMOS* data in the future, with the GSP code as a solid foundation. The GSP simplifies the wavelength calibration process with a library of reference lamps with wavelength solutions for multiple grating/filter configurations which have already been calibrated. The use of a pre-fitted calibration spectrum means that the lines only need to be identified once, and then applied to future spectra.

For a given arc lamp, the pipeline steps along the dispersion axis and collects pixel locations for lines which meet a certain count threshold. We are fitting to a model that matches a linear pixel distance from a central point to a change in wavelength. However, the mapping between pixels and wavelength is not necessarily linear, and the linear approximation can break down if the spectrum

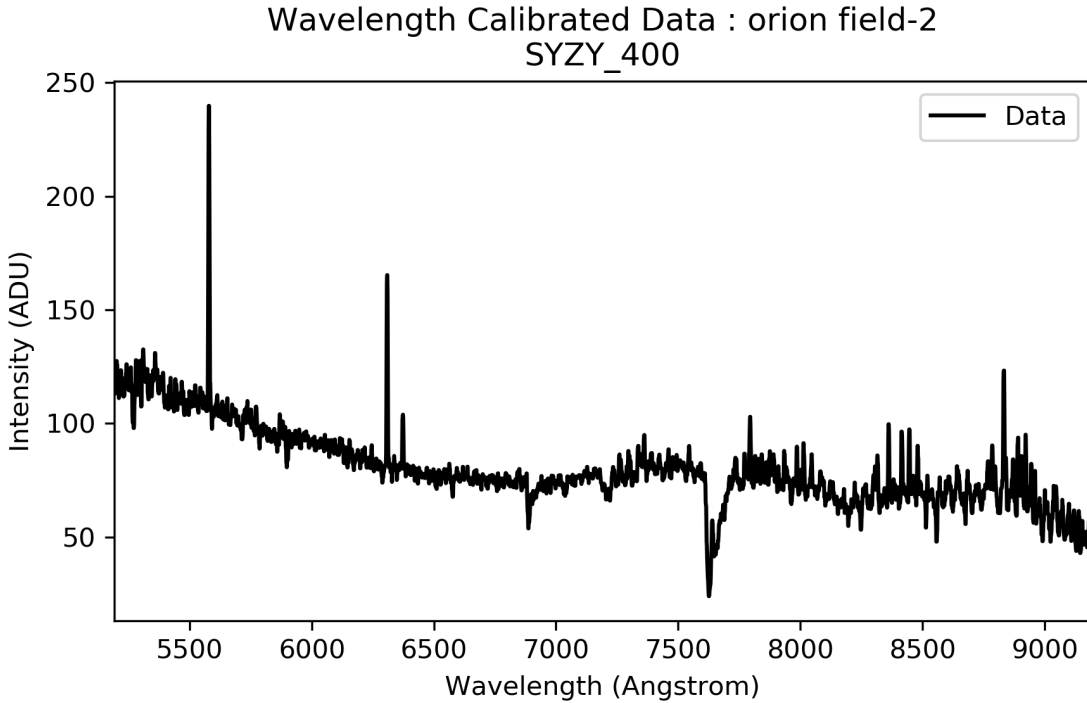


Figure 5.5: Wavelength calibrated spectrum output for *SAMOS* pipeline. Final wavelength calibrated spectrum for extracted slit. Spectrum does not include background subtraction or flux calibration.

is distorted. Finding the coefficients for the non-linear model is made simpler with a low order first-guess solution from the reference arc exposure. The pre-fitted reference lamp contains a list of emission lines with their pixel and angstrom values, along with its best fit solution stored as the coefficients of a polynomial model³. With the approximate wavelength solution, the pipeline interpolates over the locations of the known lines to estimate wavelengths of the unknown features in the spectrum. Once we have a pixel-to-angstrom map, we can convert the dispersion axis in the science exposures from pixels to angstroms. An example of the final wavelength calibrated spectrum is provided in Figure 5.5.

5.6 Remaining steps

While the pipeline is able to produce a wavelength calibrated spectrum for the test data, there is still much to be done before *SAMOS* is commissioned in 2021, and development of the pipeline

³The current pipeline version is only able to handle a Chebyshev1D model from `astropy.models`, but will be expanded in the future.

is ongoing. The remaining high priority reduction steps are described below.

- Flux calibration: The flux of an object is captured by the CCD in photon counts. Because CCDs have different sensitivities across their pixels, the pipeline will need to produce a fit to the sensitivity function and scale the photon counts to units of magnitude. Flux calibration will use the continuum emission for a standard star exposure.
- Background subtraction: Spectra contain emission from the sky within the line of sight of an object. This background emission needs to be subtracted from the science spectra. One technique for sky subtraction is nod-and-shuffle, wherein the source is shuffled between the lower edge of a slit and the upper edge. By having spectrum cover different regions of the slit, the sky emission at the opposite end can be characterized to a higher degree of accuracy.
- Tracing/Spectral extraction: As mentioned previously, spectra can be distorted with respect to the spatial axis. Currently, the SRP uses a crude method of spectral extraction which will be updated to include a routine that traces the distortion, and then extracts a spectrum based on that trace.

In addition to the remaining data reduction procedures, the SRP will include a suite of settings such that user will be able to have more control over what data is reduced and how. Right now, the user only has the options to name the directory of the data output, and whether to include flat or bias correction. A future version will include options to choose specific types of exposures, places to pause and restart the pipeline, and other features that allow the user to customize their data reduction. Before *SAMOS* is taken to *SOAR*, we plan to test the pipeline using simulated data from SAMOS. The test data from *Goodman* will therefore be replaced with simulated data from SAMOS, which should make the transition from testing to science even easier.

SAMOS will be an exciting addition to *SOAR*. As a multi-object spectrograph, it will allow an observer to take spectra of multiple targets within a single exposure, which is particularly useful for observations of galaxy clusters. *SAMOS* will be able to maximize its multi-object capabilities, as it will be able to create a number of slit mask patterns throughout the night. This key aspect

makes *SAMOS* a highly anticipated instrument, and it has received a no-cost extension and access to reserve funds to aid in completion by Summer, 2021. We have been able to build a strong foundation for the *SAMOS* pipeline using methods from the *Goodman* spectroscopic pipeline (Torres-Robledo & Briceño, 2019) and data reduction packages provided by Price-Whelan et al. (2018), and we are actively making progress towards completion.

APPENDICES

APPENDIX A

BOLOMETRIC AND K- CORRECTION PROCEDURE

The code below shows the procedure used for making corrections to bolometric and rest-frame fluxes and luminosities. The code reads in a .CSV file with the names, redshifts, temperatures, and metallicities of the clusters. Then it simulates observed fluxes for each cluster, along with the bolometric and rest-frame luminosities. The main procedure is described in Chapter 2.3. Below shows the *XSPEC* code used to simulate the observed fluxes and luminosities used to compute the correction factors.

```
# set cosmology to H0=70 q0=-0.55 Omega_Lambda=0.7
cosmo 70 -0.55 0.7

# set energy grid to cover a large range
energies 0.05 100.0 10000 log

set outfile [open outfile w+]

set f [open nocore_lumcorr_input] #read in cluster data from file
set lines [split [read $f] '\n']
close $f

puts "$lines"

# make simulated spectra
foreach row $lines {

    set line [split $row ',']
    
```

```

set name [lindex $line 0]
puts "name is $name"
set z [lindex $line 1]
puts "redshift is $z"
set T [lindex $line 2]
set Zsol [lindex $line 3]

puts "kT, Zsol, z is $T, $Zsol, $z"

# set mekal model params kT, nH, Zsolar, redshift, Switch, Normalization
model mekal
$T #set temperature
1.0
$Zsol
$z
1
1.e-4

# store the first number in the string from tclout
# into variables fluxout,lum05_70,lum_bol
flux 0.5 7.0
tclout flux
set fluxout [string range $xspec_tclout 0 [string first " " $xspec_tclout
]]
lum 0.5 7.0 $z
tclout lum ;
set lum05_70 [string range $xspec_tclout 0 [string first " " $xspec_tclout
]]

```

```

]]]

lum 0.1 100.0 $z

tclout lum

set lum_bol [string range $xspec_tclout 0 [string first " " $xspec_tclout
]]

# save kT, Zsol, z, fluxout, lum05_70, lumbol to file
# Luminosities are in units of 1e44 erg/s

puts $outfile "'$name,$T,$Zsol,$z,$fluxout,$lum05_70,$lum_bol'" ;
# writes line to file
}

close $outfile

```

The simulated fluxes are read in from the *XSPEC* results and used to compute an observed luminosity with $L \propto F((1+z)d)^2$, where F is the flux and d is the co-moving or Hubble distance of the cluster (section 1.2.1). Then we create the correction factor for each cluster as the ratio of the corrected-to-observed luminosity (and correction type) in the simulated clusters. These correction factors were multiplied by the observed luminosities in the real data. Below shows the general code used to compute the corrected luminosity for each cluster. This version has been simplified to show the main parts.

```

import numpy as np
import cosmocalc as cosmo
import pandas as pd

H0 = 70
WM = 0.3

SIMdata = pd.read_csv(sim_file)
A2data = pd.read_csv(ACCEPT2.0_data)

```

```

cosmo = cosmocalc( A2data[ 'z' ] ,H0,WM1-WM)

DL = cosmo[ 'DL_cm' ]

sim_flx = SIMdata.loc[ 'fluxout' ] #simulated flux
sim_restlum = SIMdata[ 'rest_lum' ]
sim_bollum = SIMdata[ 'bol_lum' ]

sim_obsLum = ( sim_flx*4*np.pi*DL**2)/1e44

uncorr_lum = A2data[ 'Lx' ] #uncorrected luminosity and error from
    ACCEPT2.0
uncorr_lumerr = A2data[ 'Lxe' ]

r_corr = sim_restlum/(obsLum) #correction factors from simulated
    data
b_corr = sim_bollum/(obsLum)

newLx_rest,newLx_restErr = uncorr_lum*r_corr,uncorr_lumerr*r_corr
    #multiply by observed luminosities
newLx_bol,newLx_bolErr = uncorr_lum*b_corr,uncorr_lumerr*b_corr

```

APPENDIX B

RADIAL ABUNDANCE PROFILES FOR ACCEPT2.0 CLUSTERS

Radial metallicity profiles for 154 ACCEPT2.0 clusters. (For a description, see Chapter 2.)

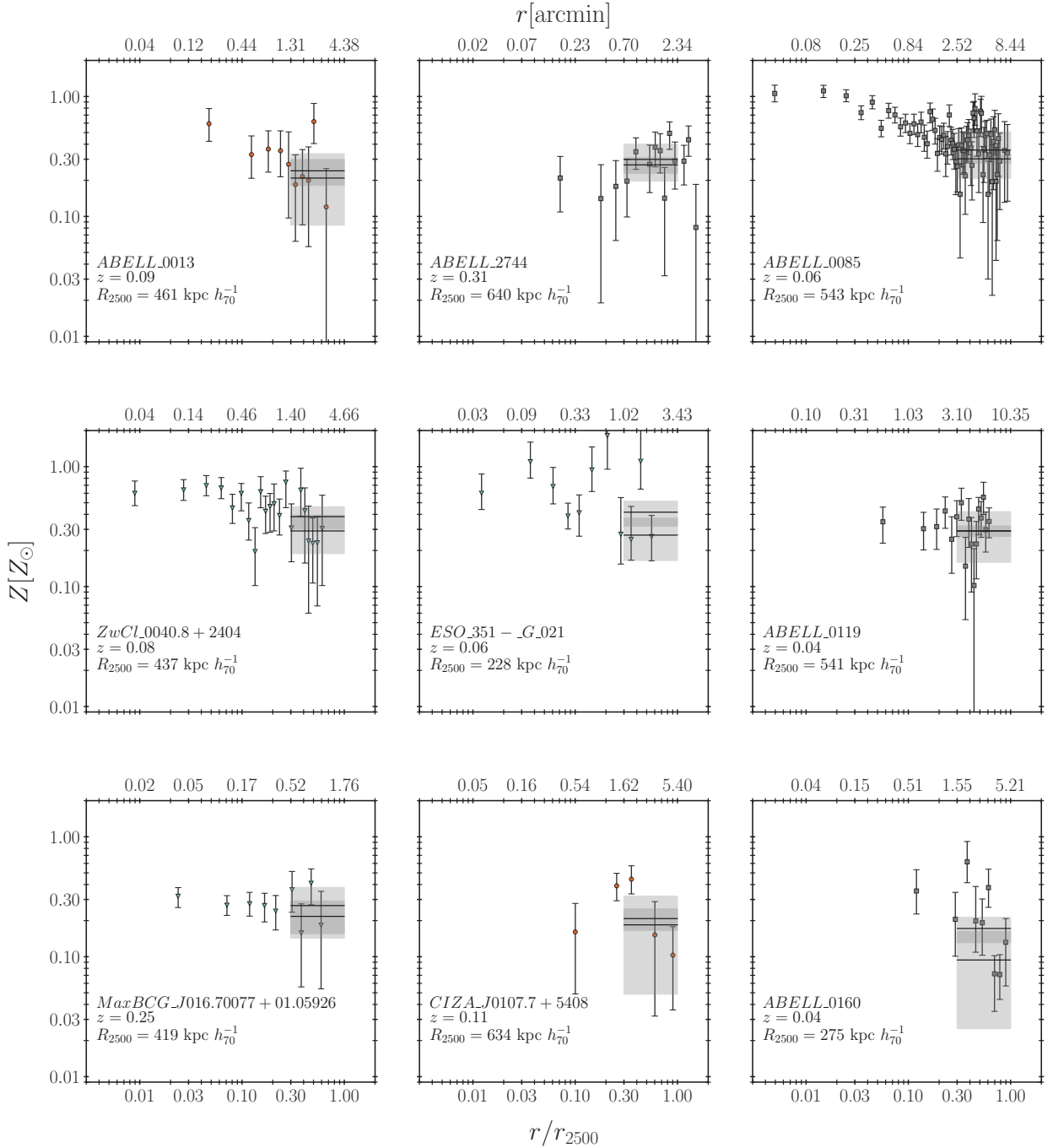


Figure B.1: Radial metallicity profile for clusters A0013 through A0160. Radial metallicity profiles for the following clusters: A0013, A2744, A0085, 00408+2404, 351-021, A0119, 01670077+0105926, 01077+5408, A0160.

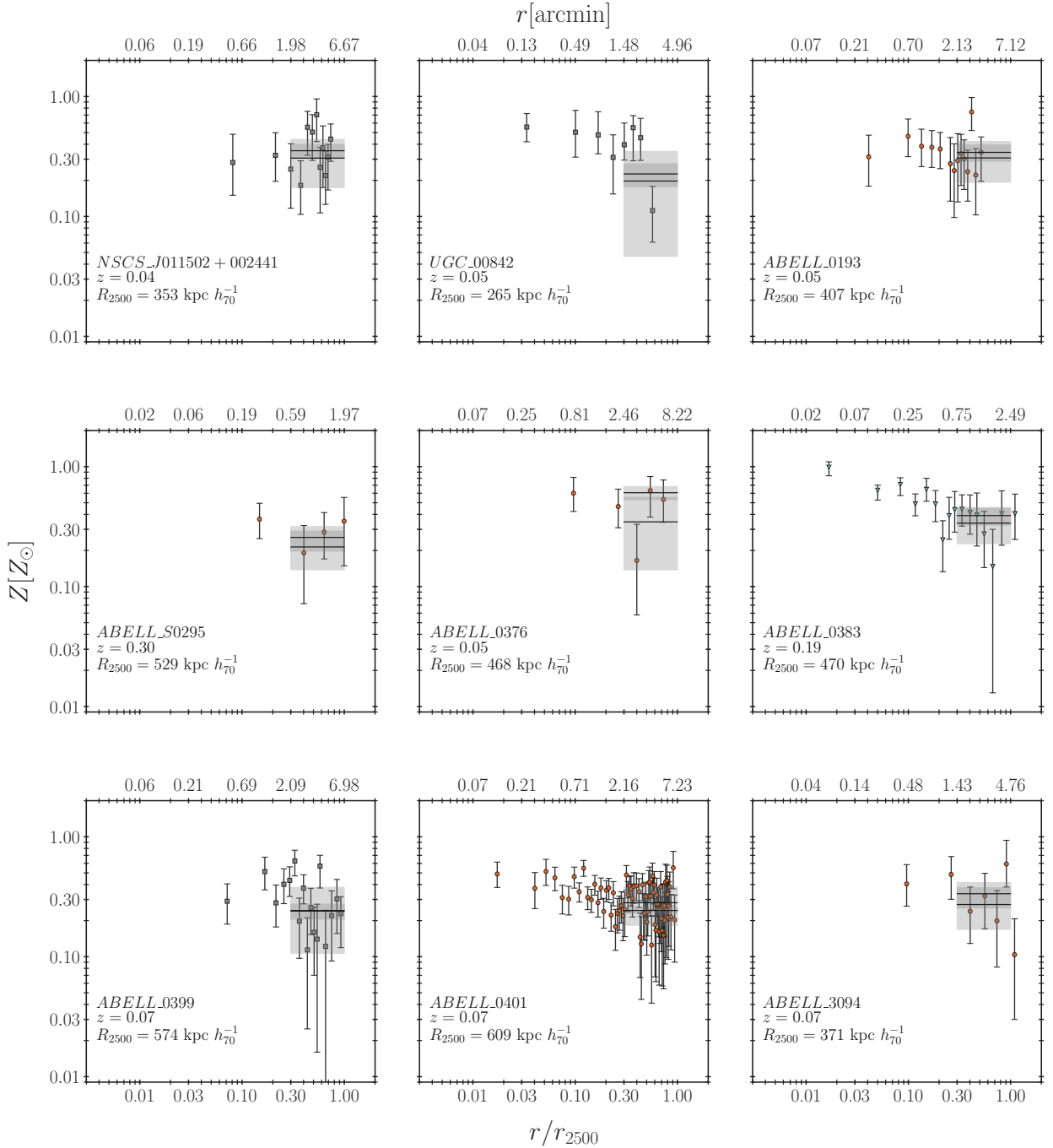


Figure B.2: Radial metallicity profile for clusters 011502+002441 through A3094. Radial metallicity profiles for the following clusters: 011502+002441, UGC00842, A0193, AS0295, A0376, A0383, A0399, A0401, A3094.

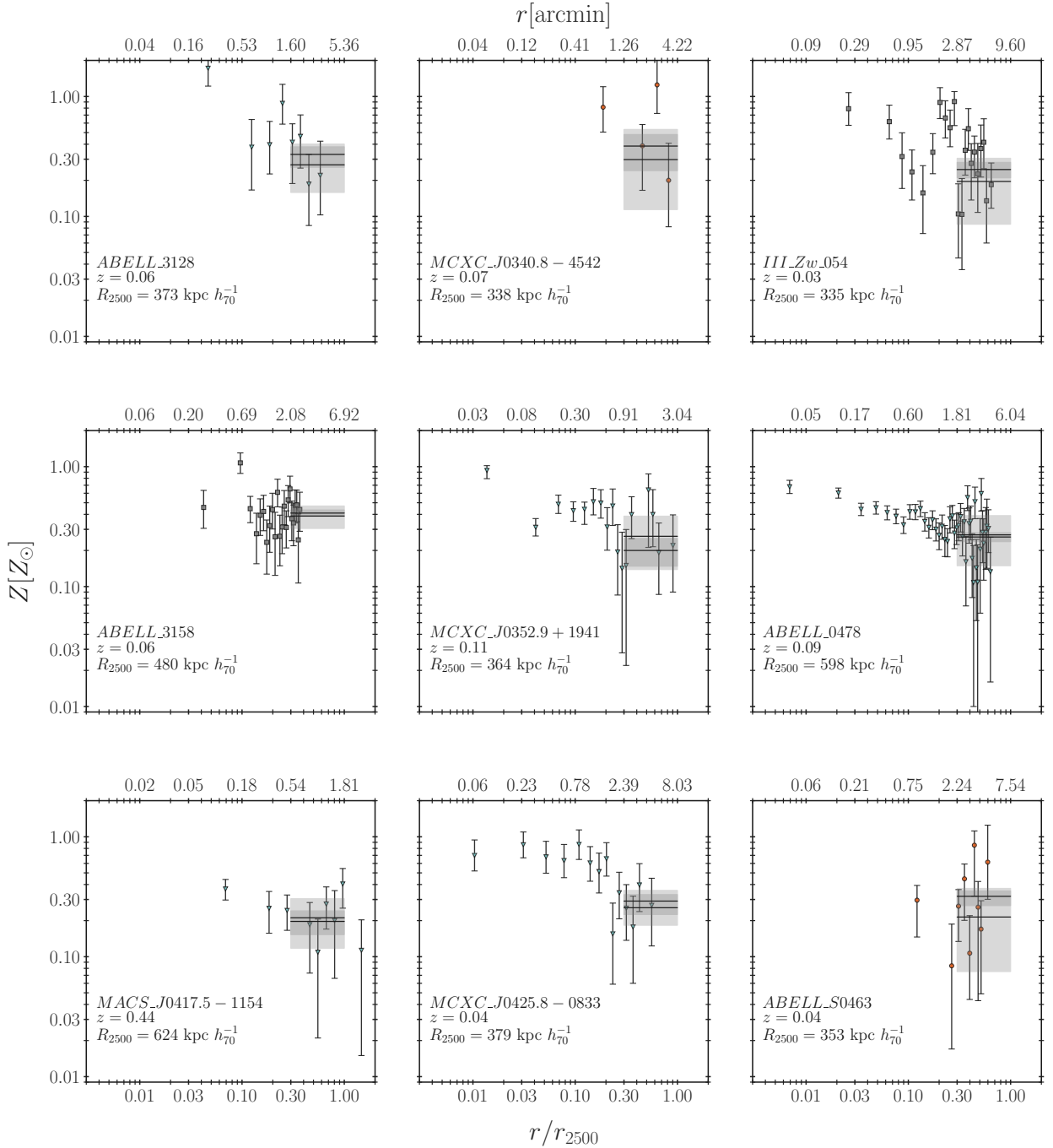


Figure B.3: Radial metallicity profile for clusters A3128 through AS0463. Radial metallicity profiles for the following clusters: A3128, 03408-4542, IIIZw054, A3158, 03529+1941, A0478, 04175-1154, 04258-0833, AS0463.

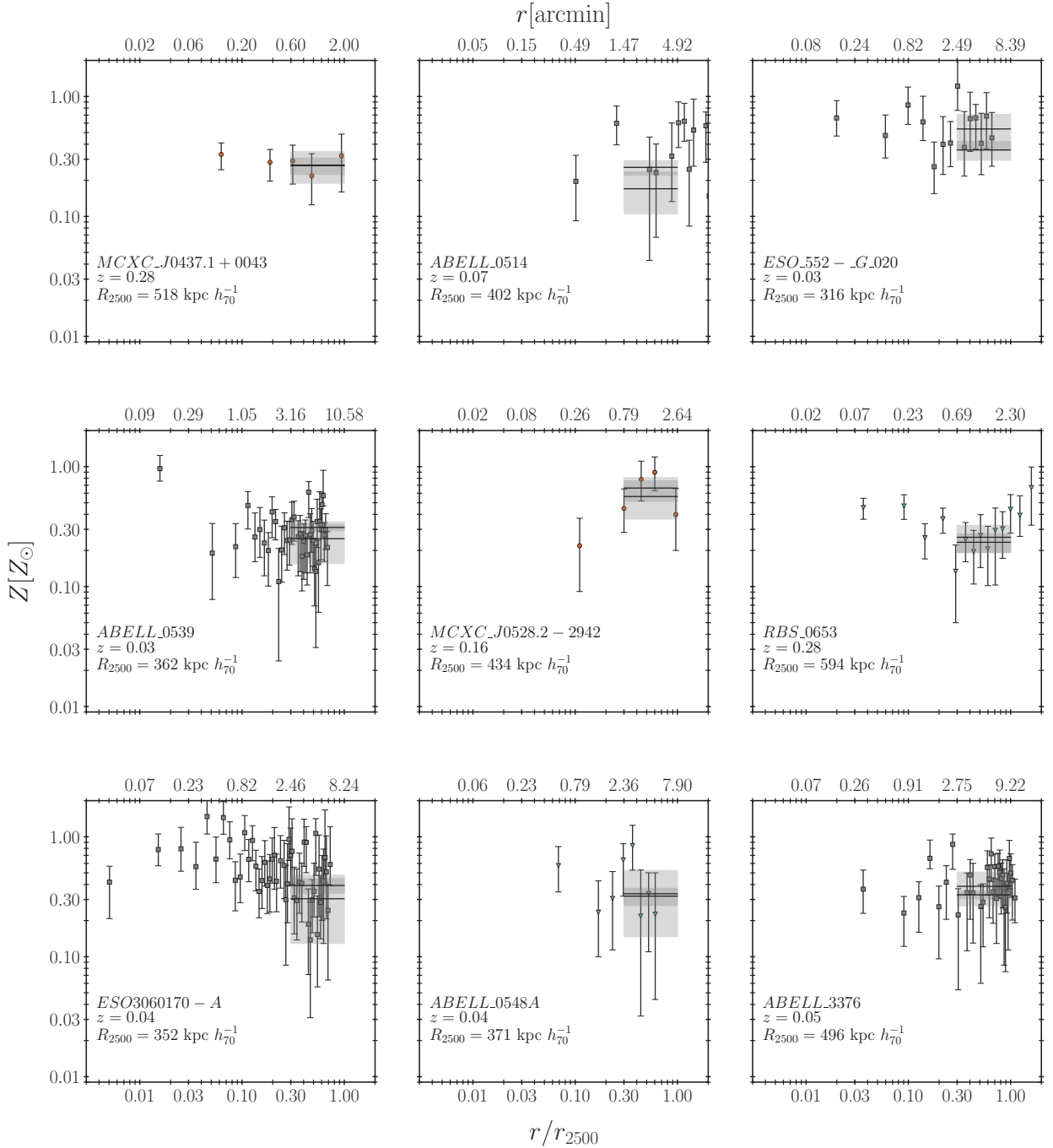


Figure B.4: Radial metallicity profile for clusters 04371+0043 through A3376. Radial metallicity profiles for the following clusters: 04371+0043, A0514, 552-020, A0539, 05282-2942, RBS0653, 3060170-, A0548A, A3376.

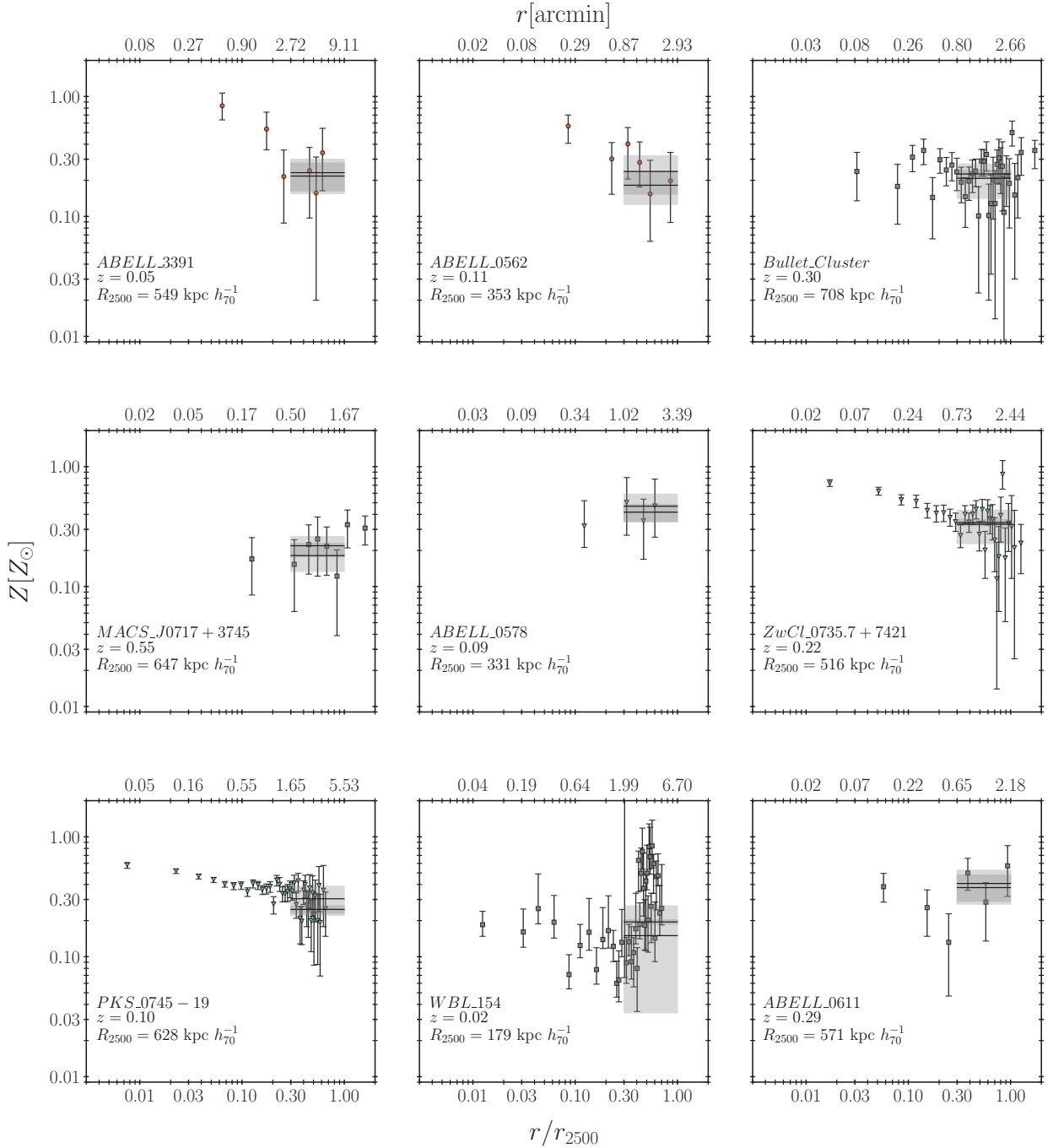


Figure B.5: Radial metallicity profile for clusters A3391 through A0611. Radial metallicity profiles for the following clusters: A3391, A0562, , 0717+3745, A0578, 07357+7421, PKS0745-19, WBL154, A0611.

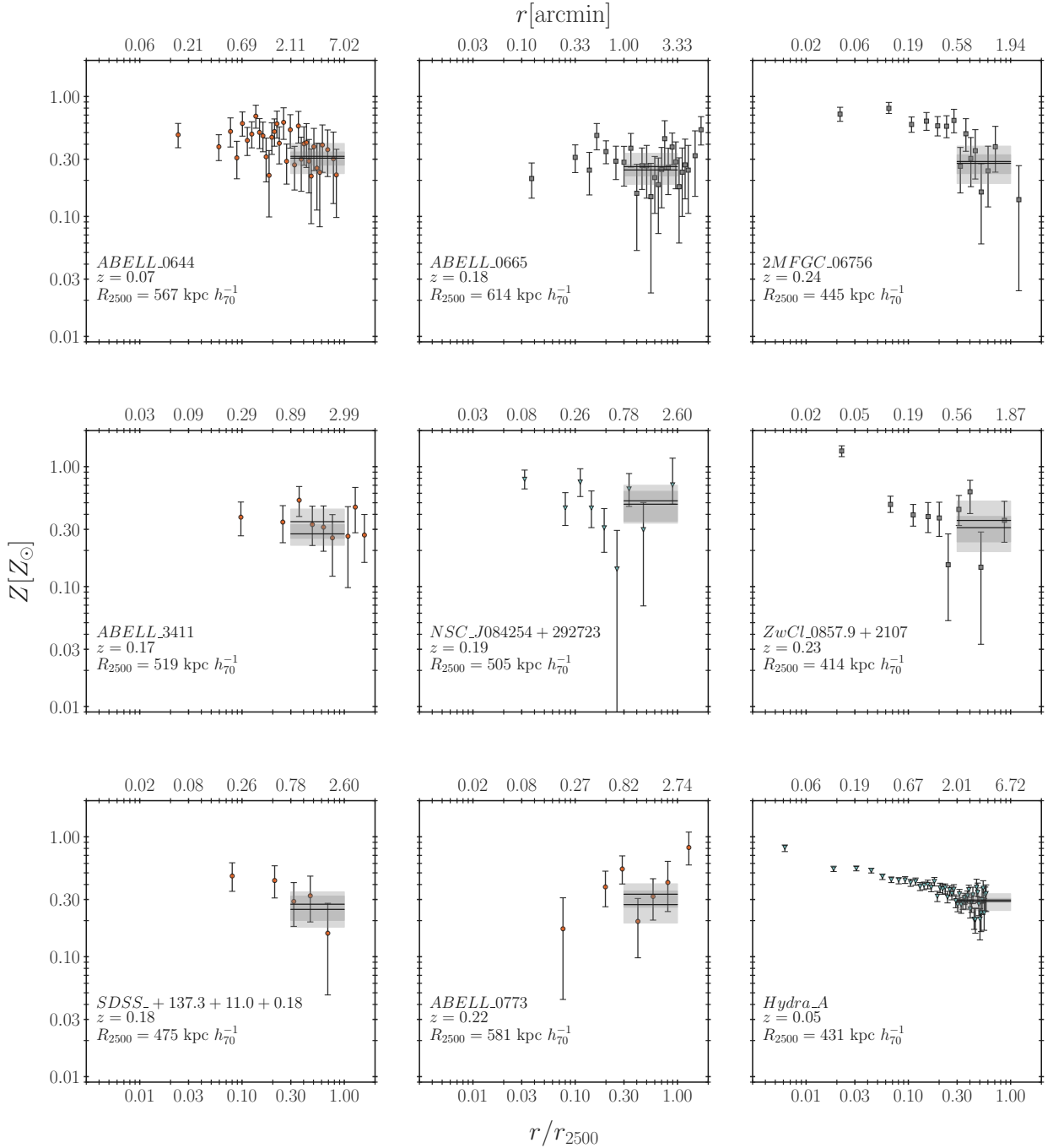


Figure B.6: Radial metallicity profile for clusters A0644 through HydraA. Radial metallicity profiles for the following clusters: A0644, A0665, 2MFGC06756, A3411, 084254+292723, 08579+2107, +1373+110+018, A0773, HydraA.

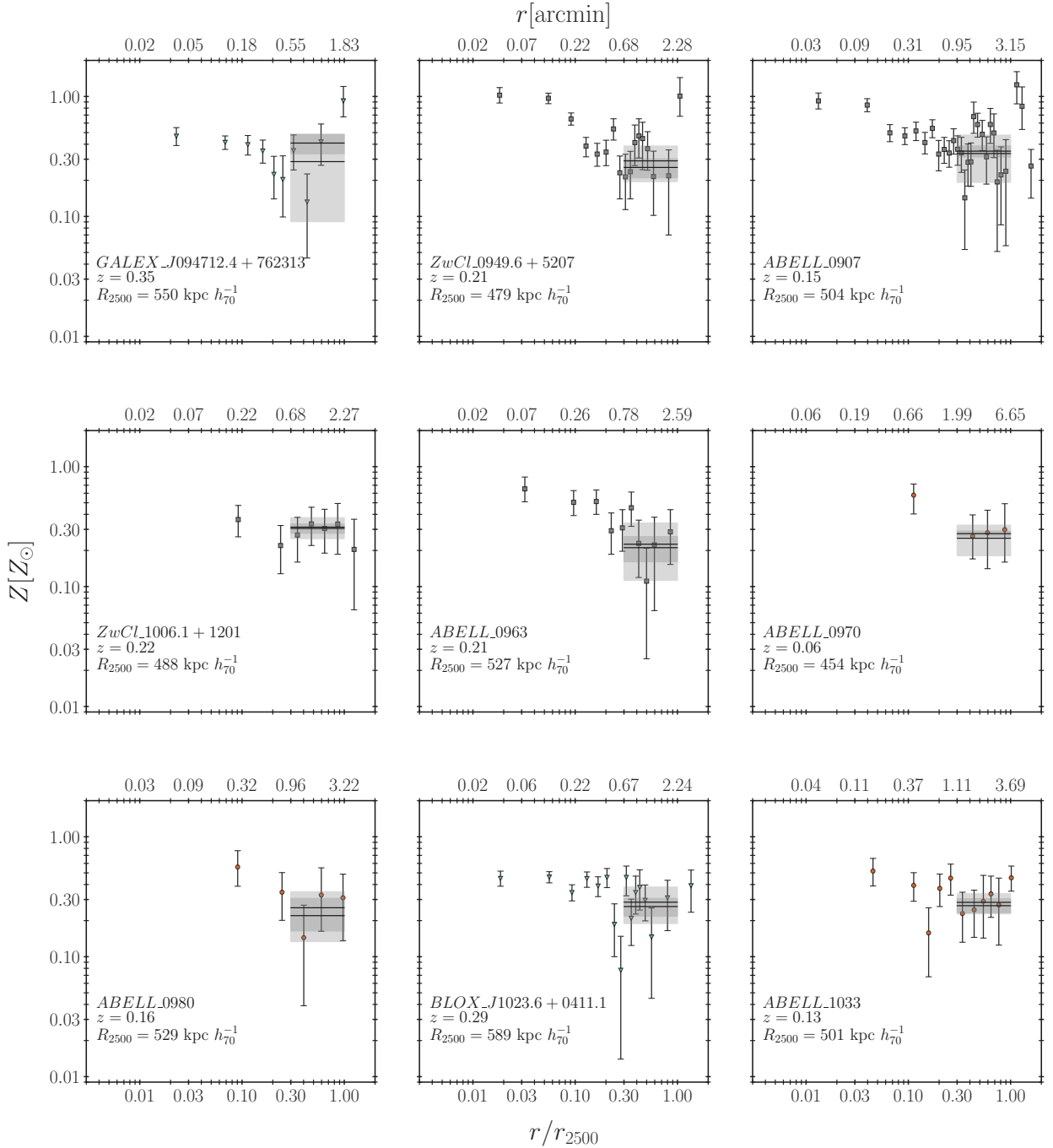


Figure B.7: Radial metallicity profile for clusters 0947124+762313 through A1033. Radial metallicity profiles for the following clusters: 0947124+762313, 09496+5207, A0907, 10061+1201, A0963, A0970, A0980, 10236+04111, A1033.

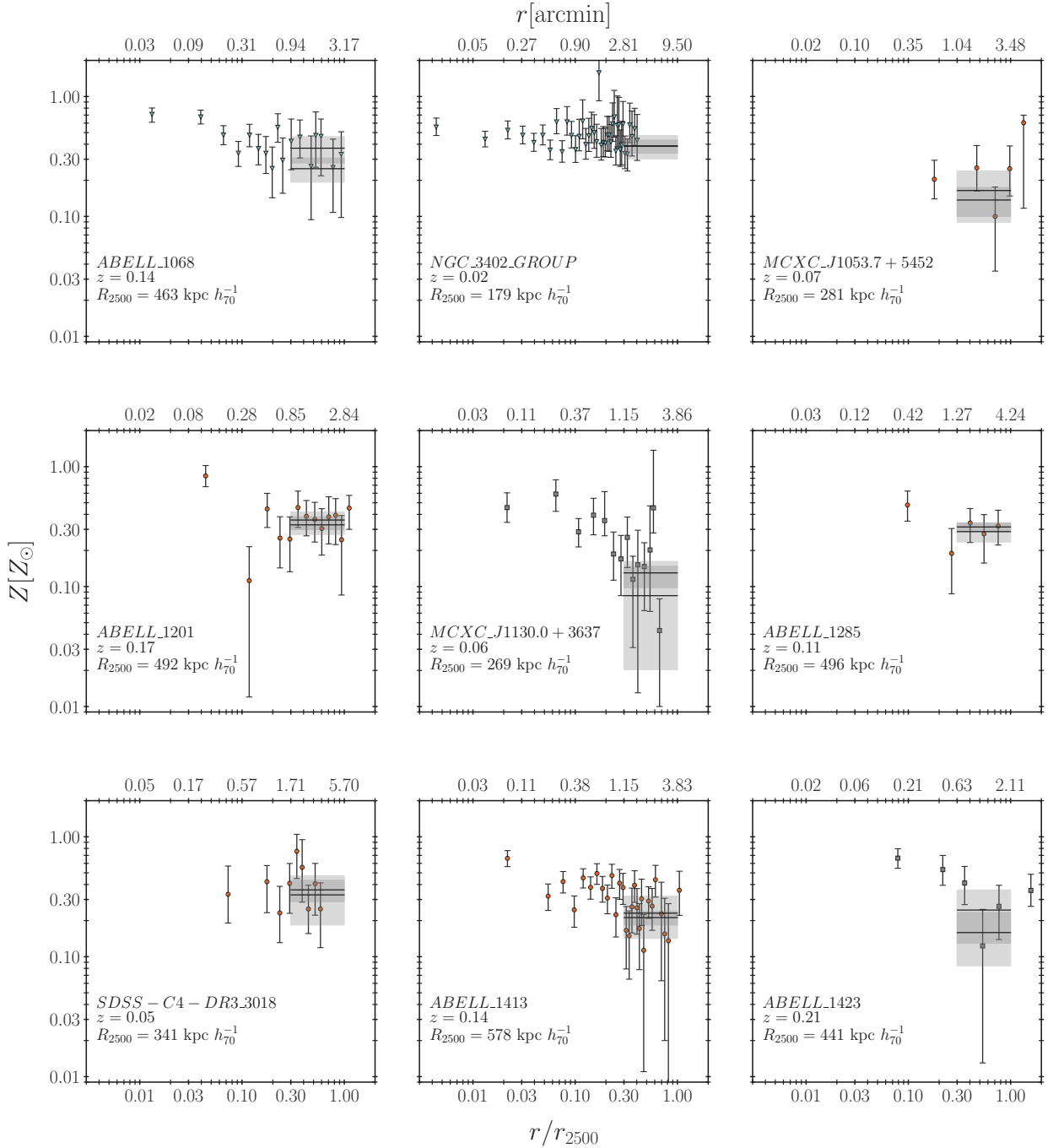


Figure B.8: Radial metallicity profile for clusters A1068 through A1423. Radial metallicity profiles for the following clusters: A1068, 3402, 10537+5452, A1201, 11300+3637, A1285, 4-33018, A1413, A1423.

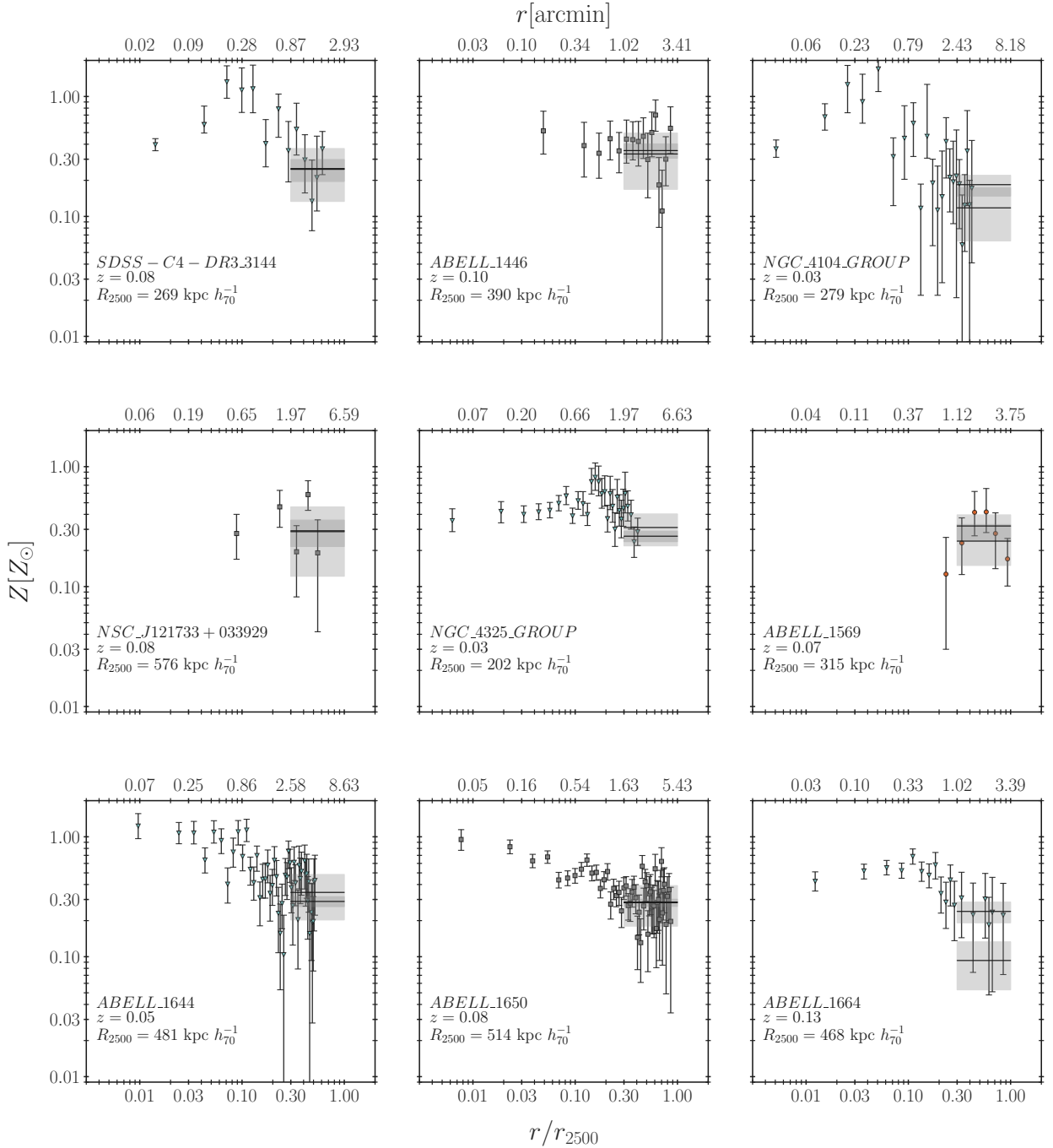


Figure B.9: Radial metallicity profile for clusters 4-33144 through A1664. Radial metallicity profiles for the following clusters: 4-33144, A1446, 4104, 121733+033929, 4325, A1569, A1644, A1650, A1664.

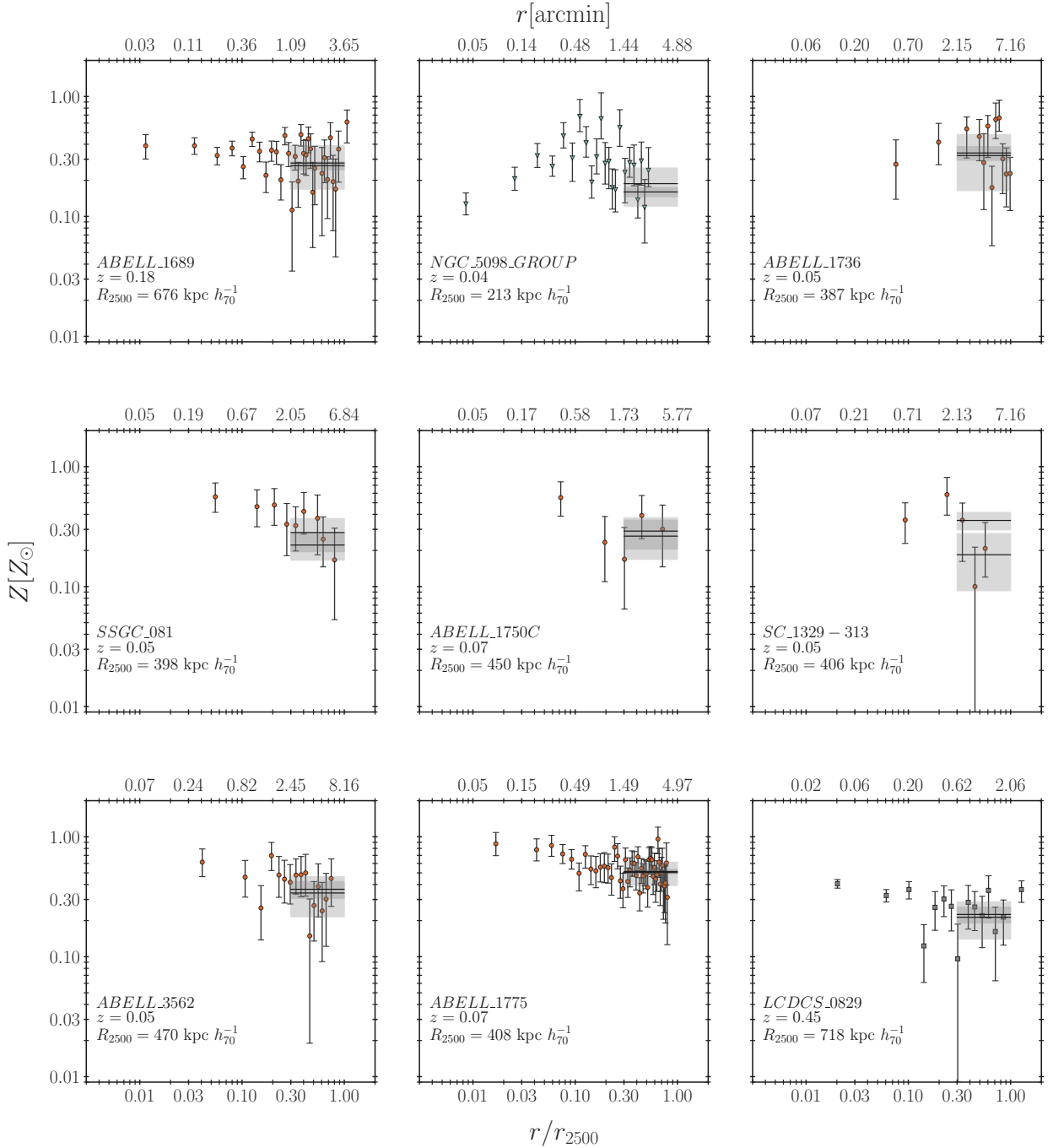


Figure B.10: **Radial metallicity profile for clusters A1689 through LCDCS0829.** Radial metallicity profiles for the following clusters: A1689, 5098, A1736, SSGC081, A1750C, SC1329-313, A3562, A1775, LCDCS0829.

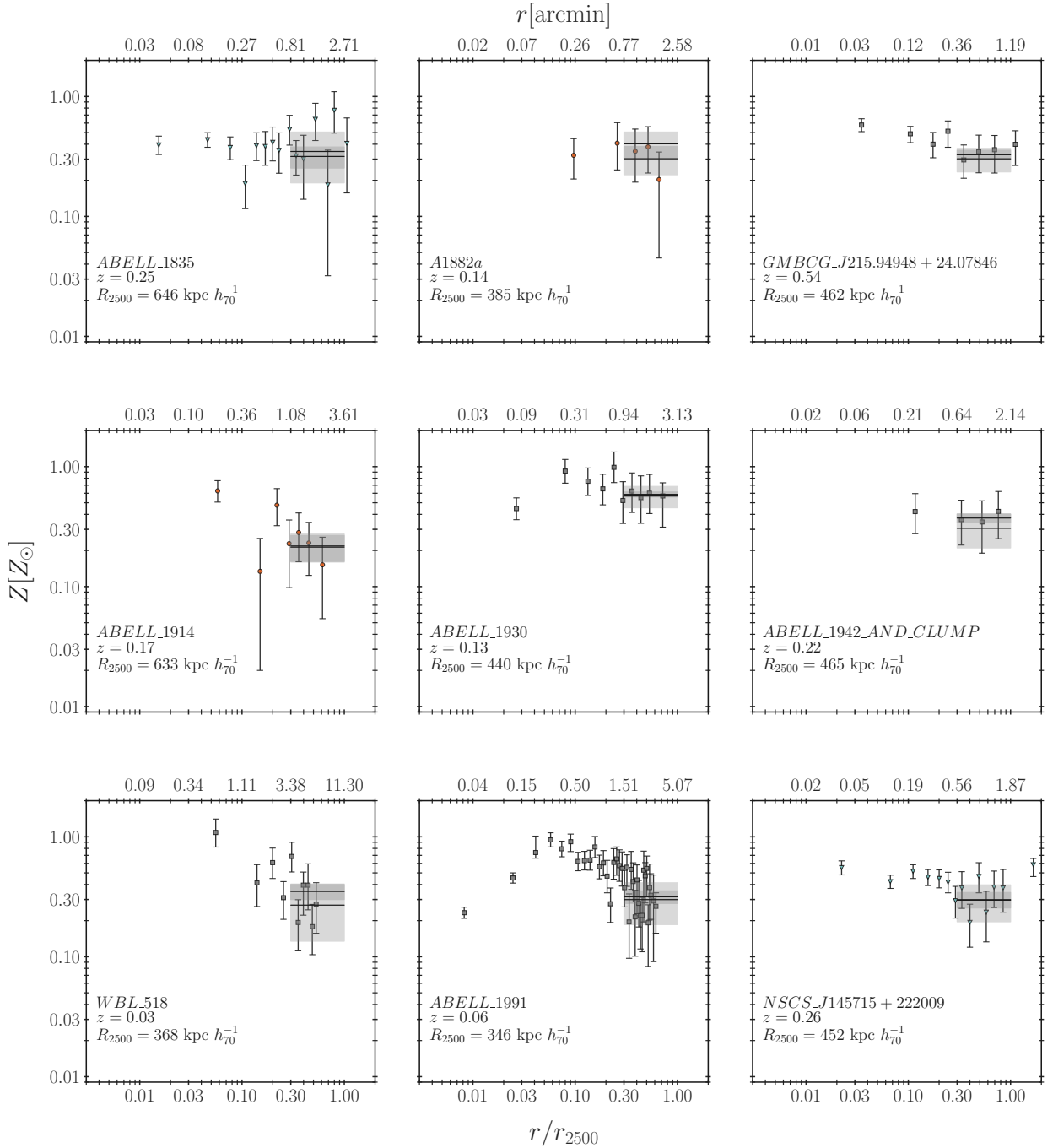


Figure B.11: Radial metallicity profile for clusters A1835 through 145715+222009. Radial metallicity profiles for the following clusters: A1835, A1882a, 21594948+2407846, A1914, A1930, 1942, WBL518, A1991, 145715+222009.

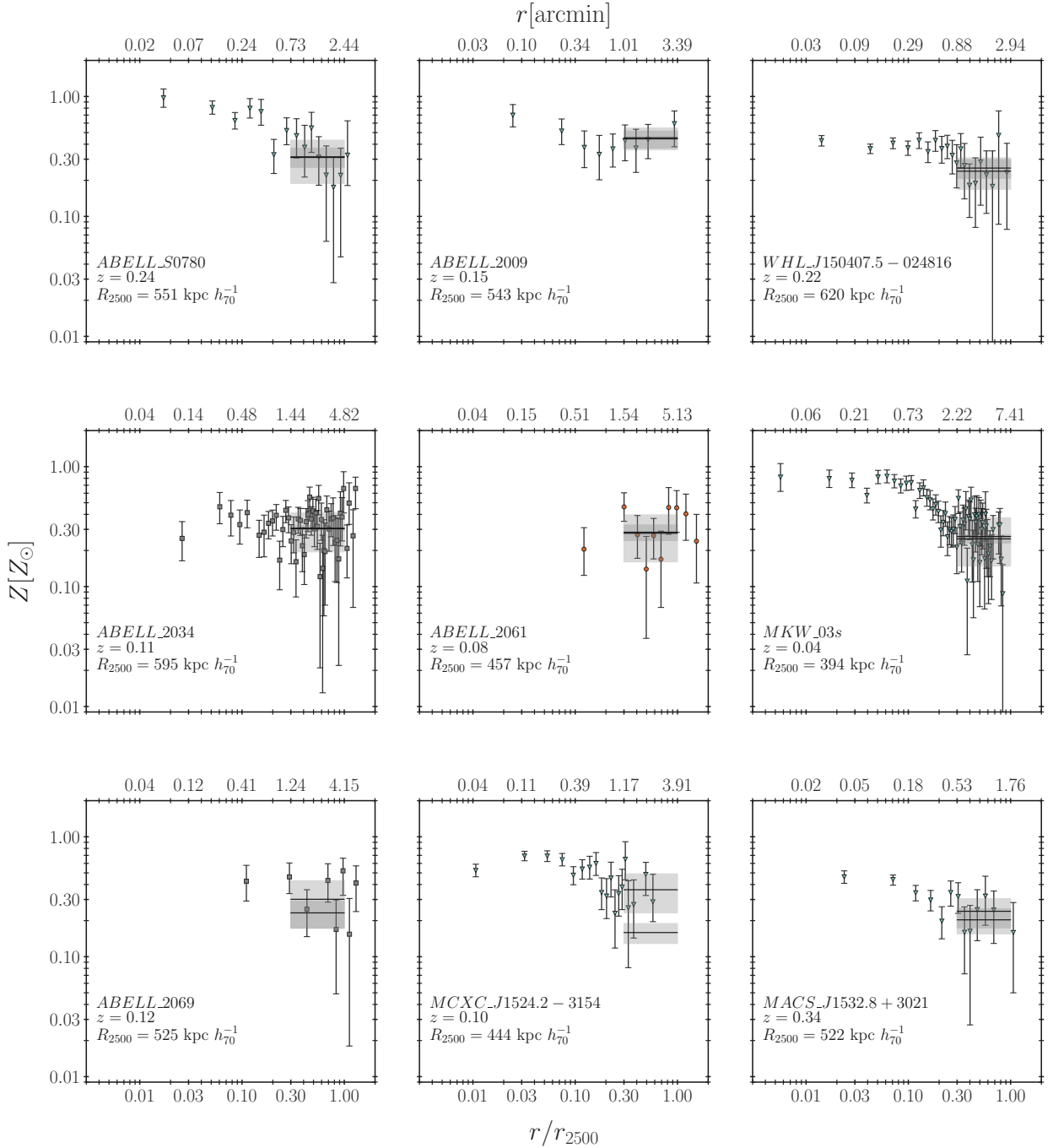


Figure B.12: **Radial metallicity profile for clusters AS0780 through 15328+3021.** Radial metallicity profiles for the following clusters: AS0780, A2009, 1504075-024816, A2034, A2061, MKW03s, A2069, 15242-3154, 15328+3021.

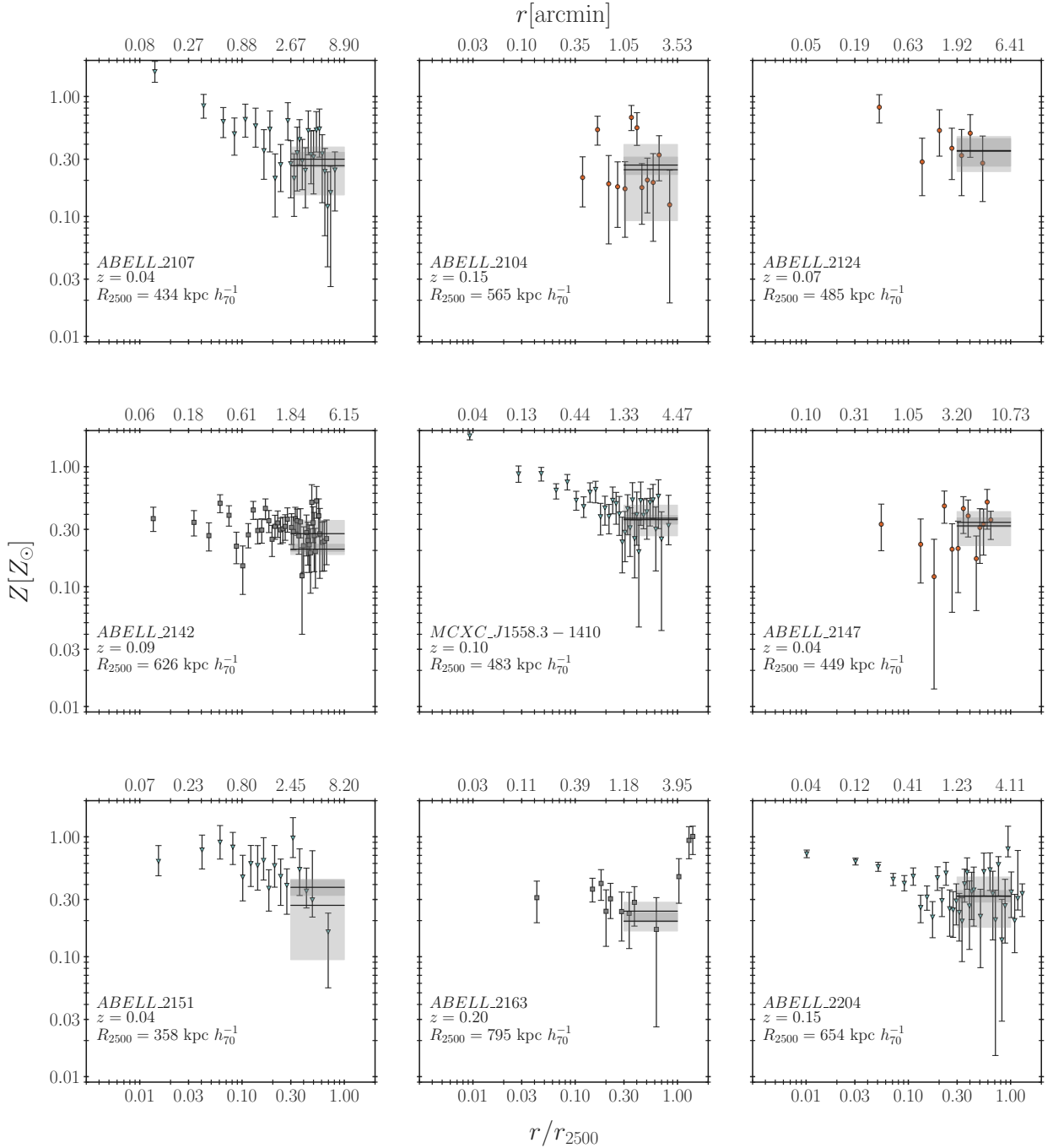


Figure B.13: Radial metallicity profile for clusters A2107 through A2204. Radial metallicity profiles for the following clusters: A2107, A2104, A2124, A2142, 15583-1410, A2147, A2151, A2163, A2204.

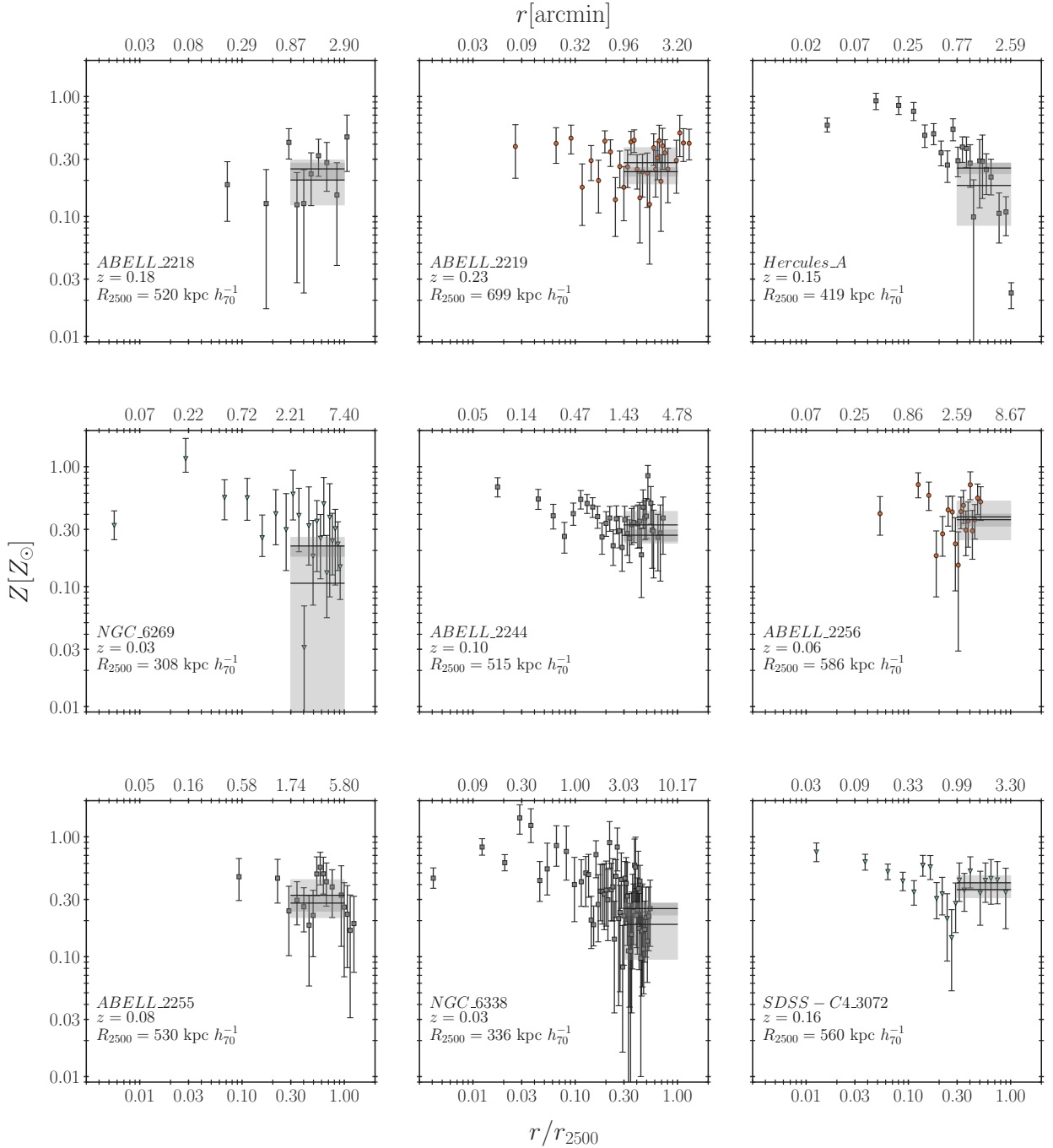


Figure B.14: Radial metallicity profile for clusters A2218 through 43072. Radial metallicity profiles for the following clusters: A2218, A2219, HerculesA, NGC6269, A2244, A2256, A2255, NGC6338, 43072.

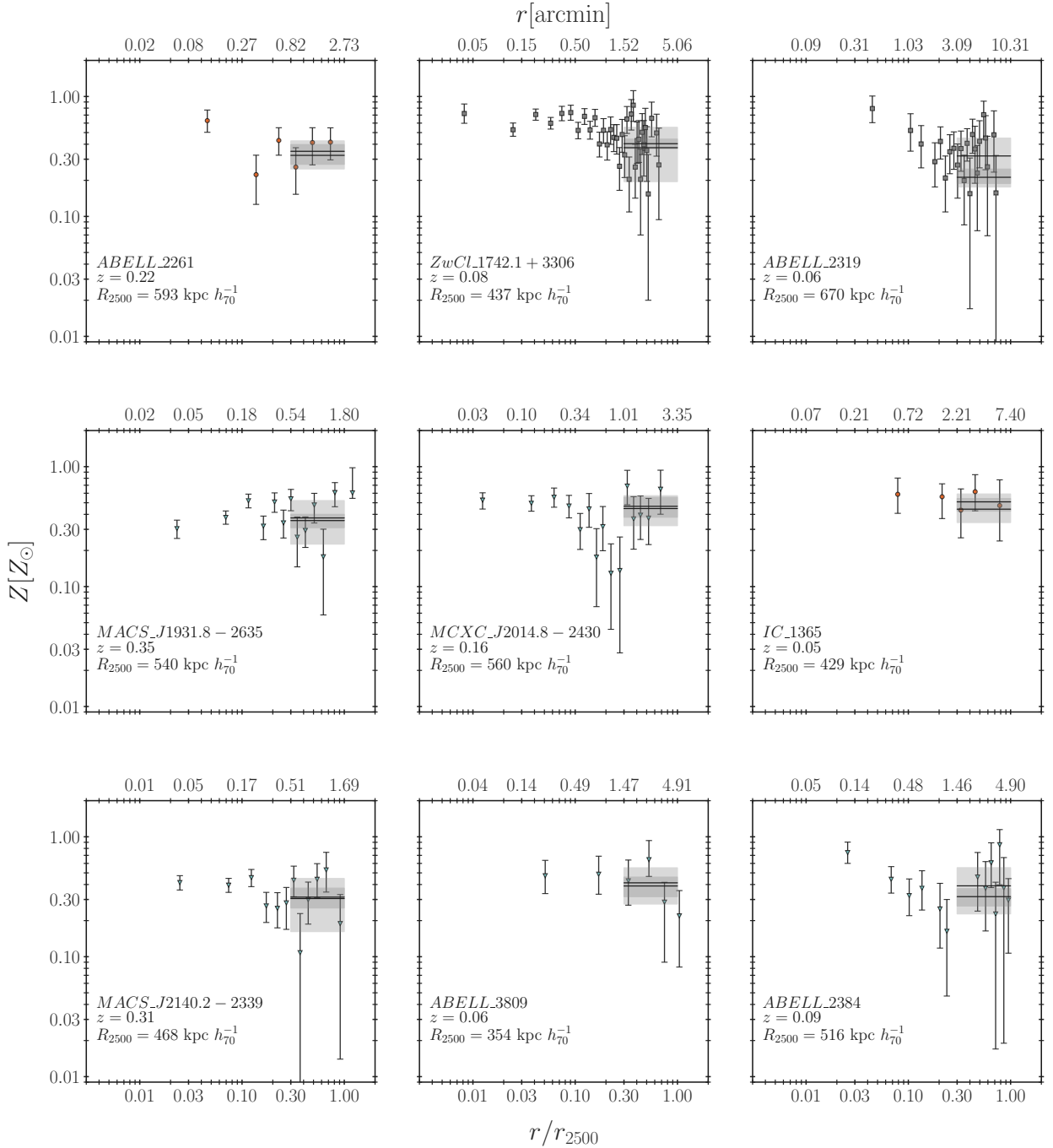


Figure B.15: Radial metallicity profile for clusters A2261 through A2384. Radial metallicity profiles for the following clusters: A2261, 17421+3306, A2319, 19318-2635, 20148-2430, IC1365, 21402-2339, A3809, A2384.

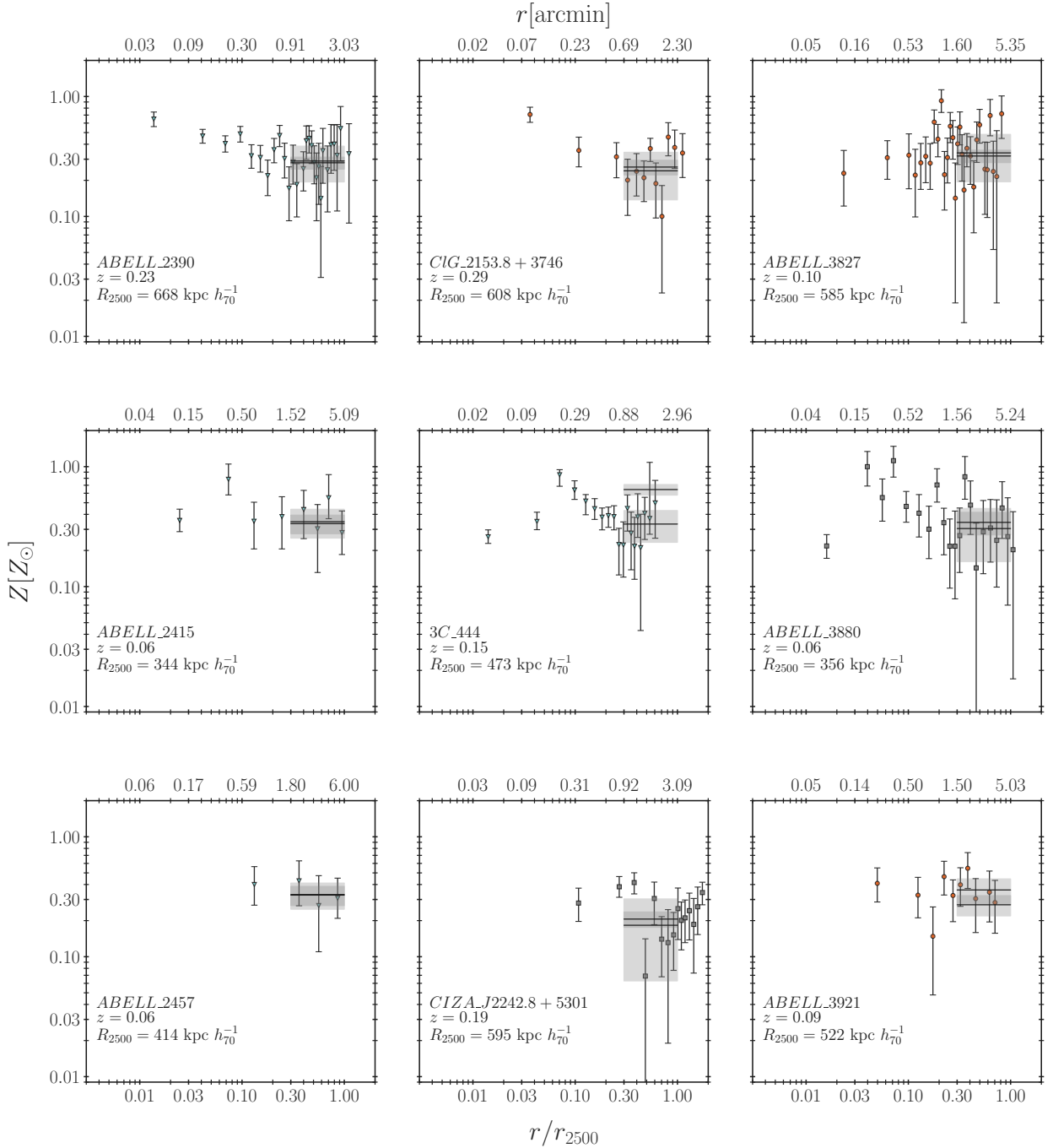


Figure B.16: Radial metallicity profile for clusters A2390 through A3921. Radial metallicity profiles for the following clusters: A2390, 2153+3746, A3827, A2415, 3C444, A3880, A2457, 22428+5301, A3921.

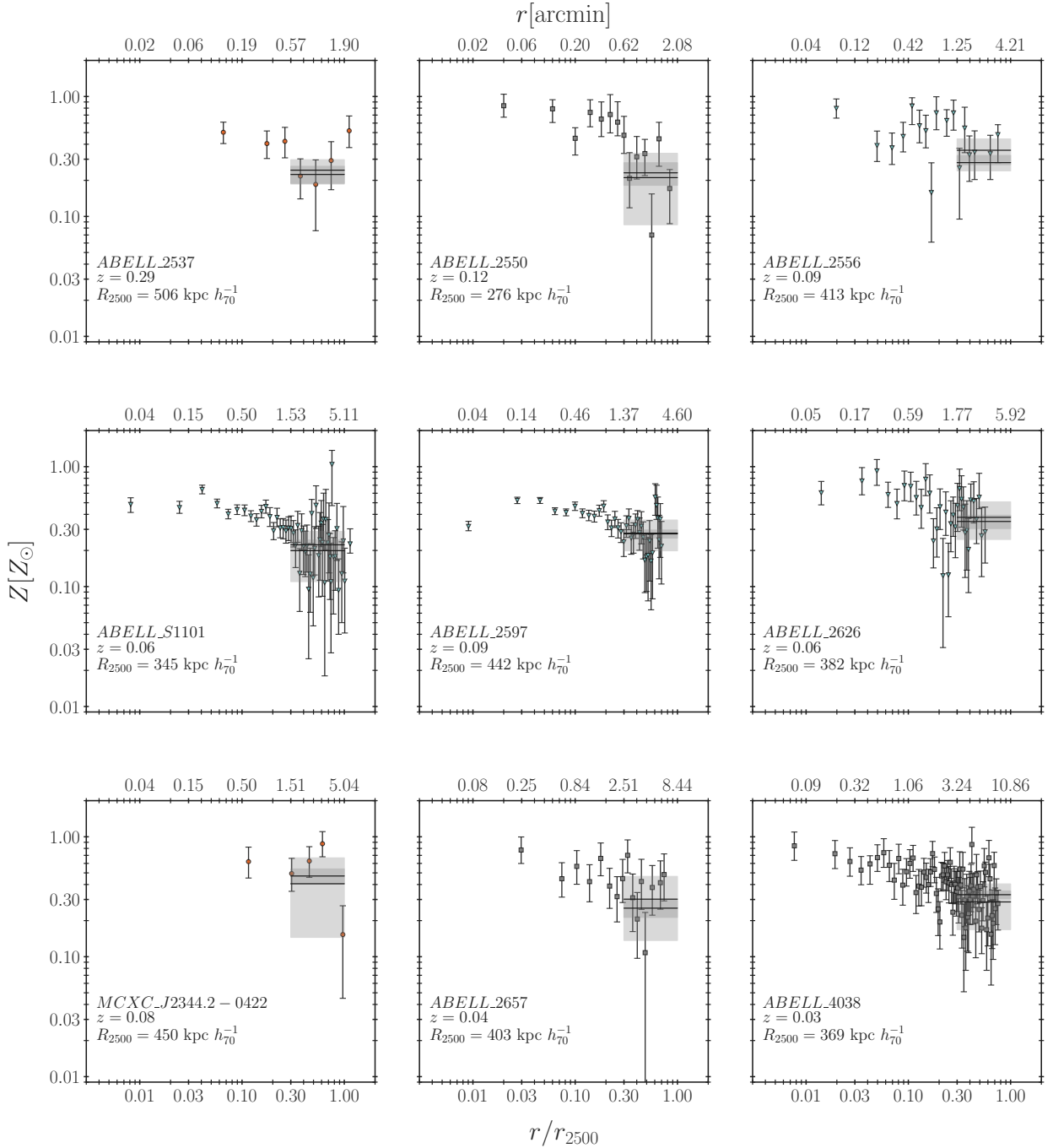


Figure B.17: Radial metallicity profile for clusters A2537 through A4038. Radial metallicity profiles for the following clusters: A2537, A2550, A2556, AS1101, A2597, A2626, 23442-0422, A2657, A4038.

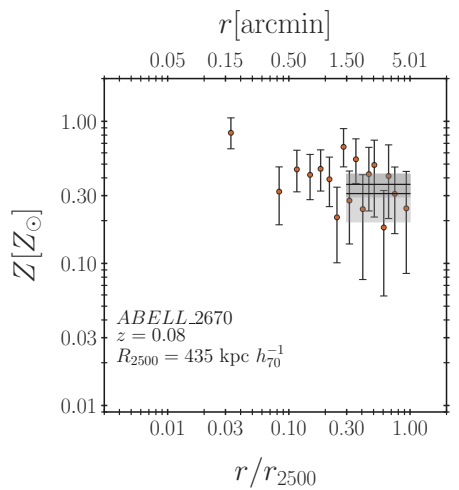


Figure B.18: **Radial metallicity profile for A2670.** Radial metallicity profile for A2670.

APPENDIX C

RADIAL TEMPERATURE PROFILES FOR ACCEPT2.0 CLUSTERS

Radial temperature profiles for 154 ACCEPT2.0 clusters. (For a description, see Chapter 2.)

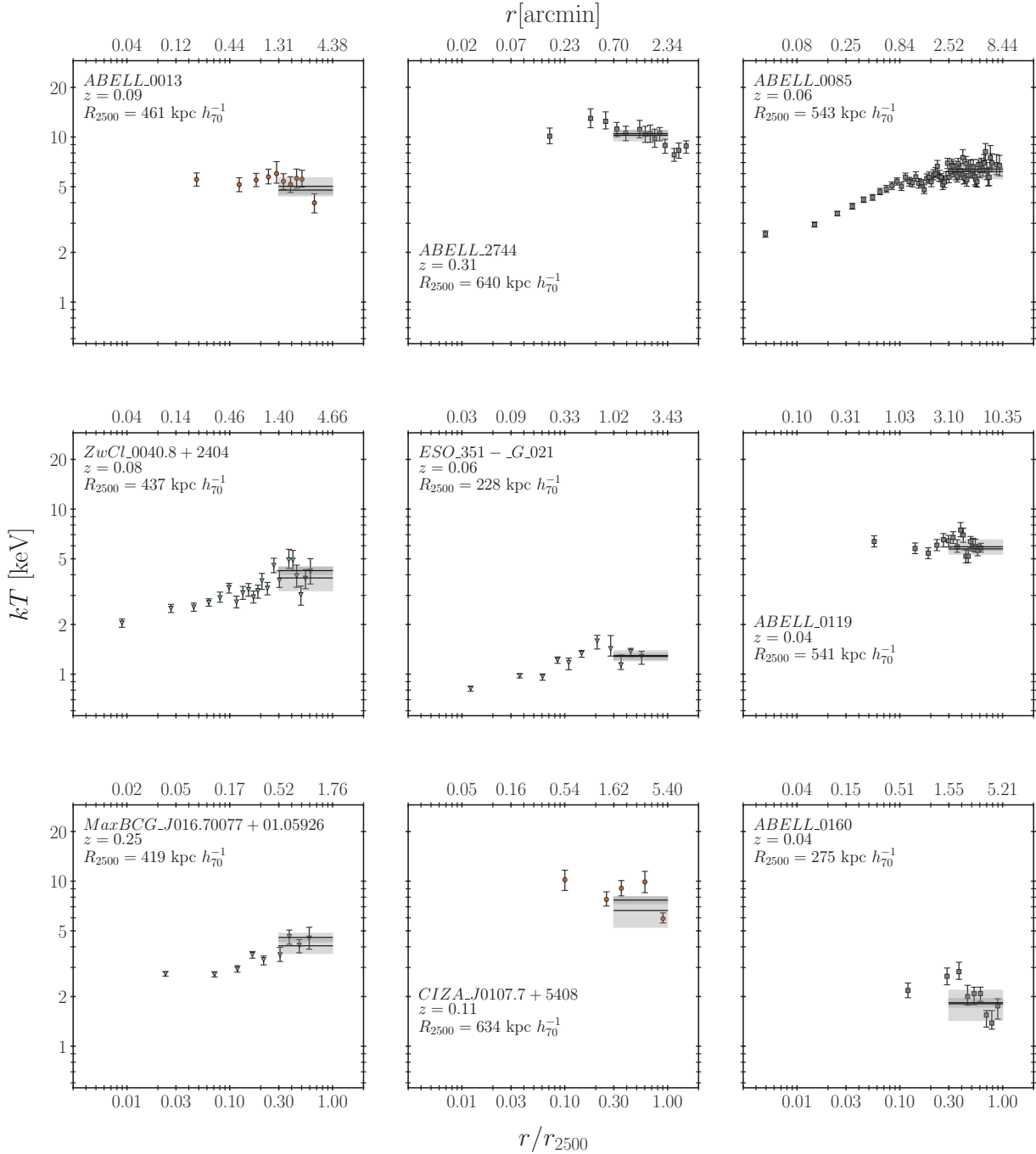


Figure C.1: Radial temperature profile for clusters A0013 through A0160. Radial temperature profiles for the following clusters: A0013, A2744, A0085, 00408+2404, 351-021, A0119, 01670077+0105926, 01077+5408, A0160.

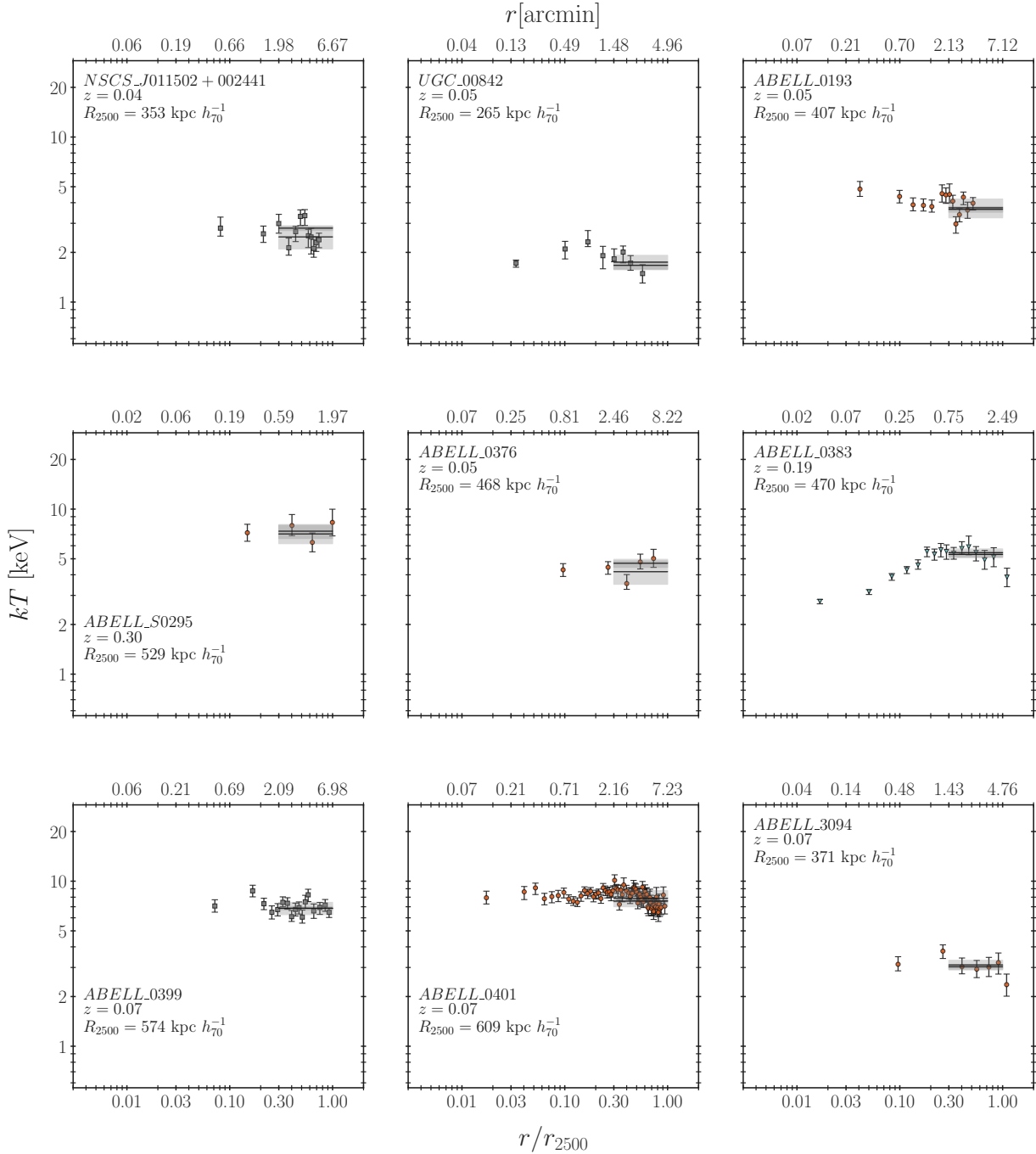


Figure C.2: Radial temperature profile for clusters 011502+002441 through A3094. Radial temperature profiles for the following clusters: 011502+002441, UGC00842, A0193, AS0295, A0376, A0383, A0399, A0401, A3094.

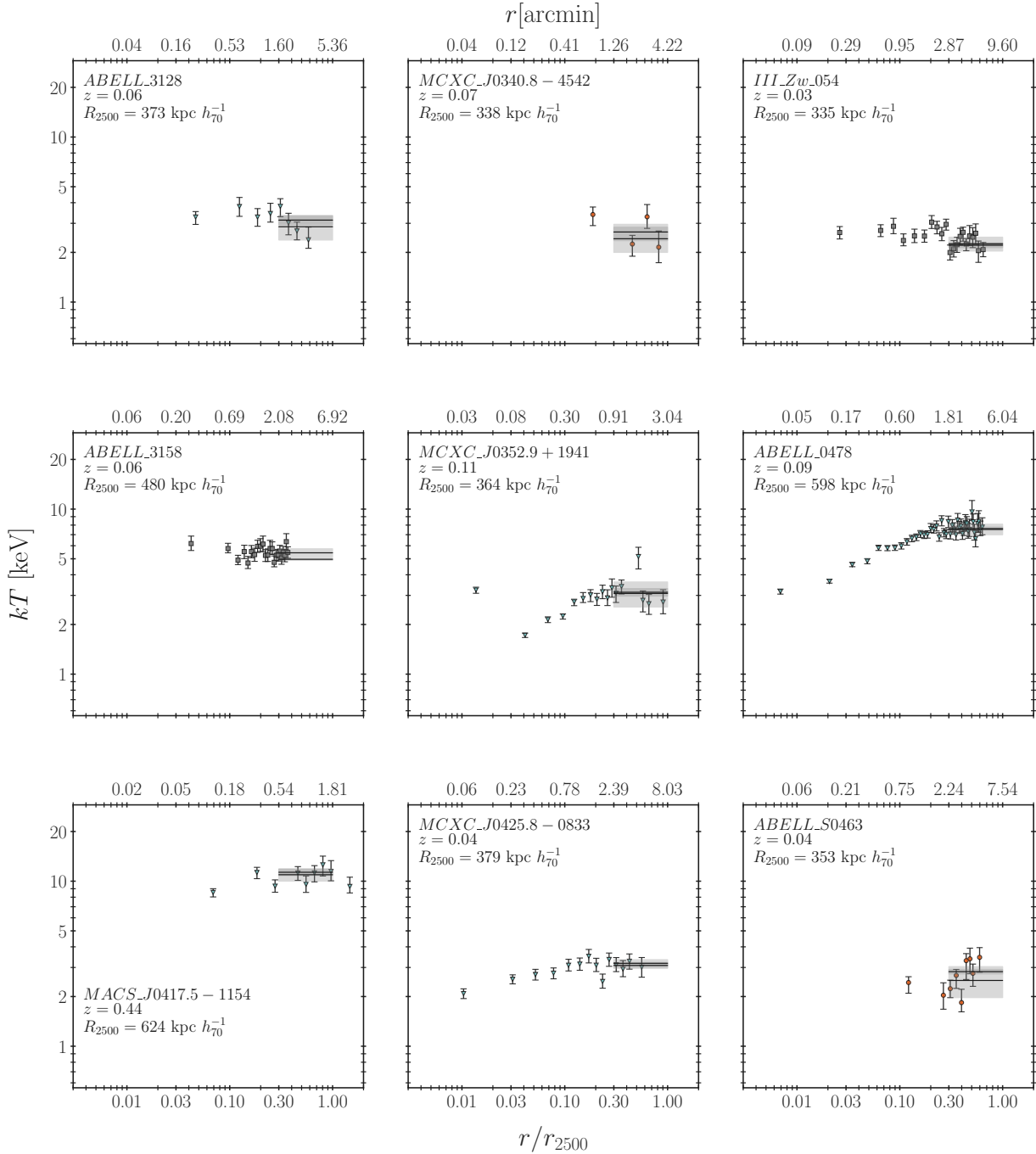


Figure C.3: Radial temperature profile for clusters A3128 through AS0463. Radial temperature profiles for the following clusters: A3128, 03408-4542, IIIZw054, A3158, 03529+1941, A0478, 04175-1154, 04258-0833, AS0463.

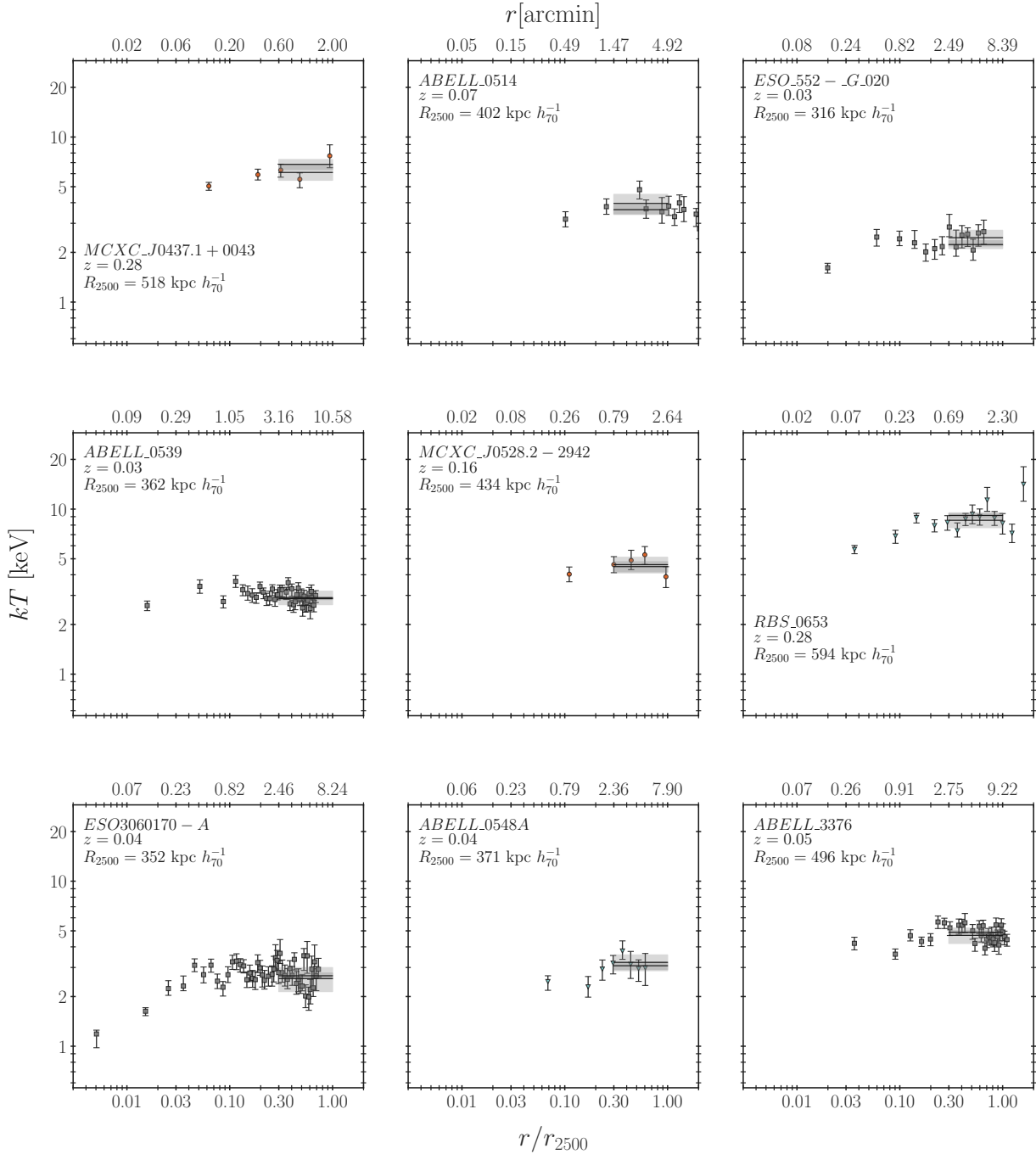


Figure C.4: **Radial temperature profile for clusters 04371+0043 through A3376.** Radial temperature profiles for the following clusters: 04371+0043, A0514, 552-020, A0539, 05282-2942, RBS0653, 3060170-, A0548A, A3376.

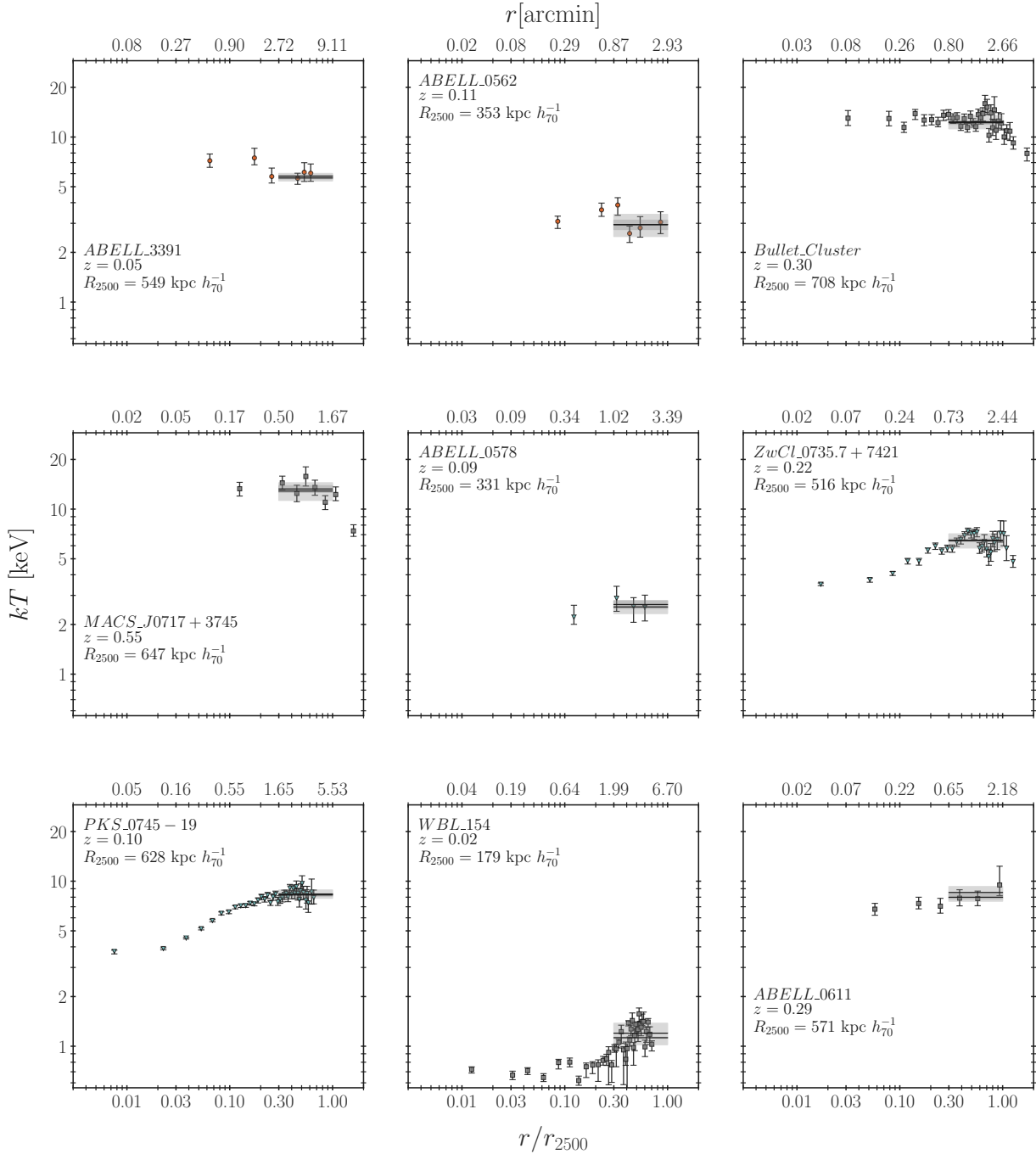


Figure C.5: Radial temperature profile for clusters A3391 through A0611. Radial temperature profiles for the following clusters: A3391, A0562, , 0717+3745, A0578, 07357+7421, PKS0745-19, WBL154, A0611.

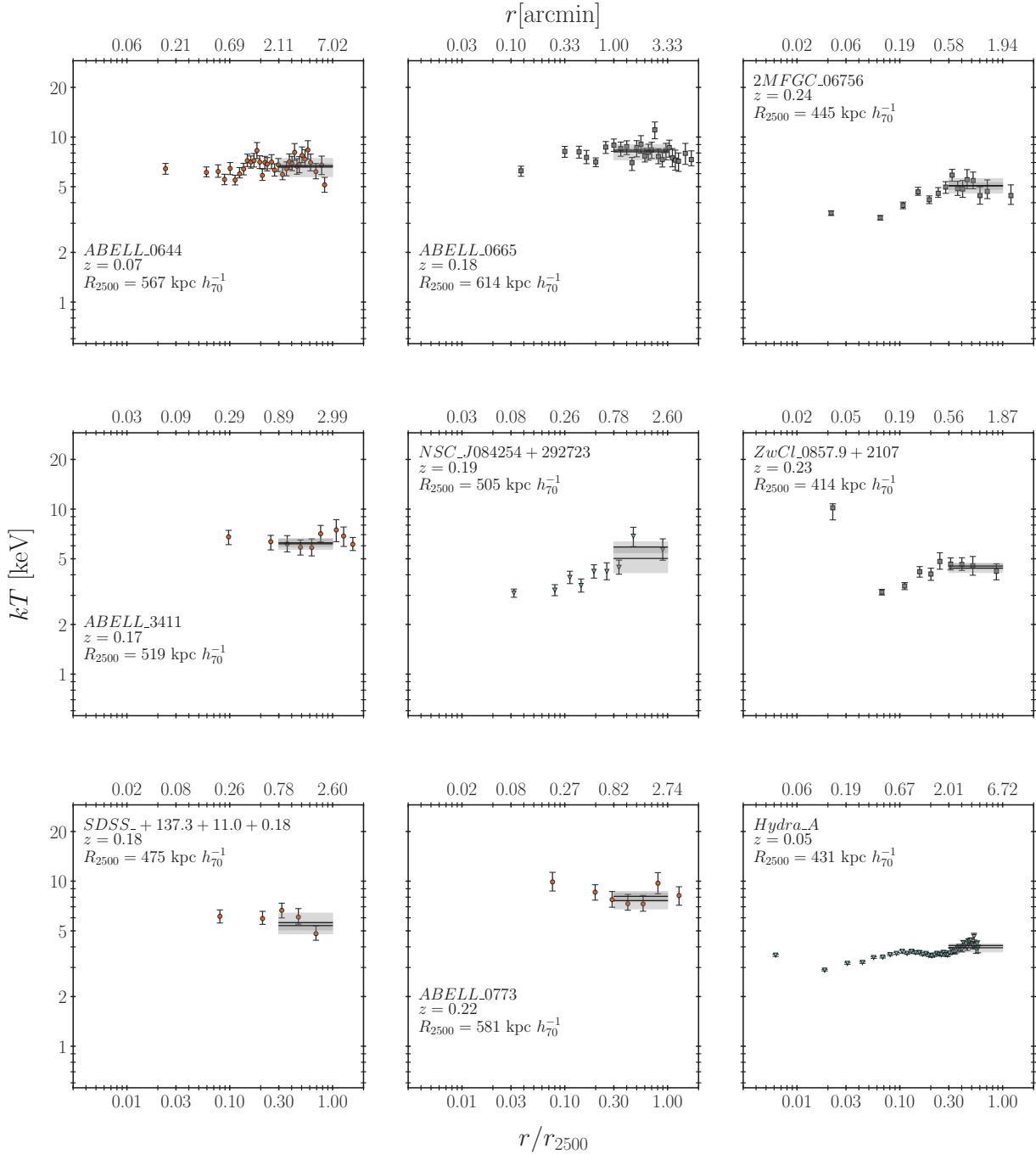


Figure C.6: Radial temperature profile for clusters A0644 through HydraA. Radial temperature profiles for the following clusters: A0644, A0665, 2MFGC06756, A3411, 084254+292723, 08579+2107, +1373+110+018, A0773, HydraA.

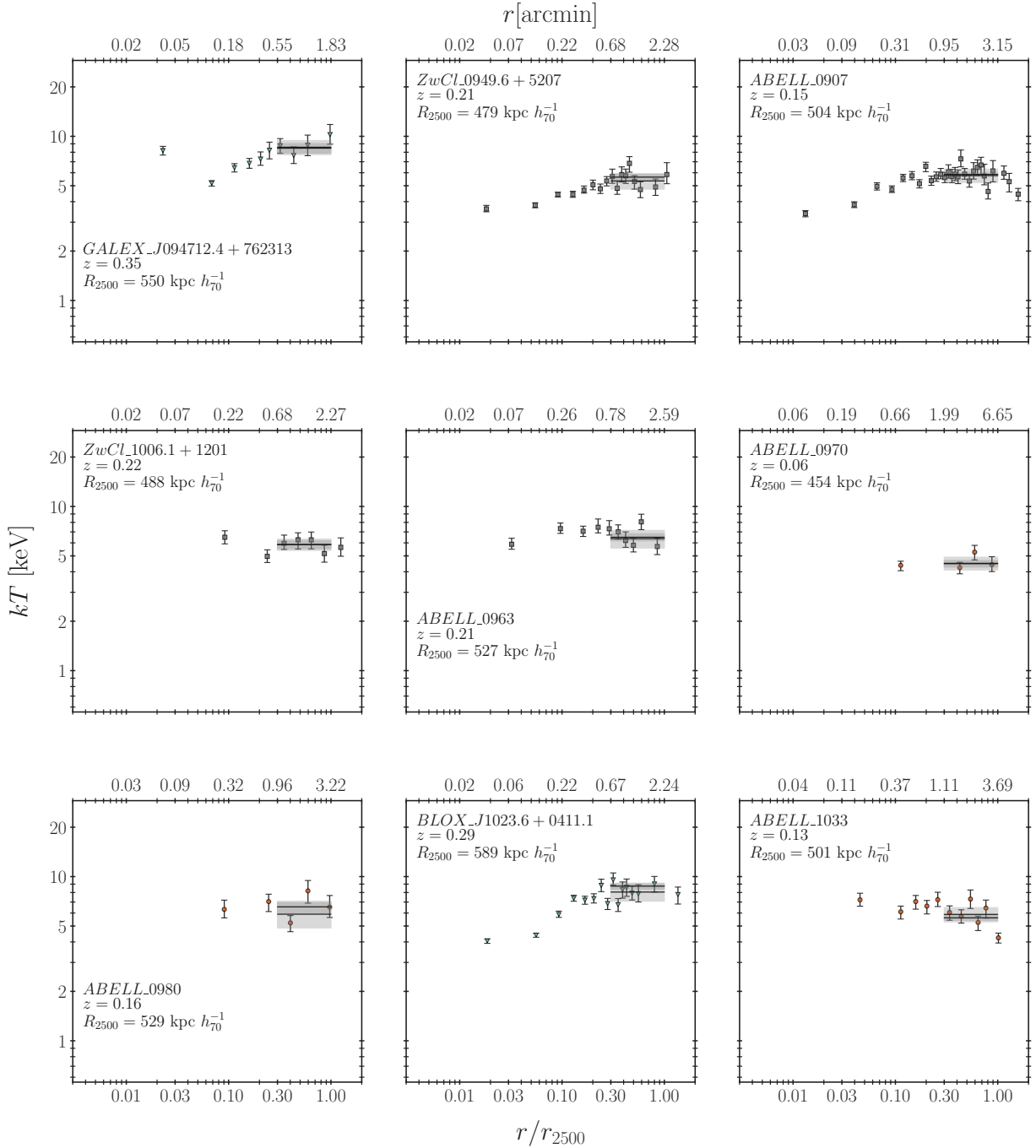


Figure C.7: **Radial temperature profile for clusters 0947124+762313 through A1033.** Radial temperature profiles for the following clusters: 0947124+762313, 09496+5207, A0907, 10061+1201, A0963, A0970, A0980, 10236+04111, A1033.

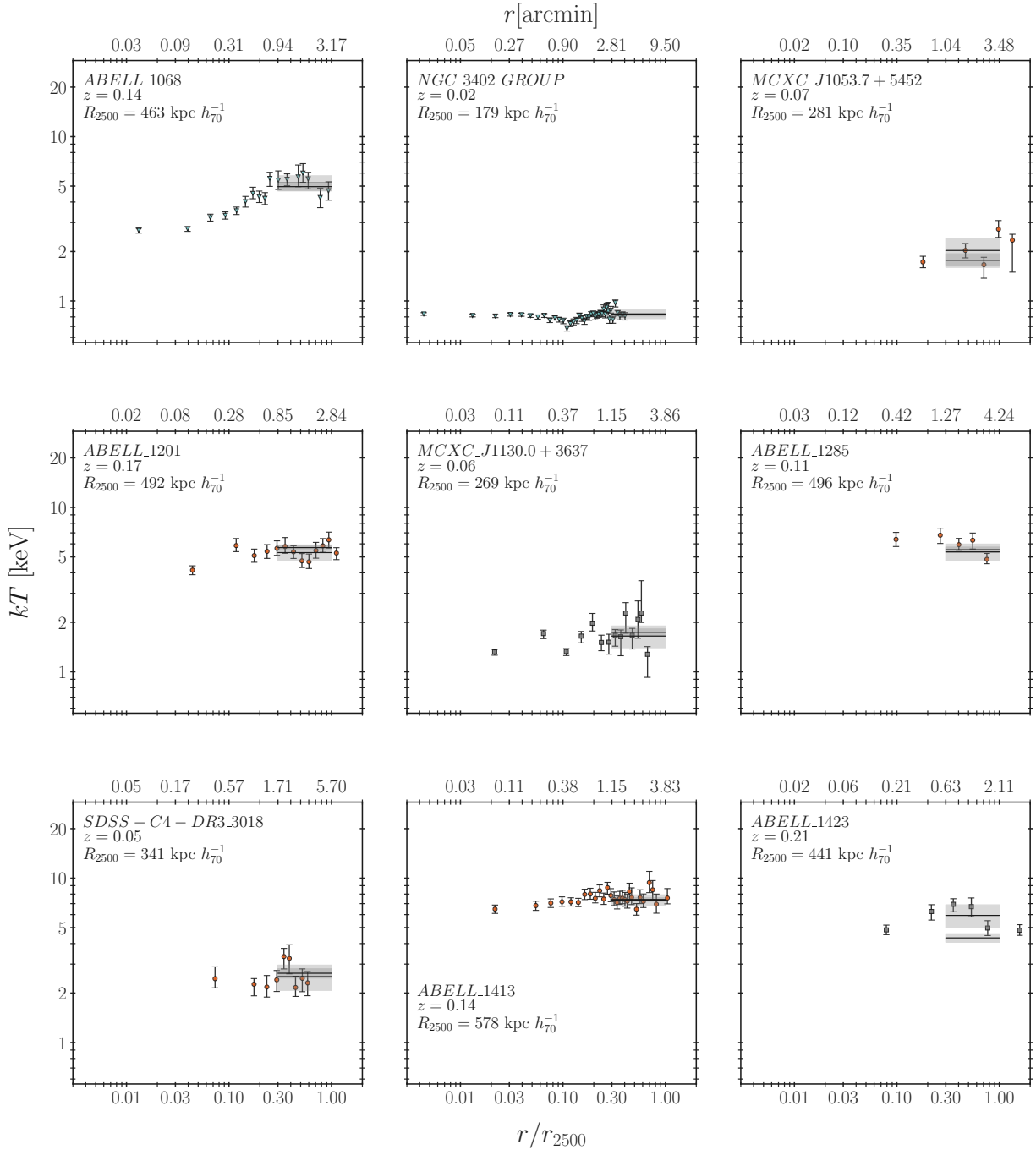


Figure C.8: Radial temperature profile for clusters A1068 through A1423. Radial temperature profiles for the following clusters: A1068, 3402, 10537+5452, A1201, 11300+3637, A1285, 4-33018, A1413, A1423.

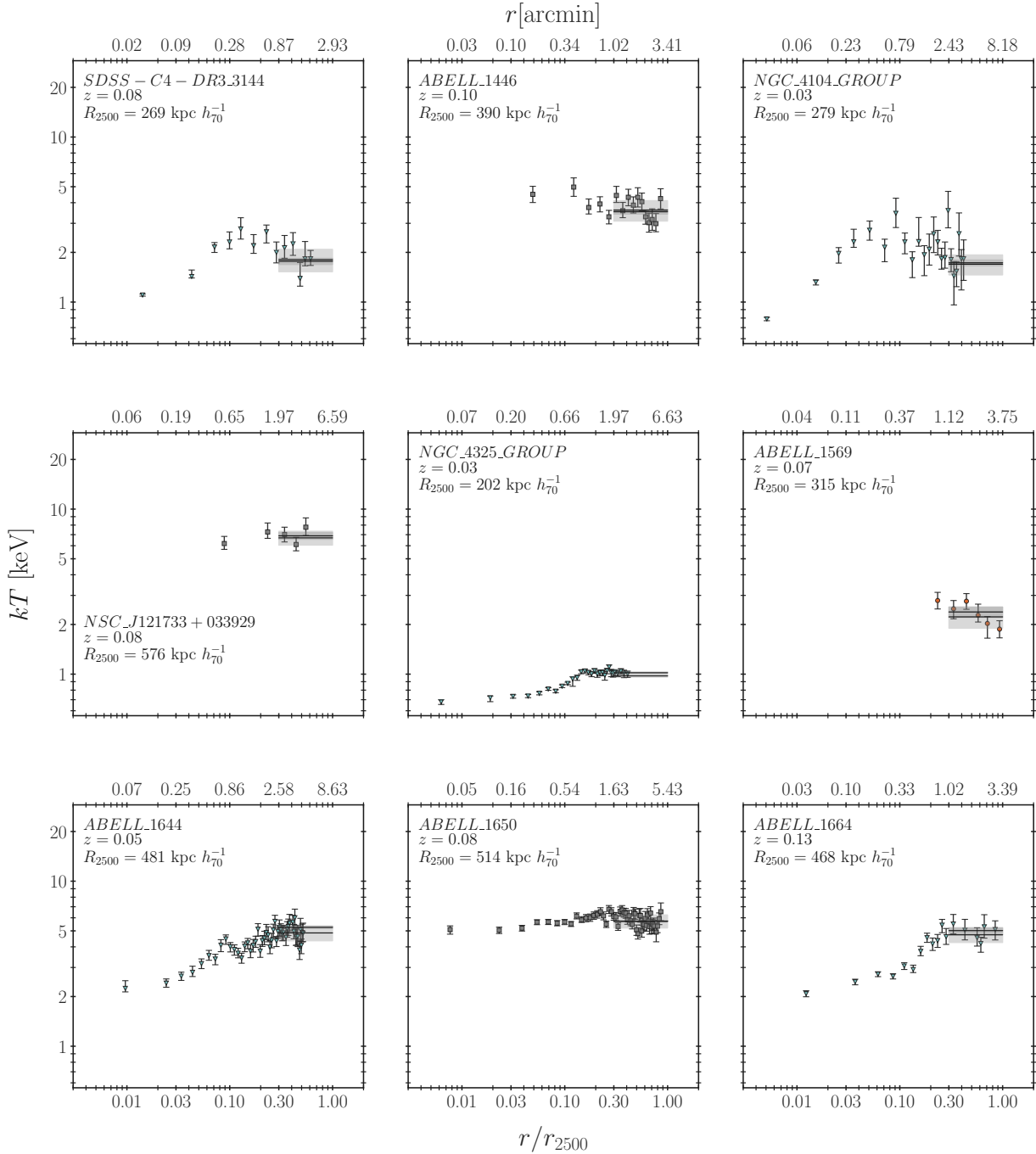


Figure C.9: Radial temperature profile for clusters 4-33144 through A1664. Radial temperature profiles for the following clusters: 4-33144, A1446, 4104, 121733+033929, 4325, A1569, A1644, A1650, A1664.

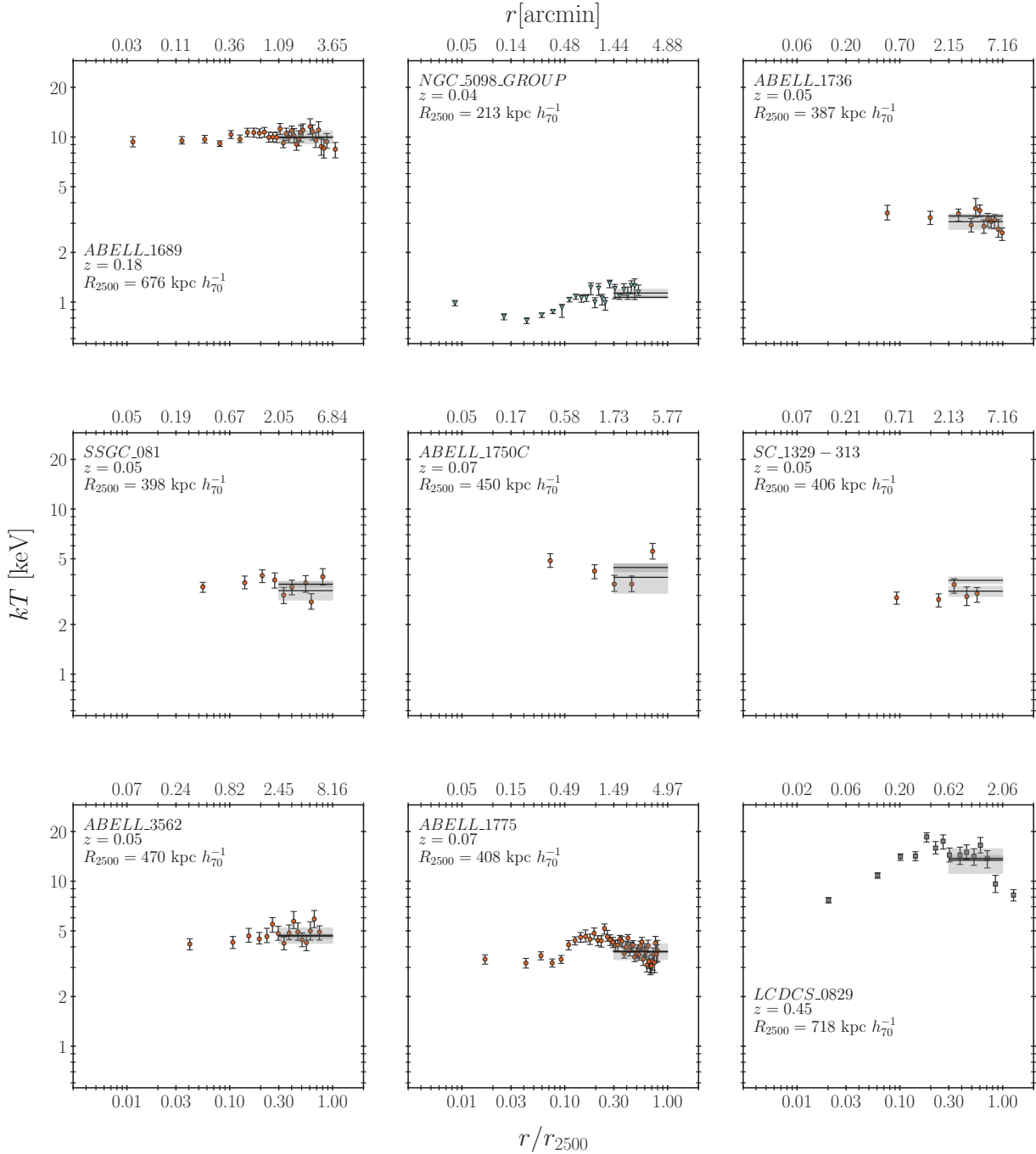


Figure C.10: **Radial temperature profile for clusters A1689 through LCDCS0829.** Radial temperature profiles for the following clusters: A1689, 5098, A1736, SSGC081, A1750C, SC1329-313, A3562, A1775, LCDCS0829.

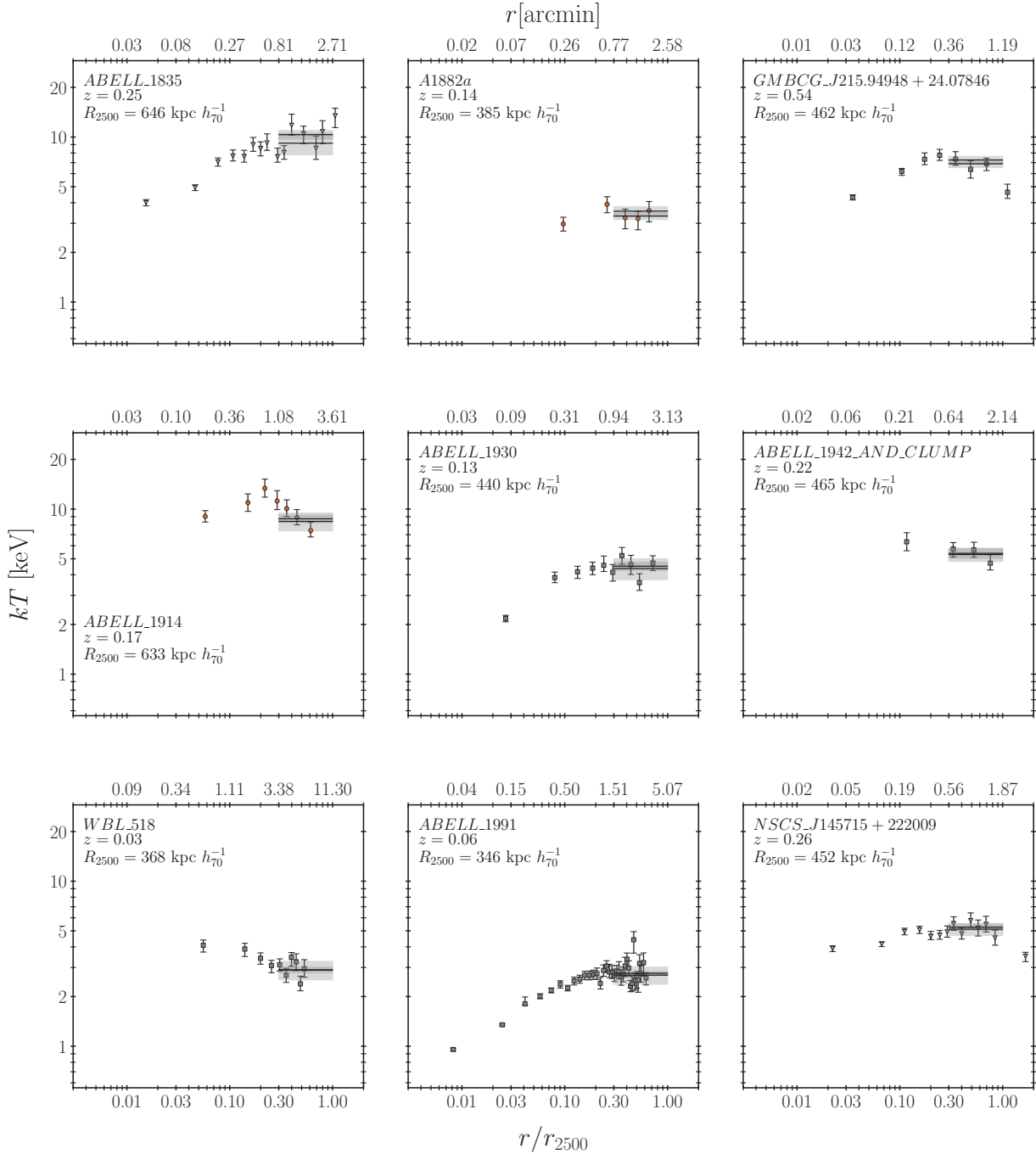


Figure C.11: **Radial temperature profile for clusters A1835 through 145715+222009.** Radial temperature profiles for the following clusters: A1835, A1882a, 21594948+2407846, A1914, A1930, 1942, WBL518, A1991, 145715+222009.

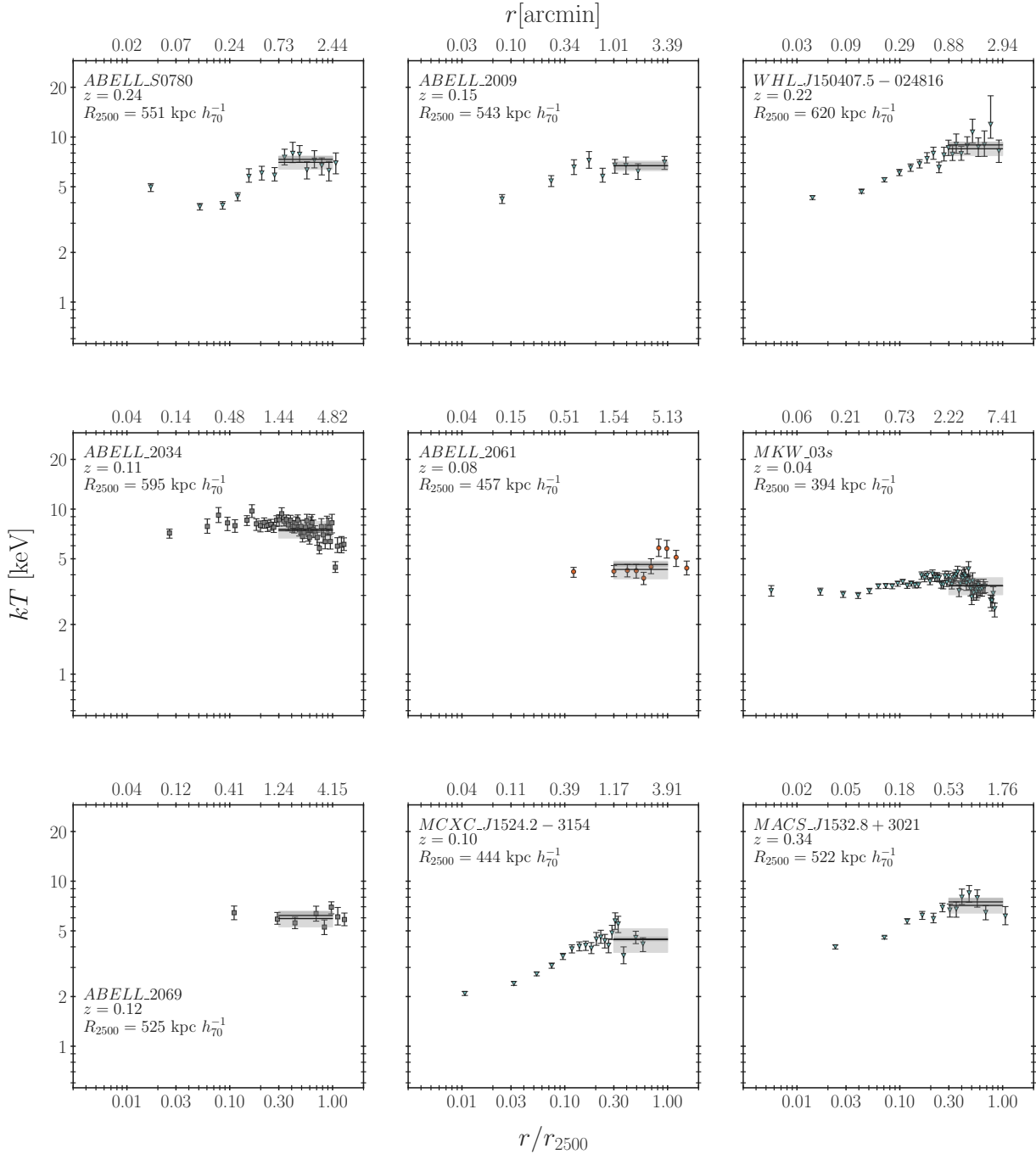


Figure C.12: **Radial temperature profile for clusters AS0780 through 15328+3021.** Radial temperature profiles for the following clusters: AS0780, A2009, 1504075-024816, A2034, A2061, MKW03s, A2069, 15242-3154, 15328+3021.

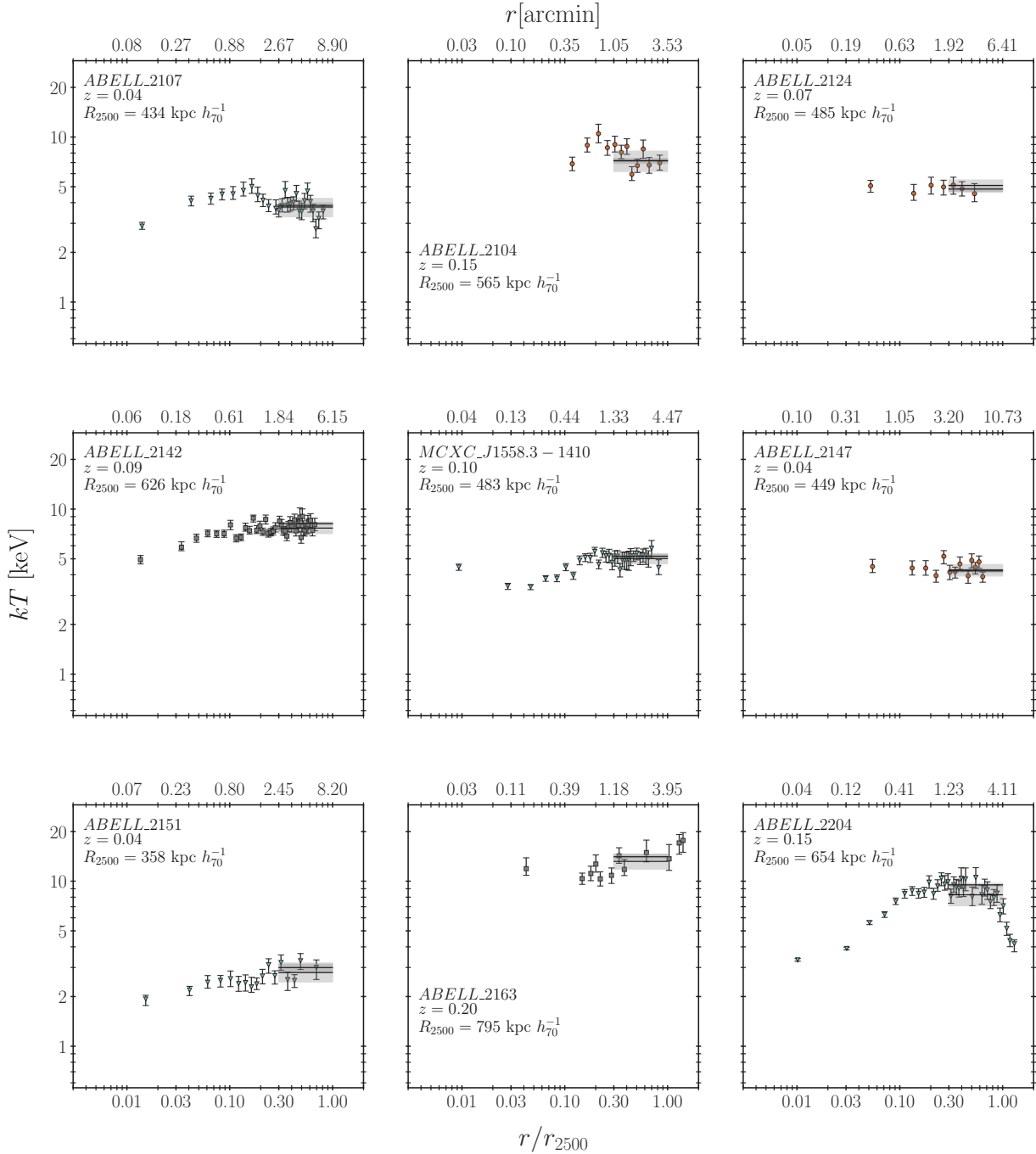


Figure C.13: Radial temperature profile for clusters A2107 through A2204. Radial temperature profiles for the following clusters: A2107, A2104, A2124, A2142, 15583-1410, A2147, A2151, A2163, A2204.

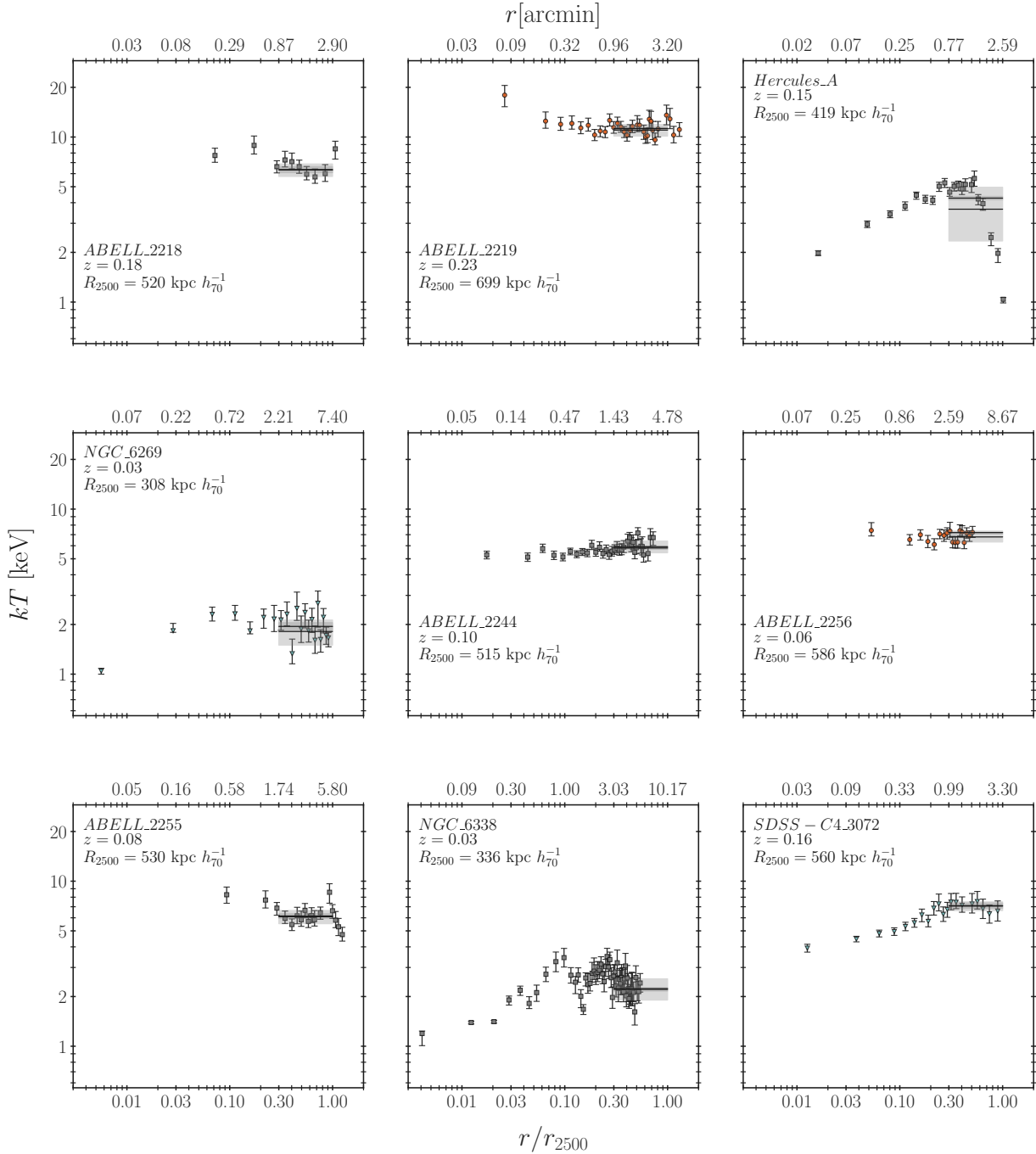


Figure C.14: Radial temperature profile for clusters A2218 through 43072. Radial temperature profiles for the following clusters: A2218, A2219, HerculesA, NGC6269, A2244, A2256, A2255, NGC6338, 43072.

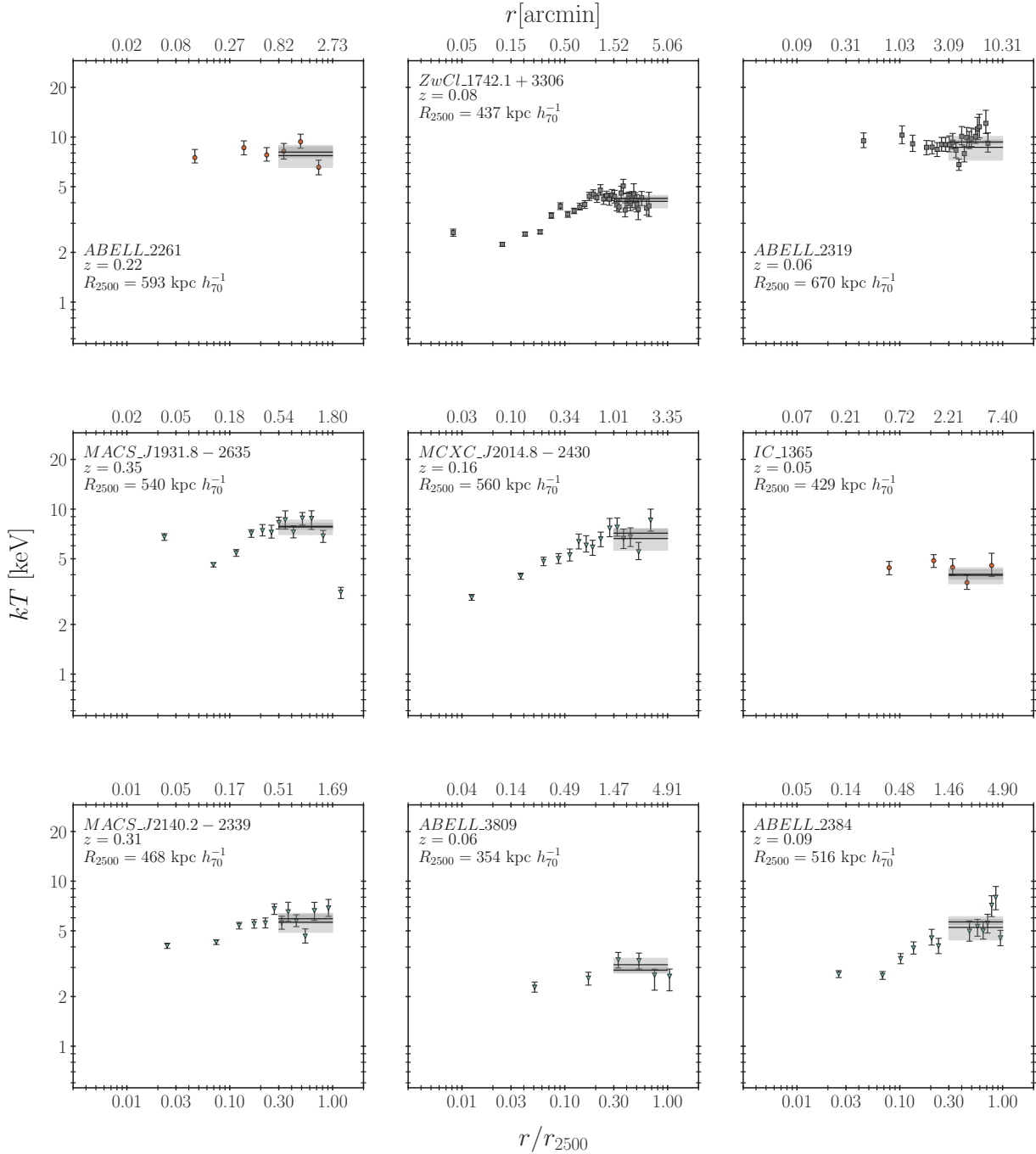


Figure C.15: Radial temperature profile for clusters A2261 through A2384. Radial temperature profiles for the following clusters: A2261, 17421+3306, A2319, 19318-2635, 20148-2430, IC1365, 21402-2339, A3809, A2384.

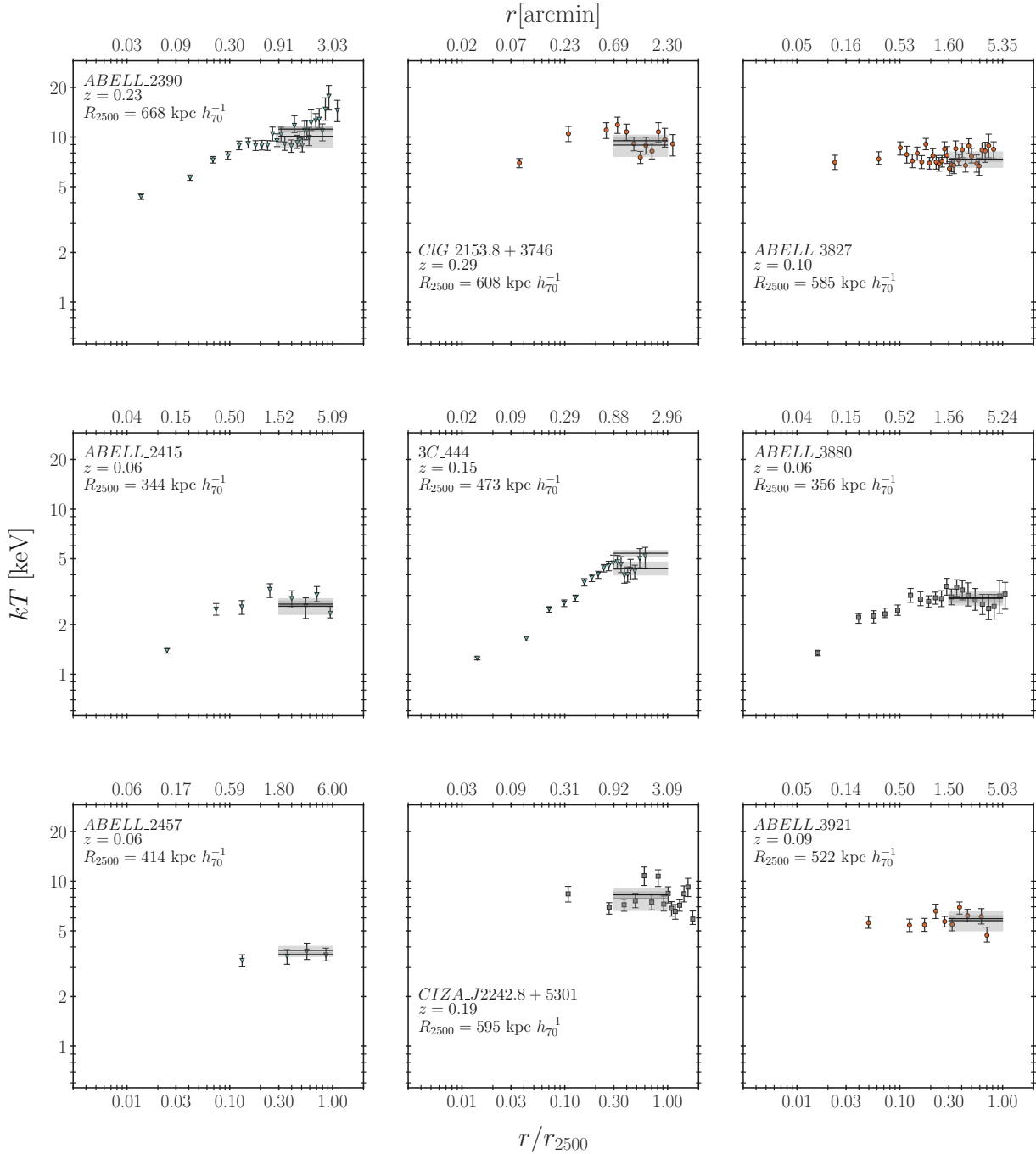


Figure C.16: Radial temperature profile for clusters A2390 through A3921. Radial temperature profiles for the following clusters: A2390, 21538+3746, A3827, A2415, 3C444, A3880, A2457, 22428+5301, A3921.

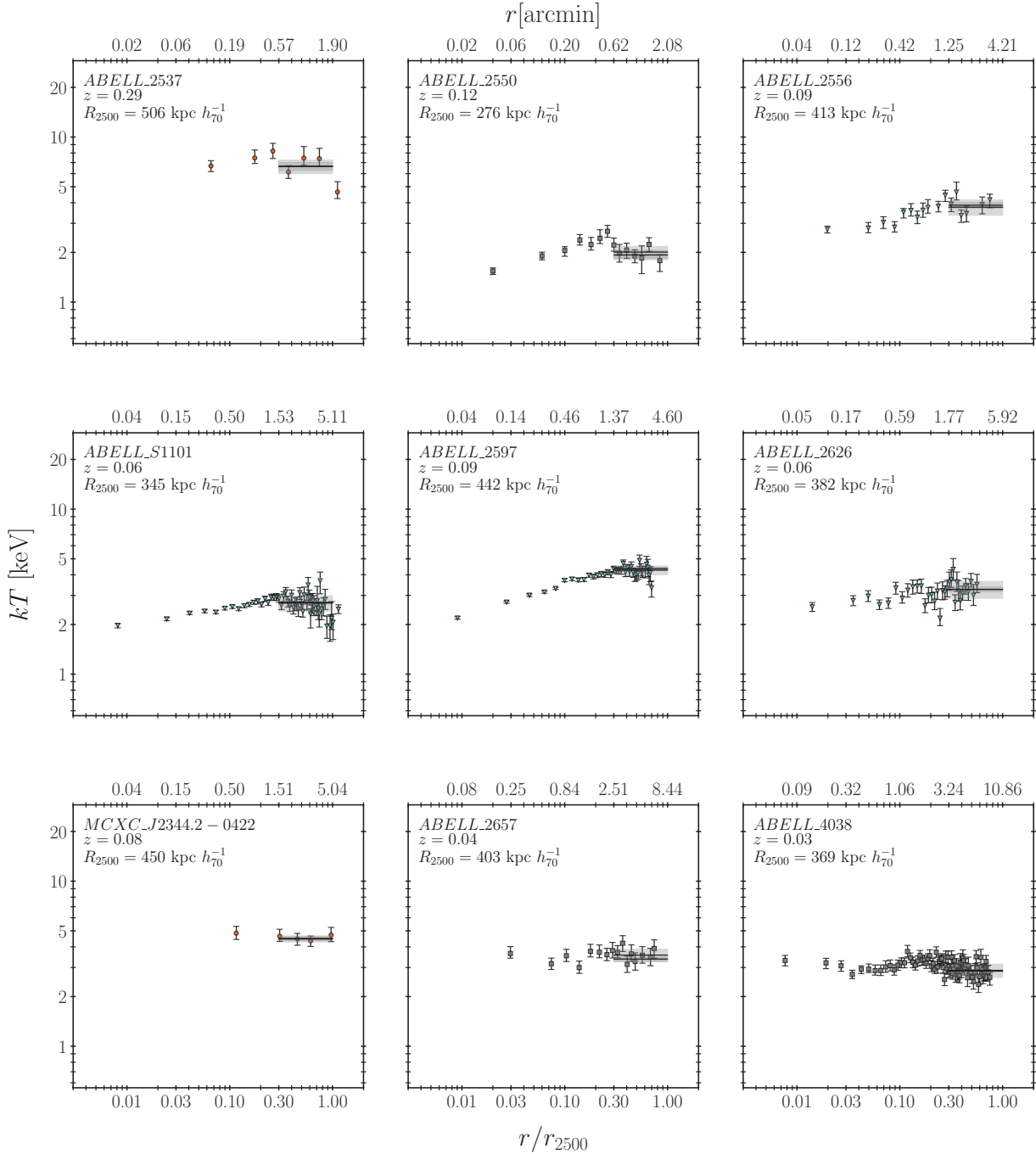


Figure C.17: Radial temperature profile for clusters A2537 through A4038. Radial temperature profiles for the following clusters: A2537, A2550, A2556, AS1101, A2597, A2626, 23442-0422, A2657, A4038.

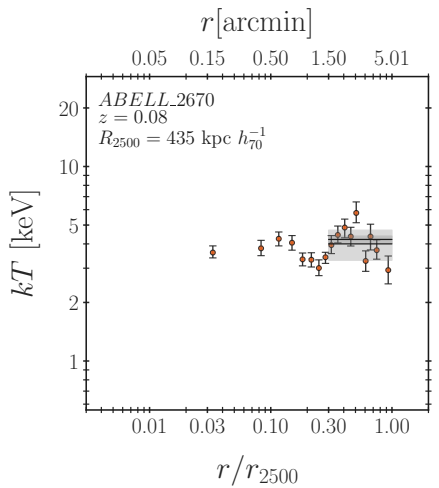


Figure C.18: **Radial temperature profile for A2670.** Radial temperature profile for A2670.

BIBLIOGRAPHY

BIBLIOGRAPHY

- Abell, G. O. 1958, *The Astrophysical Journal Supplement Series*, 3, 211
- Ahn, C. P., Alexandroff, R., Allende Prieto, C., et al. 2012, *The Astrophysical Journal Supplement Series*, 203, 21
- Alam, S., Albareti, F. D., Allende Prieto, C., et al. 2015, *The Astrophysical Journal Supplement*, 219, 12
- Anders, E., & Grevesse, N. 1989a, *Geochimica et Cosmochimica Acta*, 53, 197
- . 1989b, *Geochimica et Cosmochimica Acta*, 53, 197
- Anderson, M. E., Bregman, J. N., Butler, S. C., & Mullis, C. R. 2009, *The Astrophysical Journal*, 698, 317
- Andrade-Santos, F., Jones, C., Forman, W. R., et al. 2017, *The Astrophysical Journal*, 843, 76
- Arnaud, K. A. 1996, in *Astronomical Society of the Pacific Conference Series*, Vol. 101, *Astro-nomical Data Analysis Software and Systems V*, ed. G. H. Jacoby & J. Barnes, 17
- Arnaud, M., Aghanim, N., & Neumann, D. M. 2002, *Astronomy & Astrophysics*, 389, 1
- Arnaud, M., & Evrard, A. E. 1999, *Monthly Notices of the Royal Astronomical Society*, 305, 631
- Baldi, A., Ettori, S., Molendi, S., et al. 2012, *Astronomy & Astrophysics*, 537, A142
- Balestra, I., Tozzi, P., Ettori, S., et al. 2007, *Astronomy & Astrophysics*, 462, 429
- Balestra, I., Tozzi, P., Ettori, S., et al. 2006, *Astronomy & Astrophysics*, 462, 429
- Bennett, C. L., Hill, R. S., Hinshaw, G., et al. 2011, *The Astrophysical Journal Supplement Series*, 192, 17
- Biffi, V., Mernier, F., & Medvedev, P. 2018, *Space Science Reviews*, 214, doi:10.1007/s11214-018-0557-7
- Biffi, V., Planelles, S., Borgani, S., et al. 2017a, *Monthly Notices of the Royal Astronomical Society*, 468, 531
- . 2017b, *Monthly Notices of the Royal Astronomical Society*, 468, 531
- Bleem, L. E., Stalder, B., de Haan, T., et al. 2015, *The Astrophysical Journal Supplement Series*, 216, 27
- Böhringer, H., & Werner, N. 2009, *The Astronomy and Astrophysics Review*, 18, 127
- Borgani, S., Fabjan, D., Tornatore, L., et al. 2008, *Space Science Reviews*, 134, 379

- Bower, R. G. 1997, Monthly Notices of the Royal Astronomical Society, 288, 355
- Bower, R. G., Benson, A. J., Malbon, R., et al. 2006, Monthly Notices of the Royal Astronomical Society, 370, 645
- Bradt, H., Mayer, W., Naranan, S., Rappaport, S., & Spada, G. 1967, The Astrophysical Journal, 150, L199
- Branduardi-Raymont, G., Fabricant, D., Feigelson, E., et al. 1981, The Astrophysical Journal, 248, 55
- Branduardi-Raymont, G., Mason, K. O., Murdin, P. G., & Martin, C. 1985, Monthly Notices of the Royal Astronomical Society, 216, 1043
- Briel, U. G., Henry, J. P., & Boehringer, H. 1992, Astronomy & Astrophysics, 259, L31
- Buote, D. A. 2000, Monthly Notices of the Royal Astronomical Society, 311, 176
- Caminha, G. B., Grillo, C., Rosati, P., et al. 2017, Astronomy & Astrophysics, 600, A90
- Cavagnolo, K. W., Donahue, M., Voit, G. M., & Sun, M. 2009, The Astrophysical Journal Supplement Series, 182, 12
- Cavaliere, A., Menci, N., & Tozzi, P. 1997, The Astrophysical Journal, 484, L21
- Colgate, S. A. 1979, The Astrophysical Journal, 232, 404
- Craig, M., Crawford, S., Seifert, M., et al. 2017, astropy/ccdproc: v1.3.0.post1, doi:10.5281/zenodo.1069648
- De Grandi, S., Ettori, S., Longhetti, M., & Molendi, S. 2004, Astronomy & Astrophysics, 419, 7
- De Grandi, S., & Molendi, S. 2001, The Astrophysical Journal, 551, 153
- Donahue, M., Horner, D. J., Cavagnolo, K. W., & Voit, G. M. 2006, The Astrophysical Journal, 643, 730
- Donahue, M., Scharf, C. A., Mack, J., et al. 2002, The Astrophysical Journal, 569, 689
- Eckert, D., Molendi, S., & Paltani, S. 2011, Astronomy & Astrophysics, 526, A79
- Edge, A. C., & Stewart, G. C. 1991, Monthly Notices of the Royal Astronomical Society, 252, 414
- Ettori, S. 2005, Monthly Notices of the Royal Astronomical Society, 362, 110
- Ettori, S., Baldi, A., Balestra, I., et al. 2015, Astronomy & Astrophysics, 578, A46
- Ettori, S., Tozzi, P., Borgani, S., & Rosati, P. 2004, Astronomy & Astrophysics, 417, 13
- Fabian, A. C. 1994, Annual Review of Astronomy and Astrophysics, 32, 277
- Fabian, A. C., Arnaud, K. A., Bautz, M. W., & Tawara, Y. 1994, The Astrophysical Journal, 436, L63

- Foreman-Mackey, D., Hogg, D. W., Lang, D., & Goodman, J. 2013, Publications of the Astronomical Society of the Pacific, 125, 306
- Forman, W., Kellogg, E., Gursky, H., Tananbaum, H., & Giacconi, R. 1972, The Astrophysical Journal, 178, 309
- Freeman, P., Doe, S., & Siemiginowska, A. 2001, Astronomical Data Analysis
- Fruscione, A., McDowell, J. C., Allen, G. E., et al. 2006, in Society of Photo-Optical Instrumentation Engineers (SPIE) Conference Series, Vol. 6270, Society of Photo-Optical Instrumentation Engineers (SPIE) Conference Series, 62701V
- Fukazawa, Y., Ohashi, T., Fabian, A. C., et al. 1994, Publications of the Astronomical Society of Japan, 46, L55
- Goodman, J., & Weare, J. 2010, Communications in Applied Mathematics and Computational Science, 5, 65
- Gursky, H., Kellogg, E., Murray, S., et al. 1971, The Astrophysical Journal, 167, L81
- Horne, K. 1986, Publications of the Astronomical Society of the Pacific, 98, 609
- Hubble, E. 1936, The Astrophysical Journal, 84, 517
- Jones, C., & Forman, W. 1984, The Astrophysical Journal, 276, 38
- . 1999, The Astrophysical Journal, 511, 65
- Kaastra, J. S., Mewe, R., & Nieuwenhuijzen, H. 1996, in UV and X-ray Spectroscopy of Astrophysical and Laboratory Plasmas, 411–414
- Kaiser, N. 1986, Monthly Notices of the Royal Astronomical Society, 222, 323
- Leccardi, A., & Molendi, S. 2008, Astronomy & Astrophysics, 487, 461
- Leccardi, A., Rossetti, M., & Molendi, S. 2010, Astronomy & Astrophysics, 510, A82
- Liedahl, D. A., Osterheld, A. L., & Goldstein, W. H. 1995, The Astrophysical Journal, 438, L115
- Lucas, R. A., Desjardins, T. D., & STScI ACS (Advanced CameraSurveys) Team. 2018, in American Astronomical Society Meeting Abstracts, Vol. 232, American Astronomical Society Meeting Abstracts #232, 119.03
- Mantz, A. B., Allen, S. W., Morris, R. G., et al. 2017, Monthly Notices of the Royal Astronomical Society, 472, 2877
- Markevitch, M. 1998, The Astrophysical Journal, 504, 27
- Marsh, T. R. 1989, Publications of the Astronomical Society of the Pacific, 101, 1032
- Maughan, B. J., Giles, P. A., Randall, S. W., Jones, C., & Forman, W. R. 2012, Monthly Notices of the Royal Astronomical Society, 421, 1583

- Maughan, B. J., Giles, P. A., Randall, S. W., Jones, C., & Forman, W. R. 2012, Monthly Notices of the Royal Astronomical Society, 421, 1583
- Maughan, B. J., Jones, C., Forman, W., & Van Speybroeck, L. 2008, The Astrophysical Journal Supplement Series, 174, 117
- McDonald, M., Stalder, B., Bayliss, M., et al. 2016, The Astronomical Journal, 817, 86
- McDonald, M., Bulbul, E., Haan, T. d., et al. 2016, The Astrophysical Journal, 826, 124
- McNamara, B., & Nulsen, P. 2007, Annual Review of Astronomy and Astrophysics, 45, 117
- Meekins, J. F., Fritz, G., Chubb, T. A., Friedman, H., & Henry, Richard, C. 1971, Nature, 231, 107
- Mernier, F., de Plaa, J., Kaastra, J. S., et al. 2017, Astronomy & Astrophysics, 603, A80
- Mernier, F., Biffi, V., Yamaguchi, H., et al. 2018, Space Science Reviews, 214, doi:10.1007/s11214-018-0565-7
- Migkas, K., Schellenberger, G., Reiprich, T. H., et al. 2020, Astronomy & Astrophysics, 636, A15
- Mitchell, R. J., & Culhane, J. L. 1977, Monthly Notices of the Royal Astronomical Society, 178, 75P
- Mitchell, R. J., Culhane, J. L., Davison, P. J. N., & Ives, J. C. 1976, Monthly Notices of the Royal Astronomical Society, 175, 29P
- Mittal, R., Hicks, A., Reiprich, T. H., & Jaritz, V. 2011, The Astrophysical Journal, 532, A133
- Mushotzky, R., Loewenstein, M., Arnaud, K. A., et al. 1996, The Astrophysical Journal, 466, 686
- Mushotzky, R. F. 1984, *Physica Scripta*, T7, 157
- Mushotzky, R. F., & Loewenstein, M. 1997, The Astrophysical Journal, 481, L63
- Neumann, D. M. 2005, Astronomy & Astrophysics, 439, 465
- Pearce, F. R., Thomas, P. A., Couchman, H. M. P., & Edge, A. C. 2000, Monthly Notices of the Royal Astronomical Society, 317, 1029
- Pence, W. D., Chiappetti, L., Page, C. G., Shaw, R. A., & Stobie, E. 2010, Astronomy & Astrophysics, 524, A42
- Peterson, J., & Fabian, A. 2006, Physics Reports, 427, 1
- Piffaretti, R., Arnaud, M., Pratt, G. W., Pointecouteau, E., & Melin, J. B. 2011, Astronomy & Astrophysics, 534, A109
- Ponman, T. J., Cannon, D. B., & Navarro, J. F. 1999, Nature, 397, 135
- Ponman, T. J., Sanderson, A. J. R., & Finoguenov, A. 2003, Monthly Notices of the Royal Astronomical Society, 343, 331

- Pratt, G. W., Böhringer, H., Croston, J. H., et al. 2006, *Astronomy & Astrophysics*, 461, 71
- Pratt, G. W., Croston, J. H., Arnaud, M., & Böhringer, H. 2009, *Astronomy & Astrophysics*, 498, 361
- Price-Whelan, A. M., Sipőcz, B. M., Günther, H. M., et al. 2018, *The Astronomical Journal*, 156, 123
- Rasia, E., Borgani, S., Murante, G., et al. 2015, *The Astrophysical Journal Supplement Series*, 813, L17
- Renzini, A. 1997, *The Astrophysical Journal*, 488, 35
- Rykoff, E. S., Rozo, E., Hollowood, D., et al. 2016, *The Astrophysical Journal Supplement*, 224, 1
- Sarazin, C. L. 1986, *Reviews of Modern Physics*, 58, 1
- Sarazin, C. L. 1988, *Sky and Telescope*, 76, 639
- Serlemitsos, P. J., Smith, B. W., Boldt, E. A., Holt, S. S., & Swank, J. H. 1977, *The Astrophysical Journal*, 211, L63
- Sifón, C., Menanteau, F., Hasselfield, M., et al. 2013, *The Astrophysical Journal*, 772, 25
- Smee, S. A., Barkhouser, R., Hope, S., et al. 2018, *Ground-based and Airborne Instrumentation for Astronomy VII*
- Stark, A. A., Gammie, C. F., Wilson, R. W., et al. 1992, *The Astrophysical Journal Supplement Series*, 79, 77
- Sun, M. 2012, *New Journal of Physics*, 14, 045004
- Tanaka, Y., Inoue, H., & Holt, S. S. 1994, *Publications of the Astronomical Society of Japan*, 46, L37
- Tody, D. 1986, *Instrumentation in Astronomy VI*
- Tody, D. 1993, in *Astronomical Society of the Pacific Conference Series*, Vol. 52, *Astronomical Data Analysis Software and Systems II*, ed. R. J. Hanisch, R. J. V. Brissenden, & J. Barnes, 173
- Torres-Robledo, S., & Briceño, C. 2019, *Astronomical Society of the Pacific Conference Series*, Vol. 523, *A Real-Time Data Reduction Pipeline for the Goodman Spectrograph*, ed. P. J. Teuben, M. W. Pound, B. A. Thomas, & E. M. Warner, 203
- Tozzi, P., & Norman, C. 2001, *The Astrophysical Journal*, 546, 63
- Valdarnini, R. 2003, *Monthly Notices of the Royal Astronomical Society*, 339, 1117
- Vikhlinin, A., Kravtsov, A., Forman, W., et al. 2006, *The Astrophysical Journal*, 640, 691
- Vikhlinin, A., Markevitch, M., Murray, S. S., et al. 2005, *The Astrophysical Journal*, 628, 655

- Vogelsberger, M., Marinacci, F., Torrey, P., et al. 2018, Monthly Notices of the Royal Astronomical Society, 474, 2073
- Voit, G. M. 2005, Reviews of Modern Physics, 77, 207
- Voit, G. M. 2005, Reviews of Modern Physics, 77, 207
- Webb, T. M. A., O'Donnell, D., Yee, H. K. C., et al. 2013, The Astronomical Journal, 146, 84
- Wells, D. C., Greisen, E. W., & Harten, R. H. 1981, Astronomy and Astrophysics, Supplement, 44, 363
- Wen, Z. L., & Han, J. L. 2015, The Astrophysical Journal, 807, 178
- Wen, Z. L., Han, J. L., & Liu, F. S. 2012, The Astrophysical Journal Supplement, 199, 34
- Werner, N., Durret, F., Ohashi, T., Schindler, S., & Wiersma, R. P. C. 2008, Space Science Reviews, 134, 337
- White, S. D. M., Briel, U. G., & Henry, J. P. 1993, Monthly Notices of the Royal Astronomical Society, 261, L8
- Willingale, R., Starling, R. L. C., Beardmore, A. P., Tanvir, N. R., & O'Brien, P. T. 2013, Monthly Notices of the Royal Astronomical Society, 431, 394
- Zwicky, F. 1933, Helvetica Physica Acta, 6, 110
- Zwicky, F. 1937, The Astrophysical Journal, 86, 217